

# Neutron beam monitoring for single-event effects testing

Lyn Hongyu Zhang

School of Computing, Engineering and Physical Sciences

University of Central Lancashire

A thesis submitted for the degree of

*Doctor of Philosophy*

January 2013

## Declaration

I declare that while registered as a candidate for the research degree, I have not been a registered candidate or enrolled student for another award of the University or other academic or professional institution, and that no material contained in the thesis has been used in any other submission for an academic award. I acknowledge that the PN photodiode sensor circuit used on this research project was designed by Dr Simon Platt, while the experimental data was collected from LANSCE in October 2010, from TSL ANITA in June 2010, from TRIUMF in August 2008 and from ASP in November 2009 by Dr Platt, from TRIUMF in November 2007 by Mr R. H. Edwards and Mr C. Allabush (of Goodrich Engine Control and Electrical Power Systems, Birmingham, United Kingdom), from TSL in April 2007 by Dr Platt and myself. All work presented in this thesis, unless otherwise acknowledged, has been undertaken by myself.

Lyn Hongyu Zhang

## Dedication

This thesis is dedicated to my late parents,  
who reared me and taught me by example.

## Acknowledgements

Many people have generously offered me their help on this project. First, I would like to acknowledge my Director of Studies, Dr Simon Platt, for his unfailing help and patience at all stages of this project. Moreover, the experimental data analyzed in this thesis was collected by Simon.

I would like to thank the Single Event Effects Design for Electronics Reliability (SEEDER) project, BAE SYSTEMS and Goodrich Engine Control and Electrical Power Systems for providing the beam time for this project.

Many thanks to Professor Lik-Kwan Shark, Dr Bogdan Matuszewski, Mr Bryan Cassels, Dr Zoltán Török and Dr Peter Dunne for their help in technical, theoretical matters and project meetings.

I am equally obliged for my husband Richard Xiao and my daughter Yina Xiao. Richard has provided great financial and moral support during this project; without him it would not be possible for me to complete this project. Yina always does what needs to be done at the right time. Richard and Yina have also helped me to polish my writing.

# Abstract

The research described in this thesis aims to develop a neutron beam monitoring system using silicon photodiodes as the detecting elements for accelerated testing of electronics against neutron-induced single event effects (SEEs). The system can measure the transmission along the neutron beam line where several devices are tested simultaneously, allowing beam degradation by upstream experiments to be taken into account.

In signal processing, the pulse events from the output of the sensor are extracted by using a matched filter. This technique allows the pulse events to be detected effectively at a low false event rate. The pulse arrival times are acquired using the nonparalyzable counting system, which allows the interaction rates to be determined either indirectly based on the decay constant of the pulse interval distributions or directly on the basis of detection rates and sensor pulse widths. The optimum of sensor pulse width has been investigated in order to achieve the maximum of probability of detection with adequate energy resolution. A series of calculations have been undertaken to verify the correct operation of the detection software and to investigate system performance variations.

Results from irradiations at various neutron facilities where SEEs experiments can be carried out, such as Los Alamos Neutron Science Center (LANSCE), Tri-University Meson Facility (TRIUMF) and The Svedberg Laboratory (TSL) neutron beam, are presented and analyzed. The measurement of transmission in the neutron beam can be made via the measured pulse height spectra, pulse interval distributions and responses of the sensor irradiated. As the beam can be scattered, absorbed or enhanced by upstream devices, there are likely to be fluctuations in the

transmission along the neutron beam, which can also be characterized by the beam monitoring system.

The recommended protocols for beam monitoring used at each neutron facility are investigated. At a low interaction rate, the protocols depend on the neutron fluence provided by the facility and the response of the sensor. At a high interaction rate, the probability of detection of the sensor should be determined first, and then the protocols are based on the probability of detection, neutron fluence and the response. In this thesis, the protocols of the beam monitoring system for use at ISIS ChipIr are also predicted on the basis of the pulse interval distributions and the mean of detected energy.

Based on the work undertaken in the project and presented in this thesis, suggestions are put forward for improving the monitoring system. Geant4 techniques can be used to model pulse height spectra so as to enable direct comparisons between theoretical simulations and experimental results. Furthermore, the protocols for beam monitoring for use at ChipIr as recommended in this thesis will be verified when neutron beams become available in the future.

# Contents

Acronyms . . . . .	xxiii
List of symbols . . . . .	xxv
<b>1 Introduction</b>	<b>1</b>
1.1 Single-event effects caused by cosmic rays in the atmosphere . . . . .	1
1.2 Aim and objectives of the research . . . . .	13
1.3 Neutron detectors and beam monitoring . . . . .	14
1.3.1 Neutron detectors used at facilities . . . . .	15
1.3.2 Semiconductor neutron detectors . . . . .	17
1.4 Pulse amplification and shaping techniques . . . . .	21
1.5 An overview of the photodiode beam monitoring system . . . . .	24
1.6 The organization of this thesis . . . . .	26
<b>2 Beam monitoring design</b>	<b>29</b>
2.1 Introduction . . . . .	29

2.2	Overview of the beam monitoring system . . . . .	30
2.3	The photodiode detector circuit and its pulse shapes . . . . .	33
2.4	Signal processing system . . . . .	41
2.4.1	Nonparalyzable counting system . . . . .	42
2.4.2	Matched filter . . . . .	45
2.4.3	Estimation . . . . .	47
2.4.4	Determining beam monitoring system threshold level . . . . .	48
2.4.5	Rao test detection . . . . .	48
2.4.6	Calculation . . . . .	51
2.4.6.1	Calculation only with pile-up effect . . . . .	52
2.4.6.2	Calculation only with noise effect . . . . .	54
2.4.6.3	Calculation with both pile-up and noise effects . . . . .	58
2.5	Selection of the beam monitoring system parameters . . . . .	65
2.5.1	Determine minimum collected energy . . . . .	65
2.5.2	Signal-to-noise ratio (SNR) . . . . .	69
2.5.3	Optimum pulse width . . . . .	70
2.5.3.1	Maximum probability of detection . . . . .	70
2.5.3.2	Effect of sampling resolution on diode neutron sensor performance . . . . .	75

2.6	Software . . . . .	78
2.7	Conclusion . . . . .	78
<b>3</b>	<b>Beam monitor experimental results</b>	<b>81</b>
3.1	Introduction . . . . .	81
3.2	Properties of the output of the beam monitoring system . . . . .	82
3.2.1	Pulse height spectra and pulse interval distribution . . . . .	82
3.2.2	Photodiode sensor response measurements . . . . .	85
3.3	Neutron facilities testing . . . . .	86
3.4	Experimental results . . . . .	90
3.4.1	Neutron beam transmission measurements at LANSCE . . . . .	90
3.4.1.1	Sensor characterization at the upstream position . . . . .	91
3.4.1.2	Effect of an aluminum scatterer on neutron beam fluence measurements . . . . .	100
3.4.1.3	Effect of upstream devices on neutron beam fluence measurements . . . . .	107
3.4.1.4	LANSCE photodiode response measurements . . . . .	115
3.4.2	Effect of the photodiode window . . . . .	116
3.4.3	Effect of neutron interactions in the amplifier circuit . . . . .	121
3.4.4	Effect of the thermal neutron interaction with sensors . . . . .	122

3.4.5	Effect of the photodiode doping profile . . . . .	123
3.4.6	Effect of the sensor pulse width . . . . .	129
3.4.7	Effect of neutron activation and test results at TSL . . . . .	131
3.4.8	TSL ANITA testing in 2010 . . . . .	136
3.5	Conclusion . . . . .	139
<b>4</b>	<b>System evaluation and testing protocols</b>	<b>141</b>
4.1	Introduction . . . . .	141
4.2	The effect of gamma-ray background at neutron facilities . . . . .	142
4.3	Discussion of the experimental results . . . . .	147
4.4	Testing protocols at facilities . . . . .	151
4.4.1	Effect of pile-up in testing protocols . . . . .	152
4.4.2	TSL pulsed neutron beam . . . . .	155
4.4.3	LANSCE . . . . .	158
4.4.4	TSL continuous quasi-monoenergetic neutron beam . . . . .	158
4.5	Predicting the testing protocols using at ISIS ChipIr . . . . .	159
4.6	Discussion . . . . .	168
4.7	Conclusion . . . . .	173
<b>5</b>	<b>Conclusions</b>	<b>175</b>

5.1	A summary of the research in this project . . . . .	175
5.2	Major research findings . . . . .	181
5.3	Contributions and limitations . . . . .	182
5.4	Suggestions for future research . . . . .	183
<b>A</b>	<b>Photodiode sensor circuit</b>	<b>185</b>
<b>B</b>	<b>Matched filter threshold level determination</b>	<b>188</b>
B.1	Fundamental probability density function . . . . .	188
B.2	Threshold level . . . . .	189
<b>C</b>	<b>Additional information of experimental results captured at LANSCE193</b>	
<b>D</b>	<b>Neutron penetrating the aluminum scatterer</b>	<b>197</b>
<b>E</b>	<b>Confidence limits for the number of pulse events in beam monitoring system</b>	<b>198</b>
<b>F</b>	<b>Publications</b>	<b>201</b>
	<b>Bibliography</b>	<b>213</b>

# List of Figures

1.1	Generation of cosmic showers in the atmosphere . . . . .	2
1.2	Cosmic ray energy spectra at the sea level . . . . .	3
1.3	Spectra of cosmic-ray-induced neutrons measured at five locations .	5
1.4	Variation of the 1 to 10 MeV neutron flux in the atmosphere with altitude at 45° . . . . .	6
1.5	Variation of the 1 to 10 MeV neutron flux in the atmosphere with latitude after . . . . .	6
1.6	Neutron spectra . . . . .	10
1.7	TSL neutron spectra, 20.8 MeV, 46.5 MeV, 94.5 MeV and 173 MeV.	11
1.8	Multiple devices under testing at TSL. . . . .	12
1.9	Reverse-biased p-n junction detector . . . . .	18
1.10	Basic detector functions: radiation is absorbed in a sensor and con- verted into an electrical signal; this low-level signal is integrated in a preamplifier, fed to a pulse shaper for storage and analysis. . . .	22
1.11	Pulse processor transforms a sensor pulse into a broader pulse. . . .	22

## LIST OF FIGURES

---

1.12	Amplitude pile-up occurs when two pulses overlap (left). Reducing the shaping time allows the first pulse to return to the baseline before the second pulse arrives . . . . .	23
1.13	Beam monitoring system. . . . .	24
1.14	Beam monitoring system test in the lab at UCLan. . . . .	25
2.1	OSD1-5T PN photodiode. . . . .	32
2.2	Photodiode sensor circuit. . . . .	33
2.3	Example sensors 6 and 7 pulses. . . . .	35
2.4	Example pulse height spectrum captured by sensor 1 at TRIUMF in 2007. . . . .	37
2.5	Example detector pulses from neutron beam interaction. . . . .	38
2.6	Example voltage time series 1. . . . .	39
2.7	Example voltage time series 2. . . . .	40
2.8	Sensor 6 picture. . . . .	41
2.9	Pulse detection and estimation system. . . . .	42
2.10	Illustration of Nonparalyzable model counting system. . . . .	43
2.11	Illustration of the matched filter. . . . .	46
2.12	Example of simulated and experimental data power spectral density. . . . .	49
2.13	Example of experimental data with external noise power spectral density in low frequency. . . . .	50

## LIST OF FIGURES

---

2.14	Pulse calculation system. . . . .	51
2.15	Pile-up effect calculation results — pulse interval distributions. . . . .	55
2.16	Calculation results with the effect of pile-up — pulse height spectra. . . . .	56
2.17	Noise effect calculation results — pulse height spectra. . . . .	59
2.18	Noise effect calculation results— pulse interval distributions. . . . .	60
2.19	Noise effect calculation results — around 1 ms pulse interval histogram. . . . .	60
2.20	Calculation results with both noise and pile-up effects, interaction rate= $3000^{-1}\text{s}$ — pulse height spectra. . . . .	63
2.21	Calculation results with both noise and pile-up effects, interaction rate= $3000^{-1}\text{s}$ — pulse interval distributions. . . . .	64
2.22	Example of the minimum detectable energy with a varying number of sensors under test. . . . .	68
2.23	Example of minimum detectable energy with various pulse widths. . . . .	69
2.24	Optimum pulse width by using sensor 12 feature at sample rate 1 MHz. . . . .	73
2.25	Probability of detection at 1 MHz sample rate with various pulse widths and interaction rates. . . . .	74
2.26	Sampling various pulse shapes. . . . .	76
2.27	Sampling pulse calculation results — pulse height spectra. . . . .	77
2.28	Software main panel. . . . .	79
3.1	Example of measured pulse height spectra captured at TRIUMF. . . . .	83

## LIST OF FIGURES

---

3.2	Example of measured pulse interval distribution captured at TRIUMF.	84
3.3	Schematic of the neutron beam lines at LANSCE and TSL. . . . .	87
3.4	Schematic of the neutron beam line at TRIUMF. . . . .	88
3.5	ASP neutron beam line. . . . .	89
3.6	LANSCE pulsed neutron temporal characteristics of the beam. . . .	91
3.7	Picture of sensor 11 and 12 testing at the 78cm upstream position at LANSCE. . . . .	92
3.8	Measured pulse height spectra at the upstream position at LANSCE, CI=68.27%. . . . .	93
3.9	Measured pulse interval distributions at the upstream position at LANSCE. . . . .	94
3.10	Temporal characteristics of the WNR pulsed neutron beam. . . . .	96
3.11	Measured pulse interval distribution (integrated) at the upstream position at LANSCE, CI=68.27%. . . . .	96
3.12	Measured responses in the upstream position at LANSCE, CI=68.27%. . . . .	99
3.13	Proportional fit between counts in sensor 11 and those in sensor 12. . . . .	99
3.14	Picture and schematic diagram showing the relative position of sensors with a scatterer. . . . .	101
3.15	Measured pulse height spectra of two sensors with and without a scatterer between them at LANSCE. . . . .	103
3.16	Measured pulse height spectra in low collected energy of two sensors with or without a scatterer between them at LANSCE. . . . .	104

## LIST OF FIGURES

---

3.17	The transmission with or without a scatterer with different collected threshold energies at LANSCE, CI=68.27%. . . . .	106
3.18	The relative position of two sensors with SARBE under test at LANSCE.	108
3.19	The relative position of two sensors with three other devices under test at LANSCE. . . . .	109
3.20	Measured pulse height spectra of two sensors with one or three other samples between them at LANSCE, CI=68.27%. . . . .	111
3.21	Experiment results in low collected energy events of two sensors with one or three samples between them at LANSCE, CI=68.27%. . . .	113
3.22	The transmission with one or three samples with different collected threshold energies at LANSCE, CI=68.27%. . . . .	114
3.23	The response measurements with the testing time at LANSCE. . . .	115
3.24	Responses of the two example photodiode sensors with neutrons upstream at LANSCE, CI=68.27%. . . . .	116
3.25	Sensors under test at TRIUMF in 2008. . . . .	117
3.26	Measured pulse height spectra captured by photodiode sensors with or without window at TRIUMF, CI=68.27%. . . . .	118
3.27	Measured pulse interval distributions captured by photodiode sensors with or without window at TRIUMF. . . . .	119
3.28	Effect of photodiode window on measured pulse height spectra captured about 0.5 m away from beam at TRIUMF, CI=68.27%. . . .	121
3.29	The measured pulse height spectra for the photodiode detector and amplifier irradiated separately at TRIUMF, CI=68.27%. . . . .	123

## LIST OF FIGURES

---

3.30	Pulse height spectra showing the influence of thermal neutrons at TRIUMF and its reduction by cadmium shielding. . . . .	123
3.31	Measured pulse height spectra captured at ASP 3 MeV monoenergetic beam. . . . .	124
3.32	Measured pulse height spectra captured at ASP 3 MeV monoenergetic beam with normalized amplifier gains. . . . .	126
3.33	Measured pulse interval distributions captured at ASP 3 MeV monoenergetic beam. . . . .	126
3.34	Measured pulse height spectra captured at ASP 14 MeV monoenergetic beam, CI=68.27%. . . . .	127
3.35	Measured pulse interval distribution captured at ASP 14 MeV monoenergetic beam. . . . .	128
3.36	Response ratios of sensors 10 and 9 at ASP 14 MeV monoenergetic beam. . . . .	128
3.37	Measured pulse height spectra for sensors with different pulse widths irradiated at TRIUMF, CI=68.27%. . . . .	129
3.38	Measured pulse interval distributions for sensors with different pulse widths irradiated at TRIUMF. . . . .	130
3.39	Sensors 1, 2 and 3 under test at TSL in 2007. . . . .	132
3.40	Measured pulse height spectra captured at TSL. . . . .	132
3.41	Pulse height spectra due to neutron activation of gold in the photodiode. . . . .	133
3.42	Measured pulse height captured at TSL pulsed ANITA. . . . .	137

3.43 Measured pulse interval distributions at TSL pulsed ANITA. . . . .	138
4.1 Relative importance of the three types of gamma-ray interactions vs. energy and atomic number $Z$ of the absorber . . . . .	142
4.2 Values of the mass attenuation coefficient in silicon as a function of photon energy . . . . .	144
4.3 The fraction of gamma rays absorbed in interaction with the photo-diode sensor with a depth of $43\ \mu\text{m}$ . . . . .	144
4.4 Measured responses captured at LANSCE and TRIUMF, $\text{CI}=68.27\%$ . 147	147
4.5 LANSCE and TRIUMF response ratio. . . . .	148
4.6 Example pulse height spectra at high collected energy captured at LANSCE, $\text{CI}= 68.27\%$ . . . . .	149
4.7 Range of selected ions in silicon . . . . .	151
4.8 Interaction rate and detection rate. . . . .	153
4.9 Probability of detection of two different pulse widths in various of the neutron flux. . . . .	154
4.10 Transmission for two different sensor pulse widths and interaction rates with various percentage of the neutron flux. . . . .	155
4.11 simulated and measured pulse height spectra captured at LANSCE.	161
4.12 Simulated pulse height spectra with various average numbers of pulse events per neutron beam. . . . .	162
4.13 The probability of pulse events generated per neutron pulse with various average number of pulse events. . . . .	165

## LIST OF FIGURES

---

4.14	Estimated average detected energy with various average (number) of pulse events per neutron pulse. . . . .	166
A.1	Schematics of photodiode sensor power circuit . . . . .	186
A.2	Schematics of photodiode sensor amplifier circuit . . . . .	187
B.1	Detecting signal in Matched filter . . . . .	190
B.2	PDFs for a hypothetical testing problem . . . . .	192

# List of Tables

1.1	Error modes from terrestrial neutrons . . . . .	4
2.1	Sensor lists. . . . .	41
2.2	Calculation results with the effect of pile-up, CI=68.27%. . . . .	53
2.3	Calculation results with the effect of noise, CI=68.27%. . . . .	57
2.4	Calculation results with both noise and pile-up effect — decay constants, CI=68.27%. . . . .	61
2.5	Calculation results with both noise and pile-up effect —probability of detection, CI=68.27%. . . . .	65
2.6	Calculation results in the number of sample points of sensor pulse. .	76
3.1	Experimental conditions of two sensors irradiated at the upstream position at LANSCE. . . . .	91
3.2	Experimental results of two sensors irradiated at the upstream position at LANSCE. . . . .	92
3.3	Measured pulse height spectra parameters of two sensors irradiation at upstream at LANSCE, CI=68.27%. . . . .	93

3.4	Measured pulse interval parameters of two sensors irradiated at the upstream position at LANSCE, CI=68.27%. . . . .	97
3.5	The probability of number of pulse events per macropulse measured at LANSCE. . . . .	97
3.6	The responses of two sensors irradiated in the upstream position at LANSCE. . . . .	98
3.7	Experimental conditions of one sensor upstream and the other downstream with or without a scatterer at LANSCE. . . . .	100
3.8	Experimental results of one sensor at upstream and one at downstream with or without a scatter at LANSCE. . . . .	102
3.9	The transmission of two sensors irradiated with or without a scatterer between them at LANSCE. . . . .	105
3.10	Measured pulse height spectra parameters ( $a \exp^{-bE}$ ) of two sensors in irradiation with the scatterer at LANSCE, CI=68.27%. . . . .	106
3.11	The transmission of two sensors irradiated with or without a scatterer between at LANSCE between them events collecting above 3 MeV. . . . .	107
3.12	Experimental conditions of two sensors with one or three samples between them at LANSCE. . . . .	107
3.13	Experimental results of two sensors with one or three samples between them at LANSCE. . . . .	110
3.14	The transmissions of sensors irradiated with other samples between them at LANSCE. . . . .	110

3.15	The number of pulse events and transmissions in two sensors with one or three samples between them and 1 MeV collected threshold energy. . . . .	114
3.16	Two example pulse height spectra parameters of sensor 11 upstream at LANSCE, CI=68.27%. . . . .	116
3.17	Experimental conditions of investigating the effect of photodiode window at TRIUMF. . . . .	117
3.18	Experimental results of investigating the effect of photodiode window at TRIUMF. . . . .	118
3.19	Measured parameters of pulse height spectra and pulse interval distributions captured by photodiode sensors with or without window at TRIUMF. . . . .	119
3.20	Experimental conditions for the photodiode detector and amplifier irradiated separately at TRIUMF. . . . .	122
3.21	Experimental conditions and results for the photodiode detector and amplifier irradiated separately at TRIUMF. . . . .	122
3.22	Experimental conditions at ASP 3 MeV neutron beam. . . . .	124
3.23	Experimental results captured at ASP 3 MeV neutron beam. . . . .	125
3.24	Experimental conditions and results at ASP 14 MeV neutron beam. . . . .	127
3.25	Experimental conditions and results at ASP 14 MeV neutron beam. . . . .	127
3.26	Experimental conditions and results of two sensors in different pulse widths irradiated at TRIUMF. . . . .	129

## LIST OF TABLES

---

3.27	Measured parameters of pulse height spectra and interval distributions captured by sensors with different pulse widths at TRIUMF. . .	130
3.28	Measured pulse height spectra parameters at TSL. . . . .	133
3.29	Possibilities for various numbers of events per macropulse measured at TSL ANITA. . . . .	138
4.1	The fraction of gamma rays absorbed by the photodiode as a function of energy. . . . .	145
4.2	Measured results at LANSCE and TRIUMF for collected energy equal or above 200 keV. . . . .	147
4.3	Pulse height spectra fitting parameters $ae^{-bE}$ , CI=68.27%. . . . .	148
4.4	Symbols used in determining the TSL ANITA testing protocols. . .	156
4.5	LANSCE pile-up analysis. . . . .	158
4.6	Symbols used in determining the ChipIr testing protocols. . . . .	160
4.7	Simulation summary—the average energy of the number of pulse events per neutron beam. . . . .	163
4.8	Probability of pulse events with various the average pulse numbers per neutron beam. . . . .	163
4.9	Estimated numbers of detected and interacted pulse events with various the average pulse events generated one neutron beam macropulse at ChipIr. . . . .	164
4.10	The average energy with various mean number of pulse events per neutron macropulse beam. . . . .	166

C.1	Experimental results of two sensors irradiated in the upstream position at LANSCE . . . . .	194
C.2	The transmission of two sensors irradiated at LANSCE with or without a scatterer with various collected threshold energy . . . . .	195
C.3	The numbers of pulse events and responses in sensor 11 captured at LANSCE . . . . .	196
E.1	Limits of confidence interval of Poisson distribution for CI of 68.27% and 95%, and to one of standard deviation . . . . .	200

## Acronyms

ANITA	Atmospheric-like Neutrons from thick Target
ASER	Accelerated soft error rate
ASTEP	Altitude SEE Test European Platform
AWE	Atomic Weapons Establishment
BPSG	Borophosphosilicate glass
BREL	Boeing Radiation Effects Laboratory
CCDs	Charged Coupled Devices
CDF	Cumulative distribution function
CI	Confidence interval
CL	Confidence level
CREAM	Cosmic Radiation Environment and Activation Monitor
CREDO	Cosmic Radiation Environment and Dosimetry instrument
CVD	Chemical Vapour Deposition
DAQ	Data Acquisition
DUT	Device under test
ECC	Error correction code

FIR	Finite Impulse Response
FWHM	Full Width at Half Maximum
GWN	Gaussian white noise
ICE	Irradiation of Chips and Electronics
IEC	International Electrotechnical Commission
JEDEC	Joint Electron Device Engineering Council
JEITA	Japan Electronics and Information Technology Industry Association
LANSCE	Los Alamos Neutron Science Center
MULASSIS	MULTi-LAYered Shielding SIMulation Software
NSREC	Nuclear and Space Radiation Effects Conference
PDF	Probability density function
PSD	Power spectral density
RCNP	Research Center for Nuclear Physics
RTSER	Real time soft error rate
SABRE	Seeder Atmospheric Beam Radiation Equipment
SEEDER	Single Event Effects Design for Electronics Reliability
SEEs	Single event effects
SER	Soft error rate
SEU	Single-event upset
SNR	Signal-to-noise ratio
TFBCs	Thin-film breakdown counters
TNF	Neutron Irradiation Facility
TOF	Time-of-flight
TRIUMF	Tri-University Meson Facility
TS2	Target Station 2
TSL	The Svedberg Laboratory
WNR	Weapons Neutron Research

---

## List of symbols

$A$	Sensor amplifier gain
$A_v$	Shaping amplifier gain
$C_f$	Feedback capacitance
$E$	Deposited energy, MeV
$E_{min}$	Minimum detectable energy, MeV
$V_{smin}$	The minimum detected pulse height, V
$\gamma'$	Threshold level
$n$	Pulse interaction rate
$P_{FA}$	Probability of false alarm
$V_p$	Pre amplifier pulse height
$Q$	Charge, C
$q$	Electric charge $1.602 \times 10^{-19}$ C
$Q^{-1}(P_{FA})$	Value of $N(0, 1)$ random variable which is exceeded with probability of $P_{FA}$
$r$	Pulse detection rate
$\Phi$	Neutron fluence
$x[n]$	Input signal
$\omega[n]$	Noise signal
$s[n]$	Reference signal
$R_f$	Feedback resistance
$\sigma$	Response
$\delta$	Noise standard deviation
$\tau$	Shaping pulse width
$\varepsilon_R$	Reference signal energy
$\varepsilon$	Signal energy
$V_R$	Reference pulse height, V
$V_s$	Shaping amplifier pulse height, V

# Chapter 1

## Introduction

### 1.1 Single-event effects caused by cosmic rays in the atmosphere

Primary cosmic rays are high energy particles from the galaxy far away and solar cosmic rays. The primary particles have many collisions with the Earth's atmosphere and produce a great number of particles before they reach sea level. In this process high energy neutrons, protons, pions, electrons and mesons are produced as illustrated in figure 1.1 [1].

Less than 1% of the primary flux reaches sea level where the flux is composed of muons, protons, neutrons, and pions as shown in figure 1.2 [2]. Of these neutrons is one of the higher flux components. Since the 1990s, terrestrial neutrons have been recognized as a major source of Single event effects (SEEs) including soft-errors of semiconductor devices at the both ground and aircraft level [3–6].

SEEs results from the deposition of ionization energy within a microelectronic device, which is caused by a single particle such as a neutron, proton, alpha particle or heavy ion that interacts with the device [7,8]. These effects can be classified as hard

## 1.1 Single-event effects caused by cosmic rays in the atmosphere

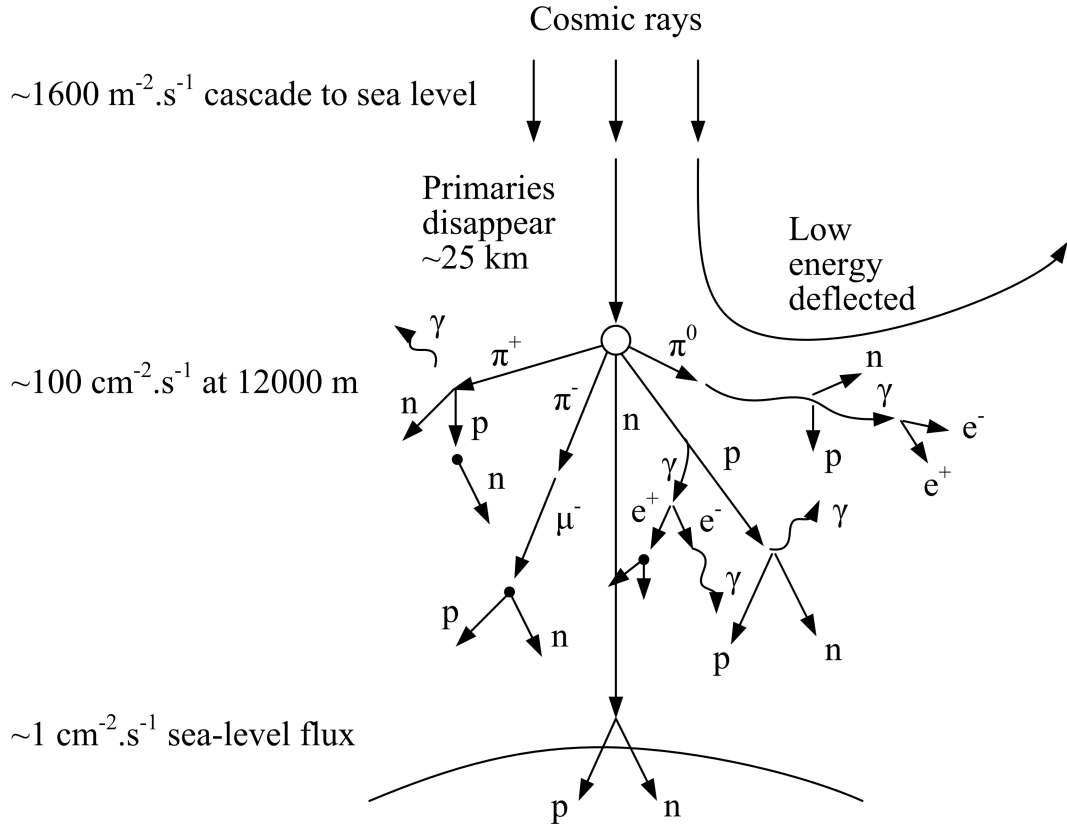


Figure 1.1: Generation of cosmic showers in the atmosphere, after Ziegler, [1]

errors and soft errors as listed in table 1.1. Hard errors can cause permanent failure in devices. Soft errors can cause a malfunctioning of a circuit or even a system crash which may result in data corruption, which may or may not be detected.

During 1954-1957, failures in digital electronics were reported in above-ground nuclear bomb tests [1]. Perhaps the first paper discussing the impact of cosmic rays on electronics was by Wallmark and Marcus [10], who forecast the eventual occurrence of Single-event upset (SEU) in electronics due to terrestrial cosmic rays; they further predicted that the minimum volume of semiconductor devices would be limited to about  $10 \mu\text{m}$  on a side due to these upsets. The first confirmed report of cosmic-ray-induced upsets in space application was presented at the Nuclear and Space Radiation Effects Conference (NSREC) in 1975 by Binder et al. [11]. In 1978, the first evidence of sea-level soft fails from energetic particle impact was revealed in a

## 1.1 Single-event effects caused by cosmic rays in the atmosphere

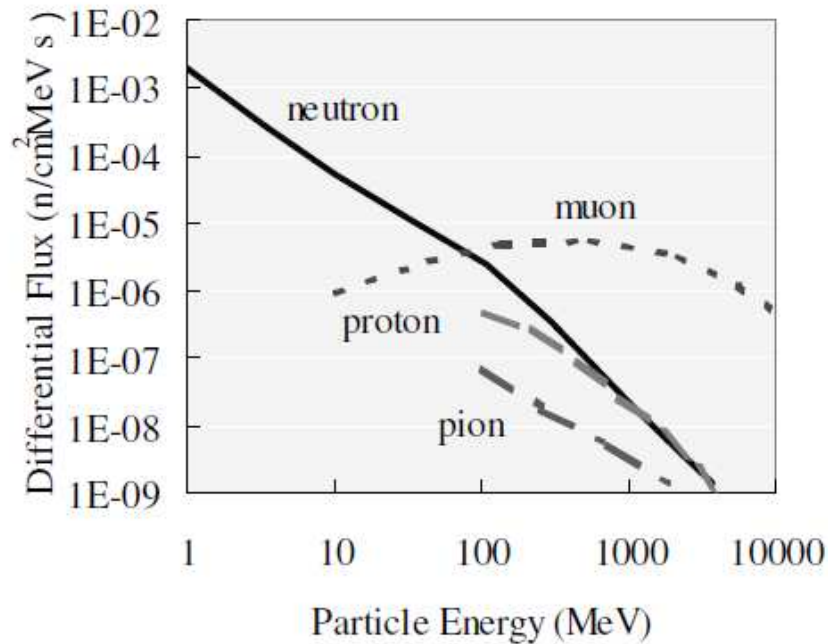


Figure 1.2: Cosmic ray energy spectra at the sea level, after Ziegler [2].

famous paper by May and Woods [12], in which the authors determined that these errors were caused by the alpha particles emitted in the radioactive decay of uranium and thorium present just in few parts-per-million levels in package materials. The paper by Guenzer et al. [13] was the first to use the term “single-event upset”, which was immediately adopted by the community to describe upsets caused by both direct and indirect ionisation. In 1979, Ziegler et al. from IBM [14] predicted that cosmic rays could result in the same upset phenomenon in electronics (not only memories) even at sea level.

Research on SEU continued to increase so that by 1980 single-event phenomena had become a dedicated session of NSREC [15]. Atmospheric neutrons were found to be the main concern of SEEs in avionics at aircraft cruising altitudes [2, 4, 7, 9, 16], and concerns have now been growing to a wider and deeper extent than ever before [9, 17–22].

The energy variation of atmospheric neutrons is usually presented by plotting the differential flux (flux per unit energy interval) as a function of energy which is

## 1.1 Single-event effects caused by cosmic rays in the atmosphere

Table 1.1: Error modes from terrestrial neutrons, after Nakamura [9].

Category	Mode	Memo
Soft Error	SBU	Single bit upset
	MCU	Multiple-bits upset for one event
	MBU	MCU in the same word (not correctable by Error correction code (ECC))
	Block error	Multiple-bits errors along the BL or WL originally due to errors in peripheral circuits
	MCBI	Multiple-bits upset due to parasitic bipolar action triggered by snapback in channel. Correctable by re-writing. Sometimes associates with low current.
	FBE	Main error mode of silicon on insulator (SOI). Mitigated by Body Tie
	SET	Error mode of logic devices such as latch, inverter and clock
Pseudo Hard Error	SESB	Bipolar action in S/D channel. Impact ionization may affect.
	PCSESEL	High current continues to flow due to parasitic cylinder. Only power cycle can resume, but sometimes destructive (hard error)
	SEFI	PCSE of logic devices
	Firm Error	Error mode of SRAM-based FPGA
Hard Error	SEGR	Destruction of thin oxide layer mainly due to high-energy heavy ions. Power MOSFET, Flash memory
	SEB	Destructive/explosive error of power MOSFET.

often called “spectrum” [8]. Figure 1.3 shows full energy range cosmic-ray neutron spectra measured outdoors (one was in a thin-roofed building) at five locations [23]. Each spectrum has been scaled to sea level and the cutoff of New York City and plotted as energy times differential flux as a function of neutron energy. The spectra have three peaks: a high-energy peak at 100 MeV up to about 10 GeV, a nuclear evaporation peak centered at around 1 or 2 MeV, and the third peak is a thermal neutron (below 1 eV) component due to neutrons slowing down by scattering with surrounding materials [9].

Predicting neutron induced soft error rates requires knowledge of the flux and energy

## 1.1 Single-event effects caused by cosmic rays in the atmosphere

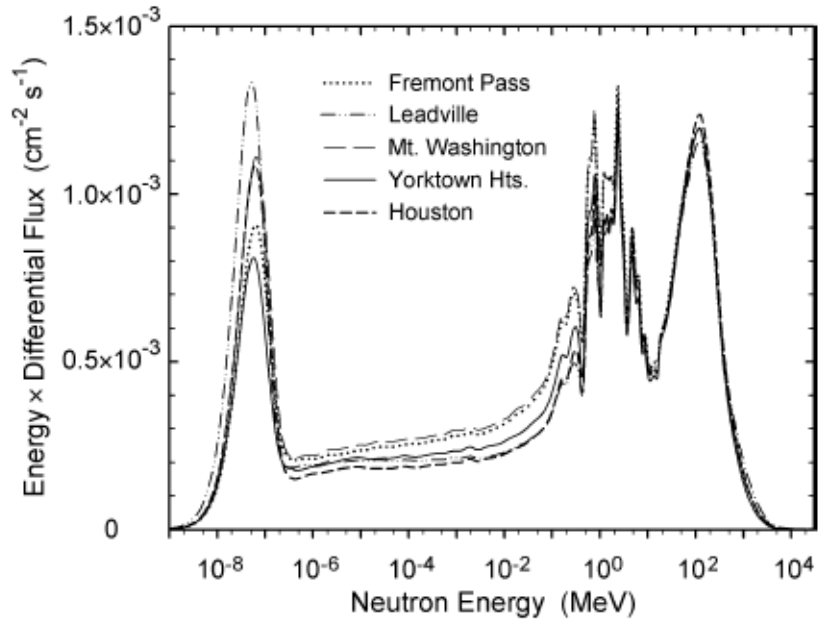


Figure 1.3: Spectra of cosmic-ray-induced neutrons measured at five locations, after Gordon [23].

distribution of the cosmic-ray-induced neutrons [24]. The variations of the SEEs rates against altitude and geographic latitude are dependent on the variation of the neutron flux with altitude and latitude. Measurements of the energy spectrum of cosmic ray neutrons have been made since the 1950s using a variety of techniques on the ground [23], at the mountain level [25], aboard an aircraft [26–29] and in space [30]. Bonner ball techniques have been widely used in neutron spectrum measurement.

The intensity of cosmic-ray-induced neutrons (and other secondary cosmic radiation, including protons) in the atmosphere varies with altitude, location in the geomagnetic field, neutron energy and solar magnetic activity [2, 16, 26]. The most important parameter determining the terrestrial neutron flux is atmospheric depth, which is proportional to barometric pressure and changes with altitude. Figures 1.4 and 1.5 show the simplified altitude and latitude variations of the neutron flux in the atmosphere respectively. The altitude variation maximum in the neutron flux at about 60 000 feet is known as the Pfozter maximum.

## 1.1 Single-event effects caused by cosmic rays in the atmosphere

The Sun has an 11 year solar cycle, with the most recent maximum in solar activity occurring in 2000—2002. During a solar maximum, big solar flares frequently occur and can have a great impact on the Earth's environment [31], which in turn corresponds to a higher neutron flux.

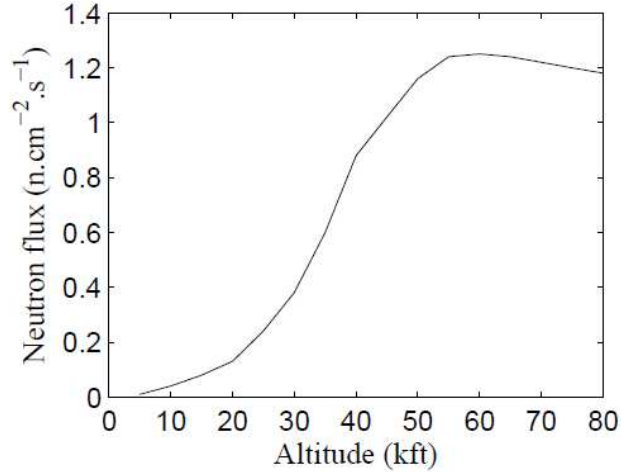


Figure 1.4: Variation of the 1 to 10 MeV neutron flux in the atmosphere with altitude at 45°, after Normand [26].

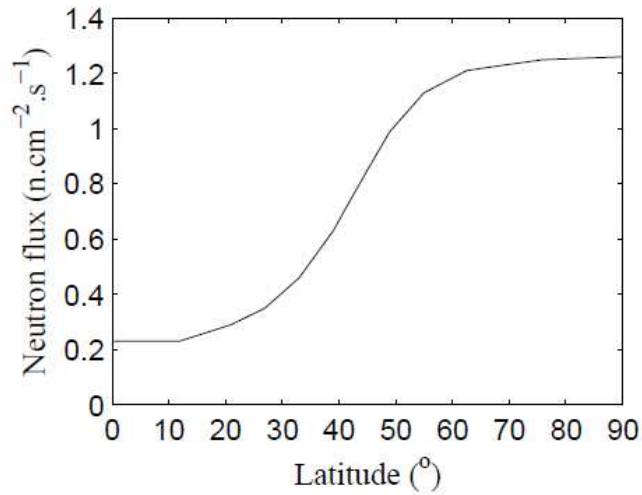


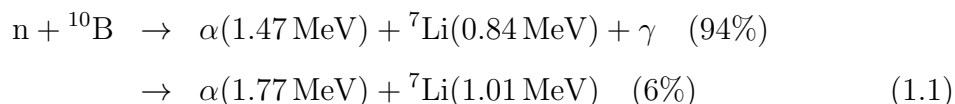
Figure 1.5: Variation of the 1 to 10 MeV neutron flux in the atmosphere with latitude after, Normand [26].

Thermal neutrons are low energy neutrons that have scattered sufficiently to be in thermal equilibrium with their surrounding [8,32]. At room temperatures, they have

## 1.1 Single-event effects caused by cosmic rays in the atmosphere

---

very low energy leading to an average energy of 0.025 eV, but they are more generally considered to be below 1 eV. At ground level, below 1 eV, the thermal neutron energy peak can be found as shown in figure 1.3. The majority of the thermal neutrons inside an aircraft are created by the interaction of the aircraft structure and all of its contents with the higher energy neutrons within the atmosphere [8]. They can significantly induce SEEs. The main cause of thermal neutron-induced soft error is the thermal neutron reacting to  $^{10}\text{B}$  nuclei and the subsequent nuclear fission [33]:



The reaction produces two charged particles in a device with combined energy; if the energy is deposited within the sensitive volume of a microelectronic device, it can lead to a single event upset (SEU) [8]. If the device does not contain any borophosphosilicate glass (BPSG), it is not susceptible to SEU from thermal neutrons [33]. The thermal neutron SEUs cross section are usually larger than the high neutron SEUs cross section in SRAMs devices [34, 35].

Soft errors in semiconductor devices have been studied over three decades. In order to standardize the characterization of the effects, test standards for Soft error rate (SER) have been developed by organizations such as the Joint Electron Device Engineering Council (JEDEC) [16, 36], the Japan Electronics and Information Technology Industry Association (JEITA) [33] and the International Electrotechnical Commission (IEC) [8, 37]. JESD89A and JESD89-3A standards are basic concepts accepted worldwide, and are widely referenced in many technical publications on soft errors in commercial ICs. These standards were issued in 2006, covering all (alpha, thermal neutron, spallation neutron, quasi-mono energetic neutron and high-altitude/underground) field sources of soft errors in detail. The standards define the requirements and procedures needed for terrestrial SER (including real-time and accelerated) testing of integrated circuits and a standardized methodology for

## 1.1 Single-event effects caused by cosmic rays in the atmosphere

---

reporting the results of tests. Standards EDR4705 [33] and IEC62396-2 [8] were issued with a similar scope to JESD89A and JESD89-3A.

There are two fundamental methods to determine a product's SER: real-time and accelerated testing [38]. But for the estimation of SER, simulation can also be used [39,40]. Real time soft error rate (RTSER) is generally used in testing a large number of devices for a long enough period of time (weeks, months or years) until enough soft errors have been accumulated to give a reasonably confident SER. An example of RTSER in practice is the project of Altitude SEE Test European Platform (ASTEP) [41,42] located in the French Alps, which has been life testing of terrestrial neutrons since 2006. The ASTEP masterpiece is the specially designed and universal SRAM automatic test equipment (ATE), capable of monitoring several thousands of synchronous/asynchronous SRAM memories and recording details of various errors detected. The advantage of real-time testing is a direct measurement of the actual SER requiring no intense radiation sources, extrapolations to use condition. The major disadvantage of real-time testing relates to its requirement for an expensive system, which is usually used in monitoring a very large number of devices simultaneously, a process that is very time consuming.

Accelerated testing is widely used to estimate SER. In accelerated soft error rate (ASER) testing, devices are exposed to a specific radiation source whose intensity is much higher than the ambient levels of radiation the device would normally encounter. ASER allows useful data to be obtained in a fraction of the time required by unaccelerated real-time testing [16]. Only a few units are needed and complete evaluations can often be done in a few hours or days instead of weeks or months. ASER can be used to complement real-time characterization, which was used, for example, when neutron beams were performed for several test chips issued from the project of ASTEP [41,42]. The results of accelerated and real-time SER were then compared against each other. After the real-time SER from the ASTEP project was corrected from the impact of alpha contamination affecting the tested devices, and the acceleration factor of the test location only for neutron-induced failures was taken into account [41], the real-time and accelerated testing SER were within the

## 1.1 Single-event effects caused by cosmic rays in the atmosphere

---

experimental error margins.

Accelerated testing is relatively easy to conduct, cheaper and fast. High-energy particle beams are widely used to enable accelerated testing of electronic devices and systems against neutron-induced SEEs [8,16,33,36,37]. Intense beams of high-energy neutrons or proxy protons<sup>1</sup> can be used to simulate the effects of cosmogenic neutrons, generating events with rates several orders of magnitude greater than those experienced in typical terrestrial or avionic applications. There are three kinds of high neutron facilities are available: spallation, monoenergetic and quasi-monoenergetic neutrons of various energies [16].

The spallation type of neutron source is created with the interaction of a high energy proton beam with a large, dense target, producing secondary neutrons [8]. This is the similar way in which the atmospheric neutrons are created. Hence this type of neutron source is closest to the neutrons in the atmosphere with respect to the energy spectrum of neutrons. There are a number of neutron spallation sources that have been used for exposing devices for SEEs testing purposes such as: Tri-University Meson Facility (TRIUMF) [43,44] accelerators in Canada, Los Alamos Neutron Science Center (LANSCE) [45] in America, Research Center for Nuclear Physics (RCNP) [46] in Japan, The Svedberg Laboratory (TSL) Atmospheric-like Neutrons from thick Target (ANITA) at Uppsala University in Sweden and ISIS neutron source [47,48] at Rutherford Appleton Laboratory in the UK.

Figure 1.6 shows the LANSCE, ISIS, TRIUMF and TSL ANITA and terrestrial neutron spectra. TRIUMF has a 500 MeV cyclotron from which neutrons are available at Neutron Irradiation Facility (TNF) up to an energy of 400 MeV. LANSCE is a pulsed neutron beam with energy spectrum up to 800 MeV, essentially without thermal neutrons. LANSCE is recommended by JEDEC as a suitable test facility for the estimation of SER at ground level. TSL ANITA facility provides a neutron beam with atmospheric-like spectrum (“white”, “spallation” neutrons),

---

<sup>1</sup>For particle energies above 100 MeV, SEU cross section measured with protons and neutrons can be taken to be essentially the same [8].

## 1.1 Single-event effects caused by cosmic rays in the atmosphere

primarily for studies and testing of electronic components and systems for neutron-induced single-event effects (SEE). Its atmospheric-like neutron spectrum is up to 150 MeV. At ISIS, protons are accelerated to 800 MeV in the synchrotron which are then directed onto a tantalum target producing neutrons for several beam lines. ISIS dosimetry is primarily provided by the proton beam current. UK Government funding has been confirmed for a new facility, ChipIr, at Rutherford Appleton Laboratory ISIS Target Station 2 (TS2) [49]

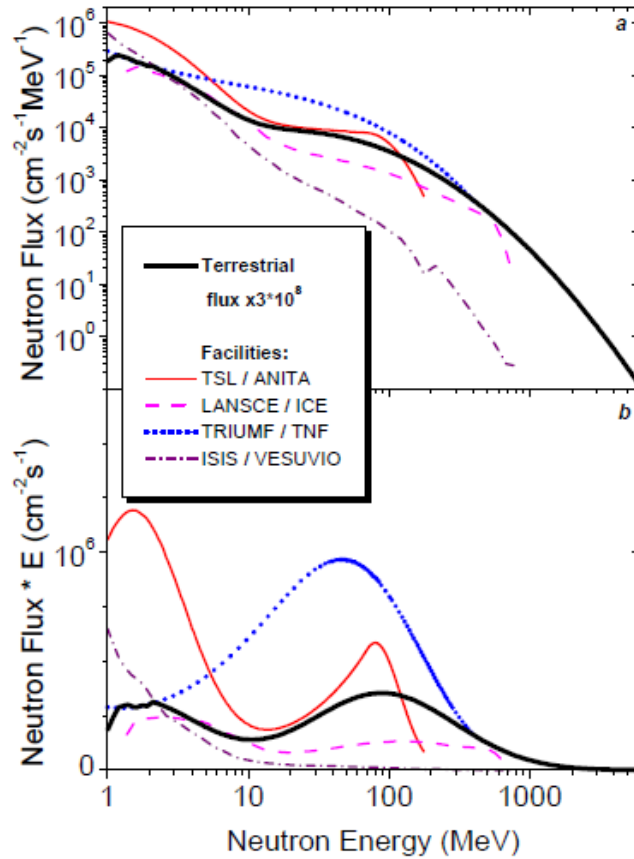


Figure 1.6: Neutron spectra, after [50].

A second type of facility produces a quasi-monoenergetic neutron spectrum, including examples such as the Theodor Svedberg Laboratory (TSL [51, 52]) at Uppsala university, Sweden. TSL provides quasi-monoenergetic neutron beams with energies in the range of 20 to 180 MeV as shown in figure 1.7. The neutrons are generated by colliding an accelerating proton beam into a monoenergetic proton beam into a

## 1.1 Single-event effects caused by cosmic rays in the atmosphere

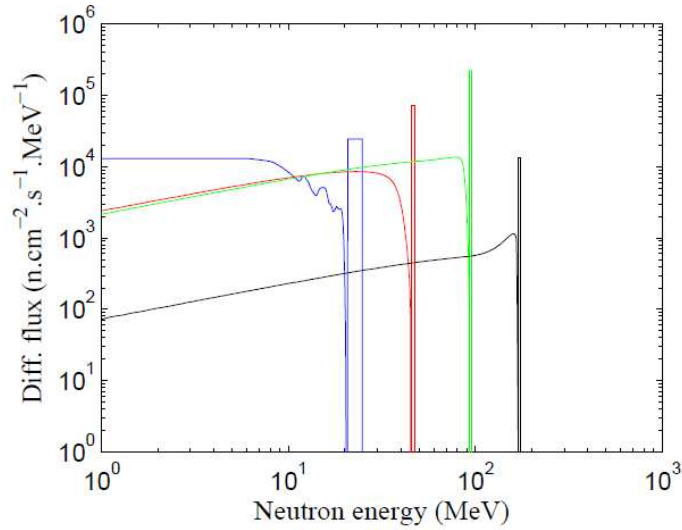


Figure 1.7: TSL neutron spectra, 20.8 MeV, 46.5 MeV, 94.5 MeV and 173 MeV.

lithium target, with roughly half the resulting neutrons having a peak about 2 MeV below the proton energy, and the remaining neutrons approximately evenly distributed over energy down to a thermal energy (the low energy “tail”). Typically, about 40% of the neutrons in the TSL field are at the nominal energy and 60% in the low-energy tail. According to the JEDEC89A standard, TSL is the site with the most experience with SEEs tests.

There are a number of facilities that produce monoenergetic neutron spectra, for example Boeing Radiation Effects Laboratory (BREL) [53] in the USA, which provides 14 MeV neutrons. The Atomic Weapons Establishment (AWE) in the UK has the ASP accelerator, producing 3 and 14 MeV neutrons. The spallation type is useful for testing conditions similar to the real natural environment. The monoenergetic sources are useful for measuring the energy dependence of single event effects. Tests conducted with monenergetic sources are time consuming but important. This is particularly true for the low energy regions close to threshold energy [9].

In ground level facility testing, such as ISIS, LANSCE and TSL, the penetrating power of neutrons permits testing to be carried out in cases where several experiments are arranged along a beam line as shown in figure 1.8. In such cases, however, the devices that are positioned further away from the beam source receive a reduced

## 1.1 Single-event effects caused by cosmic rays in the atmosphere

---

neutron flux due to absorption and scattering by upstream experiments [54, 55]. The consequent loss of neutron flux cannot be accounted for by facility dosimetry. This loss of neutron flux could be simulated, for example, by using Multi-Layered Shielding Simulation Software (MULASSIS) tool [56, 57]. However, the challenge of simulation is that it requires advanced computational methods and extensive computing time. In addition, simulation also requires collection of accurate data to verify the experimental results. Direct measurement is still required.

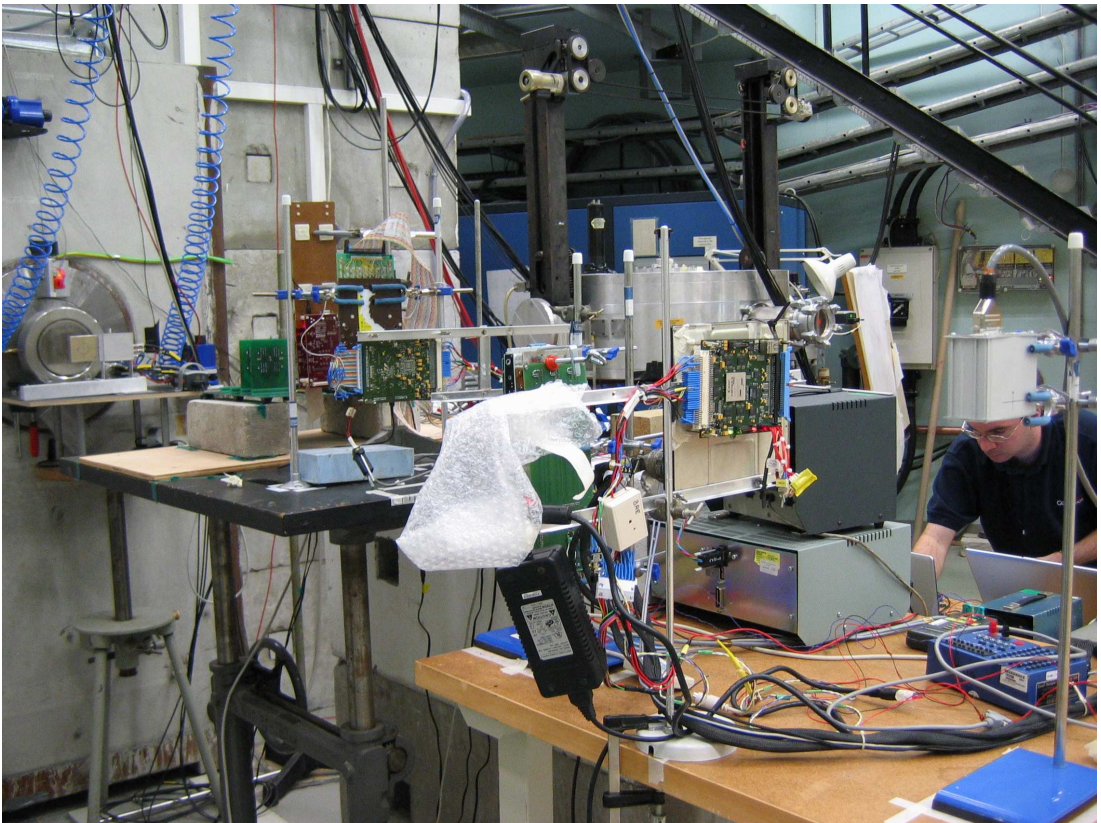


Figure 1.8: Multiple devices under testing at TSL.

The present project seeks to develop a beam monitoring system to undertake neutron fluence measurements at several devices simultaneously. The system is expected to be effective, small in size and inexpensive, and can be easily plugged into other devices in SEEs testing.

## 1.2 Aim and objectives of the research

At some facilities, including LANSCE, TSL and ISIS, multiple experiments can be carried out with several test sets arranged along the beam line for neutron induced SEEs. The neutron fluence at the upstream experiment can be provided by the facility. The devices that are positioned further away from the beam source receive a degraded beam due to absorption and scattering by the upstream experiments. The consequent loss of neutron fluence cannot be accounted for by upstream beam monitoring unless the transmission along the beam line is known. In the current state of the art, there is no direct measurement method to determine this transmission, although Monte Carlo simulation method has been used to determine it as shown by a previous study [54].

Monte Carlo simulation tools such as Geant4 [58], MCNP [59] and FLUKA [60] have been extensively used in simulating high energy experiments. Theory and experiment are generally complementary in that reconciliation between the results of simulation or calculation and experiment can lead to better understanding of both theory and experiment. The role of simulation is to imitate what happens when particles interact with the photodiode sensor, thus helping the researcher to better understand experimental conditions and performance. In addition, simulation also plays an important role in explaining and validating transmission effects (i.e. loss of neutron fluence in the beam line) and measurements.

In this thesis, however, only the experimental approach is taken. While it is certainly desirable to include simulation given its roles as noted above, simulation is not carried out in the present study because of the uncertainty in cross-section data at the high-energies, whereas in Monte Carlo simulation the collection of accurate experimental data is essential in verifying simulated results. Hence, the experimental approach is taken in this project in developing a system which can determine the transmission along the neutron beam with multiple devices undergoing SEE testing. While simulations cannot be carried out at this stage for the reason explained above, the experimental results presented in this thesis are nevertheless relevant to

### 1.3 Neutron detectors and beam monitoring

---

any Monte Carlo simulations that might be carried out in the future.

The overall aim of this research project is to improve fluence measurement for accelerated testing of electronics against neutron-induced SEEs through acquisition and analysis of pulse events via neutron sensors exposed to neutron beams. In achieving this aim, the research achieved the following objectives:

1. A method should be found to design a beam monitoring system, which will be capable of operating several detector channels simultaneously from a data acquisition system.
2. The beam monitoring system should be optimally designed in order to achieve the maximum of probability of detection by balancing the noise and pile-up effect as well as energy resolution.
3. Through analyzing the pulse height spectra and pulse intervals captured from the facility, a method should be developed to determine the transmission along the neutron beam line by measuring the neutron fluence at multiple locations in a beam in SEEs testing.
4. The testing protocols of the beam monitoring system should be recommended for using at each case of neutron facility, where multiple-experiments can be carried out in SEEs testing.

### 1.3 Neutron detectors and beam monitoring

This section describes the techniques used in neutron beam monitors. First, the neutron monitors used by facilities will be introduced. Next some semiconductor detectors will be presented.

### 1.3.1 Neutron detectors used at facilities

#### Ionization chambers

Ionization chambers are the simplest of all gas-filled radiation detectors. They usually consist of two plane electrodes (or cylinders) with potential difference on them in a gas chamber. Its normal operation is based on the collection of all the charges created by direct ionization in the gas chamber through the application of an electric field [61]. These types of devices are able to detect and count very low energy radiation at low flux as well, depending on the voltage applied between the detector plates.

Ionization chambers have been employed at ISIS, TSL [50] and LANSCE [62, 63]. The material used in the chamber, which could be uranium, plutonium, americium or other heavy isotopes, determines the low energy threshold of sensitivity to neutrons [16]. The LANSCE uranium-238 foil fission chamber provides an independent measurement of the incident neutron spectrum and flux [63] over a wide energy range using the Time-of-flight (TOF) techniques, which measure the time for the neutron to reach the facility monitor from the target.

#### Thin-film breakdown counters (TFBCs)

TFBC was first used in radiation detection by Tommasino et.al [64] in 1975. The TFBC detector is based on fission induced by neutron incidents on a target. When a neutron incident on the target produce fission fragments and that cause an electrical breakdown, they will be detected by TFBC.

The TFBC detector has been used at TSL [50, 65, 66] and VESUVIO instrument at ISIS Target Station 1 [67]. It will also be considered to be employed in ChipIr neutron beam ISIS TS2 [67]. TFBCs offer real-time operation, time resolution in sub-nanosecond scale [67].

### Primary current measurement

At TSL, the main features of the measured spectra and flux have been measured based on ionization chambers and TFBCs [50,68]. Another monitoring option is an indirect method which measure the proton beam current at the production target. It functions as a Faraday cup, used as an indirect monitor of the neutron beam, based on measurement of the proton beam current at the production target. The principle of the Faraday cup detector is that when the incident particle strikes the detector dynode surface, electrons are emitted that subsequently constitute a current, which is amplified and recorded [69].

### Moderated $\text{BF}_3$ counter neutron monitors

At TRIUMF TNF [43] and PIF [44] neutron beam facilities, the flux is monitored with  $\text{BF}_3$  (boron trifluoride) counters and dosimetry for calibrations is regularly performed using activation foils of nickel, aluminum, carbon, and gold [70]. Across the neutron beam, the flux is measured by scanning a moderated  $\text{BF}_3$  counter. However, this detector can measure the neutron fluences, but not the energy spectra [9]. A typical  $\text{BF}_3$  detector consists of a cylindrical aluminum (brass or copper) tube filled with a  $\text{BF}_3$  fill gas.  $\text{BF}_3$  serves both as the target for slow neutron conversion into secondary particles as well as a proportional fill gas [61].

### Bonner spheres

Bonner spheres techniques were first introduced in 1960 [71], used to measure neutron of various energy levels. The use of a set of spheres of selected sizes with moderators enable measurements to be obtained over a wide range of energies by using unfolding techniques. Bonner sphere detectors have been widely used in the natural environment [23,27,28,72] and in neutron beams, for example at AWE [73]

## 1.3 Neutron detectors and beam monitoring

---

and RCNP [74], and which are also considered to be used at ISIS neutron source station two [49] as well.

Bonner spheres can determine the neutron spectrum with good accuracy both in environmental and neutron beams. However, Bonner sphere detectors are usually heavy and big. For example, The Bonner sphere detector system developed by Goldhagen et al. [27] has 14 balls and the biggest ball has an 18 kg steel shell.

### 1.3.2 Semiconductor neutron detectors

Devices employing semiconductors as the basic detection medium became practically available in the early 1960s [61]. Semiconductor detectors in use are based on electron-hole pair collection from semiconductor media and have good energy resolution at room temperature. They are usually simple and cheap.

#### Diode based detectors

Diode based detectors have been used in neutron field detection with a wide energy range from thermal to several thousand MeV. Figure 1.9 illustrates the basic mechanism of generating a signal in a diode detector [75]. The operating principle of diode detectors is that when a charged particle passes through the depletion layer while the junction is in a reverse bias condition, it creates electron-hole pairs along its path in the diode, and the electron and holes move in an applied electric field to generate electric signals. The diode based detector collects this electric signals.

The detecting materials in the diode are usually silicon(Si) [75–77], carbon(C) [78, 79] or silicon carbide(SiC) [80, 81]. Seshadri et al. [78, 79] reported that the silicon carbon based detector increased device lifetime in neutron fields by orders of magnitude compared to commercial silicon based detectors [80]. As diamond has many outstanding properties such as high band-gap, high break-down field, high carrier mobility and high radiation hardness [78], diamond based detectors are expected to

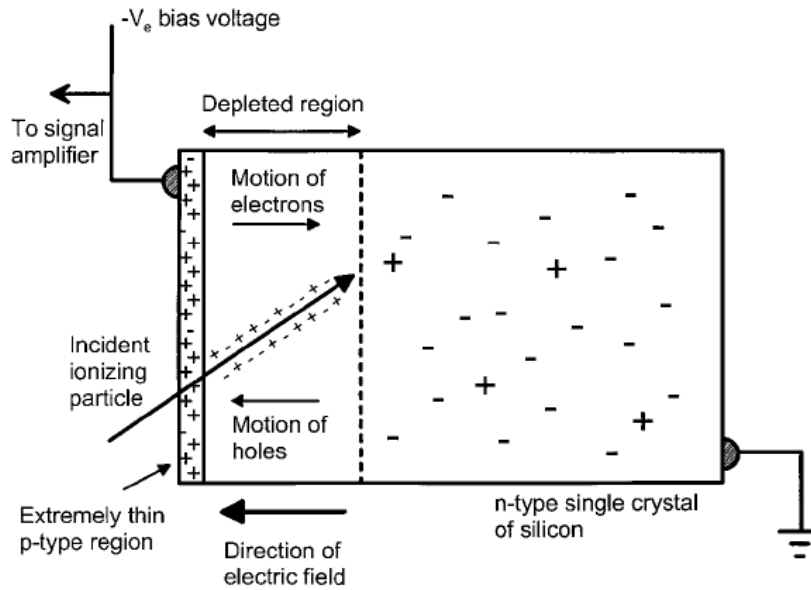


Figure 1.9: Reverse-biased p-n junction detector, after schütz [75].

offer significant advantages, such as better time resolution, higher radiation hardness under high-power irradiation, a lower counting error and so on. Mainwood [82] reported that the effect of radiation damage in diamond on the operation of the detector was much less severe than equivalent damage would be on a silicon device. On the other hand, diamond based detectors are currently much more expensive.

In both thermal and fast neutron detection, diode based detectors with converters have been widely used. The principle is that neutrons interact with the converter and produce secondary charged particles which can generate a signal in the diode. Polyethylene is often used as the converter to detect fast neutrons for neutron dosimetry [75] or spectrometry [83]. Polyethylene interacts with fast neutrons with a relatively high cross section in which charged particles are emitted. The important reaction is the elastic scattering of  ${}^1\text{H}(n, n){}^1\text{H}$ , where a proton gets kinetic energy from a neutron.

The thermal neutrons are usually captured by  ${}^6\text{Li}$  in the reaction  ${}^6\text{Li}(n, \alpha){}^3\text{H}$  [84,85] or  ${}^{10}\text{B}(n, \alpha){}^7\text{Li}$ . The  $\alpha$  has an energy of 2.05 MeV and the detected triton is 2.7 MeV, and then these charged particles will deposit their energy in the diode.

### 1.3 Neutron detectors and beam monitoring

---

QinetiQ has developed Cosmic Radiation Environment and Activation Monitor (CREAM) [86,87], Cosmic Radiation Environment and Dosimetry instrument (CREDO) [88,89] and QDOS/RayHound [76] neutron monitors based on a PIN diode combined with pulse-height analysis to measure charge deposition spectra. These detectors are designed to monitor those aspects of the primary and secondary radiation environment responsible for SEUs in microelectronics [86–90]. The CREAM has 10 arrays of PIN diodes each with  $1\text{ cm}^2$  active area and  $300\text{ }\mu\text{m}$  depleted sensitive depth, complemented by passive detectors, including activation foils and neutron bubble detectors. The later version of the CREDO detector employs a telescope technique to detect coincidences between parallel planes of PIN diodes in order to define particle arrival directions.

The QDOS/RayHound [76] detector was developed on the basis of experience gained from CREAM. It is a compact and lightweight device that uses a single PIN diode with a diameter of  $25\text{ mm}$  and a  $500\text{ }\mu\text{m}$  depleted sensitive depth, to record charge depositions caused by ionizing radiation passing through the sensitive volume. This detector can provide measurements of dose equivalent in an aviation environment as well as neutron fluxes at accelerated testing facilities. The QDOS/RayHound detector could provide accurate neutron dosimetry at positions in a beam line where the neutron intensity is uncertain due to scattering and background effects in accelerated SEEs testing on microelectronics.

Diamond (carbon) has a remarkable set of physical properties stemming mainly from the rigidity of its lattice, and the relatively small mass of the carbon atom. Natural diamond is quite expensive. In order to make it possible to contemplate the use of diamond in such detectors, the industrial technologies developed the Chemical Vapour Deposition (CVD), which, albeit although originally discovered in the 1950s, had only become widely practised and understood quite recently. It could produce large detecting areas at low cost. Angelone et al. [79] designed a CVD diamond neutron monitor that can withstand  $14\text{ MeV}$  neutron flux up to  $1.5 \times 10^8\text{ cm}^2\text{ s}^{-1}$ . When the neutron energy is below  $6\text{ MeV}$ , it can be characterized using  ${}^6\text{LiF}$  converters, as explored by [78,91].

### Pixel based detectors

In 1983, the Rutherford Laboratory group published results that showed standard Charged Coupled Devices (CCDs) could be used as radiation detectors [92]. They concluded that standard optical imaging CCDs could perform well as particle detectors in various radiation fields. The physical processes taking place when radiation penetrates CCD sensitive areas are the same as for other microelectronic devices. Image processing techniques allow very precise evaluation of images taken of interactions between high energy radiation and CCD pixels. CCDs have high charge resolution which allow precise determination of the deposited charge by a single event [93].

Chugg et al. [94] developed a radiation detector using CCD imaging with appropriate shielding to monitor high energy radiation fields (protons and electrons) for spacecraft applications. CCDs have been used as a RAM analogue, particularly in analysis of MBU occurrence by Chugg et al. [95].

Recently, UCLan has developed an Imaging Single-Event Effect Monitor (ISEEM), which uses a commercially available scientific CCD as the detecting element, to characterise SEE-inducing phenomena in neutron beams and in the natural cosmic-ray environment [55,96–98]. This monitor provides a detailed microdosimetric measure of the effects of neutron interactions in a silicon semiconductor device. Analysis of large sets of events has been used to determine received fluence [55] and support benchmarking of SEE rate prediction [48,98,99].

### Golden chips approach

Standards for neutron SEE testing [16] recommend the use of gold chips or reference chips with a relatively high SER that is capable of withstanding a relatively high total dose level as part of testing approach. The gold chips are used at the start and end of each testing session to ensure that other methods of dosimetry remain accurate [100] and provide validation of the test equipment. The chip is

mounted on its own test board so that it can be put in and taken out of the beam without interfering with other devices under test. For example, a “Reference SEU Monitor” was developed by ESA/ESTEC [101]. The setup measures the number of SEU events on an Atmel AT60142F-DC1 SRAM, which has been used by many researchers at many radiation test sites and has provided valuable calibration data in support of numerous projects [102]. IBM also used SRAM chips to validate the dosimetry [1].

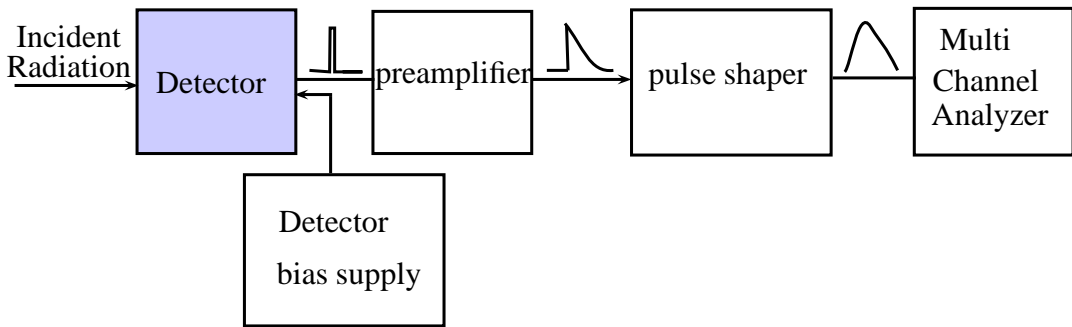
## 1.4 Pulse amplification and shaping techniques

The function of a radiation detector is shown in figure 1.10. When a particle interacts with the detector, it may generate electric signals because of the energy absorbed by the sensor. These electric signals are converted into a sensor pulse, which can be quite short (of order nanoseconds or less). The sensor pulse has to be amplified and transformed into a broader pulse with a non-zero peaking time [103] by a preamplifier and a pulse shaper.

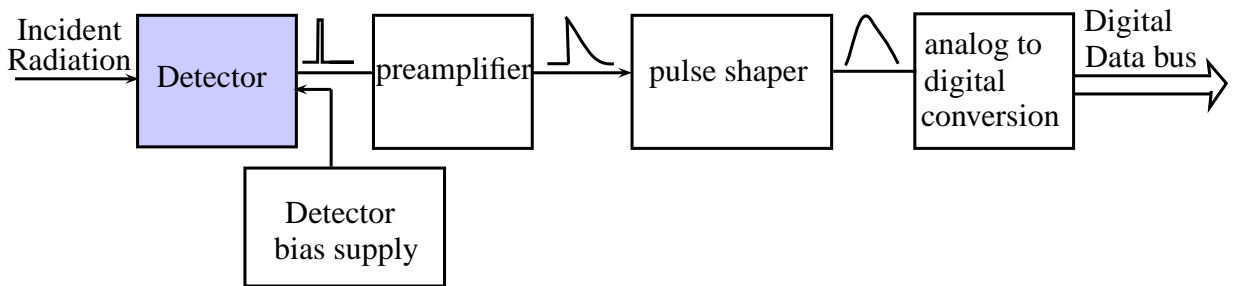
In energy measurements, the preamplifier transforms a short sensor current pulse into a pulse with a long “tail”. The pulse shaper converts the preamplifier into a kind of Gaussian pulse and also improves the Signal-to-noise ratio (SNR), thus resulting in optimal energy resolution. The time required for the shaping pulse to reach its maximum amplitude is often called the peaking time  $T_p$  [61] as shown in figure 1.11. The maximum amplitude (peak height) is a linear function of the energy collected from the detector, called amplifier gain ( $V \cdot \text{MeV}^{-1}$ ) that dominates the performance of the pulse-processing system. The shaping time is defined as the time equivalent to the “standard deviation” of the Gaussian output pulse [104]. The width of the shaping pulse at 50% of its peak amplitude is called Full Width at Half Maximum (FWHM), which can refer to the shaping pulse duration, and is greater than the shaping time by a factor of 2.4.

According to Groundling et al. [105], the sophisticated function of a shaping am-

## 1.4 Pulse amplification and shaping techniques



(a) A simple system, after Knoll [61].



(b) A system for high energy-resolution at high pulse rate, after Helmuth [103].

Figure 1.10: Basic detector functions: radiation is absorbed in a sensor and converted into an electrical signal; this low-level signal is integrated in a preamplifier, fed to a pulse shaper for storage and analysis.

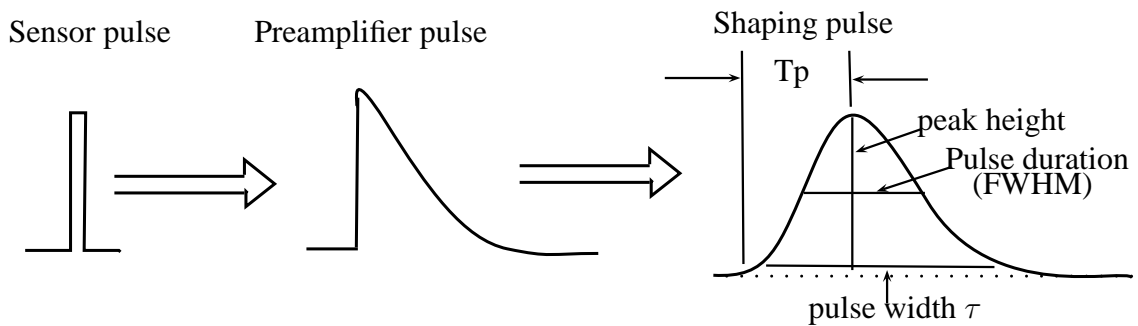


Figure 1.11: Pulse processor transforms a sensor pulse into a broader pulse.

plifier is to shape the signals to optimize spectrometry performance. This might involve a compromise between achieving the best possible signal-to-noise and permitting operation at high counting rates without degrading energy resolution. The first is to restrict the pulse width to match the measurement time, which will in-

## 1.4 Pulse amplification and shaping techniques

crease the noise without increasing the signal. The second objective is to minimize pile-up effect. In practical radiation measurement, which is not usually interested in measuring just one pulse, but many pulses and often at a very high rate, too large a pulse width will lead to pile-up of successive pulses [103] as shown in figure 1.12.

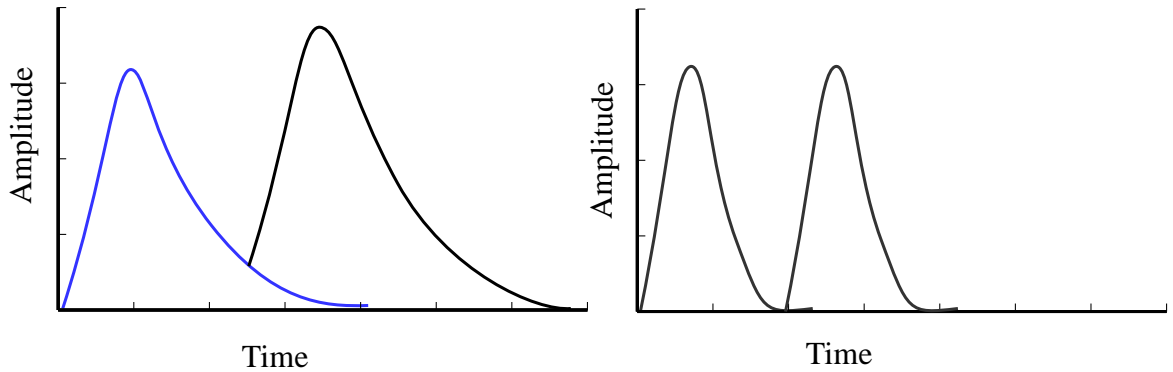


Figure 1.12: Amplitude pile-up occurs when two pulses overlap (left). Reducing the shaping time allows the first pulse to return to the baseline before the second pulse arrives, after [103].

Figure 1.10(a) [61] shows a simple pulse height analysis system for a simple application for example [106,107]. A Multi Channel Analyzer (MCA) digitizes the pulse height and time interval information. For a high-resolution detector to operate at a high pulse rate, it requires a complex digital converter as shown in figure 1.10(b). Many systems detect the presence of a pulse event by using a threshold discriminator (comparator) as the output of the shaper which provides a digital output whenever the shaper output exceeds the threshold level, e.g. the ATLAS pixel detector [108]. Pulse heights can be digitized by using the time over threshold (TOT) techniques. The advantage of the time over threshold measurement is that it has no dead time and practically no additional circuitry.

## 1.5 An overview of the photodiode beam monitoring system

The beam monitoring system is illustrated in figure 1.13. As can be seen, the photodiode is used to collect charges produced by neutron interactions in the semiconductor, with a short rise time of order of nanoseconds. The preamplifier converts the charges into pulse signals while the shaping amplifier filters noise from signals of interest and provides a quickly restored baseline to allow for high counting rates. Time series data are captured by using a Data Acquisition (DAQ) card under software control. Pulses are detected if the output from the matched filter exceeds a threshold level,  $\gamma'$ . An estimator is used to estimate the pulse height. Finally the pulse height spectra represent the neutron-induced charge energy spectra from the photodiodes, while pulse interval distribution represents the arrival times of pulse events.

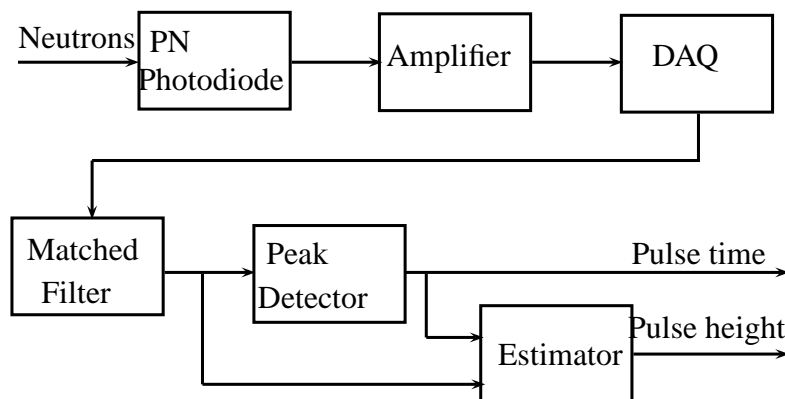


Figure 1.13: Beam monitoring system.

Figure 1.14 shows the beam monitoring system under test in the lab, which was the configuration for the first measurements at TSL and TRIUMF in 2007.

In this project, twelve sensors with slightly different circuits and two kinds of pulse widths ( $20\ \mu\text{s}$  and  $40\ \mu\text{s}$ , up to 0.1% point) were developed and irradiated at high-energy neutron beams as follows:

## 1.5 An overview of the photodiode beam monitoring system

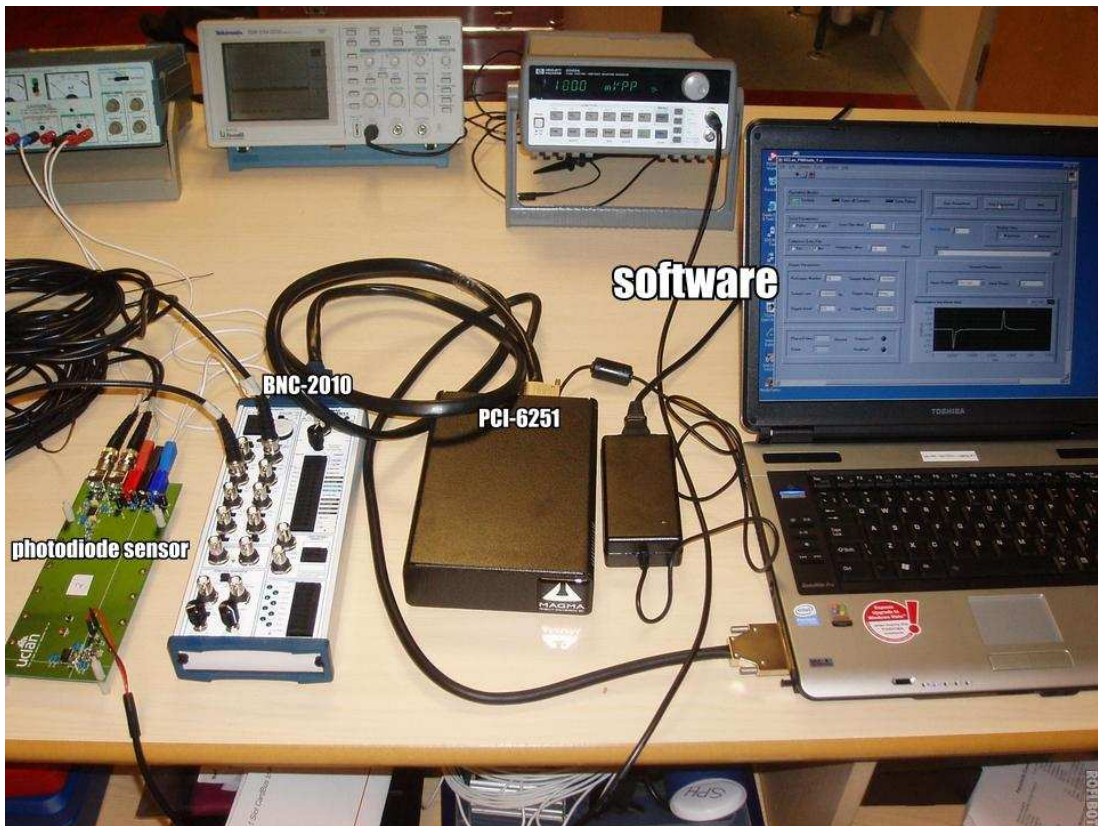


Figure 1.14: Beam monitoring system test in the lab at UCLan.

- TSL, Uppsala University, Sweden
  - In April 2007, three sensors were irradiated in neutron beams with peak energies near 50 MeV and 110 MeV, and TSL ANITA. The photodiode experiments were conducted downstream of several other devices where the beam was severely degraded. This is the preliminary study of the photodiode sensor.
  - In June 2010, one sensor was irradiated at ANITA.
- TRIUMF
  - In November 2007, three sensors were irradiated. There were two different circuit configurations: with the diode and preamplifier colocated, and with them kept separate.
  - In August 2008, five sensors were irradiated at TRIUMF. One sensor was irradiated with the amplifier alone and with the photodiode alone separately.

Four sensors have two kinds of pulse widths: 40  $\mu\text{s}$  and 20  $\mu\text{s}$ , with the photodiode with or without window in the sensors used.

- LANSCE
  - In October 2010, two sensors were irradiated to determine the transmission along the neutron beam during multi-device SEEs testing.
- Atomic Weapons Establishment, the United Kingdom
  - In November 2009, two sensors were irradiated at ASP in 3 MeV and 14 MeV monoenergetic neutron beam respectively.

The experimental results captured at these facilities will be presented in Chapter 3 through the measured pulse height spectra and pulse interval distributions. The recommended testing protocols for the beam monitoring system irradiated at each facility will be investigated in Chapter 4.

## 1.6 The organization of this thesis

Following this introductory chapter, the remainder of this thesis is divided into four chapters and six appendices, which are briefly outlined as follows:

Chapter 2 presents the development of the beam monitoring system. The photodiode detector converts the charge produced by neutron interaction in the depletion semiconductor region into the pseudo-gaussian pulses with amplitudes, which are related to the energy collected from a neutron interaction. In signal processing, pulse amplitudes are extracted from the time series data gathered from the preamplifier output using a matched filter technique, while pulse intervals are acquired using the nonparalyzable counting system. A series of calculations have been undertaken in order to verify the correct operation of the detection software and to investigate system performance variations. The minimum detectable energy and signal to noise ratio of the monitoring system are investigated. In order to achieve

the maximum of probability of detection, the optimum of sensor pulse width at different interactions rates and the number of sensors under test are investigated.

Chapter 3 discusses the experimental results captured from neutron beam facilities. The fundamental properties of the output of the beam monitoring system are pulse height spectra and interval distributions. A number of experiments of two sensors irradiated at the same time with or without an aluminum scatterer, or with other samples between them were conducted at LANSCE, in order to measure the neutron beam fluence at different positions by analyzing pulse height spectra. The experiments conducted at TRIUMF investigated the effect of neutron interactions in the amplifier, neutron interaction with photodiode window, and the thermal neutron interaction with the photodiode. The experiments conducted at TRIUMF also investigated the effect of sensor pulse width on the probability of pile-up by analyzing the pulse interval distribution. The effect of the photodiode doping profile on the rate of detected pulses were observed at ASP experiments. The pile-up rate in the sensor irradiated at TSL ANITA was also studied.

Chapter 4 evaluates the photodiode beam monitoring system and testing protocols in neutron fluence measurements. Firstly, whether or not the photodiode sensor is sensitive to gamma rays is investigated. Following from that is a discussion of LANSCE and TRIUMF experimental results to examine the potential sources of great weight in the low collected energy of the measured pulse height spectra, uncertainties in these measurements, and response ratios (LANSCE and TRIUMF). Depending on the experiment, the recommended testing protocols of the beam monitoring system for using at each case of neutron facility are analyzed. The procedure and ability of beam monitoring to be used at ChipIr ISIS Target Station 2 will be predicted. The theoretical and experimental studies of determining the pulse height and counting system will be discussed. Finally, a possible way to determine the sensor testing life and calibration will be explored.

Chapter 5 concludes the thesis by summarizing the work undertaken in this research, presenting the major research findings by evaluating the overall performance of the beam monitoring system developed in the project, discussing the contributions of

the work as well as its possible limitations, and exploring the possible directions for further work in this field.

In the appendices of the thesis, Appendix A shows the schematics of the photodiode sensor circuit. Appendix B presents the method of determining the threshold level of the output of the matched filter. Appendix C gives addition information of the experimental results captured at LANSCE. Appendix D investigates neutron penetration of the aluminum. Appendix E presents the confidence limits of the number of pulse events in the photodiode monitoring system. Finally, Appendix F includes the candidate's publications resulting from this project, followed by the Bibliography.

Before moving on to the discuss the experimental results captured by the photodiode sensor at various neutron facilities, the development of the beam monitoring system will first be presented in Chapter 2.

# Chapter 2

## Beam monitoring design

### 2.1 Introduction

This chapter introduces the design of the beam monitoring system. An overview of the system will first be presented. The system uses small, inexpensive and commercial photodiodes as the detecting elements. Commercial and inexpensive low noise amplifiers are used to convert the charge produced in the photodiode to a voltage signal. A DAQ card is used to download time series data from the sensor. The software package was written using LabVIEW in conjunction with NI-DAQmx, to download the time series data or acquire the pulse height spectra from the sensors for further storage or analysis.

Following this overview is an introduction of the design of the photodiode detector circuit, and a discussion of why the sensor pulse width is a key factor in the beam monitoring system. Twelve sensors have been designed in this project, and a review of the development of the photodiode sensors and their pulse shapes will be presented.

Next, the signal processing system will be discussed. The nonparalyzable method

## 2.2 Overview of the beam monitoring system

---

will be introduced in the counting system to get pulse time intervals. Whether the pulse exists or not is detected by using a matched filter when the data is not disturbed externally; otherwise pulses are detected by the Rao test detection [109]. The method of how to estimate the pulse heights and time intervals also will be presented.

A series of calculation were undertaken to verify the correct operation of the detection software and to investigate variations in the system performance. In each calculation case, the theory and detected probability of detection agreed very well. It was verified that the interaction rate can be determined either by using the detection rate and the sensor pulse width or the exponential fit of the pulse interval distribution.

Then the key parameters of the beam monitoring system are introduced. These include the minimum detectable energy, the minimum signal-to-noise ratio, and the false alarm rate.

Finally, this chapter will introduce a method of determining the optimum shaping pulse width, which is achieved by considering the balance of the random noise of the photodiode neutron detector and the pile-up effect; the effect of sampling resolution on diode neutron sensor performance is also taken into account.

## 2.2 Overview of the beam monitoring system

The aim of the research is to develop a small, simple and inexpensive beam monitoring system, which can be easily incorporated into test sets or otherwise used to instrument SEE experiments. A Centronic OSD1-5T silicon PN photodiode [110] shown in figure 2.1(a) is used as the detecting element, and its active area is estimated about to be  $2.92 \text{ mm}^2$  as shown in figure 2.1(b). The TO-18 diode package is covered with aluminium foil to exclude ambient light, which can be operated either delidded (as shown in figure 2.1(c)) or not. The size of this photodiode is very small,

## 2.2 Overview of the beam monitoring system

---

with an external diameter of 4.7 mm, and an external package length of 5.1 mm. The OSD1-5T photodiode has a high speed rise time of the order of nanoseconds [110]. It costs approximately £6 per photodiode in the current market.

The photodiode junction region is produced by diffusion or ion implantation of boron into selected areas of the surface of a high resistivity n-type silicon wafer<sup>1</sup>. When the photodiode is operated with 12 V reverse bias, its capacitance is about 7 pF [110]. Its active (depletion) depth is estimated from its geometry and typical capacitance:

$$d = \varepsilon_0 \varepsilon_r \frac{A}{C} \quad (2.1)$$

where  $\varepsilon_0$  is permittivity of free space, with the numerical value of  $8.85 \times 10^{-12} \text{ F} \cdot \text{m}^{-1}$ .  $\varepsilon_r$  is relative permittivity or the dielectric constant. The silicon dielectric constant is 11.7.  $A$  is active area of the photodiode, and  $C$  is the capacitance of the photodiode. The photodiode active (depletion) depth is estimated to be about 43  $\mu\text{m}$ .

The TLE207x [111] series of JFET-input operational amplifiers were used in the multi-stage amplifiers. These comprise a charge-sensitive preamplifier followed by a pulse shaper.

A National Instruments PCI 6251 DAQ card [112] was used to collect the time series data from sensors. The device resolution is 16 bits with 8 differential analog inputs; the maximum sample rate is 1.25 MHz for a single channel, and 1 MHz for multiple-channels. Its maximum voltage range is  $\pm 10 \text{ V}$  and its minimum is  $\pm 0.1 \text{ V}$ . PCI 6251 can be used to download all the time series data; it also has the trigger function and allows acquisition of individual pulses. A shielded connector block BNC 2120 [113] was used to connect the PCI 6251 and photodiode sensors. Figure 1.13 (on page 24) shows the overview of the beam monitoring system, and figure 1.14 (on page 25) shows the system being tested.

---

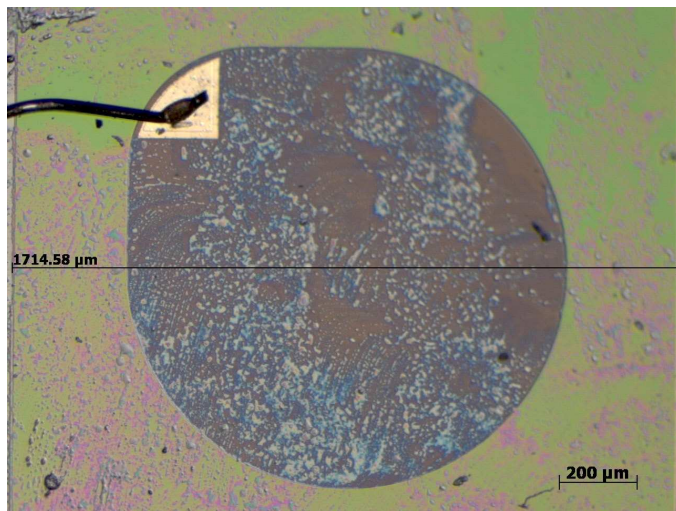
<sup>1</sup>Experimental results in §3.4.5 will show the effect of the different doping profiles.

## 2.2 Overview of the beam monitoring system

---



(a) OSD1-5T photodiode, after [110].



(b) Photodiode die.



(c) Photodiode delidded.

Figure 2.1: OSD1-5T PN photodiode.

## 2.3 The photodiode detector circuit and its pulse shapes

The PN photodiode sensor circuit was shown in figure 2.2. Full schematics are given in Appendix A. The photodiodes were operated with 12V reverse bias and d.c. coupled to a multiple-stage amplifier comprising a charge-sensitive preamplifier followed by a pseudo-gaussian pulse shaper. When neutrons hit the photodiode, they collide with atomic nuclei in the diode causing ejection of ions, which creates a trail of ionization, generating electron-hole pairs along its path in photodiode detector by the collision processes. For a silicon, an electron-hole is generated for every approx 3.6 eV lost by the charged particle during its trajectory. The electrons and holes move in an applied electric field and generate an electric signal at the photodiode terminals.

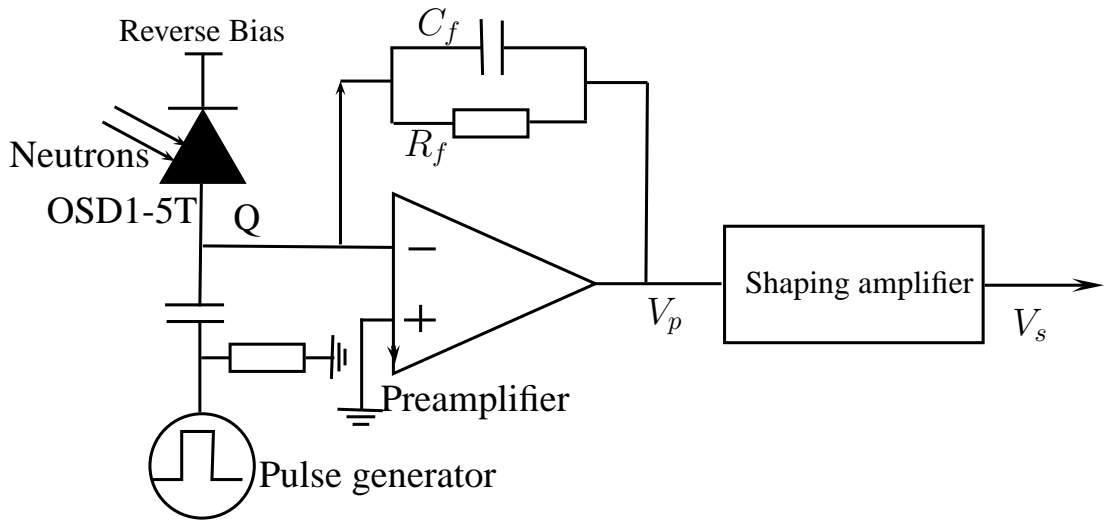


Figure 2.2: Photodiode sensor circuit.

The result of the neutron interaction in the photodiode detectors is the appearance of a given amount of electric charge within the detector active volume. The output signal is pulse with charge  $Q$  having a width of the order of nanoseconds. The preamplifier integrates charge pulses and converts the narrow charge pulse from the sensor into a voltage step  $V_p$  with a long decay time through the feedback capacitance  $C_f$ . The function of the feedback resistor is to discharge the feedback

### 2.3 The photodiode detector circuit and its pulse shapes

---

capacitor. The pulse shaper transforms a preamplifier pulse to a pulse with a longer peaking time. The feedback capacitance ( $C_f$ ) is 2.2 pF and feedback resistance ( $R_f$ ) is 10 M $\Omega$ . The output voltage from the preamplifier has an amplitude  $V_p$ , and a decay time constant  $\tau_f$ :

$$V_p = \frac{Q}{C_f} \quad (2.2)$$

$$\tau_f = R_f C_f \quad (2.3)$$

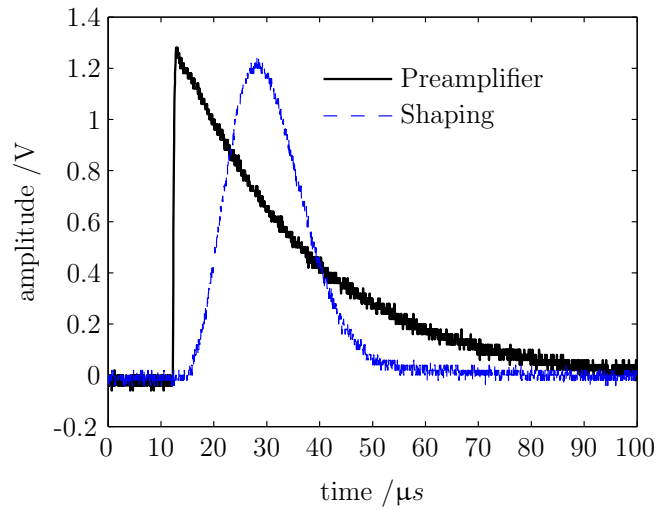
$Q$  is the charge collected by the detector, which is related to the total energy deposited in the sensor by a particle, which is:

$$Q = \frac{qE}{\epsilon} \quad (2.4)$$

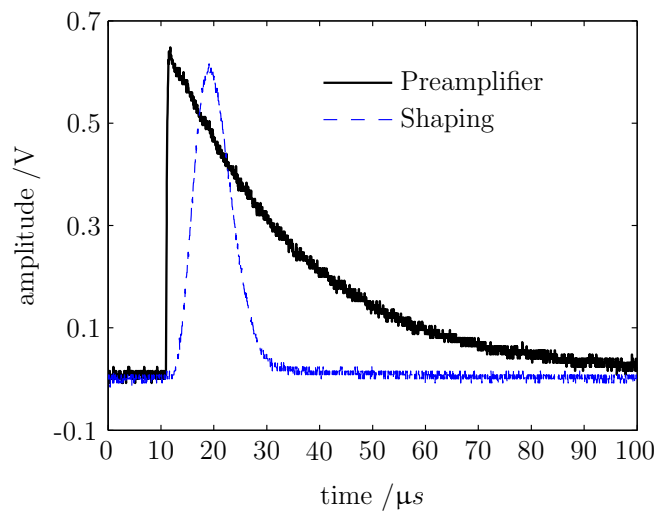
$E$  is the energy of the neutron incident radiation,  $q$  is the charge of an electron ( $1.602 \times 10^{-19}$  C), and  $\epsilon$  is the ionization energy required to produce an electron-hole pair in the detector. In silicon this is about 3.6 eV [61].

Figure 2.3 shows examples of preamplifier and shaping pulses of two sensors (number 6 and 7). These pulses were generated by sending a square pulse to the sensors via the test input as shown in figure 2.2, which were captured by an oscilloscope. The information of the sensors is given in table 2.1. The shaping pulse width  $\tau$  is a key parameter for the beam monitoring system. First it must be long enough to allow the interface DAQ card to download the shaping pulse from the sensor. In contrast, in high counting rates, a longer shaping pulse will have a higher probability of pile-up than short pulses. In this case, the shaping pulse width is required to be as short as possible. The optimum pulse width will be discussed in detail in §2.5.3.

### 2.3 The photodiode detector circuit and its pulse shapes



(a) sensor 6.



(b) sensor 7.

Figure 2.3: Example sensors 6 and 7 pulses.

### 2.3 The photodiode detector circuit and its pulse shapes

---

The amplitude of the shaping pulse at the peaking time reaches maximum, which is called the shaping pulse amplitude  $V_s$ , proportional to the preamplifier output. Overall the output of the photodiode detector consists of time series data of individual signal pulses, each representing the results of a particle interacting with the photodiode sensor. The amplitude of each individual pulse reflects the amount of charge collected from the photodiode due to the interaction. So the amplitude of the shaping pulse height equals:

$$\begin{aligned} V_s &= A_v V_p \\ &= A_v \frac{Q}{C_f} \\ &= A_v \frac{q}{\epsilon C_f} E \end{aligned} \tag{2.5}$$

where  $A_v$  is the shaping amplifier gain. Calling the photodiode sensor amplifier gain  $A$  ( $\text{mV} \cdot \text{MeV}^{-1}$ ):

$$A = \frac{V_s}{E} \tag{2.6}$$

or:

$$A = A_v \frac{q}{\epsilon C_f} \tag{2.7}$$

If a large number of such pulses are examined, their amplitudes will not all be the same. Variations may be due to differences in the particle interaction with the sensor. The pulse height distributions are the fundamental properties of the detector output of the information about collected energy from neutrons interaction with the sensor. Figure 2.4 shows one example of a measured pulse height spectrum captured by sensor 1 at TRIUMF.

This project developed twelve sensors (shown in table 2.1) with slightly different circuits and two kinds of pulse widths<sup>1</sup> ( $20 \mu\text{s}$  and  $40 \mu\text{s}$ ). The sensor shaping time-equivalent is the “standard deviation” of pulse widths. The sensor amplifier

---

<sup>1</sup> Pulse width is defined to the 0.1% point.

## 2.3 The photodiode detector circuit and its pulse shapes

---

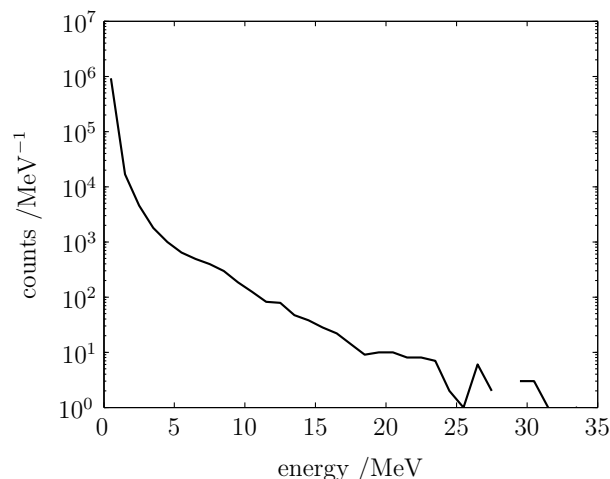


Figure 2.4: Example pulse height spectrum captured by sensor 1 at TRIUMF in 2007.

gains are determined by the nominal value of amplifier parameters and assuming an ionization energy of 3.6 eV [61]. Sensors 1, 2 and 3 have the same pulse shape as shown in figure 2.5(a)<sup>1</sup>. Sensors 4, 6 and 8 have the same pulse shape and circuit as shown in figure 2.5(b). Sensors 5 and 7 have the same pulse shape and circuit as shown in figure 2.5(c). Sensors 9 and 10 have the same pulse shape and circuit as shown in figure 2.5(d). Sensors 11 and 12 have the same pulse shape and circuit as shown in 2.5(e).

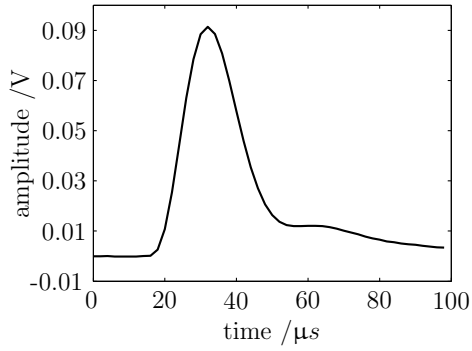
Example time series data are shown in figures 2.6 and 2.7. Experiments were made at the downstream position of several other experiments at TSL in 2007, where the neutron beam was severely degraded. The experimental data captured at TRIUMF in 2007 were interfered with by external noise as shown in figure 2.7(a). The other experiment time series data gathered were irradiated at the upstream position without other devices in front.

Figure 2.8 on page 41 shows the picture of sensor 6. As can be seen the sensor part is smaller than a British 5 pence piece.

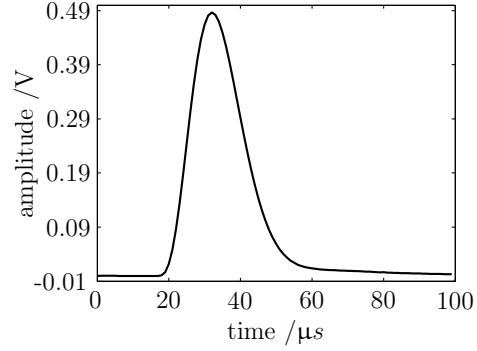
---

<sup>1</sup>This pulse shape has a long tail, which was removed by later design.

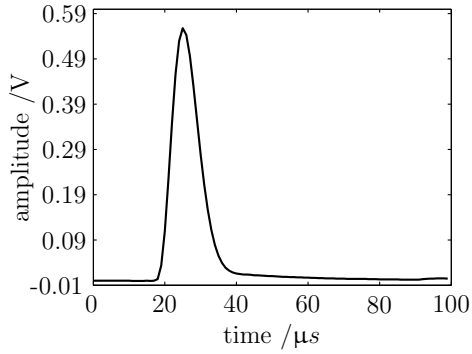
### 2.3 The photodiode detector circuit and its pulse shapes



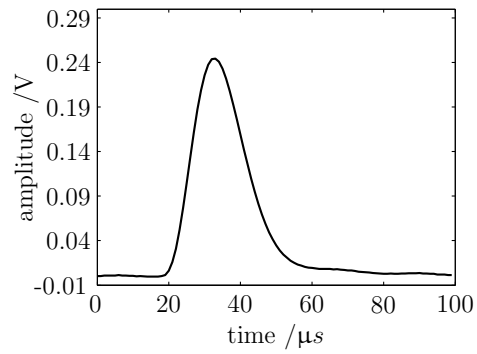
(a) sensor 1 from a 23 MeV interaction.



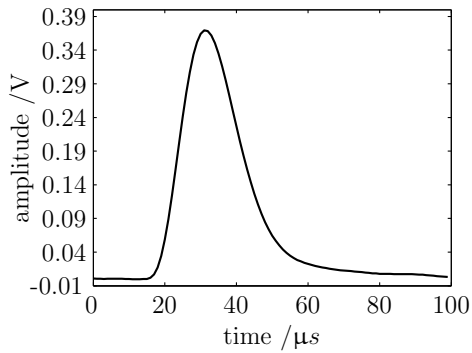
(b) sensor 4 from a 24 MeV interaction.



(c) sensor 5 from a 27 MeV interaction.



(d) sensor 9 from a 13 MeV interaction.

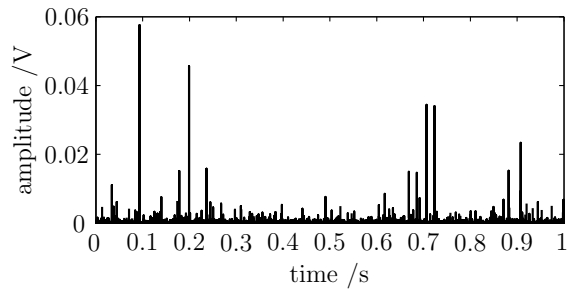


(e) sensor 12 from a 20 MeV interaction.

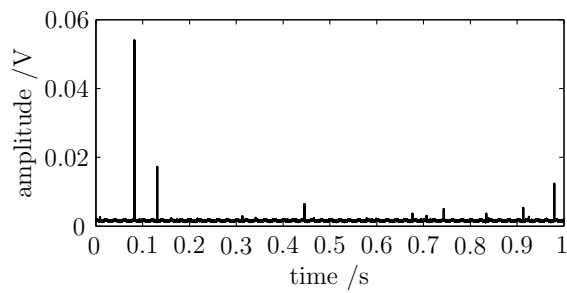
Figure 2.5: Example detector pulses from neutron beam interaction.

### 2.3 The photodiode detector circuit and its pulse shapes

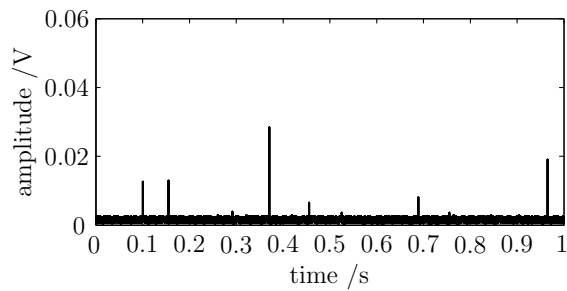
---



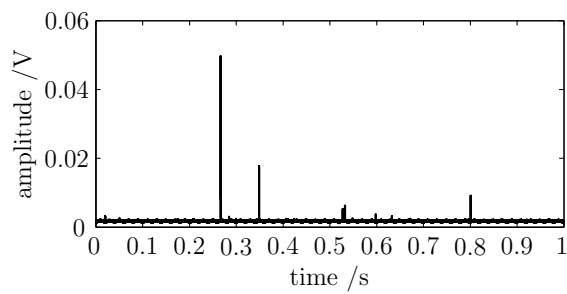
(a) TRIUMF 2007.



(b) TSL 2007 ANITA.



(c) TSL 2007 110 MeV.

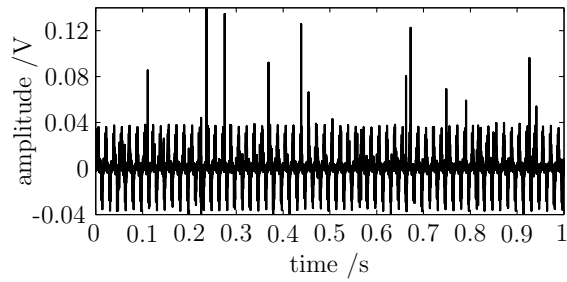


(d) TSL 2007 50 MeV.

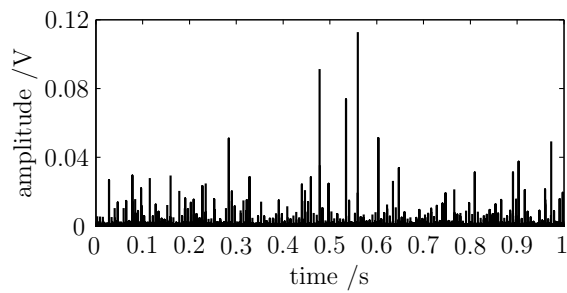
Figure 2.6: Example voltage time series 1.

## 2.3 The photodiode detector circuit and its pulse shapes

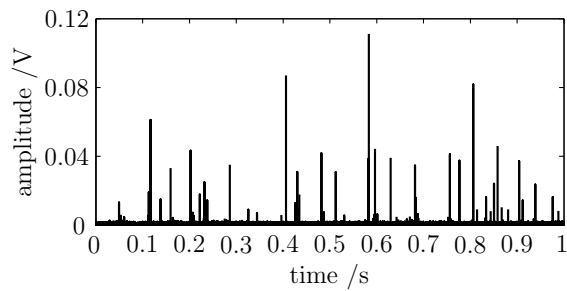
---



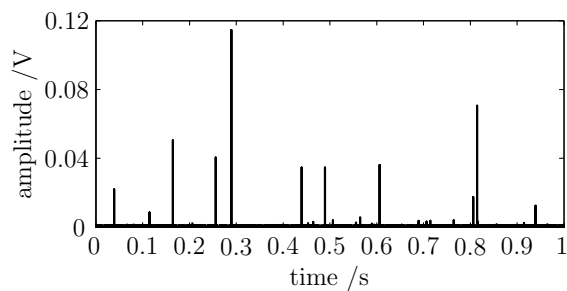
(a) TRIUMF 2007.



(b) TSL 2010 ANITA.



(c) ASP 2009 14 MeV.



(d) LANSCE 2010.

Figure 2.7: Example voltage time series 2.

Table 2.1: Sensor lists.

sensor	component exposed	pulse width,	pulse	amplifier gain,	neutron beam
		$\tau$	FWHM	$A$	
		$\mu\text{s}$	$\mu\text{s}$	$\text{mV} \cdot \text{MeV}^{-1}$	
1	Diode+Amplifier	40	18	4.0	TSL2007
2	Amplifier only	40	18	4.0	TRIUMF2007
3	Diode only	40	18	4.0	
4	Diode only	40	18	20.2	
5	Diode only	20	9	20.2	TRIUMF2008
6	Diode only	40	18	20.2	TSL2008
7	Diode only	20	9	20.2	
8	Amplifier only	40	18	20.2	
	Diode only	40	18	20.2	
9	Diode only	40	18	18.9	ASP2009
10	Diode only	40	18	18.9	TSL2010
11	Diode only	40	18	18.6	LANSCE2010
12	Diode only	40	18	19.0	

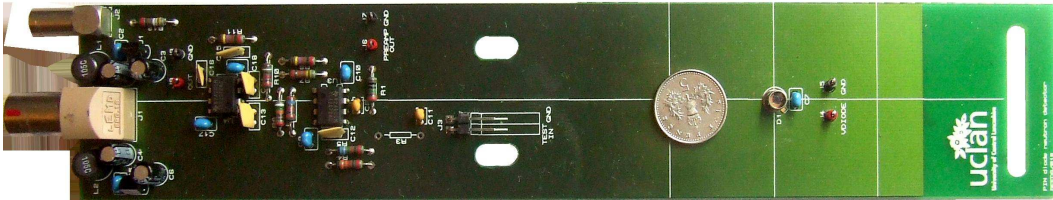


Figure 2.8: Sensor 6 picture.

## 2.4 Signal processing system

The purpose of signal processing is to acquire the pulse amplitude and arrival time from time series data at a low false alarm rate.

Electronics is a key component of all modern detector systems, and noise is in-

evitable in all electronic circuits and devices. In a photodiode neutron detector, both the sensor and the amplifier introduce noise. Moreover, external noise sources may be more significant than intrinsic noise source especially as accelerator facilities are often electrically noisy environments. The measurements made at TRIUMF in 2007 were subject to intermittent interference as shown in figure 2.7(a). However, the external electrostatics noise can be reduced by electronic shielding, which is illustrated in Appendix A.

The pulse time dependence was determined from the time series data gathered from the shaping amplifier output using the nonparalyzable counting system [61], and pulse amplitudes were extracted using a matched filter [109, 114] when the time series data were not interfered by with external noise. A block diagram of the pulse detection and estimation system is shown in figure 2.9. Some experimental data captured at TRIUMF in 2007 were interfered by with external noise as shown in figure 2.7(a). The pulse amplitudes were detected by Rao test detection [109], an enhanced matched filtering technique which is suitable for pulse detection in more demanding noise environments at the cost of greater computational complexity [115].

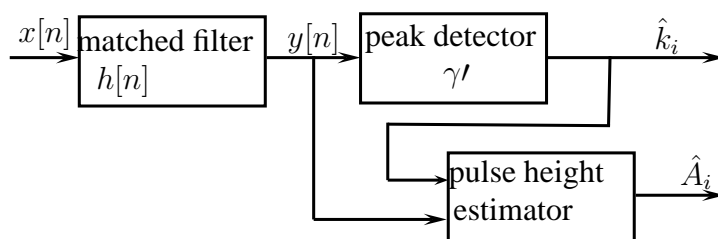


Figure 2.9: Pulse detection and estimation system.

### 2.4.1 Nonparalyzable counting system

This subsection is a description of the nonparalyzable system based on Knoll [61].

The time of a pulse occurrence is determined by using timing measurements. In order for two events to be recorded as two separate pulses, it is necessary that

they are separated by an amount of time in a radiation detector system, which is known as “the dead time of the counting system”. However, as radioactive decay is a random phenomenon, it is possible that some true pulses can be lost if they occur too quickly after the previous event. These are called “dead time losses”, which are particularly severe in cases of high counting rates, as happens with the beam monitoring system under test for high flux neutron beams (e.g. TSL ANITA). Hence, it is important to use correction for such losses, under these circumstances, in order to achieve accurate counting.

There are two models of dead time behaviour of counting systems which have been found in common use: paralyzable response and nonparalyzable response. The fundamental assumptions of these models are illustrated in figure 2.10, where  $\tau$  is the shaping pulse width. In the middle part of the figure, the line represents six events as they occur along the horizontal time axis. At the upper part of the figure is the corresponding dead time behavior of a detector which is assumed to be paralyzable. It would record six counts from the six interactions. At the bottom of the figure is the corresponding dead time behavior of a detector which is assumed to be nonparalyzable. It would record four counts from the six interactions. As the paralyzable method uses more computational complexity than the nonparalyzable, nonparalyzable techniques are used in the counting system for the beam monitoring.

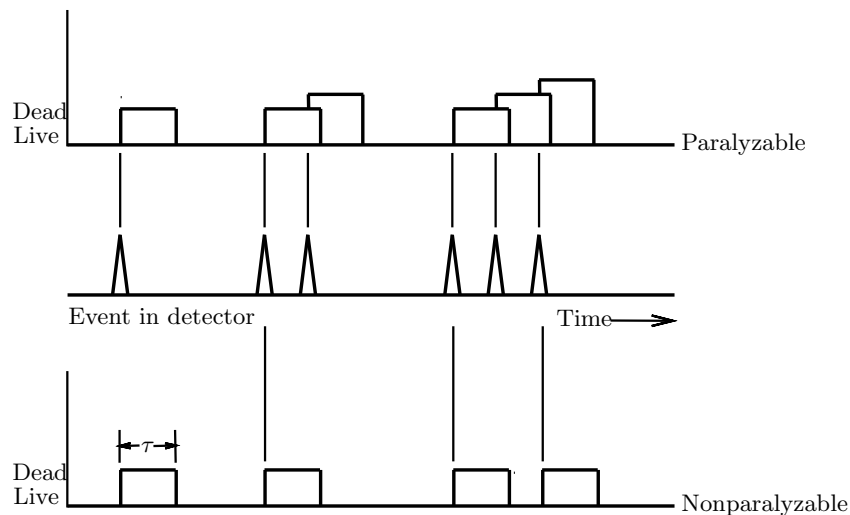


Figure 2.10: Illustration of Nonparalyzable model counting system.

The following definitions are assumed:

- $n$  = interaction rate
- $r$  = detection rate

If the counting time is long enough so that both  $n$  and  $r$  may be regarded as average rates, in the nonparalyzable case, the fraction of all time that the detector is dead is given by the product of  $r\tau$ . Therefore, the rate at which true events are lost is simply  $nr\tau$ .  $n - r$  is another expression for the rate of losses, so:

$$n - r = nr\tau \quad (2.8)$$

Solving for  $n$ , it will obtain:

$$n = \frac{r}{1 - r\tau} \quad (2.9)$$

Assuming the pulse event is without the effect of noise, the probability of detection  $P_r$  can be expressed as:

$$\begin{aligned} P_r &= \frac{r}{n} \quad \text{or} \\ &= 1 - r\tau \end{aligned} \quad (2.10)$$

and the probability of pile-up can be calculated by:

$$\begin{aligned} P_{pile-up} &= 1 - P_r \\ &= r\tau \end{aligned} \quad (2.11)$$

### 2.4.2 Matched filter

This subsection is a description of matched filtering technique based on Kay [114].

A matched filter is a linear Finite Impulse Response (FIR) filter. Its impulse response is determined by a specific signal in such a way that the maximum attainable SNR will result from the output of the filter when that particular signal pulses through the filter. The matched filter detection is approached by considering the problem of detecting a known deterministic signal in Gaussian white noise (GWN).

If  $s[n]$  is the specific signal (also called reference signal),  $x[n]$  is the input to a filter with impulse response  $h[n]$ , which is a “flipped around” version of the signal  $s[n]$  [114]. It will have:

$$h[n] = s[N - 1 - n] \quad n = 0, 1, \dots, N - 1 \quad (2.12)$$

where  $N$  is the number of pulse points; then the output of the filter is:

$$\begin{aligned} y[n] &= \sum_{k=0}^n h[n - k]x[k] \\ &= \sum_{k=0}^n s[N - 1 - (n - k)]x[k] \end{aligned} \quad (2.13)$$

The output of the matched filter is the convolution of  $x[n]$  and  $h[n]$ , which is illustrated in figure 2.11, where  $x[n]$  is an example pulse of the output of sensor 12 (see figure 2.5(e)).

The matched filter impulse response is obtained by flipping  $s[n]$  about  $n=0$  and shifting it to the right by  $N - 1$  samples, and it also attains maximum by sampling at point  $N - 1$ , which is:

$$y[N - 1] = \sum_{k=0}^{N-1} s[k]x[k] \quad (2.14)$$

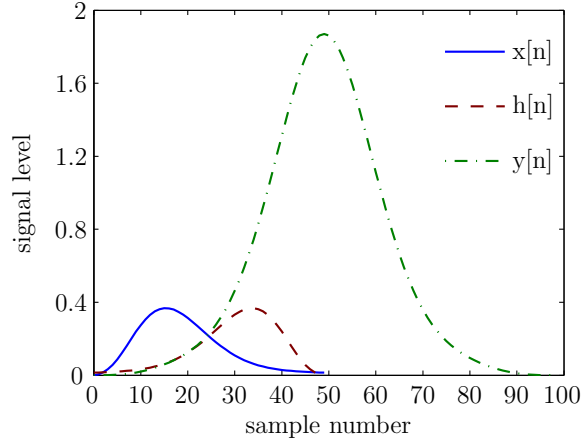


Figure 2.11: Illustration of the matched filter.

When noise is present, assuming the noise is denoted by  $\omega[n]$  and the input of signal to be  $x[n]_2$ , it equals:

$$x[n]_2 = x[n] + \omega[n] \quad n = 0, 1, \dots, N - 1 \quad (2.15)$$

Assuming the output of the matched filter with GWN noise present to be  $y[N - 1]_2$ , it equals:

$$\begin{aligned} y[N - 1]_2 &= \sum_{k=0}^{N-1} s[k]x[k]_2 \\ &= \sum_{k=0}^{N-1} s[k](x[k] + \omega[k]) \\ &= y[N - 1] + \sum_{k=0}^{N-1} s[k]\omega[k] \end{aligned} \quad (2.16)$$

The mean of the value  $\sum_{k=0}^{N-1} s[k]\omega[n]$  should be zero. In this case, the maximum of the matched filter output may be affected, but the best detection performance should be obtained by sampling still at around  $N - 1$  (this will be explained in Appendix B and supported by calculations in §2.4.6.2). This maximum is then

compared to a threshold level  $\gamma'$  to indicate the presence of a pulse event. In this case the threshold can be chosen to control the probability of false alarm,  $P_{FA}$  using the (standard) inverse  $Q^{-1}(P_{FA})$  function [114]:

$$\gamma' = \delta Q^{-1}(P_{FA}) \sqrt{\varepsilon_R} \quad (2.17)$$

where  $\delta^1$  is the noise level, and  $\varepsilon_R$  is the reference signal  $s[n]$  energy:

$$\varepsilon_R = \sum_{n=0}^{N-1} s^2[n] \quad (2.18)$$

$P_{FA}$  is the probability of false alarm of the detected pulse from the time series data, for example, when  $P_{FA}=1 \times 10^{-9}$  and sample rate is 1 MHz, the false pulse rate is  $1 \times 10^{-3} \text{ s}^{-1}$ .

The details of determining the threshold level  $\gamma'$  are given in Appendix B.

### 2.4.3 Estimation

Peak detection determines the estimated locations  $\hat{k}_i$  of pulses where  $y[n]$  exceeds  $\gamma'$ ; pulse heights are estimated as:

$$\begin{aligned} \hat{A}_i &= \frac{y[\hat{k}_i]}{\sum_{n=0}^{N-1} s^2[n]} \\ &= \frac{y[\hat{k}_i]}{\varepsilon_R} \end{aligned} \quad (2.19)$$

Statistics of pulse heights  $\hat{A}_i$  and intervals  $\hat{k}_i - \hat{k}_{i-1}$  are straightforward to generate from simulated or real sample sequences. The experimental results are presented

---

<sup>1</sup>The symbol of noise standard deviation usually is  $\sigma$ . In this thesis,  $\sigma$  represents the response of the photodiode irradiated at neutron facilities, and  $\delta$  is used to express the noise standard deviation.

in Chapter 3 by using  $\hat{A}_i$  and intervals  $\hat{k}_i - \hat{k}_{i-1}$  to deduce the information of the neutron interaction with the sensor.

### 2.4.4 Determining beam monitoring system threshold level

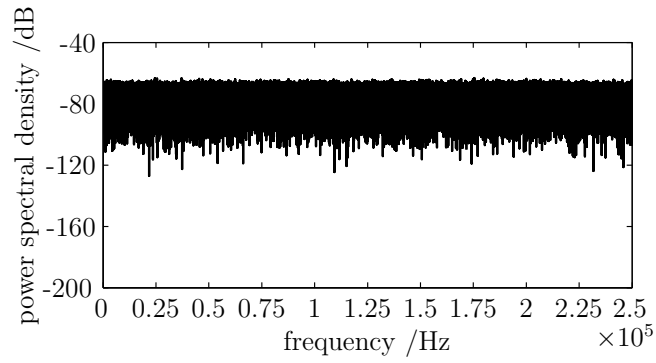
Figure 2.12 shows an example of power spectral density (PSD) of simulated Gaussian white noise, time series noise data gathered at TRIUMF beam and time series data interfered with by external noise at TRIUMF. The power spectral density of data gathered in the neutron beam is not as flat as the Gaussian white noise power spectral density. This is caused by the photodiode sensor pulse shaper, which removed parts of the noise bandwidth. In such cases, the PN photodiode sensor noise is not exactly Gaussian white noise, the measured noise standard deviation of the photodiode sensors would be smaller than if the parts of noise bandwidth were not removed.

According to Kay [114], for non-Gaussian noise, the matched filter may still be said to maximize the SNR at the output of a linear FIR filter. Based on the lab testing, it has been found that the threshold level  $\gamma'$  could be three times as high as the value indicated in equation 2.17, and as a result the signal processing is unlikely to isolate any false event. So the threshold level  $\gamma'$ , which is used to determine whether the pulse events are present or not in the photodiode sensor, can be calculated:

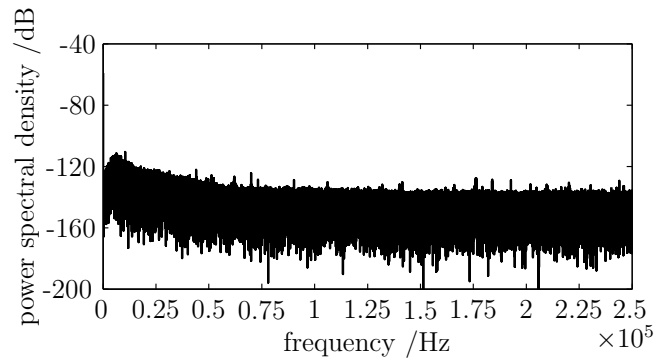
$$\gamma' = 3\delta Q^{-1}(P_{FA})\sqrt{\varepsilon_R} \quad (2.20)$$

### 2.4.5 Rao test detection

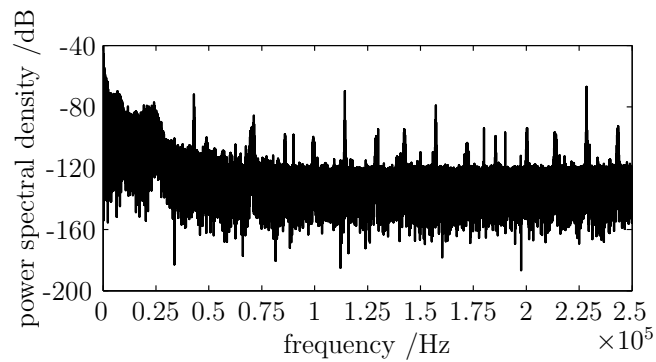
Parts of the photodiode sensor experimental data suffered interference as shown in figure 2.7(a). This external noise may be more significant than intrinsic noise. As can be seen from the example time series data as shown in figure 2.7(a), its PSD



(a) Simulated data with Gaussian White Noise.



(b) Experimental data without external interference.



(c) Experimental data with external interference.

Figure 2.12: Example of simulated and experimental data power spectral density.

is not as flat as data without external noise shown in figure 2.12; and also there is 60 Hz noise with its harmonics in PSD as shown in figure 2.13. In this case, the signal processing first removes the 60 Hz contamination with its harmonics, then Rao test detection is used.

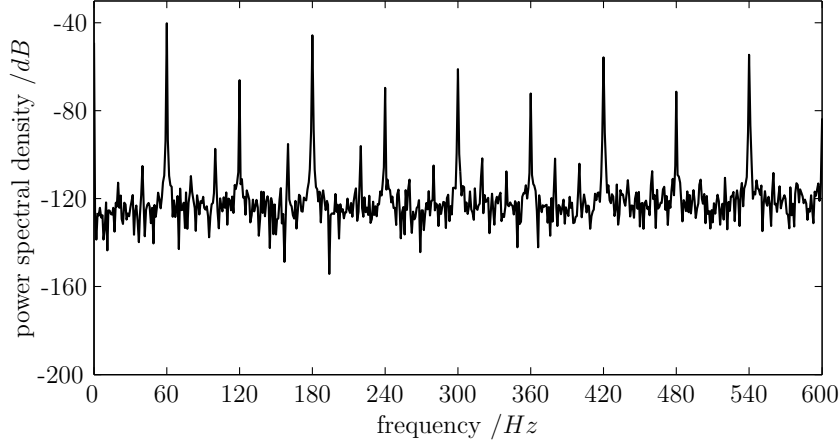


Figure 2.13: Example of experimental data with external noise power spectral density in low frequency.

The rest of this subsection gives a summary of the Rao test detection based on Kay [114].

For large data records, the output of the Rao test detection can be shown to be equivalent to:

$$T_R(x) = \frac{(\sum_{n=1}^{N-1} (s[n] + \hat{a}_0[1]s[n-1])(x[n] + \hat{a}_0[1]x[n-1]))^2}{\sigma_{\mu 0}^2 \sum_{n=1}^{N-1} (s[n] + \hat{a}_0[1]s[n-1])^2} \quad (2.21)$$

where  $x[n]$  is the input signal,  $s[n]$  is the reference signal,  $\omega[n]$  is the noise signal, and  $\delta_{\mu 0}^2$  is estimated:

$$\delta_{\mu 0}^2 = \frac{1}{N} \sum_{n=1}^{N-1} (x[n] + \hat{a}_0[1]x[n-1])^2 \quad (2.22)$$

where  $\hat{a}_0[1]$  is estimated by :

$$\hat{a}_0[1] = -\frac{\hat{r}_{xx}[1]}{\hat{r}_{xx}[0]} \quad (2.23)$$

where  $\hat{r}_{xx}$  is the autocorrelation function of  $x[n]$ :

$$\hat{r}_{xx}[k] = \frac{1}{N} \sum_{n=0}^{N-1-k} x[n]x[n+k] \quad (2.24)$$

### 2.4.6 Calculation

A series of calculations were undertaken in order to verify the correct operation of the detection software and to investigate system performance variations, as illustrated in figure 2.14. For the calculation, sensor 12 pulse shape was used as the input pulse with width of  $40 \mu\text{s}$  (to 0.1% point), the amplifier gain was  $19 \text{ mV} \cdot \text{MeV}^{-1}$ , and the sample rate was 1 MHz.

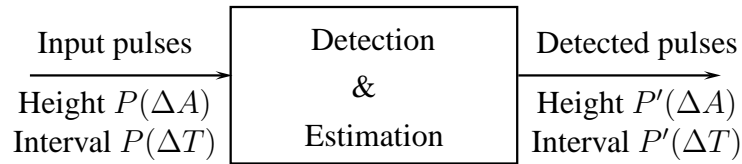


Figure 2.14: Pulse calculation system.

The calculations were undertaken in three aspects. The first only considered the effect of “pile-up”; the second focused on the effect of thresholds  $\gamma'$  corresponding to minimum detectable pulse energies; In the last both pile-up and noise effects were taken into account.

### 2.4.6.1 Calculation only with pile-up effect

In this calculation, a constant pulse with 0.4 MeV energy is postulated. The pulse interval distribution is postulated based on the exponential characteristic. There are four mean interaction pulse rates,  $n$ ; these are  $3000\text{ s}^{-1}$ ,  $2000\text{ s}^{-1}$ ,  $1000\text{ s}^{-1}$ ,  $200\text{ s}^{-1}$ .  $3000\text{ s}^{-1}$  is similar to the pulse rate detected at TSL ANITA (see §3.4.8).  $2000\text{ s}^{-1}$  is somewhat greater than the pulse rate detected at TRIUMF (see §3.2.1).  $1000\text{ s}^{-1}$  is similar to the pulse rate detected at TSL ANITA downstream testing,  $200\text{ s}^{-1}$  is very unlikely to be exceeded by the pulse rate detected at LANSCE and TSL quasi-monoenergetic neutron beam. The calculation results are summarized in table 2.2.

Based on the equation 2.8, the detection rate  $r$  is:

$$r = \frac{n}{1 + n\tau} \quad (2.25)$$

where  $n$  is the interaction rate,  $\tau$  is the pulse width, and  $r$  is the detection rate. If  $r$  is known,  $n$  will be:

$$n = \frac{r}{1 - r\tau} \quad (2.26)$$

The input interaction, detected and calculated detection pulse rates are summarized in table 2.2(a) where the input interaction rate was calculated from the number of input pulse events divided by the input duration; and the detected detection rate was calculated for the number of detected events divided by the input duration. The calculated interaction rates were determined by using the equation 2.26. The calculated detection rates were determined by using the equation 2.25, where  $n$  is the input interaction rate. It can be seen that the detected and calculated rate agree well. It proves that the interaction rate can be determined by using the sensor pulse width and the detection rate.

## 2.4 Signal processing system

(a) detected and calculated pulse rate ( $s^{-1}$ ).

$/s^{-1}$	interaction rate		detection rate	
	input	calculated	detected	calculated
$n \rightarrow 200$	199.93	$199.84 \pm 0.63$	$198.26 \pm 0.63$	198.34
$n \rightarrow 1000$	998.62	$999.02 \pm 3.08$	$960.63 \pm 3.08$	960.26
$n \rightarrow 2000$	2005.50	$2002.31 \pm 6.09$	$1853.84 \pm 6.09$	1856.56
$n \rightarrow 3000$	3013.88	$3005.77 \pm 8.88$	$2683.17 \pm 8.88$	2689.63

(b) probability of detection.

$/s^{-1}$	theoretical	detected
	/%	/%
$n \rightarrow 200$	99.21	$99.17 \pm 0.31$
$n \rightarrow 1000$	96.16	$96.20 \pm 0.31$
$n \rightarrow 2000$	92.58	$92.43 \pm 0.30$
$n \rightarrow 3000$	89.24	$89.03 \pm 0.29$

(c) decay constant.

$/s^{-1}$	input	detected
	$/s^{-1}$	$/s^{-1}$
$n \rightarrow 200$	$199.26 \pm 1.06$	$199.24 \pm 1.06$
$n \rightarrow 1000$	$993.65 \pm 5.65$	$993.29 \pm 5.78$
$n \rightarrow 2000$	$2006.19 \pm 6.35$	$2007.11 \pm 6.58$
$n \rightarrow 3000$	$3011.08 \pm 11.75$	$3016.44 \pm 15.59$

Table 2.2: Calculation results with the effect of pile-up, CI=68.27%.

So the probability of detection only with pile-up effect is:

$$P_{pile-up} = \frac{r}{n} = \frac{1}{1 + n\tau} \quad (2.27)$$

For example, when  $n \rightarrow 3000 s^{-1}$ , the theoretical probability of detection is 89.29%. Tables 2.2(b) summarizes the probability of detection calculation results. The theoretical and detected probability of detection agree very well. The probability of

detection only with pile-up for various interaction rates will be discussed in §4.4.1.

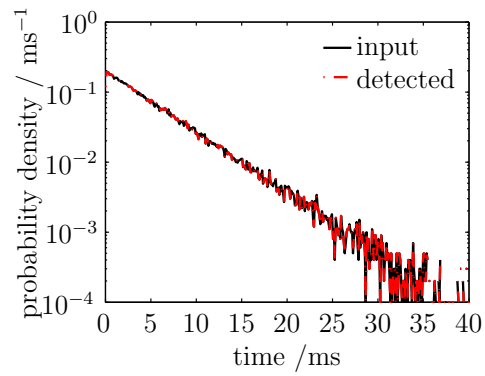
The detected and input pulse interval distributions match well as shown in figure 2.15. Table 2.2(c) summarizes the decay constant. The detail of how to get the decay constant will be discussed in §3.2. According to Knoll [61], the decay constant is the reciprocal of the mean of pulse intervals for a large number of pulse events. In this case, the interaction rate for photodiode irradiated at facilities can be calculated by determining the decay constant of the pulse interval distribution. For instance, when the interaction rate is about  $3000\text{ s}^{-1}$ , the input rate was  $3013.58\text{ s}^{-1}$ , and the decay constant of its pulse interval distribution was  $3011.08\text{ s}^{-1}$ . It proves that the interaction rates can be determined by the decay constants of the pulse interval distribution.

Figure 2.16 shows the detected pulse height spectra. As a constant energy is postulated in the calculation, the detected energy above  $0.4\text{ MeV}$  should be produced by the pile-up effect. There should be two pulses occurring within  $40\text{ }\mu\text{s}$  if any detected energy is above  $0.4\text{ MeV}$  and under  $0.8\text{ MeV}$ . If the detected energy is above  $0.8\text{ MeV}$ , there must be three pulses or more occurring within  $40\text{ }\mu\text{s}$ . The number of pulses detected above  $0.4\text{ MeV}$  increases with the increase of interaction rate as shown in figure 2.16. These prove that the pile-up rate increases with the increase of interaction rate.

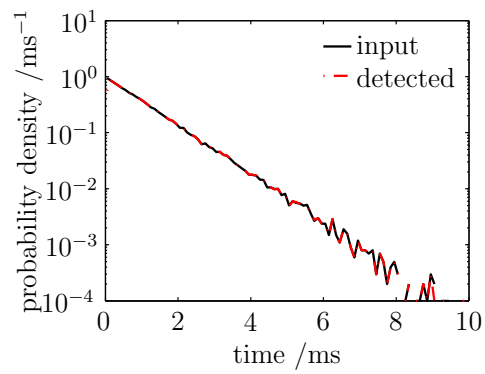
This calculation proves that the rate of interaction between neutrons and photodiode sensors can be determined either by the rate of the detected events and the sensor pulse width or by the exponential fit (as shown in table 2.2(c)) of the pulse interval distribution.

### 2.4.6.2 Calculation only with noise effect

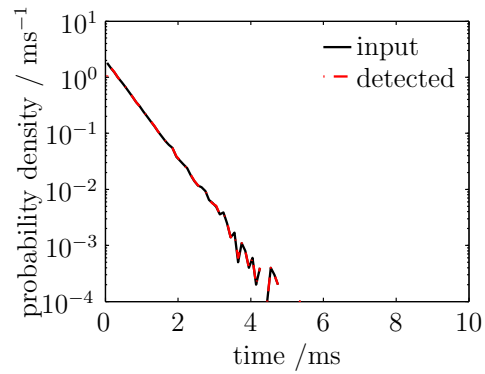
In this subsection, a pulse height distribution based on the exponential characteristic, as reported by a previous study [115], that is with a decay constant  $0.3\text{ MeV}^{-1}$ , was postulated. Input pulse heights were selected randomly to meet this distribution



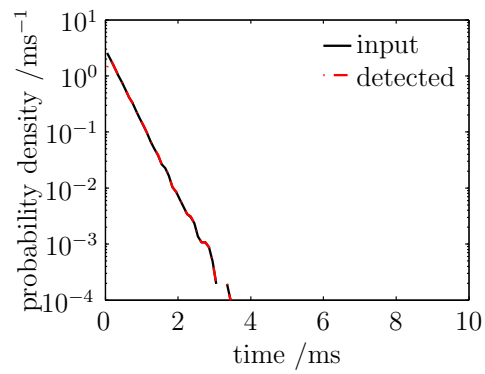
(a)  $n \rightarrow 200 \text{ s}^{-1}$ .



(b)  $n \rightarrow 1000 \text{ s}^{-1}$ .



(c)  $n \rightarrow 2000 \text{ s}^{-1}$ .



(d)  $n \rightarrow 3000 \text{ s}^{-1}$ .

Figure 2.15: Pile-up effect calculation results — pulse interval distributions.

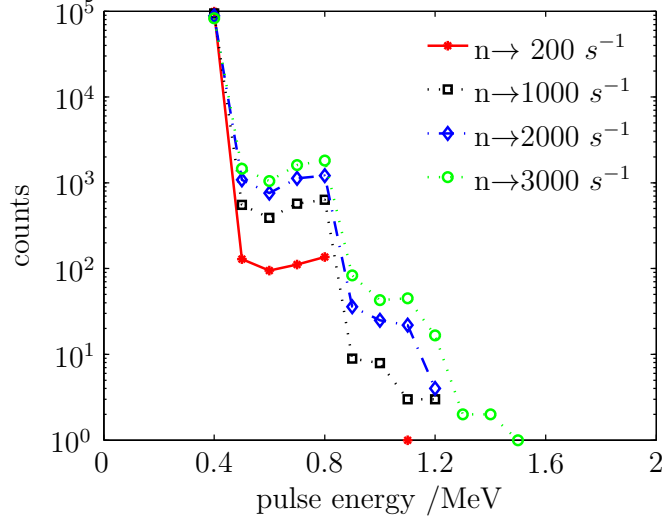


Figure 2.16: Calculation results with the effect of pile-up — pulse height spectra.

and used to construct the input sequence. The pulse interval used in the calculation was assumed to be 1 ms. The number of input pulses were about 100 000. The input data fit an exponential curve of the general form described by the following equation:

$$N = a \exp^{-\lambda E} \quad (2.28)$$

where  $a$  is the fit parameter,  $\lambda$  is the exponential decay constant. The detail of the fitted pulse height spectrum will be discussed in §3.2.1. Assuming the minimum detectable energy to be  $E_{min}$ , the probability of detection between energy  $E_{min}$  and  $\infty$  is:

$$\begin{aligned} P_{\gamma t} &= -\lambda \int_{E_{min}}^{\infty} \exp^{-\lambda E} dE \\ &= -\exp^{-\lambda E} \Big|_{E_{min}}^{\infty} \\ &= \exp^{-\lambda E_{min}} \end{aligned} \quad (2.29)$$

The photodiode sensors' noise standard deviation is between 100  $\mu\text{V}$  and 300  $\mu\text{V}$ . r.m.s.

## 2.4 Signal processing system

---

As discussed in 2.4.4, the photodiode sensor pulse shaper removed parts of the noise bandwidth. In this case, the sensor noise is not exactly Gaussian white noise. As a consequence, the threshold level of the beam monitoring system is three times of the level of the determined output of the matched filter (see equation 2.20) if the noise is Gaussian white. In this calculation, the noise train was generated by using LabVIEW function Gaussian White Noise, and standard deviation was three times of either 100  $\mu\text{V}$  or 300  $\mu\text{V}$  r.m.s.

Assuming the false alarm rate  $P_{FA}$  to be  $1 \times 10^{-9}$ , the sample rate used to download the time series data was 1 MHz. The former noise level corresponds to a minimum detected energy of 26.75 keV<sup>1</sup>, and the latter one corresponds to a minimum detected energy of 82.45 keV. The experiments are often carried out with multiple sensors under test; then the sample rate used to collect the experimental data for each sensor will be reduced. Another calculation was undertaken assuming two sensors under test simultaneously, so the sample rate was 0.5 MHz for each sensor; in this case, the minimum detectable energy was 116.6 keV.

(a) probability of detection.

Noise standard deviation / $\mu\text{V}$	sample rate, /MHz	theoretical /%	detected /%
$\delta \rightarrow 100$	1	99.20	99.21 $\pm$ 0.31
$\delta \rightarrow 300$	1	97.56	97.54 $\pm$ 0.31
$\delta \rightarrow 300$	0.5	96.56	96.54 $\pm$ 0.31

(b) pulse height spectra decay constant.

Noise standard deviation / $\mu\text{V}$	sample rate /MHz	input /MeV <sup>-1</sup>	detected /MeV <sup>-1</sup>
$\delta \rightarrow 100$	1	0.309 $\pm$ 0.007	0.309 $\pm$ 0.007
$\delta \rightarrow 300$	1	0.296 $\pm$ 0.005	0.295 $\pm$ 0.006
$\delta \rightarrow 300$	0.5	0.299 $\pm$ 0.007	0.296 $\pm$ 0.007

Table 2.3: Calculation results with the effect of noise, CI=68.27%.

---

<sup>1</sup>The detail of how to determine the minimum detected energy will be introduced in §2.5.1.

The theoretical (by using equation 2.29) and the detected probability of detection (CI=68.27%) agree well as summarized in table 2.3. These calculation results suggest that the minimum detectable energy reduces with the increase of the noise level and the decrease of the sample rate; further details will be analyzed in §2.5.1. As a consequence, the detected probability of detection decreases with the increase of the minimum detected pulse energy as expressed in equation 2.29.

The detected and input pulse height spectra (as shown in figure 2.17) and decay constants (as listed in table 2.3(b)) agree well.

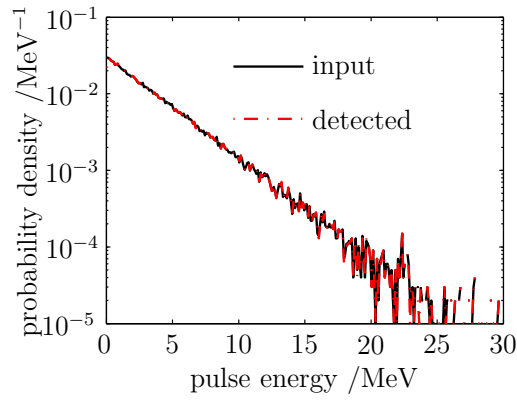
The detected pulse interval distributions are displayed in figure 2.18. The pulse interval is  $m$  ms, where  $m$  is an integer. When  $m$  is greater than 1, there will be  $m - 1$  events missed because their heights are too small to be detected.

Figure 2.19 shows the detected histogram at pulse interval around 1 ms when the noise level is  $300 \mu\text{V}$  and sample rate is 0.5 MHz. This shows that when noise is present, the maximum of the matched filter output may be affected, but the best detection performance should be obtained by sampling still at around  $N - 1$  (see §2.4.2).

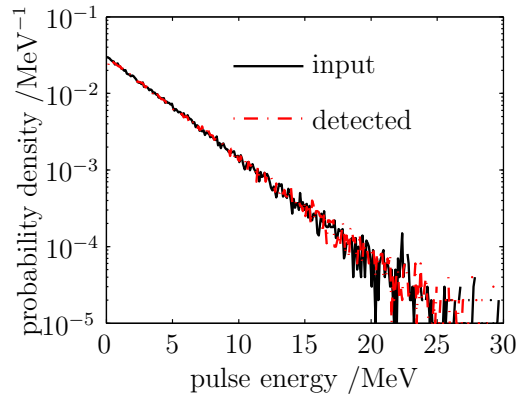
### 2.4.6.3 Calculation with both pile-up and noise effects

Twelve separate cases were calculated. The sample rate was assumed to be 1 MHz for one sensor under test and to be 0.5 MHz for two sensors under test simultaneously. There were two kinds of noise levels with standard deviation of  $100 \mu\text{V}$  and  $300 \mu\text{V}$ , and four kinds of interaction rates  $n \rightarrow 3000 \text{ s}^{-1}$ ,  $n \rightarrow 2000 \text{ s}^{-1}$ ,  $n \rightarrow 1000 \text{ s}^{-1}$  and  $n \rightarrow 200 \text{ s}^{-1}$ . A pulse height distribution based on an exponential characteristic with decay constant  $0.3 \text{ MeV}^{-1}$  was postulated.

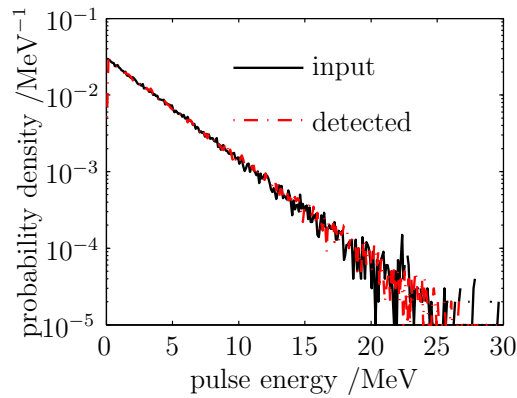
The input and detected interaction rates and the decay constants of the pulse height spectra are summarized in tables 2.4. It can be seen that the detected pulse interval decay constants reduce with the increase of the noise level, because that the probability of detection decreases with the increase of the noise level. They



(a)  $\delta \rightarrow 100 \mu\text{V}$ , sample rate=1 MHz.



(b)  $\delta \rightarrow 300 \mu\text{V}$ , sample rate=1 MHz.



(c)  $\delta \rightarrow 300 \mu\text{V}$ , sample rate=0.5 MHz.

Figure 2.17: Noise effect calculation results — pulse height spectra.

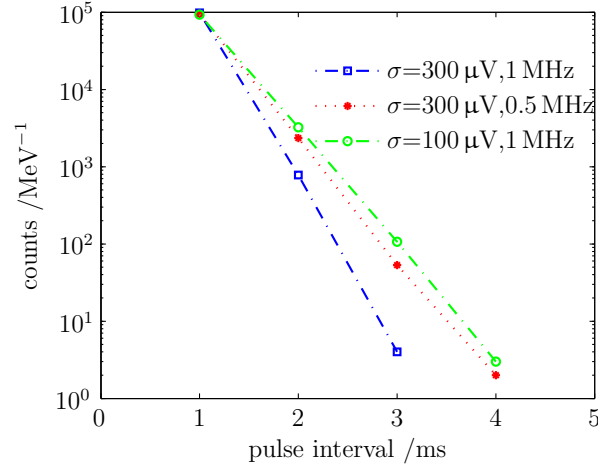


Figure 2.18: Noise effect calculation results— pulse interval distributions.

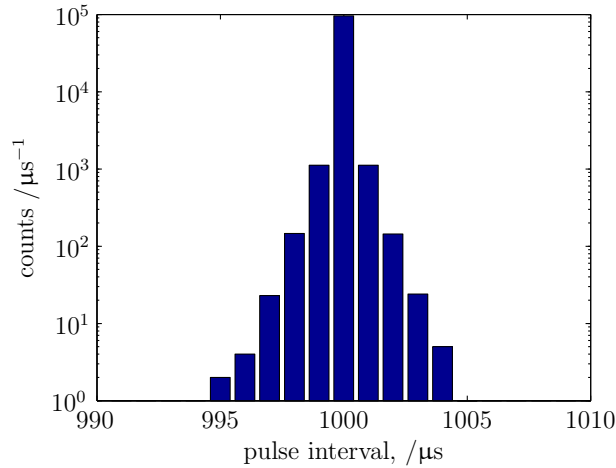


Figure 2.19: Noise effect calculation results — around 1 ms pulse interval histogram.

also reduce significantly with the decrease of the sample rate as well, this is because the minimum detected energy increases with the decrease of the sample rate. The detected decay constant of pulse height spectra is much smaller than the input as the interaction rate increases, because the probability of detection decreases with the increase of the interaction rate; and the pile-up rate increases with the increase of the interaction rate.

The input and detected pulse height spectra are shown in figure 2.20 and pulse interval distributions are shown in figure 2.21 at an interaction rate of about  $3000\text{ s}^{-1}$ . The difference between the input and detected pulse height spectra and interval

## 2.4 Signal processing system

(a)  $\delta=100\ \mu\text{V}$ , sample rate=1 MHz.

		$/\text{s}^{-1}$		$/\text{MeV}^{-1}$	
		simulated	detected	simulated	detected
$n \rightarrow$	200	$201.4 \pm 1.0$	$199.6 \pm 1.0$	$0.302 \pm 0.006$	$0.302 \pm 0.007$
$n \rightarrow$	1000	$1005.1 \pm 5.5$	$995.7 \pm 5.0$	$0.300 \pm 0.007$	$0.296 \pm 0.006$
$n \rightarrow$	2000	$1998.8 \pm 13.4$	$1978.8 \pm 13.3$	$0.300 \pm 0.006$	$0.290 \pm 0.005$
$n \rightarrow$	3000	$3003.8 \pm 21.8$	$2977.4 \pm 22.2$	$0.301 \pm 0.007$	$0.284 \pm 0.007$

(b)  $\delta=300\ \mu\text{V}$ , sample rate=1 MHz.

		$/\text{s}^{-1}$		$/\text{MeV}^{-1}$	
		simulated	detected	simulated	detected
$n \rightarrow$	200	$201.3 \pm 0.8$	$196.4 \pm 0.8$	$0.304 \pm 0.007$	$0.303 \pm 0.006$
$n \rightarrow$	1000	$997.6 \pm 5.3$	$970.7 \pm 5.29$	$0.300 \pm 0.006$	$0.295 \pm 0.006$
$n \rightarrow$	2000	$2013.6 \pm 9.7$	$1960.7 \pm 8.3$	$0.293 \pm 0.006$	$0.283 \pm 0.005$
$n \rightarrow$	3000	$2994.3 \pm 13.3$	$2919.4 \pm 12.8$	$0.303 \pm 0.007$	$0.284 \pm 0.007$

(c)  $\delta=300\ \mu\text{V}$ , sample rate=0.5 MHz.

		$/\text{s}^{-1}$		$/\text{MeV}^{-1}$	
		simulated	detected	simulated	detected
$n \rightarrow$	200	$198.6 \pm 1.9$	$193.2 \pm 1.9$	$0.303 \pm 0.008$	$0.301 \pm 0.007$
$n \rightarrow$	1000	$998.9 \pm 7.2$	$964.3 \pm 7.8$	$0.300 \pm 0.007$	$0.293 \pm 0.007$
$n \rightarrow$	2000	$1997.6 \pm 11.7$	$1929.8 \pm 12.5$	$0.294 \pm 0.005$	$0.286 \pm 0.004$
$n \rightarrow$	3000	$3006.5 \pm 17.6$	$2899.5 \pm 14.8$	$0.309 \pm 0.007$	$0.293 \pm 0.006$

Table 2.4: Calculation results with both noise and pile-up effect — decay constants, CI=68.27%.

distributions are visible at high noise level and low sample rate as shown in figure 2.20(c) and 2.21(c).

Table 2.2(b) summarizes the theory of the probability of detection only with the pile-up effect, which can be expressed:

$$P_r = \frac{1}{1 + n\tau}$$

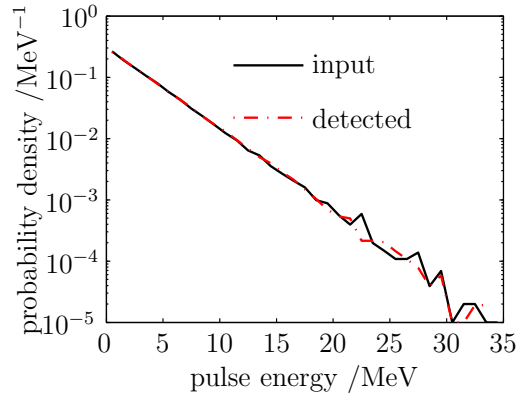
Table 2.3 summarizes the theory of the probability of detection only with the noise effect, which can be modeled by:

$$P_{\gamma'} = \exp^{-E_{min}\lambda}$$

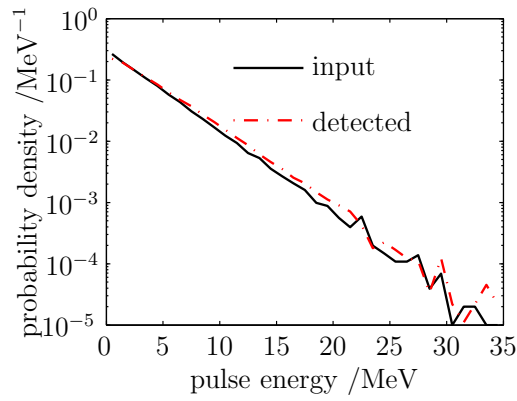
The probability of detection in taking account of both pile-up and noise effects are summarized in table 2.5, where the detected probability of detection (expressed as  $P_{r\gamma'}$ ) is the calculation results, and the theoretical probability detection are calculated by  $P_r P_{\gamma'}$ . It can be seen that the theoretical and detected results agree very well. So it can be concluded that:

$$\begin{aligned} P_{r\gamma'} &\approx P_r P_{\gamma'} \\ &= \frac{1}{1 + n\tau} \exp^{-E_{min}\lambda} \end{aligned} \quad (2.30)$$

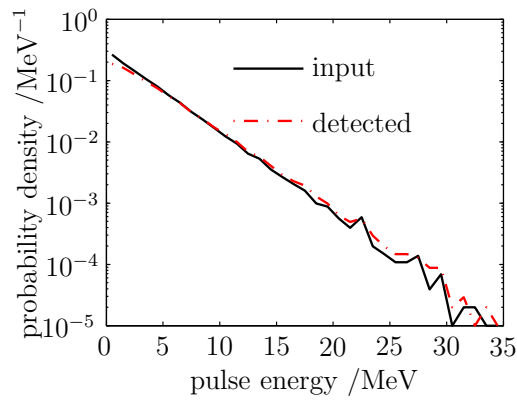
Overall, the results with the effect of pile-up prove that the system correctly used the nonparalyzable counting system to determine the pulse interval. The results with the effect of noise show that the system has correctly used the matched filter techniques to determine the pulse height. The interaction rate can be determined either by the rate of detected pulses with the sensor pulse width or by the exponential fit of the pulse interval distribution. The results of accounting for both pile-up and noise indicated that the system can correctly determine the probability



(a)  $\delta=100 \mu\text{V}$ , sample rate= 1 MHz.

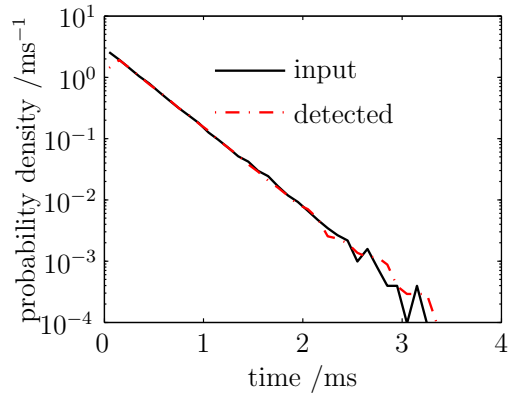


(b)  $\delta=300 \mu\text{V}$ , sample rate= 1 MHz.

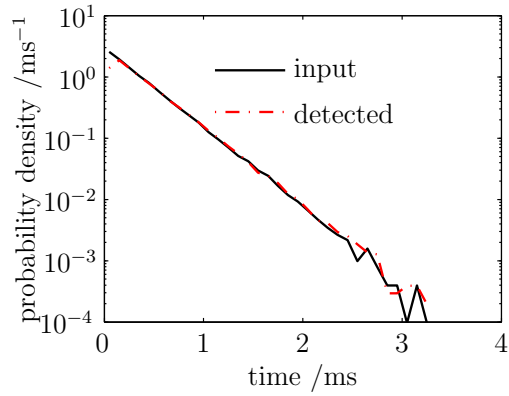


(c)  $\delta=300 \mu\text{V}$ , sample rate= 0.5 MHz.

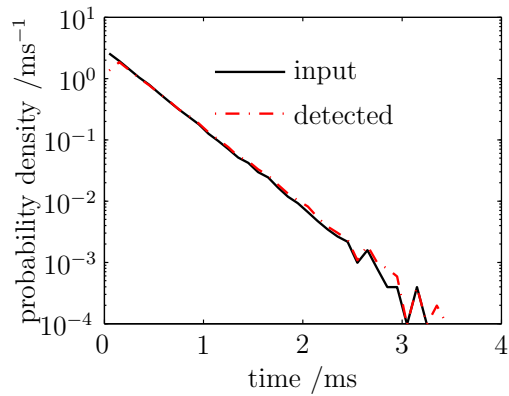
Figure 2.20: Calculation results with both noise and pile-up effects, interaction rate= $3000 \text{ s}^{-1}$  — pulse height spectra.



(a)  $\delta=100 \mu\text{V}$ , sample rate= 1 MHz.



(b)  $\delta=300 \mu\text{V}$ , sample rate= 1 MHz.



(c)  $\delta=300 \mu\text{V}$ , sample rate= 0.5 MHz.

Figure 2.21: Calculation results with both noise and pile-up effects, interaction rate= $3000 \text{ s}^{-1}$  — pulse interval distributions.

## 2.5 Selection of the beam monitoring system parameters

---

Table 2.5: Calculation results with both noise and pile-up effect —probability of detection, CI=68.27%.

	sample rate=1 MHz 100 $\mu$ V		sample rate=1 MHz 300 $\mu$ V		sample rate=0.5 MHz 300 $\mu$ V	
	theoretical	detected	theoretical	detected	theoretical	detected
	$n \rightarrow 200 \text{ s}^{-1}$	98.41	98.37 $\pm$ 0.31	96.78	96.86 $\pm$ 0.31	95.79
$n \rightarrow 1000 \text{ s}^{-1}$	95.38	95.43 $\pm$ 0.31	93.80	93.94 $\pm$ 0.31	92.84	93.01 $\pm$ 0.30
$n \rightarrow 2000 \text{ s}^{-1}$	91.85	91.86 $\pm$ 0.30	90.33	90.47 $\pm$ 0.30	89.41	89.57 $\pm$ 0.30
$n \rightarrow 3000 \text{ s}^{-1}$	88.58	88.35 $\pm$ 0.29	87.11	87.16 $\pm$ 0.29	86.22	86.58 $\pm$ 0.29

of detection with various noise levels and interaction rates. In each case, the input and detected results agree well, which suggests that the detection software can correctly capture the pulse events and the signal processing system performs well in variations of the interaction rates, noise level and sample rates.

## 2.5 Selection of the beam monitoring system parameters

This section will discuss the minimum detectable energy, SNR of the monitoring system, and the optimum sensor pulse width of the system design.

### 2.5.1 Determine minimum collected energy

Assuming the reference signal height to be  $V_R$  and the input signal height to be  $V_s$ , the input signal  $x[n]$  can be expressed as:

$$x[n] = \frac{V_s}{V_R} s[n] + \omega[n] \quad n = 0, 1, \dots, N - 1 \quad (2.31)$$

Based on equation. 2.16, the output of the matched filter at the maximum point will be:

## 2.5 Selection of the beam monitoring system parameters

---

$$y[N - 1] = \frac{V_s}{V_R} \varepsilon_R + \sum_{k=0}^{N-1} \omega[k] s[k] \quad (2.32)$$

where  $\varepsilon_R$  is the reference energy. The expectation of  $\sum_{k=0}^{N-1} \omega[k] s[k]$  approaches zero. When the output of the matched filter at maximum point equals the threshold level, the minimum collected pulse height will be detected by the signal processing system. Assuming the minimum detectable pulse height to be  $V_{smin}$ , then:

$$\frac{V_{smin}}{V_R} \varepsilon_R = 3\delta Q^{-1}(P_{FA}) \sqrt{\varepsilon_R} \quad (2.33)$$

where  $\delta$  is the noise level, and  $P_{FA}$  is the probability of pulse false alarm. So the minimum detectable pulse height  $V_{smin}$  should be:

$$V_{smin} = 3\delta Q^{-1}(P_{FA}) \frac{V_R}{\sqrt{\varepsilon_R}} \quad (2.34)$$

And the minimum detectable energy  $E_{min}$  is:

$$E_{min} = 3 \frac{\delta Q^{-1}(P_{FA})}{A} \frac{V_R}{\sqrt{\varepsilon_R}} \quad (2.35)$$

where  $A$  is the sensor's amplifier gain. The photodiode sensor's amplifier gains are listed in table. 2.1, which are determined by the nominal value of amplifier parameters, assuming an ionization energy of 3.6 eV [61].  $V_R/\sqrt{\varepsilon_R}$  for a given sensor is a constant, for example, sensor 12's  $V_R/\sqrt{\varepsilon_R}$  is 1/3.55. It can be seen that minimum detectable energy increases with the increase of the noise level as expected.

However, for a sensor, the noise level  $\delta$  may slightly change during testing. The experimental data to be analyzed in Chapter 3 show that the noise level does not change significantly. So the minimum detectable pulse height or energy decreases with the decrease of the inverse function  $Q^{-1}(P_{FA})$ , which can be determined either by MATLAB `erfinv(x)` function [116] or [117]:

## 2.5 Selection of the beam monitoring system parameters

---

$$Q^{-1}(x) = \sqrt{-\frac{2}{\pi a} - \frac{\ln(1-x^2)}{2}} + \sqrt{\left(\frac{2}{\pi a} + \frac{\ln(1-x^2)}{2}\right)^2 - \frac{1}{a} \ln(1-x^2)} \quad (2.36)$$

where  $a$  is the constant 0.147. When  $P_{FA}$  is  $1 \times 10^{-9}$ ,  $Q^{-1}(P_{FA})$  equals 5.99.

For example, when the noise standard deviation is  $300 \mu\text{V}$ , the minimum detectable pulse energy is  $82.45 \text{ keV}$  at the sample rate of  $1 \text{ MHz}$ .

### Minimum detectable energy with various sample rates

Assuming there are  $i$  sensors under test, the sample rate for each sensor will be:

$$M_i = \frac{M}{i} \quad (2.37)$$

The corresponding reference signal energy  $\varepsilon_i$  is:

$$\varepsilon_i \approx \varepsilon_R \frac{M_i}{M} \quad (2.38)$$

So the equation 2.35 is:

$$\begin{aligned} E_{min} &= 3 \frac{\delta Q^{-1}(P_{FA})}{A} \frac{V_R}{\sqrt{\varepsilon_i}} \\ &= 3 \frac{\delta Q^{-1}(P_{FA})}{A} \frac{V_R}{\sqrt{\varepsilon_R \frac{M_i}{M}}} \\ &= 3 \frac{\delta Q^{-1}(P_{FA})}{A} \frac{V_R}{\sqrt{\varepsilon_R}} \sqrt{\frac{M_i}{M}} \end{aligned} \quad (2.39)$$

The minimum detectable energy increases with the number of sensors under test. Assuming the reference signal is the output of sensor 12, the noise standard deviation is  $300 \mu\text{V}$ , the minimum detectable energy with a varying number of sensors under test is shown in figure 2.22.

## 2.5 Selection of the beam monitoring system parameters

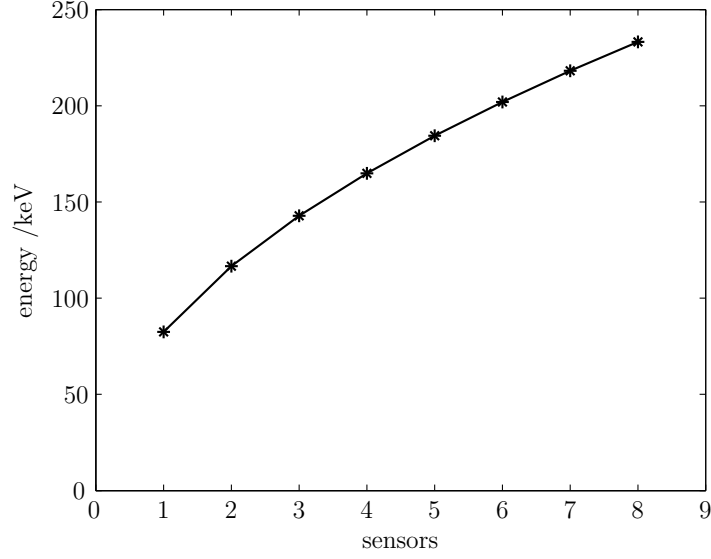


Figure 2.22: Example of the minimum detectable energy with a varying number of sensors under test.

### Minimum detectable energy with various sensor pulse widths

Assuming the output of sensor 12 is the reference pulse, the following will discuss the minimum detectable energy with different pulse widths. Assuming one sensor pulse width to be  $\tau$ , and its signal energy  $\varepsilon$  is:

$$\varepsilon \approx \frac{\tau}{\tau_R} \varepsilon_R \quad (2.40)$$

where  $\tau_R$  is the reference signal pulse width, so the minimum detectable energy:

$$\begin{aligned} E_{min} &= 3 \frac{\delta Q^{-1}(P_{FA}) V_R}{A \sqrt{\varepsilon}} \\ &\approx 3 \frac{\delta Q^{-1}(P_{FA}) V_R}{A \sqrt{\frac{\tau}{\tau_R} \varepsilon_R}} \\ &\approx 3 \frac{\delta Q^{-1}(P_{FA}) V_R}{A \sqrt{\varepsilon_R}} \sqrt{\frac{\tau}{\tau_R}} \end{aligned} \quad (2.41)$$

The minimum detectable energy reduces with the increase of the pulse width as shown in figure 2.23.

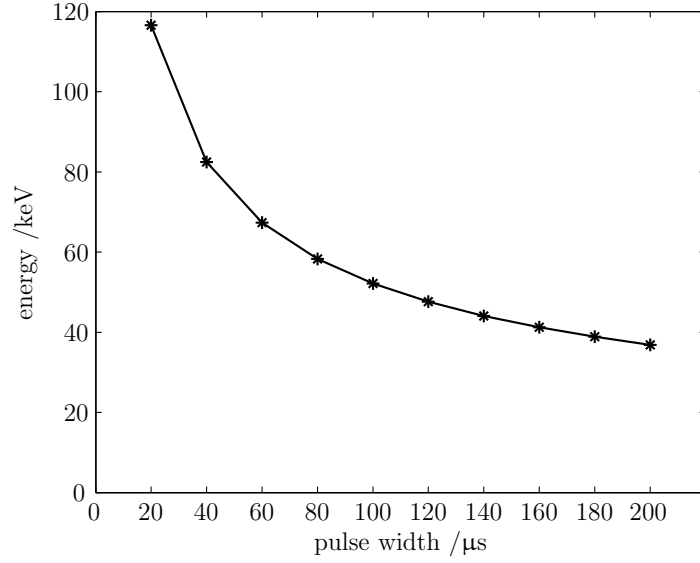


Figure 2.23: Example of minimum detectable energy with various pulse widths.

Overall the minimum detectable energy will increase as follows:

1. with the increase of the sensor noise level;
2. with the decrease of the sample rate;
3. with the decrease of the sensor pulse width;
4. with the increase of the number of the sensor in-beam monitoring system.

### 2.5.2 Signal-to-noise ratio (SNR)

According to Kay [114], the SNR can be defined as:

$$SNR = \frac{\varepsilon}{\delta^2} \quad (2.42)$$

where  $\varepsilon$  is the signal energy, and  $\delta$  is the noise standard deviation. The minimum detectable signal energy can be modeled as:

$$\varepsilon_{min} = \left(\frac{V_{smin}}{V_R}\right)^2 \varepsilon_R \quad (2.43)$$

## 2.5 Selection of the beam monitoring system parameters

---

Based on equation 2.34, SNR can also be calculated:

$$\begin{aligned}
 SNR_{min} &= \frac{1}{\delta^2} \left( \frac{V_{smin}}{V_R} \right)^2 \varepsilon_R \\
 &= \frac{1}{\delta^2} \frac{\varepsilon_R}{(V_R)^2} (3\delta Q^{-1}(P_{FA}) \frac{V_R}{\sqrt{\varepsilon_R}})^2 \\
 &= 9 * (Q^{-1}(P_{FA}))^2
 \end{aligned} \tag{2.44}$$

When  $P_{FA} = 1 \times 10^{-9}$ , the  $(Q^{-1}(P_{FA}))^2$  is 5.99, the minimum detectable SNR is 25 dB.

### 2.5.3 Optimum pulse width

In general, the optimum pulse width is determined by balancing the sensor's random noise and the pile-up effect while also taking into account the effect of pulse width sampling resolution on diode neutron sensor performance.

#### 2.5.3.1 Maximum probability of detection

In this section, the optimum pulse width will first be determined in a single sensor under test, then multiple sensors under testing will be discussed.

##### Single sensor under test

Assuming the reference pulse width to be  $\tau_R$ , the reference signal energy to be  $\varepsilon_R$  at sample rate  $M_R$ , the pulse width to be  $\tau$  and the signal energy to be  $\varepsilon$  at sample rate  $M$ ,  $\varepsilon$  approximates to:

$$\varepsilon \approx \frac{M}{M_R} \frac{\tau}{\tau_R} \varepsilon_R \tag{2.45}$$

The probability of detection is (see §2.4.6.2):

$$P_{\gamma',r} \approx P_r P_{\gamma'}$$

## 2.5 Selection of the beam monitoring system parameters

---

where  $P_r$  is the probability of detection only with the effect of pile-up,  $P_{\gamma'}$  is the probability of detection only with the effect of noise.  $P_{\gamma',r}$  is the probability of detection given threshold  $\gamma'$  and rate  $r$ .

$P_r$  equals the detection rate  $r$  over interaction rate  $n$ , therefore (based on equation 2.9):

$$P_r = \frac{r}{n} = \frac{1}{1 + r\tau}$$

The pulse height spectrum for photodiode irradiation in neutron beam approximates to a type of exponential distribution [54, 115], so  $P_{\gamma'}$  can be determined by:

$$P_{\gamma'} \approx e^{-E_{min}\lambda}$$

where  $E_{min}$  is the minimum detectable pulse energy, and  $\lambda$  is the decay constant of pulse height spectrum.  $E_{min}$  (see equation 2.35) is:

$$E_{min} = 3 \frac{\delta Q^{-1}(P_{FA})}{A} \sqrt{\frac{M_R}{M}} \sqrt{\frac{\tau_R}{\varepsilon_R}} \sqrt{\frac{1}{\tau}} V_R \quad (2.46)$$

Assuming  $b$  to be  $3 \frac{\delta Q^{-1}(P_{FA})}{A} \sqrt{\frac{M_R}{M}} \sqrt{\frac{\tau_R}{\varepsilon_R}} \lambda V_R$ , the probability of detection  $P_{\gamma'}$  can be calculated:

$$\begin{aligned} P_{\gamma'} &\approx \exp^{-E_{min}\lambda} \\ &\approx \exp^{-b/\sqrt{\tau}} \end{aligned} \quad (2.47)$$

It has:

$$P_{\gamma',r} \approx \exp^{-\frac{b}{\sqrt{\tau}}} \frac{1}{n\tau + 1} \quad (2.48)$$

## 2.5 Selection of the beam monitoring system parameters

---

To maximize  $P_{\gamma',r}$  and determine the pulse width  $\tau$ ,  $\frac{\partial P_{\gamma',r}}{\partial \tau}$  should be 0, therefore:

$$\begin{aligned}\frac{\partial P_{\gamma',r}}{\partial \tau} &= \frac{1}{n\tau + 1} \exp^{-\frac{b}{\sqrt{\tau}}} \frac{b}{2} - \exp^{-\frac{b}{\sqrt{\tau}}} \frac{n}{(n\tau + 1)^2} \\ &= 0\end{aligned}\tag{2.49}$$

So:

$$\begin{aligned}\frac{b}{2}\tau^{-\frac{3}{2}} &= \frac{n}{n\tau + 1} \\ \frac{b}{2} &= \frac{n}{n\tau + 1}\tau^{\frac{3}{2}}\end{aligned}\tag{2.50}$$

The parameters of sensor 12 are chosen to calculate the constant  $b$  at the sample rate of 1 MHz, therefore:  $b=1.574 \times 10^{-4}$ .

Based on equation 2.50, using the numerical value of  $(n\tau + 1)$  and  $\tau^{\frac{3}{2}}$ , the optimum pulse width can be calculated. For example, assuming the interaction rate to be  $100\text{ s}^{-1}$ , the optimum pulse width is  $86\ \mu\text{s}$ , and when the interaction rate is  $2000\text{ s}^{-1}$ , the optimum pulse width is  $12\ \mu\text{s}$ . The optimum pulse widths increase with the decrease of the interaction rate as shown in figure 2.24, this is because the probability of detection decreases with the increase of interaction rates due to pile-up. The probability of detection increases with the increase of the sensor pulse width (due to the increase of the signal energy) and the decrease of the interaction rate as shown in figure 2.25(a).

### Multi-sensors under test

Assuming  $i$  sensors in the beam monitoring system are under test, the input signal energy should be:

$$\varepsilon \approx \frac{M}{M_R} \frac{\tau}{\tau_R^i} \varepsilon_R\tag{2.51}$$

## 2.5 Selection of the beam monitoring system parameters

---

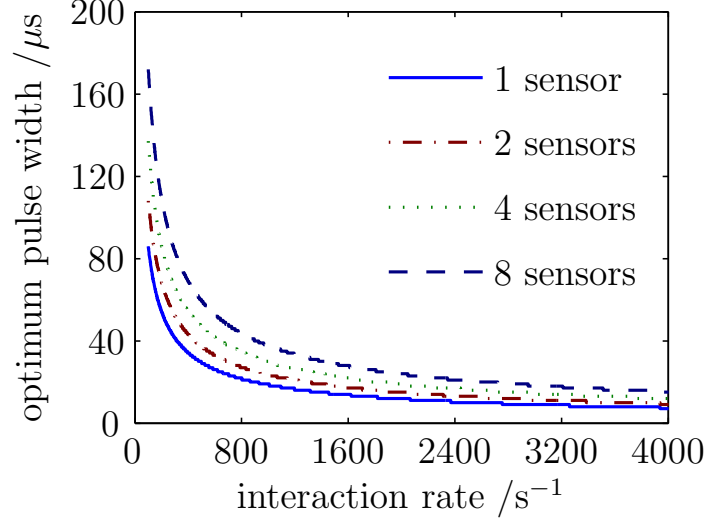


Figure 2.24: Optimum pulse width by using sensor 12 feature at sample rate 1 MHz ·

The minimum detectable energy should be:

$$E_{min} = 3 \frac{\delta Q^{-1}(P_{FA})}{A} \sqrt{\frac{M_R}{M}} \sqrt{i} \sqrt{\frac{\tau_R}{\varepsilon_R}} \sqrt{\frac{1}{\tau}} V_R \quad (2.52)$$

Therefore, the probability of detection  $P_{\gamma,t,r}$  is:

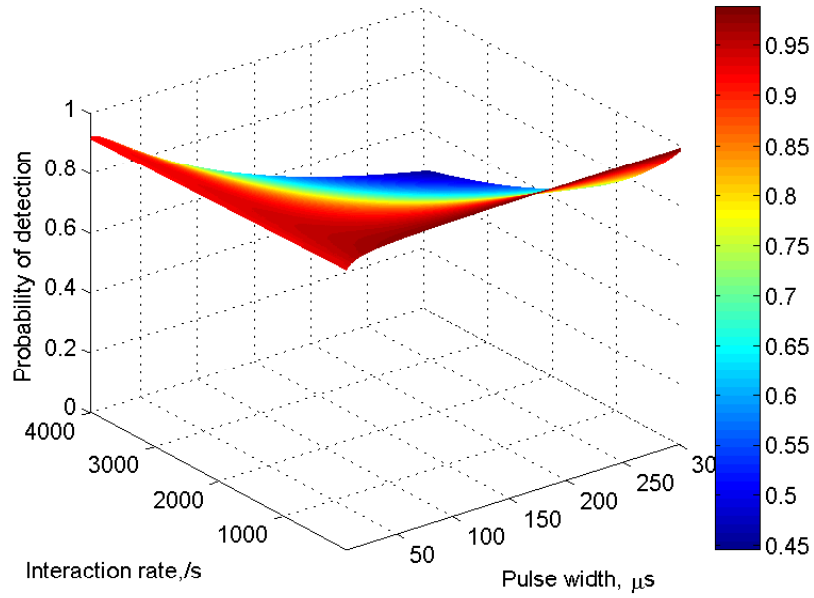
$$P_{\gamma,t,r} = \exp^{-\frac{b\sqrt{i}}{\sqrt{\tau}}} \frac{1}{n\tau + 1} \quad (2.53)$$

When the maximum probability of detection is achieved,  $\frac{\partial P_{\gamma,t,r}}{\partial t} = 0$ , so:

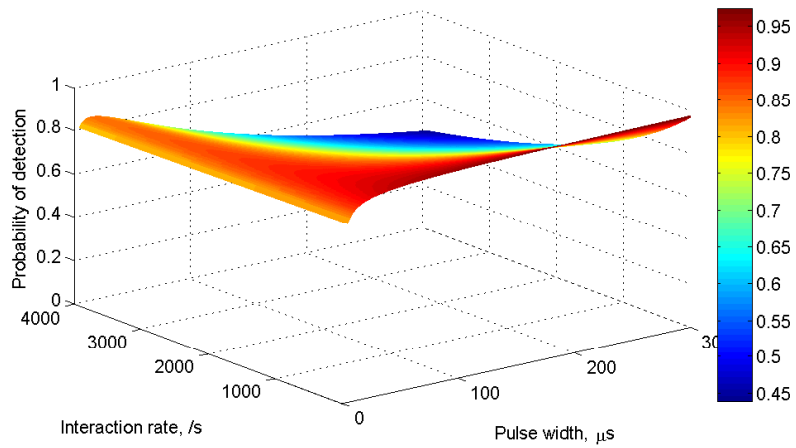
$$\frac{b\sqrt{i}}{2} = \frac{n}{n\tau + 1} \tau^{\frac{3}{2}} \quad (2.54)$$

The optimum pulse widths are shown in figure 2.24. For example, assuming 4 sensors (such as sensor 12) in the beam monitoring system are under test, the maximum DAQ sampling rate is 1 MHz. When the interaction rate is  $100 \text{ s}^{-1}$ , its optimum pulse width will be  $137 \mu\text{s}$ . This means that 35 sampling points can be downloaded for one pulse. When the interaction rate is  $2000 \text{ s}^{-1}$ , its optimum pulse

## 2.5 Selection of the beam monitoring system parameters



(a) single sensor.



(b) 4 sensors.

Figure 2.25: Probability of detection at 1 MHz sample rate with various pulse widths and interaction rates.

## 2.5 Selection of the beam monitoring system parameters

---

width will be  $19\ \mu\text{s}$ , then there will be 5 sampling points downloaded for each pulse. The optimum pulse width increases with the increase of the number of sensors under test due to the decrease of sample rate for each sensor.

By using equation 2.53, the probability of detection can be calculated. Figure 2.25(b) shows 4 sensors' probability of detection at 1 MHz sample rate with various pulse widths and interaction rates. Compared to figures 2.25(a) and 2.25(b), it can be seen that the probability of detection decreases with the increase of the number of sensors under test (due to the decrease of the sensor pulse energy), the decrease of the interaction rate (due to the increase of the effect of pile-up), and the increase of the sensor pulse width (due to the decrease of the sensor pulse energy).

### 2.5.3.2 Effect of sampling resolution on diode neutron sensor performance

As discussed in the previous section, at a high interaction rate, to achieve the maximum probability of detection, the optimum pulse width should be quite narrow. In such a case, the energy resolution of the detection system is very poor [103]. Figure 2.26 shows few example pulses with 5 sampling points. There is only a small chance that the reference signal is the same as one of these various shapes. As a result, the true value of the detected pulse energy will be smaller than its real value.

Two kinds of calculations, with or without the noise effect, have been undertaken in order to verify the energy resolution in the effect of sampling resolution, and investigate the suitable sampling points on the photodiode neutron sensor performance. Based on the shape of the output of the sensor 12, 100 000 pulses with 0.4 MeV energy were input in the calculation. The input Gaussian white noise standard deviation is  $300\ \mu\text{V}$ .

The calculation results are summarized in tables 2.6. Their pulse height spectra are shown in figure 2.27(a) and 2.27(b). The peaks of the detected energy were not significantly different whether the noise was present or not. However, when the noise was present, the detected energy resolution was poorer than the others. The

## 2.5 Selection of the beam monitoring system parameters

---

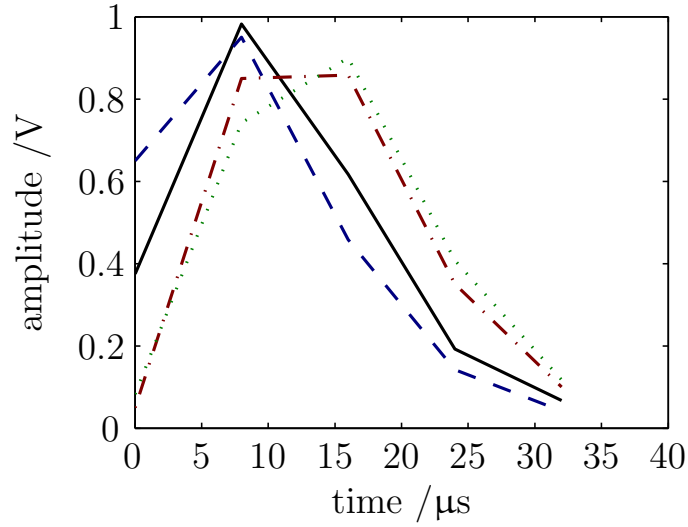


Figure 2.26: Sampling various pulse shapes.

difference between the detected peak energy and the input energy decreases with the increase of the number of sampling points.

(a) without noise effect.

sampling points	peak energy /MeV	standard deviation, /MeV
40	0.398	0.001
20	0.396	0.001
10	0.393	0.001
8	0.380	0.002
5	0.366	0.005

(b) with noise effect.

sampling points	peak energy MeV	standard deviation, MeV
40	0.398	0.013
20	0.396	0.018
10	0.393	0.026
8	0.380	0.028
5	0.366	0.034

Table 2.6: Calculation results in the number of sample points of sensor pulse.

## 2.5 Selection of the beam monitoring system parameters

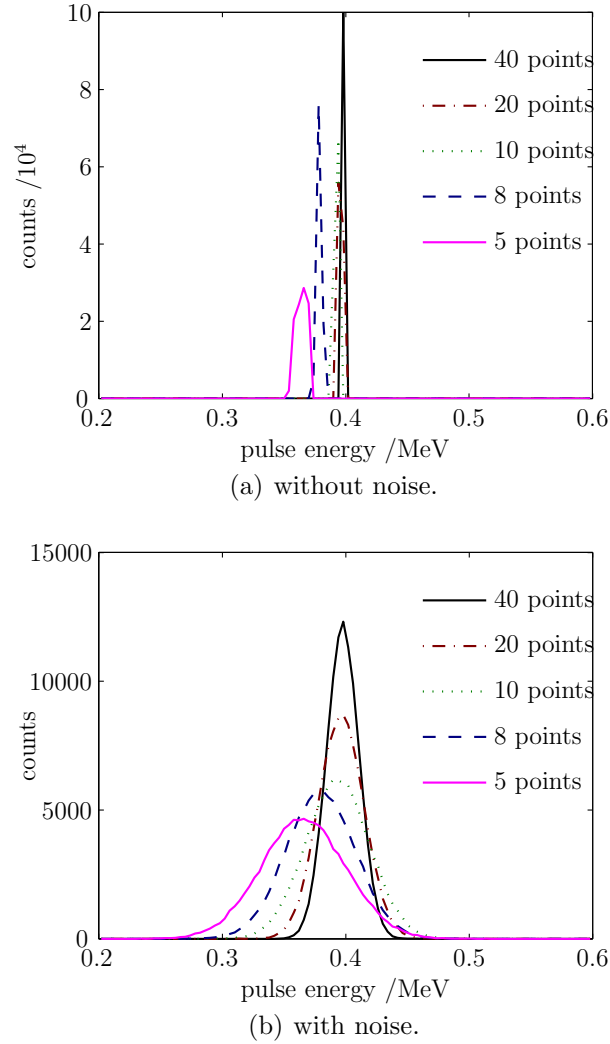


Figure 2.27: Sampling pulse calculation results — pulse height spectra.

When the number of sampling points is less than 10, the difference between detected peak energy and the true value is quite significant. When the sampling point is equal to or above 10, the percent of difference between detected and input peak energy is about 1.75%. The detected standard deviation in energy also reduces with the increase of the number of sampling point. It can be safely concluded that the number of sampling points for each pulse should be more than 10 in order to achieve a adequate energy resolution on photodiode sensor's performance.

The number of sampling points of the experimental data (presented in Chapter 4) was between 12 and 40; in this case, the energy resolution of the experimental

results should achieve a good performance.

## 2.6 Software

The software was written by using LabVIEW in conjunction with NI-DAQmx. Figure 2.28 shows the main window of the software. Five kinds of measurements can be undertaken by this software package:

1. The “Save all samples” mode is used to collect time series data from both the preamplifier and the shaping amplifier channels;
2. The “Save all pulse” mode is used to collect pulse event data only from the shaping amplifier channel;
3. The “Get threshold” mode is used to acquire threshold level for the “save pulse height” mode;
4. The “Save pulse height” mode is used to collect data from the shaping amplifier channels first, then through the signal processing to plot and record the pulse height spectra and pulse interval distribution;
5. The “Set threshold level manually” mode is used to set the threshold level by the user for the “Save pulse height” mode.

This software was used to capture data during experiments at various beam trials described in Chapter 3

## 2.7 Conclusion

This chapter discussed the development of the beam monitoring system. First, the photodiode detector circuit and its pulse shapes were introduced. The function of

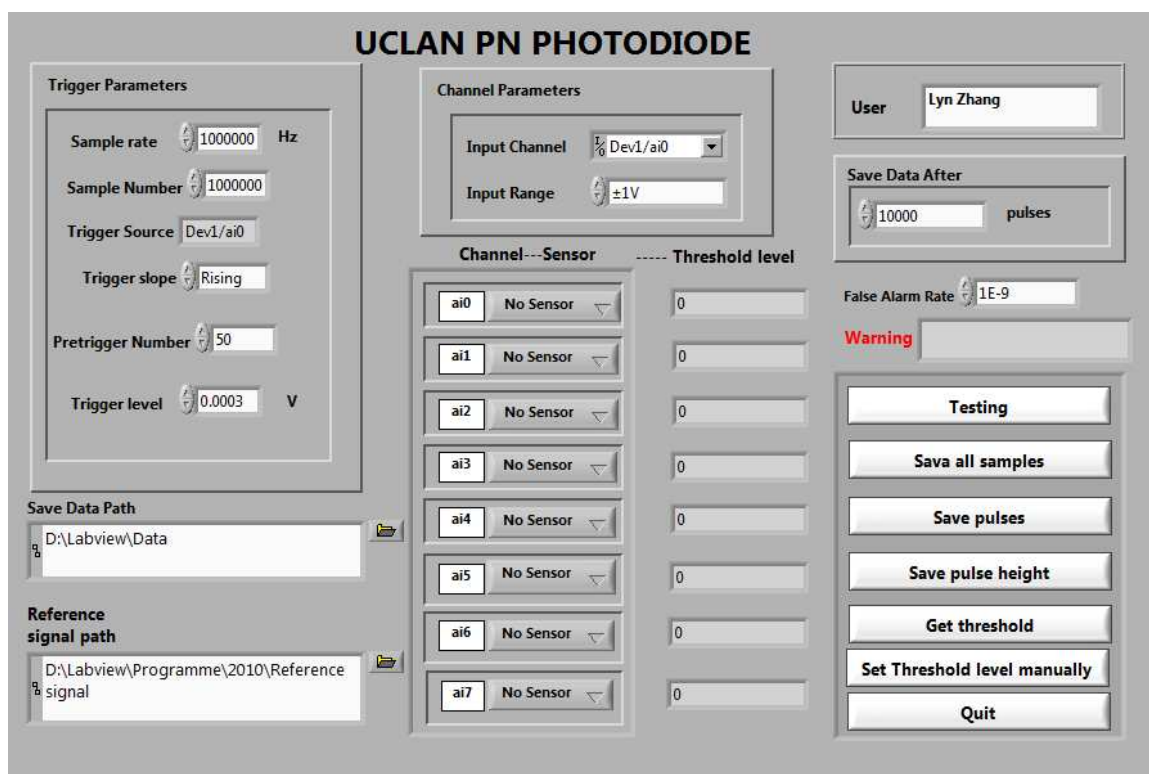


Figure 2.28: Software main panel.

the photodiode detector is to generate electrical signals when particles interact with the detector. A preamplifier and pulse shapers convert this electrical signal into a pulse which can be processed by the data acquisition system. Twelve sensors with five different circuits were developed in this project. This chapter also discussed the pulse shapes of these sensors and presented the time series data collected using these sensors.

In the signal processing system, the nonparalyzable method was used in the counting system to get the arrival times of pulses. Pulses are detected if the matched filter output exceeds a threshold level  $\gamma I$ . A series of calculations was undertaken to verify the correct operation of the detection software and to investigate system performance variations. In each calculation case, the theoretical and detected probability of detection agreed very well. It demonstrates that the interaction rate can be determined either by using the detection rate and the sensor pulse width or the exponential fit of the pulse interval distribution.

The minimum detectable energy of the monitoring system decreases with the increase of the sample rate, noise level and the increase of the number of sensors under test.

Next the pulse width sampling resolution, and the optimum pulse width with various interaction rates and the number of sensors under test were investigated. In general, sampling points for each pulse should be more than 10 in order to achieve a good energy resolution on the photodiode sensor performance. The optimum width decreases with the increase of the interaction rate. Finally, the software package developed for this project was briefly introduced.

The next chapter will present the experimental results captured by the beam monitoring system at various neutron facilities.

# Chapter 3

## Beam monitor experimental results

### 3.1 Introduction

This chapter will introduce the fundamental properties of the output of the beam monitoring system, describe how the devices were tested at neutron beam facilities, and present the experimental results captured from the neutron beams.

The fundamental properties of the output of the beam monitoring system are: the deposited energy collected in the sensor is described by the pulse height spectra, the arrival times of pulse events are displayed by the pulse interval distribution.

This is followed by an introduction of the neutron facilities used in SEEs testing, along with a discussion of how the neutron fluence was determined at a distance from the facility standard point.

Finally, experimental results captured at LANSCE, TSL, TRIUMF and ASP will be presented. At LANSCE, to determine the sensor characteristics and the effect of the pulsed neutron beam, two sensors were tested together at upstream positions; to investigate the influence of degrading experiments in the beam line the sensors were also irradiated, one in upstream and one in downstream, with or without an

## 3.2 Properties of the output of the beam monitoring system

---

aluminum scatterer; Two sensors were also irradiated upstream and downstream of one or three other devices under test. Experiments were made at TRIUMF in order to investigate the effect of neutron interaction in the amplifier circuit, and photodiode window, and of thermal neutrons. Experiments made at TSL show the effect of neutron activation decay in the photodiode. The experimental results from ASP show the effect of the photodiode doping profile. The pile-up rate in sensor irradiated at TSL ANITA will also be described.

## 3.2 Properties of the output of the beam monitoring system

### 3.2.1 Pulse height spectra and pulse interval distribution

The collected energy generated by neutrons or other particles interacting with the photodiode sensor are displayed through the differential pulse height spectrum, which is a continuous curve that shows the number of pulses observed within an increment of pulse deposited energy against the value of the pulse deposited energy [61]. Figure 3.1 illustrates the measured pulse height spectrum for collecting events above 50 keV captured from sensor 1 at TRIUMF in November 2007. The x-axis is the collected energy of the pulse events that runs from zero to the maximum. The y-axis is the differential number  $dN$  of pulses observed with an energy within the differential energy increment  $dE$ , divided by that increment. The x-axis scale has units of pulse energy (MeV), whereas the vertical scale has units of inverse energy ( $\text{MeV}^{-1}$ ).

Error bars plotted in figure 3.1 are upper and lower limits at 84.13% confidence level (CL), containing a 68.27% confidence interval (CI). The calculation of limits for the number of pulse events is based on standard equations derived from Poisson statistics [118] (see Appendix E).

Approximately above 5 MeV collected energy of pulse height spectra shown in fig-

## 3.2 Properties of the output of the beam monitoring system

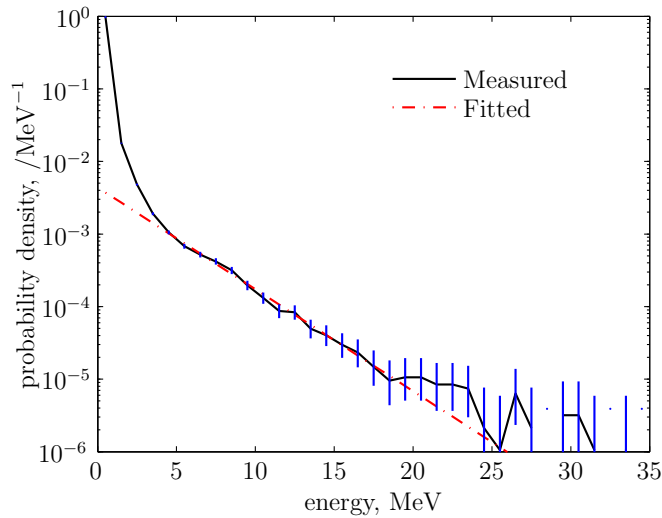


Figure 3.1: Example of measured pulse height spectra captured at TRIUMF.

Figure 3.1, the following equation describes the exponential curve resulting from the exponential fit algorithm:

$$dN = a \exp^{-b E} \quad (3.1)$$

where  $a$  and  $b$  ( $\text{MeV}^{-1}$ ) are fit parameters;  $b$  is also called the exponential decay constant which displays the shape of the curve. In figure 3.1,  $b$  is  $(0.286 \pm 0.009) \text{ MeV}^{-1}$ , which is determined by the LabVIEW functions ‘exponential fit’ and ‘exponential fit interval’ using the least square method at  $\text{CI} = 68.27\%$ . Based on equation 3.1, following the exponential fit, a fit to the pulse height spectra is displayed in figure 3.1. It can be seen that there is a significant difference in low collected energy between the measured and fitted pulse height spectra. This difference will be discussed in §4.3.

Between the collected energy 20 MeV and 25 MeV, there is a peak in pulse height spectra, which is random as a result of a small number of pulse events. This will be discussed in §4.3.

In radiation measurements, the time intervals separating random events are often

## 3.2 Properties of the output of the beam monitoring system

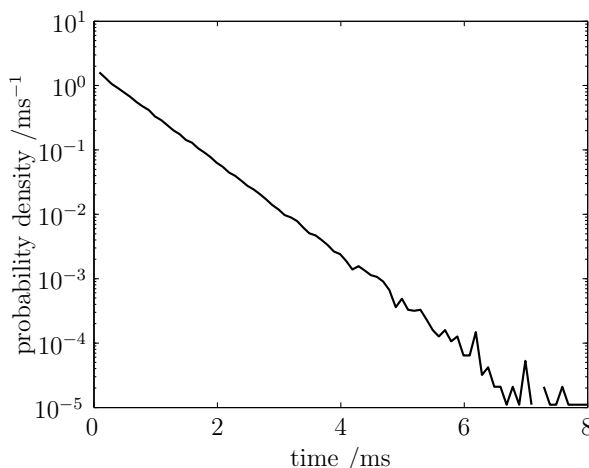


Figure 3.2: Example of measured pulse interval distribution captured at TRIUMF.

of practical interest. The pulse interval distribution is used to record the number of pulses that occur over a given measurement time and to indicate the rate at which pulses occur. Figure 3.2 shows the measured pulse interval for collecting events above 50 keV captured from sensor 1 at TRIUMF in November 2007. The x-axis is the increment of the pulse interval time while the y-axis shows the probability of this increment occurring. Neutron interactions with the photodiode sensor are a Poisson process; its pulse interval distribution follows an exponential fit and can be modeled as:

$$dN = ce^{n dt} \quad (3.2)$$

where  $dt$  is the pulse time interval (s),  $c$  specifies the interception, and  $n$  is the average rate of occurrence (interaction rate,  $s^{-1}$ ) [61]. In figure 3.2,  $n$  is  $1672 \pm 9.6 s^{-1}$  when CI is 68.27%.  $n$  is 6% greater than the rate estimated roughly from the number of detected events and run duration ( $1570 s^{-1}$ ). As discussed in §2.4.1, in nearly all detector systems, there will be a minimum amount of time that must separate the two events in order for them to be recorded as two separate pulses. The nonparalyzable counting system is used in signal processing to record the pulse time intervals. So when the time interval between two pulses is less than the shaping pulse width, it is considered as a ‘pile-up’ (see §2.4.1). The probability of detection

## 3.2 Properties of the output of the beam monitoring system

---

is:

$$p = \frac{r}{n}$$

where  $r$  is the detection rate, which is  $1570 \text{ s}^{-1}$  captured by sensor 1 from TRIUMF, and  $n$  is the interaction rate, which is  $1672 \text{ s}^{-1}$ , giving  $p$  95.90%. According to equation 2.10 (see §2.4.1), the probability of detection can also be modified as:

$$p = 1 - r\tau$$

where  $\tau$  is the sensor pulse width, which is  $40 \mu\text{s}$ , giving  $p$  93.27%. The theoretical and experimental of probability of detection for collecting events above 50 keV agree well.

### 3.2.2 Photodiode sensor response measurements

The response of photodiode sensor interaction with neutrons is defined as:

$$\sigma = \frac{N_{events}}{\Phi} \tag{3.3}$$

where  $\sigma$  is the response of the photodiode sensor irradiated in a neutron beam,  $N_{events}$  is the number of collected events, and  $\Phi$  is the neutron fluence received by the device under test. The uncertainty in  $\Phi$  is 5% at LANSCE, 10% at TSL, and about 30% at TRIUMF. The uncertainty of  $N_{events}$  can be determined based on confidence interval, which is presented in Appendix E.

The standard deviation of  $N_{events}$  events is  $\sqrt{N_{events}}$ . The fraction of standard deviation is  $\sqrt{N_{events}}/N_{events} = 1/\sqrt{N_{events}}$  [119]. The uncertainty in  $\sigma$  can be calculated by:

$$\sigma_{uncertain} = \sqrt{\left(\frac{1}{\sqrt{N_{events}}}\right)^2 + (\Phi_{uncertain})^2} \quad (3.4)$$

If experiment sample  $\sigma_{uncertain}$  is limited to a certain level, it requires that  $N_{events}$  should be more than a certain number of events. For example, assuming the experiments are made at LANSCE, the uncertainty in  $\sigma$  is less than 5.1%;  $1/\sqrt{N_{events}}$  should be less than 1%. As a result,  $N_{events}$  should be greater than 10 000.

### 3.3 Neutron facilities testing

In this project, beam monitors were irradiated at LANSCE in October 2010, at TRIUMF in November 2007 and July 2008, at TSL in April 2007, and June 2010 and at ASP in November 2009. In April 2007, beam time was provided by BAE SYSTEMS, United Kingdom, and the experimental data were captured by the author and Dr.Platt. In November 2007, beam time was provided by Goodrich Engine Control and Electrical Power Systems, Birmingham, United Kingdom, and experimental data were captured by Mr.R. H. Edwards and Mr.C. Allabush. Other beam time were provided by the Single Event Effects Design for Electronics Reliability (SEEDER) (<http://www.seeder.org.uk/>) project, and the experimental data were collected by Dr. Platt.

At LANSCE and TSL, the facility beam monitoring provided a certain count number  $K$  and a calibration factor  $C$  from which the neutron fluence  $\Phi_d$  can be obtained at the standard point:

$$\Phi_d = KC \quad (3.5)$$

Figure 3.3 shows schematically the beam lines at LANSCE and TSL. The facility dosimetry provides fluence values only at the standard point. A beam divergence can be estimated at distance  $r$  from the standard point in the beam line by the

### 3.3 Neutron facilities testing

$1/r^2$  law if the distance between the target and the standard point ( $R_D$ ) is known (provided that there is no additional scattering); it can be modeled as:

$$D(r) = \frac{R_D^2}{(R_D + r)^2} \quad (3.6)$$

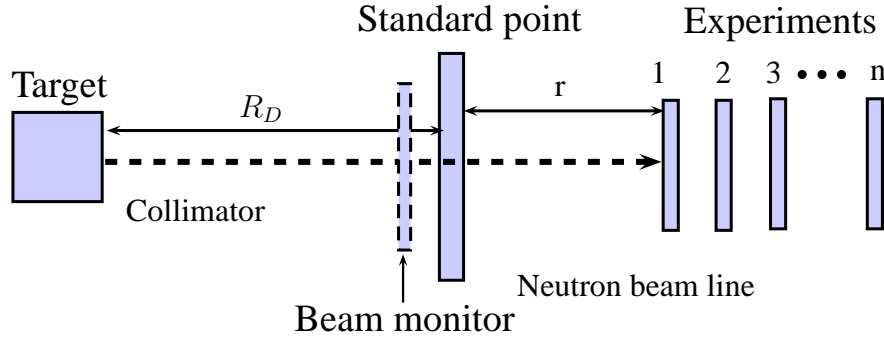


Figure 3.3: Schematic of the neutron beam lines at LANSCE and TSL.

So the neutron fluence  $\Phi$  at the distance  $r$  could be modeled as:

$$\Phi = \Phi_d \frac{R_D^2}{(R_D + r)^2} \quad (3.7)$$

At LANSCE and TSL multiple experiments can be carried out with several test sets arranged along the beam line. The neutron fluence at the first experiment can be calculated by using equation 3.7. Both divergence and scattering of the neutron fluence have to be taken into account for the downstream experiments (2, 3  $\dots$  n). The neutron fluence at a certain point of the beam line behind a set of experiments can be determined if the transmission  $\tau(r)$  is known :

$$\Phi = KC \frac{R_D^2}{(R_D + r)^2} \tau(r) \quad (3.8)$$

However, as the  $\tau(r)$  is unknown, the challenge of this project is to develop a system which can determine the transmission  $\tau(r)$ .

At TRIUMF NIF, the experimental arrangement was different from that of TSL and LANSCE. The beam monitoring equipment was positioned behind the experiment, and calibrated to the position of the experiments as shown in figure 3.4. Therefore the measured flux and fluence had to be corrected for the attenuation of the experiment itself (divergence was included in the calibration factor).

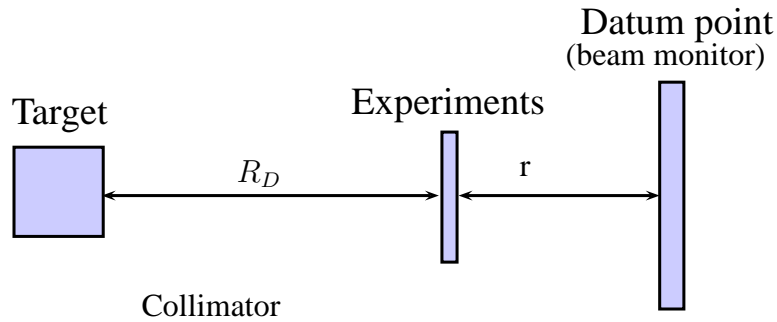
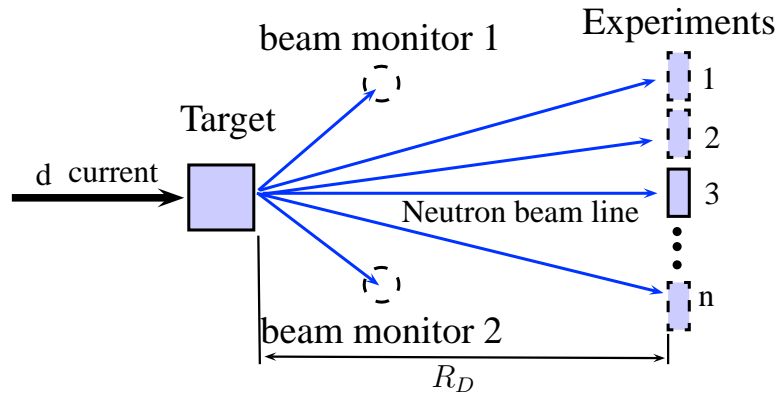


Figure 3.4: Schematic of the neutron beam line at TRIUMF.

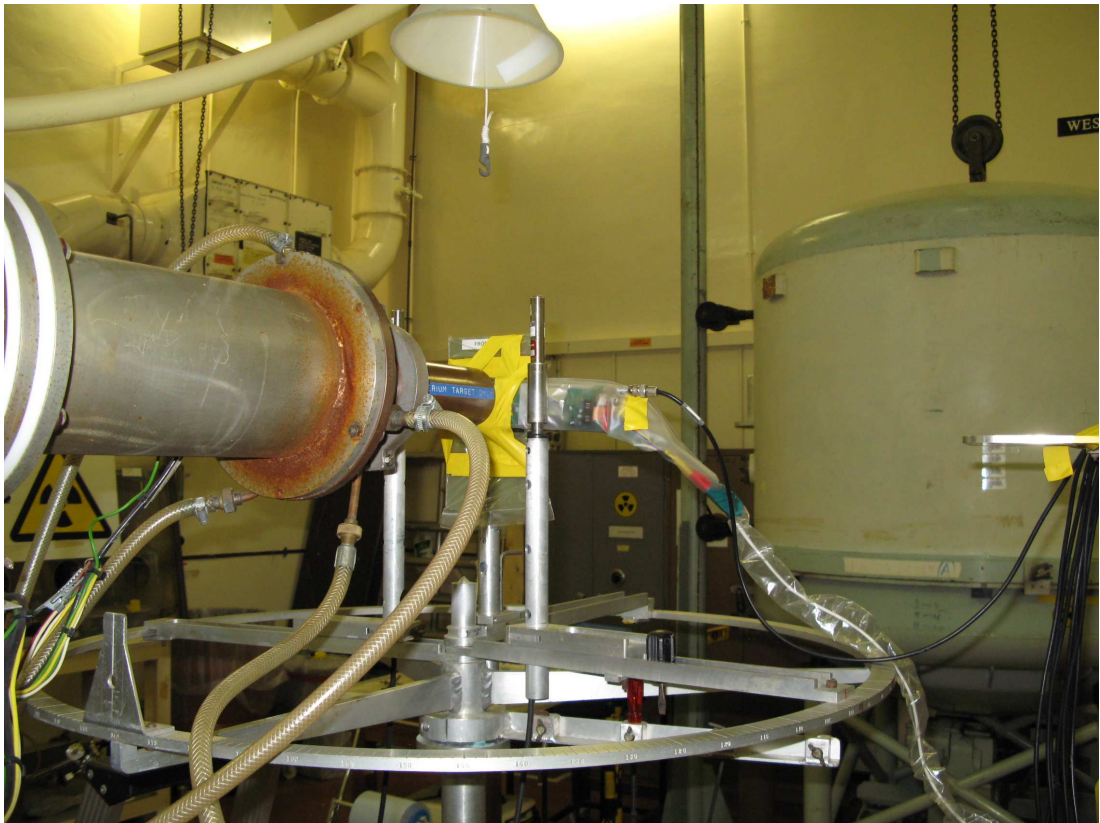
In this project, the strongest beam neutron flux that beam monitor was irradiated at TRIUMF NIF, which was typically at  $4.0 \times 10^6 \text{ n.cm}^{-2}\text{s}^{-1}$ . Measuring at the standard point at LANSCE and TSL ANITA, the typical flux at LANSCE was around  $1.5 \times 10^5 \text{ n.cm}^{-2}\text{s}^{-1}$ . TSL ANITA approximated to  $1.25 \times 10^6 \text{ n.cm}^{-2}\text{s}^{-1}$ . However, as TSL ANITA is a pulsed neutron beam, the fluence rate received by the beam monitor during each neutron pulse was very high. Figures 2.6 (on page 39) and 2.7 (on page of 40) show example 1 s voltage time series captured in each of the neutron beams. The greater pulse rate reflects both the greater neutron flux at TRIUMF facility and also the effect of upstream experiments (eg. measurements made in April 2007), which degrade the neutron beam further down the beam line.

Figure 3.5(a) shows schematically the beam line at ASP. The ASP facility has two beam monitors providing the neutron fluence for the device under test (DUT). Figure 3.5(b) shows sensor 9 under test at ASP.

LANSCE and TSL ANITA are pulsed neutron beams. The LANSCE beam is generated from a 60 Hz linac beam which is shared between the Weapons Neutron Research (WNR) facility and the Lujan Neutron Scattering Center. Two out of every three pulses are delivered to the WNR. The macropulse length is about  $625 \mu\text{s}$ .



(a) Schematic neutron beam.



(b) Sensor 9 under test.

Figure 3.5: ASP neutron beam line.

TSL ANITA macropulses length is about 500  $\mu\text{s}$ . TSL quasi-monoenergetic beams with energy above 100 MeV are also pulsed. TSL quasi-monoenergetic beams with energies below 100 MeV, TRIUMF NIF and ASP are continuous neutron beams.

### 3.4 Experimental results

In this section, the experimental results from irradiation at LANSCE, TSL, TRIUMF and ASP will be presented. Appendix C gives the additional information of LANSCE experimental results. The photodiode responses captured at TSL and TRIUMF are calculated with neutron energies above 10 MeV. The CI for calculating the uncertainty of the pulse events is 68.27%.

#### 3.4.1 Neutron beam transmission measurements at LANSCE

LANSCE allows multiple devices to be irradiated at the same time by placing several samples along the neutron beam one behind another. In order to determine the transmission along the neutron beam, a number of experiments were made by using sensors 11 and 12 in October 2010.

To determine sensor characteristics and the effect of the pulsed neutron beam, two sensors were irradiated apart in the upstream position. To determine the degrading influence of upstream experiments in the beam line, two sensors were irradiated one upstream and the other downstream with or without an aluminium scatterer between them. Two sensors were also irradiated upstream and downstream with one or three other devices under test between them.

The temporal characteristics of the LANSCE beam are shown in figure 3.6. The primary particles have a repetition rate of 60 Hz. The accelerator simultaneously delivers one out of every three pulses of the neutron beam to the Lujan Neutron

Scattering Center and two out of every three pulses to WNR Target 4 of which the Irradiation of Chips and Electronics (ICE) House is part.

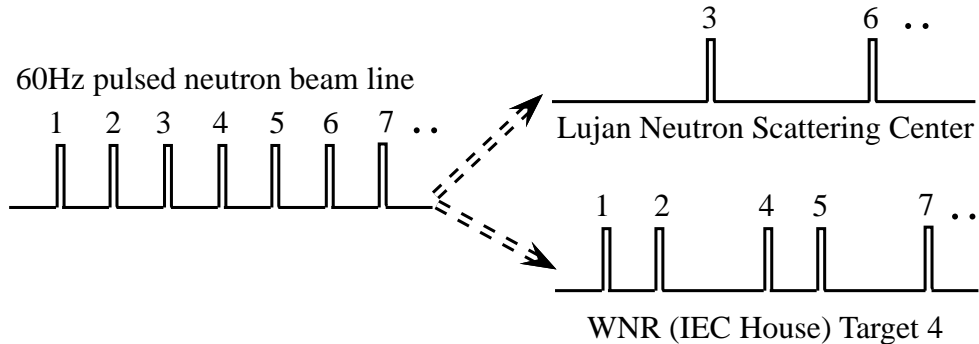


Figure 3.6: LANSCE pulsed neutron temporal characteristics of the beam.

#### 3.4.1.1 Sensor characterization at the upstream position

Sensors 11 and 12 were irradiated in the front of the beam at the same position 78 cm away from the standard point (in figure 3.7). The distance between the target and the standard point is 20 m. The experimental conditions are summarized in table 3.1. The pulse events were captured either in real-time or through post-processing.

Table 3.1: Experimental conditions of two sensors irradiated at the upstream position at LANSCE.

Run	Signal Processing	neutron fluence, /n.cm <sup>-2</sup>	
		above 1.5 MeV	above 10 MeV
LAN01	post-processing	$1.93 \times 10^8$	$1.04 \times 10^8$
LAN02	real-time	$3.92 \times 10^8$	$2.11 \times 10^8$
LAN03	real-time	$2.80 \times 10^8$	$1.51 \times 10^8$
LAN04	real-time	$1.79 \times 10^8$	$9.67 \times 10^7$
LAN05	real-time	$6.97 \times 10^8$	$3.76 \times 10^8$

The experimental data were collected for each sensor at a 0.5 MHz sample rate. At this sample rate, the minimum detected energy for sensor 11 was 132 keV and for sensor 12 was 112 keV. The number of pulse events is summarized in table C.1.

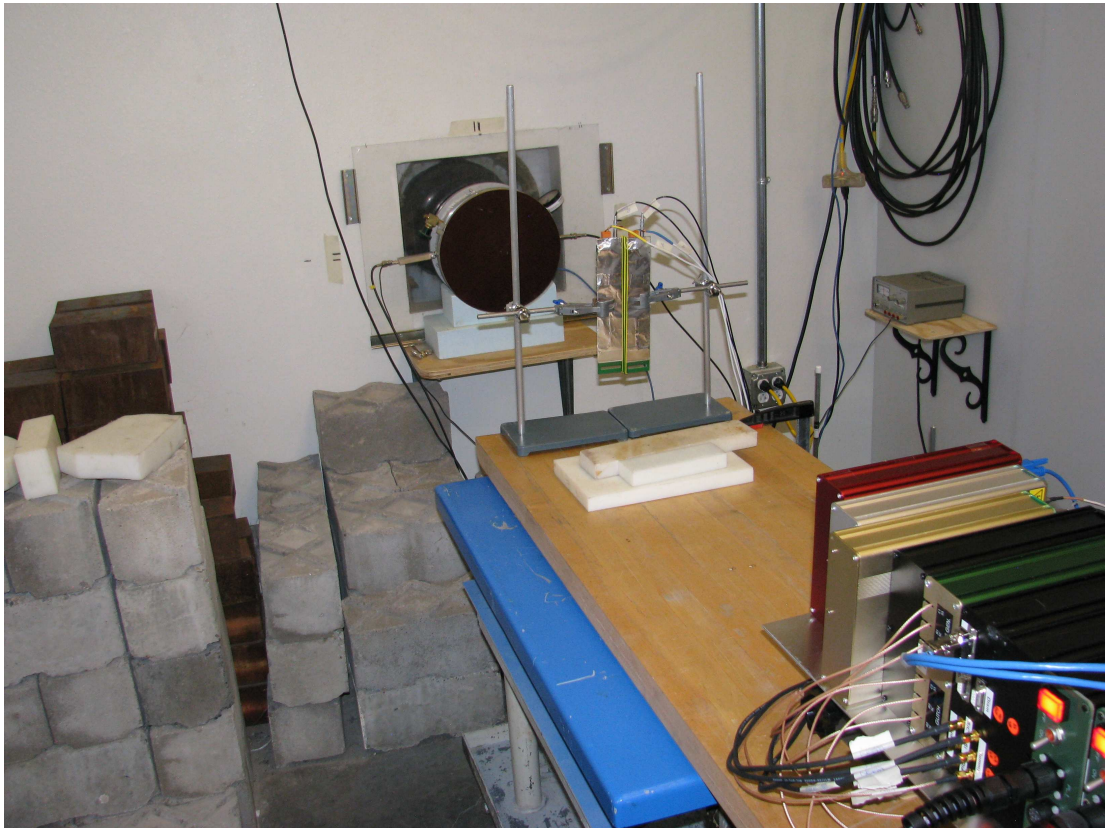


Figure 3.7: Picture of sensor 11 and 12 testing at the 78cm upstream position at LANSCE.

Table 3.2 summarizes the number of pulses above the collected energy 132 keV and the ratio of the pulse number of sensor 12 over sensor 11.

Table 3.2: Experimental results of two sensors irradiated at the upstream position at LANSCE.

Run	Max. energy, /MeV		sensor 11 events	sensor 12 events	$\frac{\text{Sensor11}}{\text{sensor12}}$ /%
	sensor 11	sensor 12			
LAN01	30.12	35.18	5760	5460	94.79
LAN02	33.18	32.39	11922	11499	96.45
LAN03	33.56	28.04	8335	7864	94.35
LAN04	33.44	31.79	5090	4802	94.34
LAN05	32.69	32.49	19299	18656	96.67

Real-time signal processing was used for the first time to collect the pulse events

during the LANSCE experiments. The experimental results of real-time and post signal processing agree well as shown in figure 3.8, which displays the measured pulse height spectra of runs LAN01 and LAN05. The measured pulse interval distributions are shown in figure 3.9 on page 94.

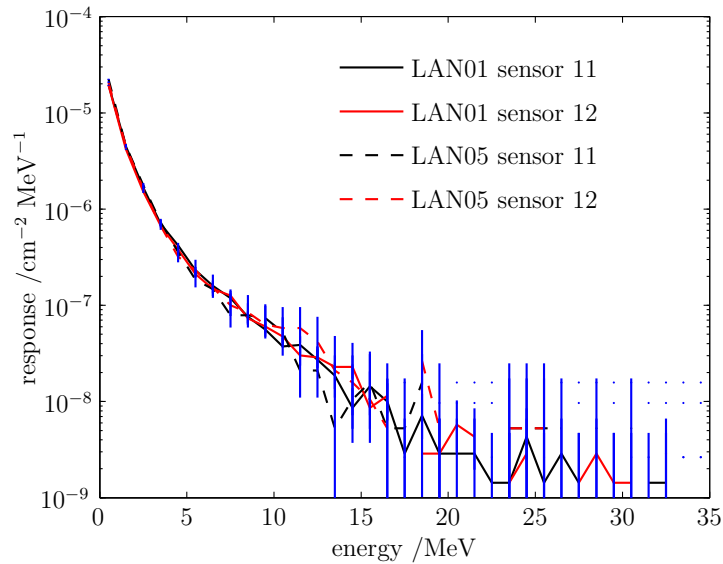


Figure 3.8: Measured pulse height spectra at the upstream position at LANSCE, CI=68.27%.

The exponential fits of the run LAN05 pulse height distribution above 5 MeV are listed in table 3.3.

Table 3.3: Measured pulse height spectra parameters of two sensors irradiation at upstream at LANSCE, CI=68.27%.

Run	Sensor Type	decay constant /MeV <sup>-1</sup>
LAN01	11	0.336±0.031
	12	0.323±0.039
LAN05	11	0.321±0.015
	12	0.301±0.023

The WNR target pulsed neutron beam structure is shown in figure 3.10. Assuming two pulse events are generated by, eg. first and second, or second and third, beam

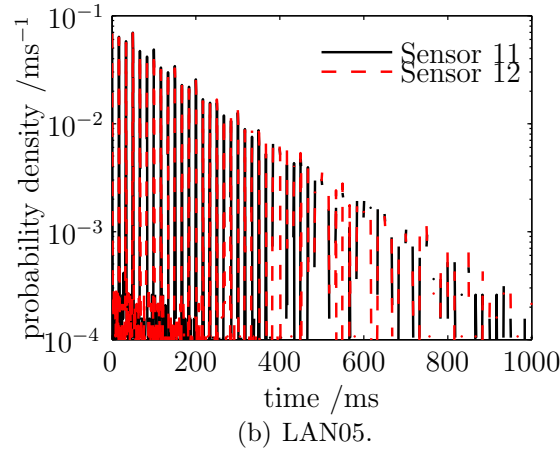
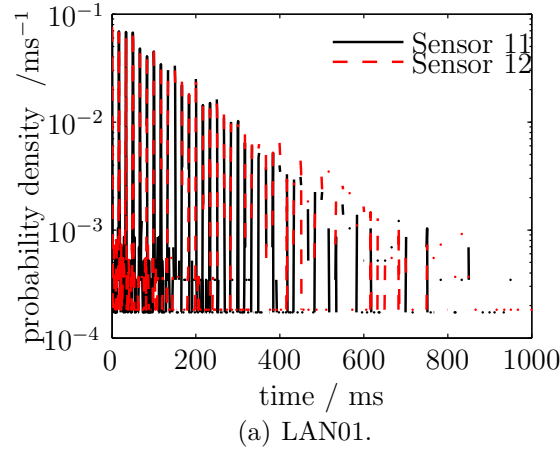


Figure 3.9: Measured pulse interval distributions at the upstream position at LANSCE.

macropulses interacting with the photodiode sensor, the pulse time interval would be  $1/60$  s and  $2/60$  s respectively. If two pulse events are generated by, eg. first and third, or second and fourth neutron beam, their pulse time intervals are both  $3/60$  s. Assuming  $n$  to be the neutron beam interval, the pulse event interval ( $\Delta t$ ) can be determined as follows:

1. If one pulse event occurs in the first neutron beam, the next pulse event generates in the  $(n + 1)^{th}$  (where  $n = 1, 2, 3, \dots$ ) neuron beam, then:

$$\begin{aligned}
 \frac{1}{60}s &= \frac{1}{60}s & n=1 \\
 \left(\frac{1}{60} + \frac{2}{60}\right)s &= \frac{3}{60}s & n=2 \\
 \left(\frac{1}{60} + \frac{2}{60} + \frac{1}{60}\right)s &= \left(\frac{1}{60} + \frac{3}{60}\right)s & n=3 \\
 \left(\frac{1}{60} + \frac{3}{60} + \frac{2}{60}\right)s &= 2 \times \frac{3}{60}s & n=4 \\
 \left(\frac{1}{60} + \frac{3}{60} + \frac{2}{60} + \frac{1}{60}\right)s &= \left(\frac{1}{60} + 2 \times \frac{3}{60}\right)s & n=4 \\
 \left(\frac{1}{60} + \frac{3}{60} + \frac{2}{60} + \frac{1}{60} + \frac{2}{60}\right)s &= 3 \times \frac{3}{60}s & n=6 \\
 &\vdots
 \end{aligned}$$

So:

- when  $n$  is an odd number,  $\Delta t = \left(\frac{1}{60} + \frac{n+1}{2} \times \frac{3}{60}\right)s$
- when  $n$  is an even number,  $\Delta t = \frac{n}{2} \times \frac{3}{60}s$

2. If one pulse event occurs in the second neutron beam, the next pulse event generates in the  $(n + 2)^{th}$  neutron beam, then:

$$\begin{aligned}
 \frac{2}{60}s &= \frac{2}{60}s & n=1 \\
 \left(\frac{2}{60} + \frac{1}{60}\right)s &= \frac{3}{60}s & n=2 \\
 \left(\frac{2}{60} + \frac{1}{60} + \frac{2}{60}\right)s &= \left(\frac{2}{60} + \frac{3}{60}\right)s & n=3 \\
 \left(\frac{2}{60} + \frac{3}{60} + \frac{2}{60}\right)s &= 2 \times \frac{3}{60}s & n=4 \\
 \left(\frac{2}{60} + \frac{3}{60} + \frac{1}{60} + \frac{2}{60}\right)s &= \left(\frac{1}{60} + 2 \times \frac{3}{60}\right)s & n=4 \\
 \left(\frac{2}{60} + \frac{3}{60} + \frac{1}{60} + \frac{2}{60} + \frac{1}{60}\right)s &= 3 \times \frac{3}{60}s & n=6 \\
 &\vdots
 \end{aligned}$$

So:

- when  $n$  is an odd number,  $\Delta t = \left(\frac{2}{60} + \frac{n+1}{2} \times \frac{3}{60}\right)s$
- when  $n$  is an even number,  $\Delta t = \frac{n}{2} \times \frac{3}{60}s$

Overall, the possibilities of  $(1/60 + 3i/60)$  s and  $(2/60 + 3i/60)$  s are the same, and the possibility of  $(3i/60)$  s pulse time interval is double either  $(1/60 + 3i/60)$  s or  $(2/60 + 3i/60)s$ , where  $i$  is an integer. Figure 3.9 shows the measured pulse interval distribution, which reflects the characteristics of the neutron beam. The distribution forms a comb at multiples of the accelerator repetition period 16.7 ms (which is the reciprocal of the 60 Hz) modified by the characteristic exponential form of a Poisson process.

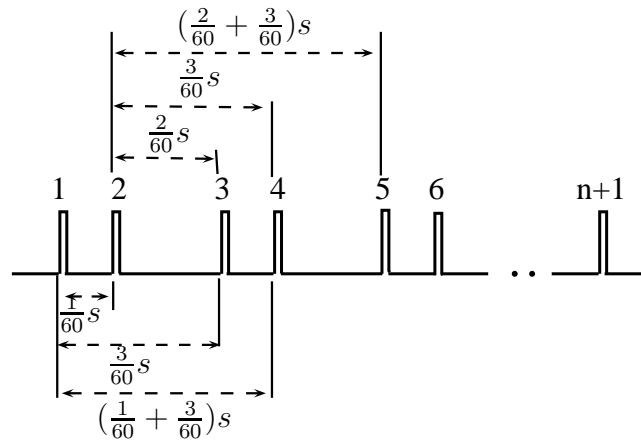


Figure 3.10: Temporal characteristics of the WNR pulsed neutron beam.

Figure 3.11 shows the integrated counts of run LAN05 at the repetition of 16.7 ms. The  $n \times 16.7$  ms component of the beam (i.e. every first peak) and  $n \times 33.3$  ms component of the beam are similar. The  $n \times 50$  ms component of the beam is enhanced by a factor of 2, reflecting the 20 Hz periodicity of the incident neutron beam.

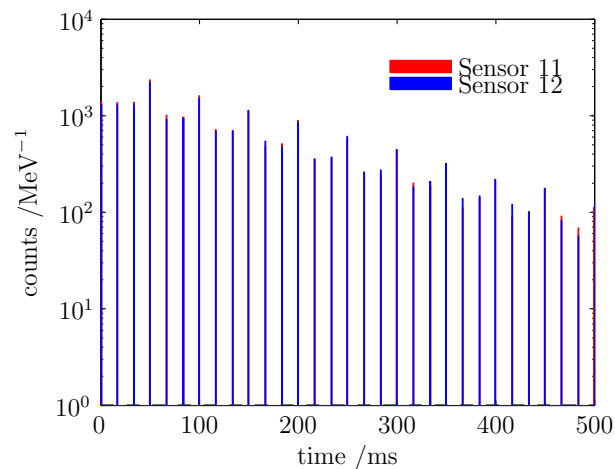


Figure 3.11: Measured pulse interval distribution (integrated) at the upstream position at LANSCE, CI=68.27%.

The exponential fits of the run LAN01 pulse interval distribution in the pulse interval of  $n \times 16.7$  ms,  $n \times 33.3$  ms and  $n \times 50$  ms are similar to those shown in table 3.4, which indicates that the pulse interaction rates agree well in these three intervals of the neutron beam.

Table 3.4: Measured pulse interval parameters of two sensors irradiated at the upstream position at LANSCE, CI=68.27%.

pulse interval	decay constant
/ $\mu\text{s}$	/ $\text{s}^{-1}$
$n \times 16.7$	$6.67 \pm 0.12$
$n \times 13.3$	$6.66 \pm 0.06$
$n \times 50.0$	$6.77 \pm 0.15$

The duration of run LAN05 duration was 776 s. For collected energy above 132 keV, the event rate in sensor 11 was  $7.4 \text{ s}^{-1}$  and that in sensor 12 was  $7.1 \text{ s}^{-1}$ , an event probability per macropulse of approximately 0.185. Because the statistical distribution of photodiode sensor interactions with neutrons is a Poisson process, no matter what the interaction rate is, there is always a possibility of pile-up; the interaction event probability per macropulse is always higher than the detected probability. Assuming the event probability per macropulse to be 0.19, the probability of the number of events per macropulse is listed<sup>1</sup> in table 3.5.

Table 3.5: The probability of number of pulse events per macropulse measured at LANSCE.

events number	possibility
0	0.827
1	0.157
2	0.015
3	$9.45 \times 10^{-4}$

The probability of three events per macropulse is very small ( $9.45 \times 10^{-4}$ ), meaning that the pile-up rate in this case can be ignored. The beam macropulse length is  $625 \mu\text{s}$ , then the average interaction rate (assuming to be  $r$ ) of two events occurring in one macropulse is:

---

<sup>1</sup>These are determined by using MATLAB function ‘poisscdf’

$$r = \frac{1000000}{\frac{625}{2}} = 3200s^{-1}$$

So the probability of pile-up rate (assuming to be  $P$ , and irradiated in continuous neutron beam) for two events per macropulse is (see §2.4.1):

$$p = r\tau$$

where  $\tau$  is the sensor pulse width, giving  $p = 0.128$ . It is assumed that the photodiode sensor under test in continuous beam. In the case of pulsed neutron beam, the probability of pile-up should be less than 0.128 because the pile-up only occurs when two or more pulse events are generated in one macropulse neutron beam. So the probability of pile-up measured at LANSCE should be less than  $0.015 \times 0.128 = 1.88 \times 10^{-3}$ . It can be concluded that pile-up is not significant in the LANSCE measurements.

The responses of these two sensors are summarized in table 3.6 and plotted in figure 3.12, which indicate that the response of the photodiode sensor reduces as an increasing amount of fluence is received over time. This decrease is attributable to radiation damage.

Table 3.6: The responses of two sensors irradiated in the upstream position at LANSCE.

Run	sensor 11, /cm <sup>2</sup>		sensor 12, /cm <sup>2</sup>	
	above 10 MeV,	above 1.5 MeV	above 10 MeV,	above 1.5 MeV
LAN01	$5.59 \times 10^{-5}$	$3.01 \times 10^{-5}$	$5.27 \times 10^{-5}$	$2.84 \times 10^{-5}$
LAN02	$5.64 \times 10^{-5}$	$3.04 \times 10^{-5}$	$5.44 \times 10^{-5}$	$2.94 \times 10^{-5}$
LAN03	$5.52 \times 10^{-5}$	$2.97 \times 10^{-5}$	$5.21 \times 10^{-5}$	$2.81 \times 10^{-5}$
LAN04	$5.26 \times 10^{-5}$	$2.83 \times 10^{-5}$	$4.97 \times 10^{-5}$	$2.68 \times 10^{-5}$
LAN05	$5.13 \times 10^{-5}$	$2.77 \times 10^{-5}$	$4.99 \times 10^{-5}$	$2.69 \times 10^{-5}$
Average	$5.43 \times 10^{-5}$	$2.93 \times 10^{-5}$	$5.16 \times 10^{-5}$	$2.79 \times 10^{-5}$

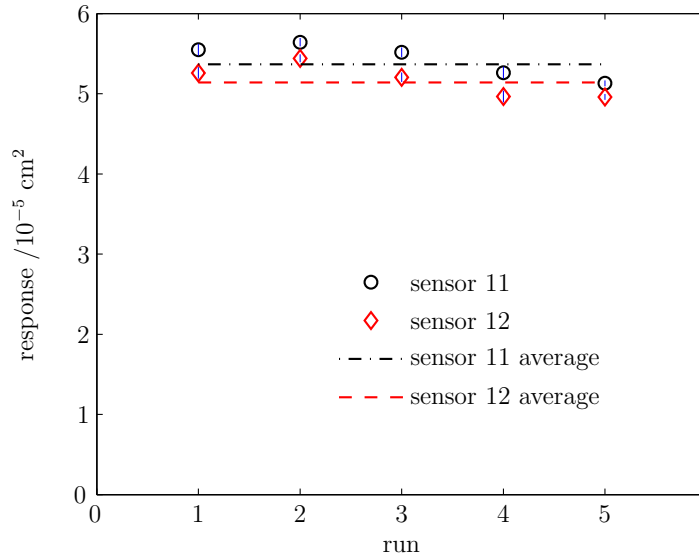


Figure 3.12: Measured responses in the upstream position at LANSCE, CI=68.27%.

As the sensor amplifier gains were calculated, this dominates the uncertainty in collected energy, 132.2 keV may not be the true minimum collected value. In table 3.2, the number of sensor 12 pulse events is smaller than that for sensor 11, which indicates that the true minimum collected energy in sensor 12 may be smaller than sensor 11. Figure 3.13 shows a proportional fit between the counts observed in the two sensors. The constant of proportionality is 0.9578.

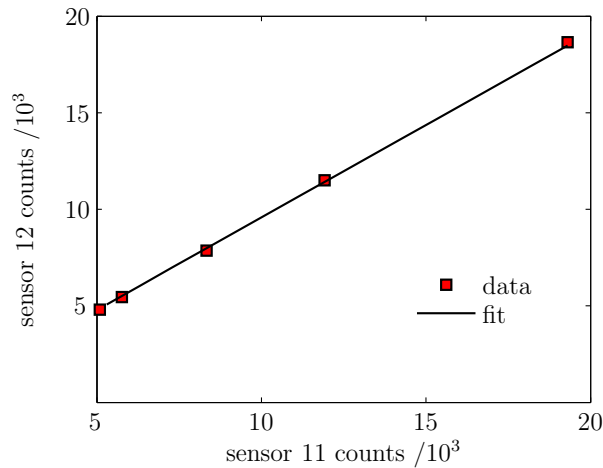


Figure 3.13: Proportional fit between counts in sensor 11 and those in sensor 12.

Assuming the number of sensor 11 pulse events to be the reference count, the

equivalent sensor 12 pulse events  $N_e$  can be calculated:

$$N_e = \frac{N}{0.9578} \quad (3.9)$$

where  $N$  is the original number of sensor 12 pulse events. Assuming that the amount of neutron fluence  $\Phi_{12}$  received by sensor 12 is unknown, it can be determined by:

$$\Phi_{12} = \frac{N_e}{N_{11}} \Phi = \frac{N_e}{\sigma_{11}} \quad (3.10)$$

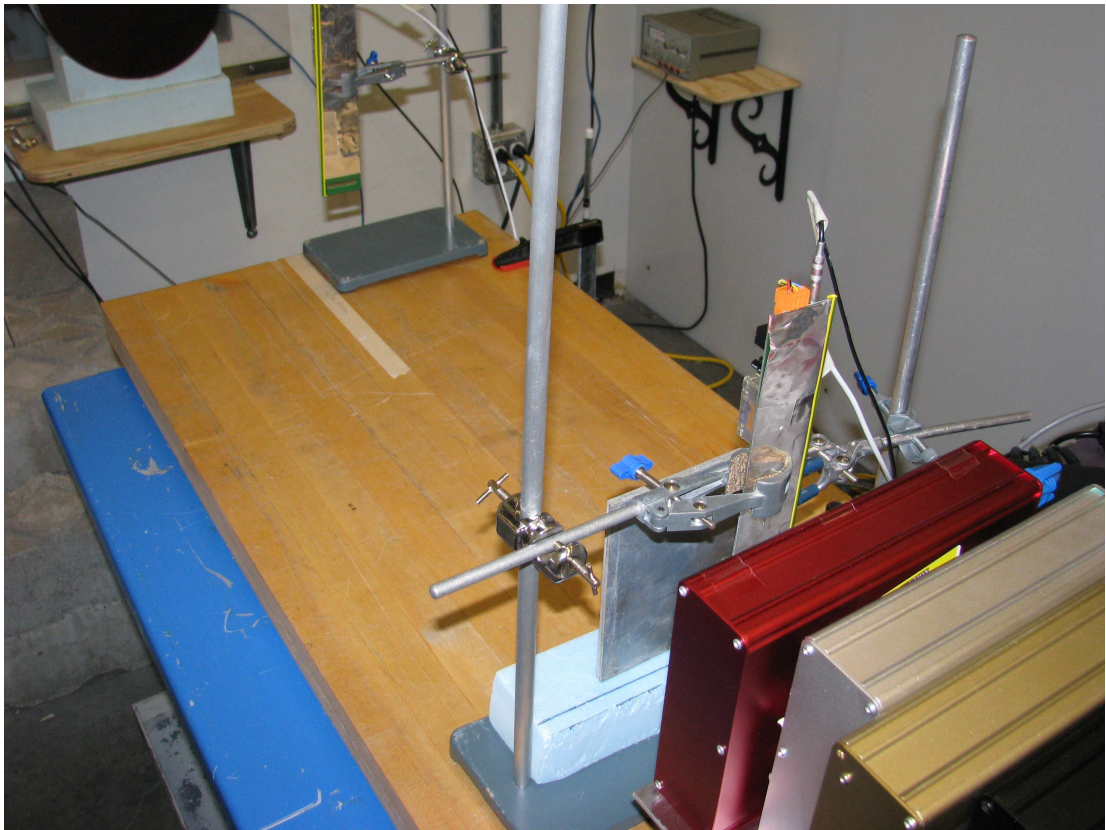
where  $N_{11}$  is the number of sensor 11 pulse events,  $\Phi$  is the amount of neutron fluence received by sensor 11 (and provided by LANSCE dosimetry), and  $\sigma_{11}$  is the sensor 11 response.

#### 3.4.1.2 Effect of an aluminum scatterer on neutron beam fluence measurements

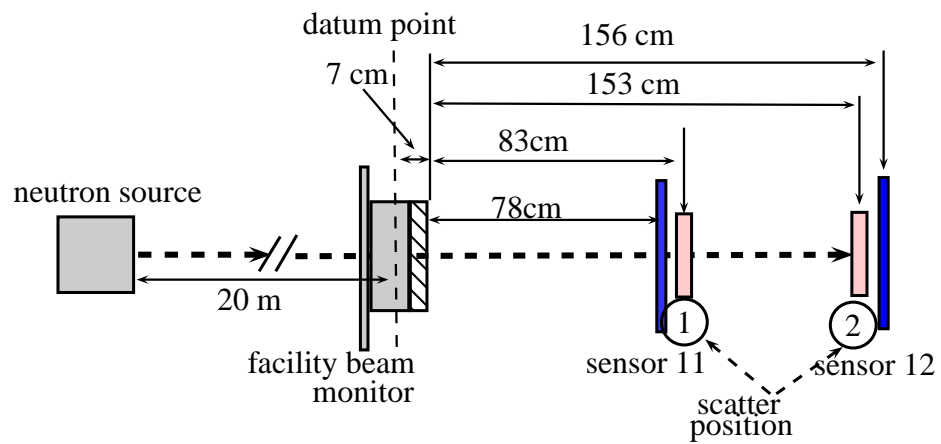
Experiments were made in which sensors 11 and 12 were irradiated apart at the same time, when sensor 11 was placed 78 cm away the standard point without other experiments before it, and sensor 12 was placed 156 cm away the standard point with or without an aluminum scatterer in front at different positions along the neutron beam as shown in figure 3.14(a). Figure 3.14(b) illustrates the schematic diagram showing the relative positions of the sensors with a scatterer. The experimental conditions are summarized in table 3.7.

Table 3.7: Experimental conditions of one sensor upstream and the other downstream with or without a scatterer at LANSCE.

Run	upstream sensor received Fluence, /n.cm <sup>-2</sup> above 1.5 MeV	Fluence, /n.cm <sup>-2</sup> above 10 MeV	Scatterer position, /cm
LAN06	$2.444 \times 10^8$	$1.307 \times 10^8$	no
LAN07	$2.798 \times 10^8$	$1.501 \times 10^8$	83
LAN08	$2.416 \times 10^8$	$1.292 \times 10^8$	153



(a) Picture.



(b) Schematic diagram.

Figure 3.14: Picture and schematic diagram showing the relative position of sensors with a scatterer.

### 3.4 Experimental results

As discussed in §2.5.1, the minimum detectable energy increases as the sample rate decreases. The experimental data were captured in these experiments at sample rate of 0.3 MHz for each sensor. The minimum detected pulse energy from sensor 11 was 171.7 keV and that from sensor 12 was 140.1 keV.

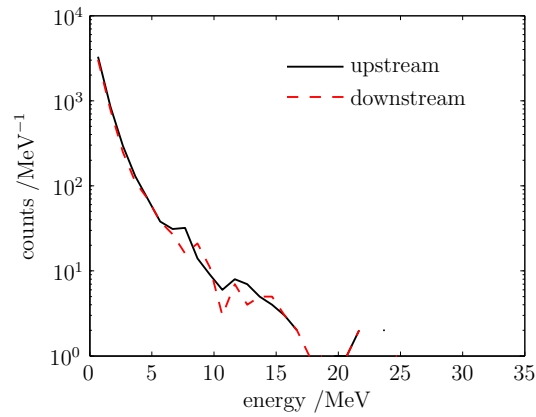
Table 3.8 summarizes the numbers of measured pulse events and the responses of sensor 11 above the collected energy 171.7 keV. The numbers of sensor 12 events in runs LAN06 and LAN07 is smaller than sensor 11. In contrast, the number of sensor 11 events in run LAN08 is much higher than sensor 11. Figure 3.15 shows the measured pulse height spectra. It can be seen that the measured results in runs LAN06 and LAN07 from the two sensors are similar, but the measured pulse high spectrum of sensor 12 is much steeper than that of sensor 11 in run LAN08.

Figure 3.16 on page 104 shows the pulse height spectra with the collected energy below 5 MeV. It can be seen that the numbers of pulse events from sensor 12 are much greater than those in sensor 11 only when the energy of collected events is below 2 MeV.

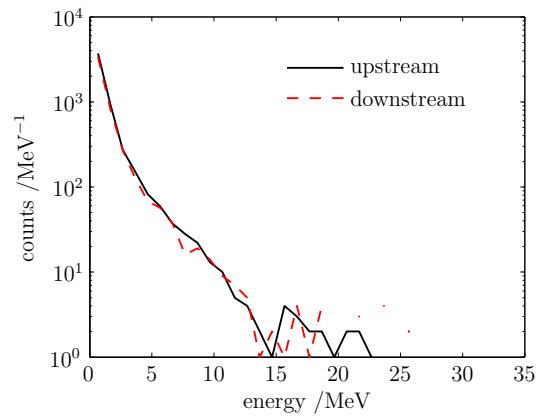
Table 3.8: Experimental results of one sensor at upstream and one at downstream with or without a scatter at LANSCE.

Run	upstream sensor response /cm <sup>2</sup>		upstream sensor pulse number	downstream sensor number	equivalent pulse number
	above 1.5 MeV	above 10 MeV			
LAN06	$1.966 \times 10^{-5}$	$3.677 \times 10^{-5}$	4806	4377	4570
LAN07	$1.913 \times 10^{-5}$	$3.566 \times 10^{-5}$	5352	4830	5043
LAN08	$1.950 \times 10^{-5}$	$3.646 \times 10^{-5}$	4710	6707	7003

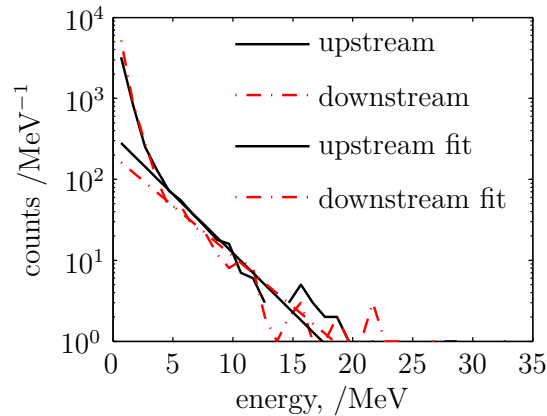
Considering the neutron beam divergence, the neutron beam fluence  $\Phi_r$  at the distance  $r$  from the standard point can be calculated by using equation 3.7. Assuming the amount of neutron fluence received by sensor 12 (downstream) to be  $\Phi_{12}$ , (which can be determined by using equation 3.10), the transmission measured can be defined by:



(a) LAN06 without a scatterer.



(b) LAN07 with a scatterer at 83 cm.



(c) LAN08 with a scatterer at 151 cm.

Figure 3.15: Measured pulse height spectra of two sensors with and without a scatterer between them at LANSCE.

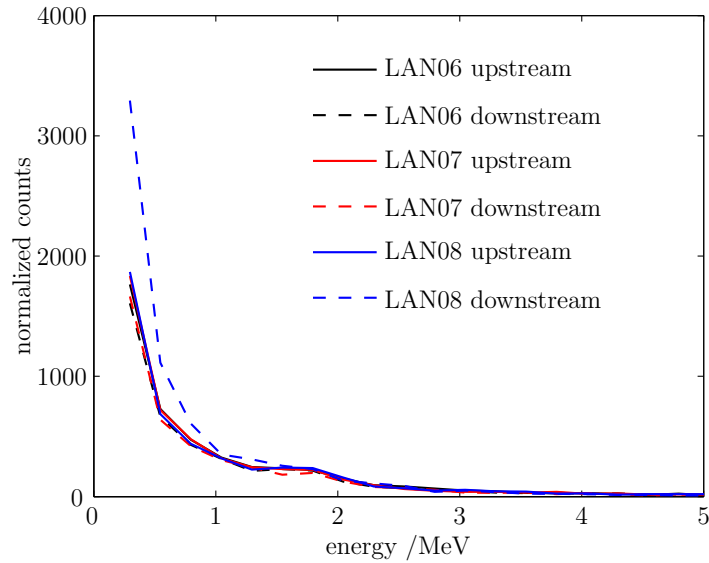


Figure 3.16: Measured pulse height spectra in low collected energy of two sensors with or without a scatterer between them at LANSCE.

$$\tau(r) = \frac{\Phi_{12}}{\Phi_r} \quad (3.11)$$

Truscott et al. [54] irradiated a diode detector at TSL and also simulated it by using the Geant4 toolkit. The experiments were made in such a way that the diode detector was positioned in different positions along the neutron beam with a series of printed circuit boards, cadmium plates and small equipment enclosures forming other experiments upstream of the diode detector. The simulation and measured results agreed well. The simulation results showed that greater numbers of secondary particles (eg.neutrons) were generated as they passed through the equipment, but these particles were not traveling near enough to the beam axis to affect equipment downstream.

The thickness of the aluminum scatterer was about 4 mm, and so majority of neutron fluence could penetrate; for example; 95% of neutron with 1 MeV energy can penetrate this scatterer (see Appendix D). The high-energy neutron interaction with an aluminum scatterer can generate secondary particles. In this case, the neutron beam near the scatterer can be enhanced, and the transmission to downstream can

increase dramatically.

The measured transmissions as summarized in table 3.9 are consistent with Truscott et al. [54]. In the case with no scatterer (run LAN06), the measured transmission was slightly higher than 100%, but it was within counting uncertainties of 100%. There was a small decrease in transmission in run LAN07 (with a scatterer in position 1); it means that there was only a small effect in degrading the beam. In contrast, there was a large enhancement of the beam in run LAN08, which was probably due to secondary particles generated by neutrons interacting with the aluminium scatterer. The same phenomenon must have happened in run LAN07; as the scatterer in position 2 was much further away the upstream sensor than in position 1, in that case the highly-divergent second source was insignificant to a downstream sensor.

Table 3.9: The transmission of two sensors irradiated with or without a scatterer between them at LANSCE.

Run	$\Phi_r, /n.cm^{-2}$ above 1.5 MeV	$\Phi_{12}, /n.cm^{-2}$	transmission /%
LAN06	$2.271 \times 10^8$	$2.3 \times 10^8$	102.34
LAN07	$2.600 \times 10^8$	$2.66 \times 10^8$	101.40
LAN08	$2.245 \times 10^8$	$3.59 \times 10^8$	160.00

Table 3.10 lists estimated parameters for exponential fits between 5 MeV and 14 MeV. The pair of pulse height spectra parameters in runs LAN06 and LAN07 are similar. In contrast, in run LAN08, the decay constant  $b$  of the downstream sensor is significantly lower than that of the upstream sensor. The decay constant  $b$  is the reciprocal of average collected energy, so the average energy of the downstream sensor in run LAN08 is higher than upstream. These results are also consistent with [54], which suggests that greater scattering occurs to the low-energy of the neutron spectrum.

If only larger events are considered, the transmissions of run LAN06 and run LAN07 are still similar and there is not a significant variation with the threshold collected

### 3.4 Experimental results

Table 3.10: Measured pulse height spectra parameters ( $a \exp^{-bE}$ ) of two sensors in irradiation with the scatterer at LANSCE, CI=68.27%.

Run number		upstream sensor	downstream sensor
LAN06	$b / \text{MeV}^{-1}$	$0.321 \pm 0.037$	$0.349 \pm 0.042$
LAN07	$b / \text{MeV}^{-1}$	$0.360 \pm 0.011$	$0.334 \pm 0.030$
LAN08	$b / \text{MeV}^{-1}$	$0.336 \pm 0.015$	$0.286 \pm 0.037$

energy as shown in figure 3.17. In contrast, the transmission in run LAN08 decreases rapidly with the increase of the threshold for collected energy. The number of pulse events captured by these two sensors and the transmission with the different threshold collected energy are summarized in Appendix C table C.2, and one example is summarized in table 3.11 with the collected threshold energy 3 MeV.

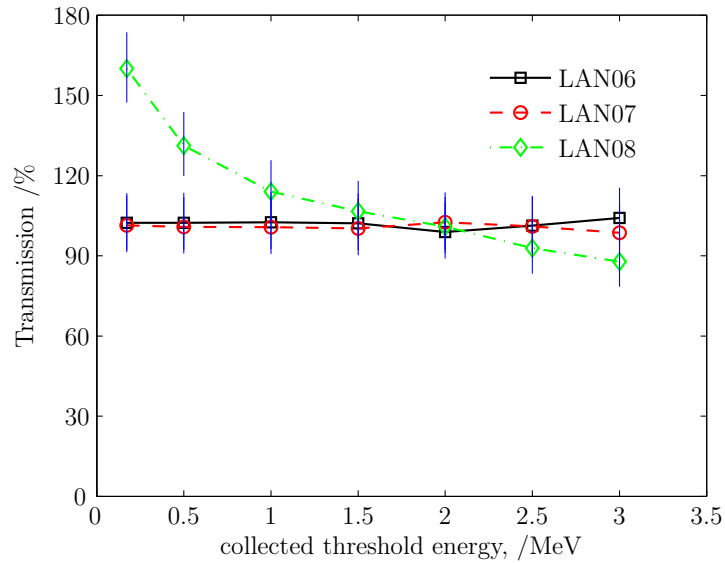


Figure 3.17: The transmission with or without a scatterer with different collected threshold energies at LANSCE, CI=68.27%.

### 3.4 Experimental results

Table 3.11: The transmission of two sensors irradiated with or without a scatterer between at LANSCE between them events collecting above 3 MeV.

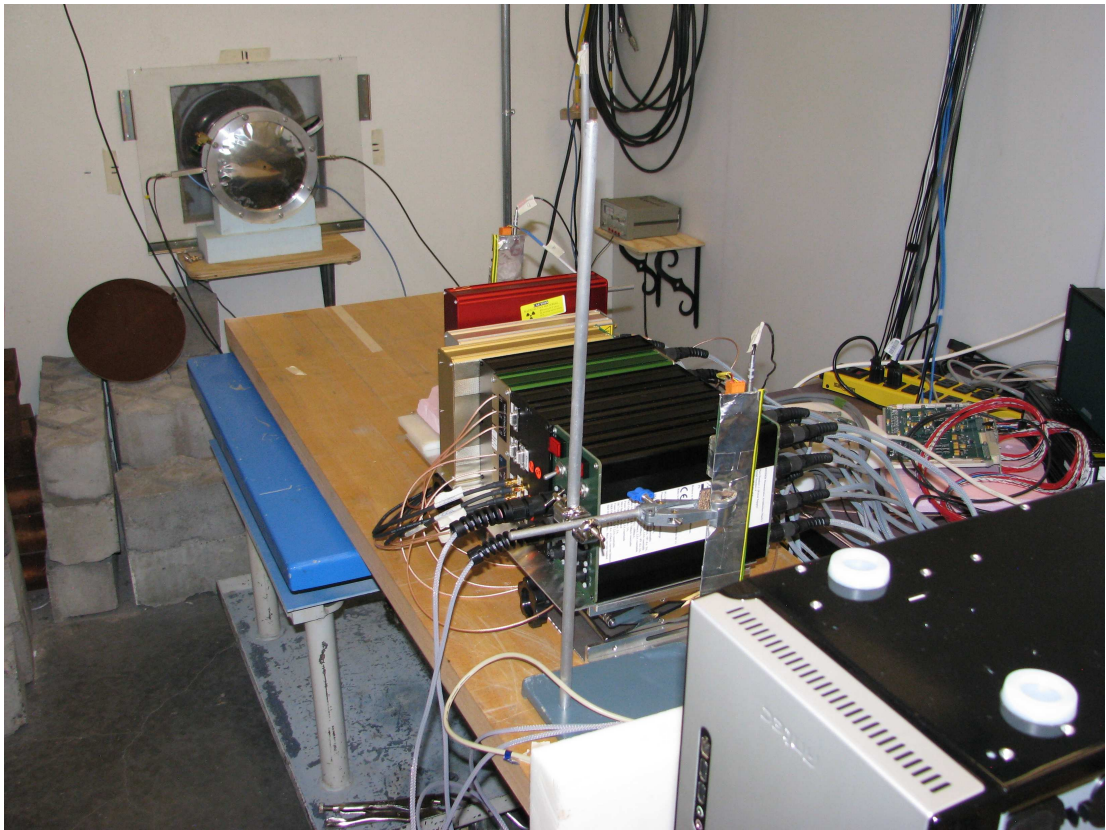
Run	upstream sensor pulse number	downstream sensor pulse number	transmission $\tau(r)$ , %
LAN06	396	362	104.19
LAN07	462	404	98.61
LAN08	429	334	87.10

#### 3.4.1.3 Effect of upstream devices on neutron beam fluence measurements

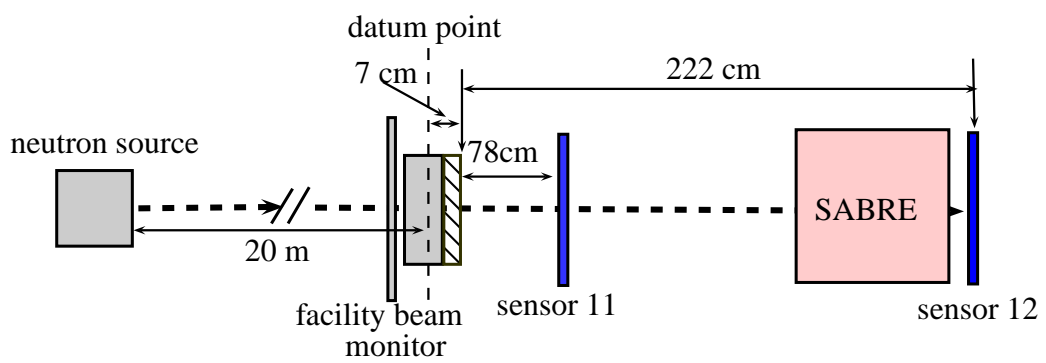
Sensors 11 and 12 were irradiated with one upstream and the other downstream with one or three samples between them as summarized in table 3.12. Runs LAN09 and LAN11 had similar experimental conditions, in which sensor 12 was placed just behind Seeder Atmospheric Beam Radiation Equipment (SABRE) along the neutron beam as shown in figure 3.18(a). The schematic diagram of the relative position is shown in figure 3.18(b). SABRE is a big test set whose length is about 60 cm. In run LAN10, SABRE was placed behind sensor 11; a separate memory device test set (which was installed in an old PC case with a length of about 50 cm) was arranged just behind SABRE. One small device under test was positioned along the neutron beam as shown in figure 3.19(a). Figure 3.19(b) shows the schematic diagram of the relative position of the 3 samples between the two sensors under test (run LAN10).

Table 3.12: Experimental conditions of two sensors with one or three samples between them at LANSCE.

Run	received fluence, /n.cm <sup>-2</sup> above 10 MeV	upstream sensor position, /cm	downstream sensor position, /cm	samples between two sensors
LAN09	$2.69 \times 10^8$	78	222	1 sample
LAN10	$1.18 \times 10^8$	78	318	3 samples
LAN11	$3.41 \times 10^8$	155	222	1 sample

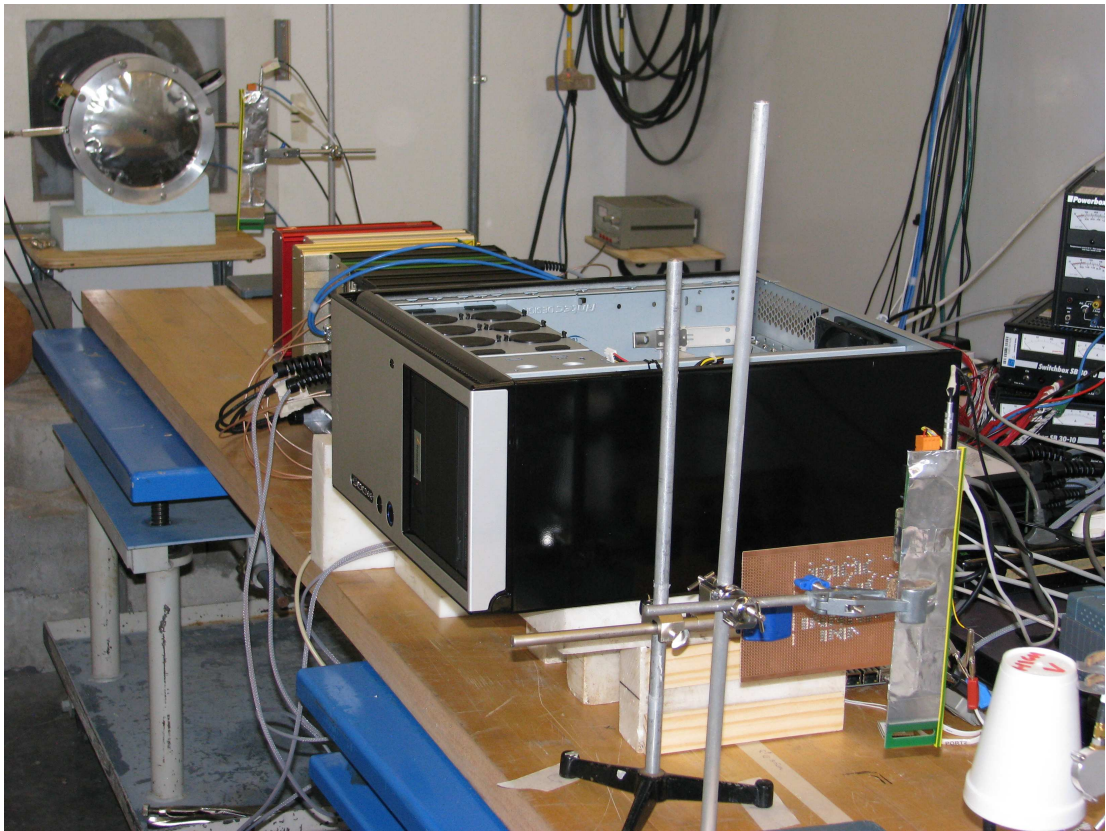


(a) Picture.

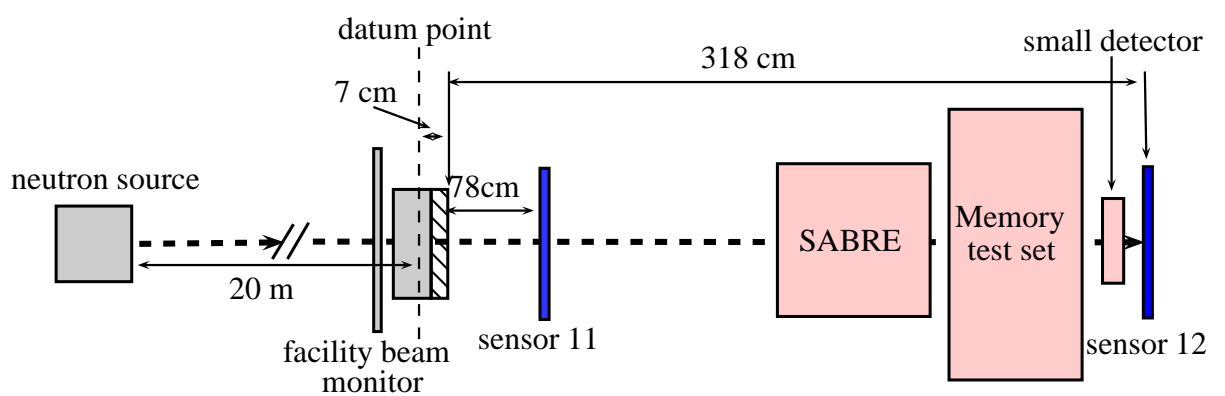


(b) Schematic diagram.

Figure 3.18: The relative position of two sensors with SARBE under test at LANSCE.



(a) Picture.



(b) Schematic diagram.

Figure 3.19: The relative position of two sensors with three other devices under test at LANSCE.

### 3.4 Experimental results

Data were captured in these experiments at a sample rate of 0.3 MHz. The minimum detected pulse energy in sensor 11 (upstream sensor) was 171.7 keV and that in sensor 12 (downstream sensor) was 140.1 keV. The pulse number in the two sensors will be discussed in the remainder of this section with the collected threshold energy 171.7 keV.

Table 3.13 summarizes the neutron fluence received by the upstream sensor and the number of the detected pulse events. Except for a different placement of the downstream sensor, runs LAN09 and LAN11 were under the same experimental conditions. The pulse height spectra as shown in figure 3.20 agree well, where the number of events in the two sensors are similar when the collected energy is below 1 MeV, but they are significantly different in higher collected energy. In run LAN10, the number of pulse events in the upstream sensor is visibly higher than that in the downstream sensor in all energy collected.

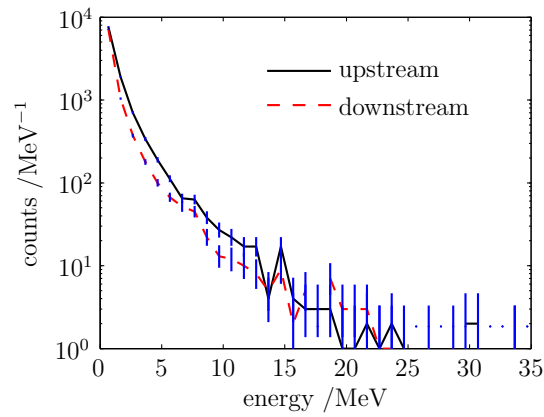
Table 3.13: Experimental results of two sensors with one or three samples between them at LANSCE.

Run	upstream sensor pulse events	downstream sensor pulse events	equivalent events
LAN09	11 188	9101	9537
LAN10	3637	1572	1647
LAN11	12 250	10 710	11 223

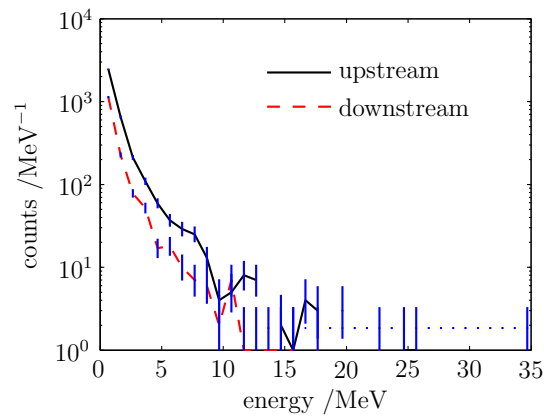
Table 3.14: The transmissions of sensors irradiated with other samples between them at LANSCE.

Run	$\Phi_r, /n.cm^{-2}$ above 1.5 MeV	$\Phi_{12}, /n.cm^{-2}$	transmission /%
LAN09	$4.36 \times 10^8$	$4.25 \times 10^8$	97.41
LAN10	$1.78 \times 10^8$	$1.00 \times 10^8$	56.29
LAN11	$5.86 \times 10^8$	$5.71 \times 10^8$	97.39

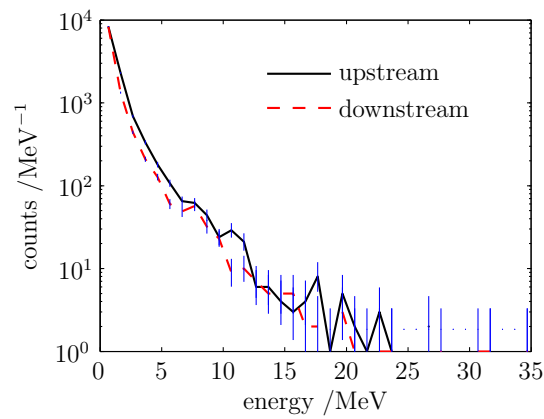
The transmissions of these experiments are summarized in table 3.14. The transmissions of runs LAN09 and LAN11 are both over 97%, which seems unreasonably high. Figure 3.21 shows the counts with the collected energy ranging between 171.7 keV



(a) LAN09 — with one sample.



(b) LAN10 — with three samples.



(c) LAN11 — with one sample.

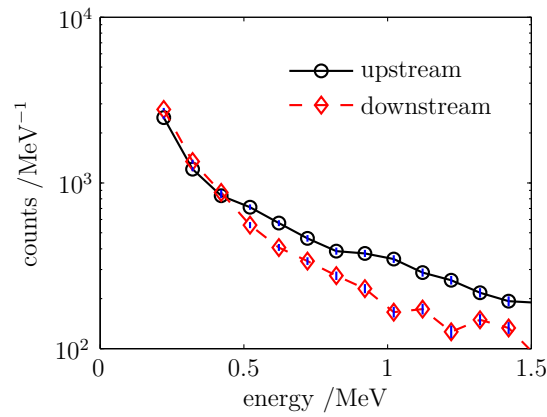
Figure 3.20: Measured pulse height spectra of two sensors with one or three other samples between them at LANSCE, CI=68.27%.

and 1.5 MeV. As can be seen, under about 500 keV, in runs LAN09 and LAN11, the number of pulse events in the downstream sensor is much higher than the upstream sensor. These may be caused by SABRE interacting with the neutron beam and then generating secondary particles, some of which deposited their energy in the downstream sensor.

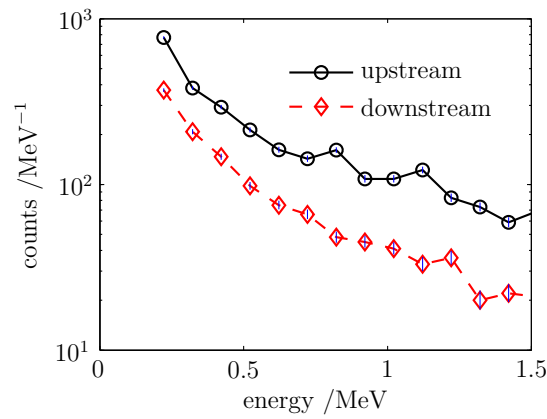
If only larger events are considered, the transmissions of runs LAN09 and LAN11 are still similar and there is not a significant variation with the threshold energy collected, as shown in figure 3.22. The trend of transmissions of these runs is similar; that is the transmissions decrease significantly when the threshold collected energy is below 1 MeV, and slightly increase when the threshold energy is above 1 MeV. Table 3.15 summarizes the number of pulse events and transmissions for event collecting above 1 MeV. The transmissions of runs LAN09 and LAN11 are about 67%, and run LAN10 is about 47%. These experimental results indicate:

- The scattering of neutrons out of the beam by SARBE and memory test was significant.
- The neutron beam can be enhanced by the secondary particles which were generated by the upstream experiments interacting with neutrons. However, the secondary particles could only deposit low energy events in photodiode sensors.
- Low-energy neutrons are more easily scattered by upstream devices than high-energy.

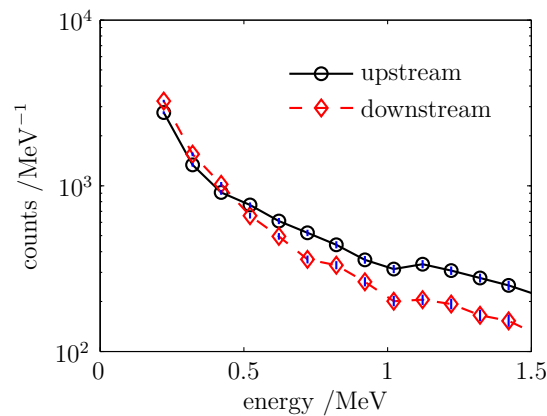
Runs LAN09 and LAN11 had similar experimental conditions; their transmissions are still similar even at different collected threshold energies. It indicates that the experiments are reproducible. The transmission of runs LAN09 and LAN11 decreased more significantly than run LAN10 at low collected energy. One possible reason for this decrease is that more secondary particles were generated by SABRE interacting with neutrons than the memory test set; another reason is that there was one more sample (a small device) between memory test set and the downstream



(a) LAN09 — with one sample.



(b) LAN10 — with three samples.



(c) LAN11 — with one sample.

Figure 3.21: Experiment results in low collected energy events of two sensors with one or three samples between them at LANSCE, CI=68.27%.

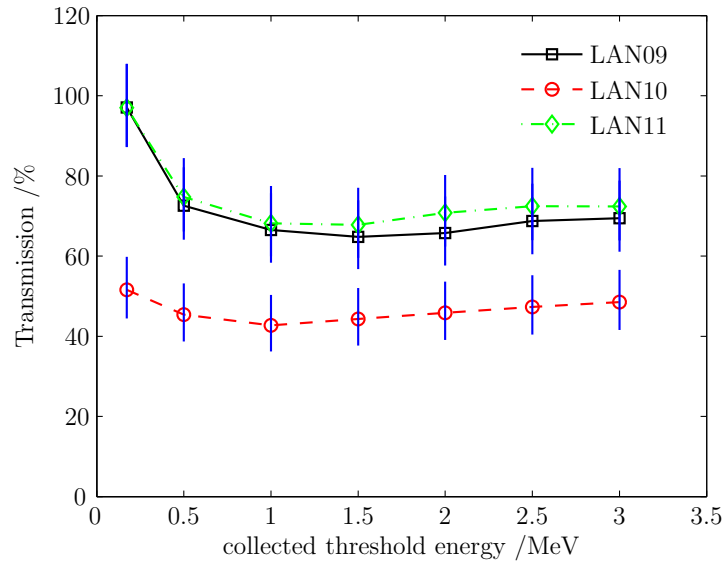


Figure 3.22: The transmission with one or three samples with different collected threshold energies at LANSCE, CI=68.27%.

Table 3.15: The number of pulse events and transmissions in two sensors with one or three samples between them and 1 MeV collected threshold energy.

Run	upstream sensor pulse number	downstream sensor pulse number	downstream sensor equivalent pulse number	Transmission /%
LAN09	4041	2252	2360	66.7
LAN10	1378	494	518	46.7
LAN11	4463	2741	2872	68.4

sensor than SABRE; as a consequence, the highly absorption second source has become insignificant in the downstream device.

According to Truscott et al. [54], the greater scattering occurs in the low-energy neutron of the spectrum. The transmission slightly increases with the increase of above 1 MeV threshold energy as shown in figure 3.22. The neutron spectrum of the downstream sensor received might have more weight in high energy neutron than the upstream sensor. In such cases, the photodiode beam monitoring could provide useful information of the fluence and hardness of a neutron field at multiple

locations in a beam.

#### 3.4.1.4 LANSCE photodiode response measurements

The photodiode monitor system was irradiated over four days during the experiments, including 18 runs. Parts of the experimental details were described in the last three sections. For all these runs, sensor 11 was tested at the upstream position without any other experiments before it. The measured responses in sensor 11 for events collected above 171.7 keV are shown in figure 3.23 along the test time. The number of pulse events and neutron fluence are presented in Appendix C.

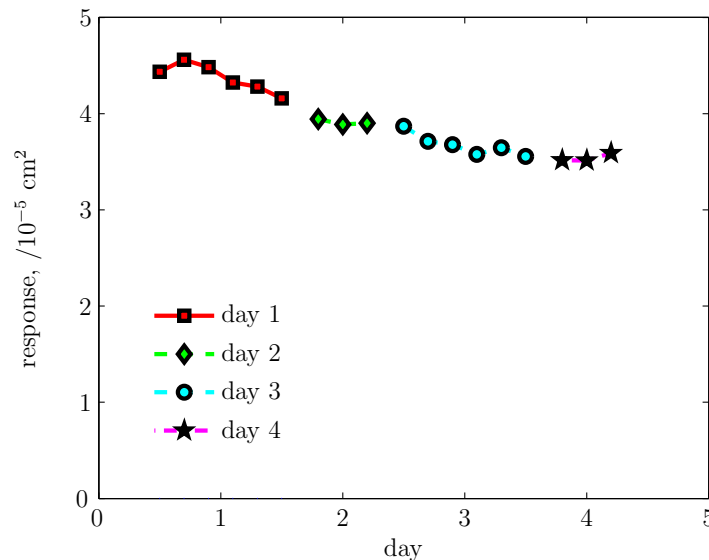


Figure 3.23: The response measurements with the testing time at LANSCE.

One example of the measured pulse height spectra of run LAN02 (first day of the experiments) and LAN11 (the last run captured on the final day) are shown in figure 3.24. The distributions are approximately exponential above about 5 MeV collected energy, with parameters (CI= 68.27% ) agreed within the uncertainties as listed in table 3.16. The response in run LAN02 ( $4.559 \times 10^{-5} \text{ cm}^2$ ) showed a decrease of 21% in comparison with run LAN11 ( $3.592 \times 10^{-5} \text{ cm}^2$ ) for event collecting above 171.7 keV. This decrease must have been caused by radiation damage.

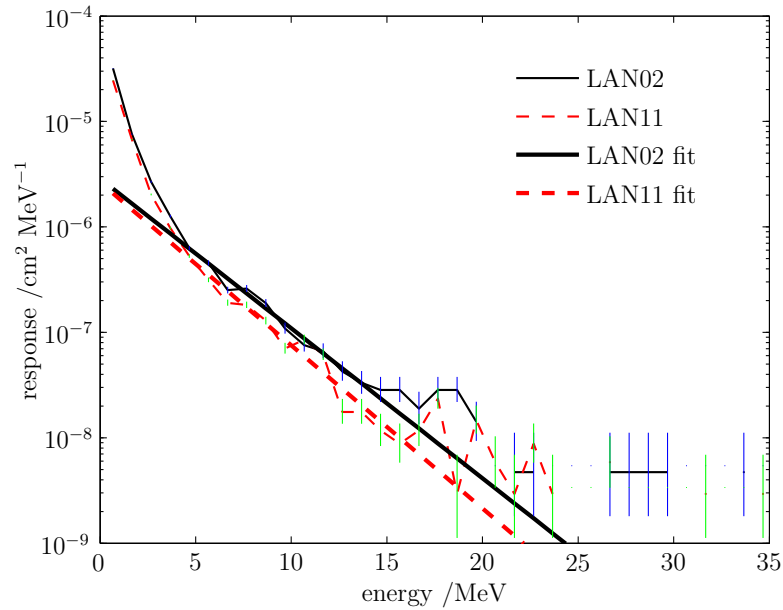


Figure 3.24: Responses of the two example photodiode sensors with neutrons upstream at LANSCE, CI=68.27%.

Table 3.16: Two example pulse height spectra parameters of sensor 11 upstream at LANSCE, CI=68.27%.

Run	decay constant /MeV <sup>-1</sup>
LAN02	0.327±0.022
LAN11	0.356±0.030

### 3.4.2 Effect of the photodiode window

To investigate the effect of neutron interaction with the photodiode window, there were two different photodiode configurations: sensor 5 that used the delidded photodiode (as shown in figure 2.1(c)) and sensor 7 that used the photodiode with window (as shown in figure 2.1(a)). The pulse width of these two sensors was 20  $\mu$ s. Two sensors were irradiated separately either in the beam or about 0.5 m away from the beam without cadmium shielding at TRIUMF in 2008 (in figure 3.25), and their experimental conditions are summarized in table 3.17.

### 3.4 Experimental results

Table 3.17: Experimental conditions of investigating the effect of photodiode window at TRIUMF.

sensor type	durations /s	beam position	neutron fluences, /cm <sup>-2</sup>	neutron fluxes, /cm <sup>-2</sup> s <sup>-1</sup>
delidded photodiode	2151	in beam	$8.78 \times 10^9$	$4.13 \times 10^6$
delidded photodiode	331	0.5 m	$1.36 \times 10^9$	$4.11 \times 10^6$
photodiode with window	622	in beam	$2.54 \times 10^9$	$4.11 \times 10^6$
photodiode with window	316	$\approx 0.5$ m	$1.28 \times 10^9$	$4.05 \times 10^6$



Figure 3.25: Sensors under test at TRIUMF in 2008.

The experimental results are given in table 3.18 for event collecting energy above 91.35 keV. The response in the sensor with window showed an increase of 28% than the other; this increase is also illustrated in figures 3.26 and 3.27. Figure 3.26 shows that the measured pulse height spectra, where the two sensors' responses were similar at low collected energy. The response of the sensor using a photodiode

### 3.4 Experimental results

with a window was higher than that without at in high collected energy.

Table 3.18: Experimental results of investigating the effect of photodiode window at TRIUMF.

Sensor type	position	pulse of events	pulse rates /s <sup>-1</sup>	max energy /MeV	responses, /cm <sup>2</sup>
delidded photodiode	in beam	2114793	983.16	43.83	$2.41 \times 10^{-4}$
delidded photodiode	$\approx 0.5$ m	1098	3.43	7.35	$8.03 \times 10^{-7}$
photodiode with window	in beam	783424	1259.52	41.47	$3.08 \times 10^{-4}$
photodiode with window	$\approx 0.5$ m	1449	4.59	11.8	$1.13 \times 10^{-6}$

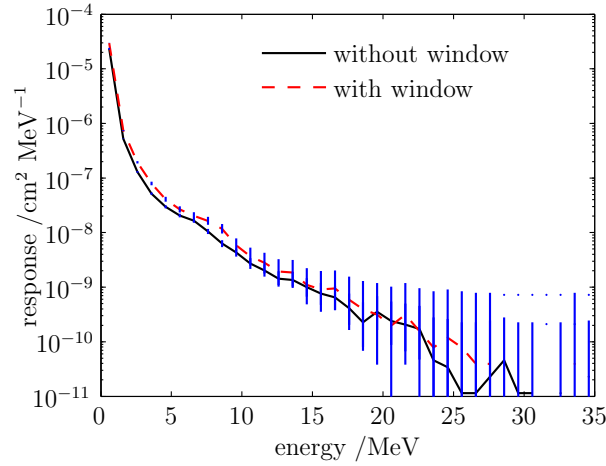


Figure 3.26: Measured pulse height spectra captured by photodiode sensors with or without window at TRIUMF, CI=68.27%.

The measured pulse interval distribution of the sensor with delidded photodiode is less steep than the other as shown in figure 3.27, which indicates that the interaction rate of the sensor that used photodiode with a window was higher than the other. Such results agree with the measured pulse height spectra as shown in figure 3.26.

The measured parameters of pulse height spectra and interval distribution are summarized in table 3.19. The decay constant of pulse height of the sensor with a window was lower than the other, suggesting that the mean collected energy in the sensor with a window was higher than the other. These results are also consistent with the experimental results from two sensors with a scatterer as discussed in §3.4.1.2 (see table 3.10 and figure 3.15(c)). Due to the aluminum scatterer, the

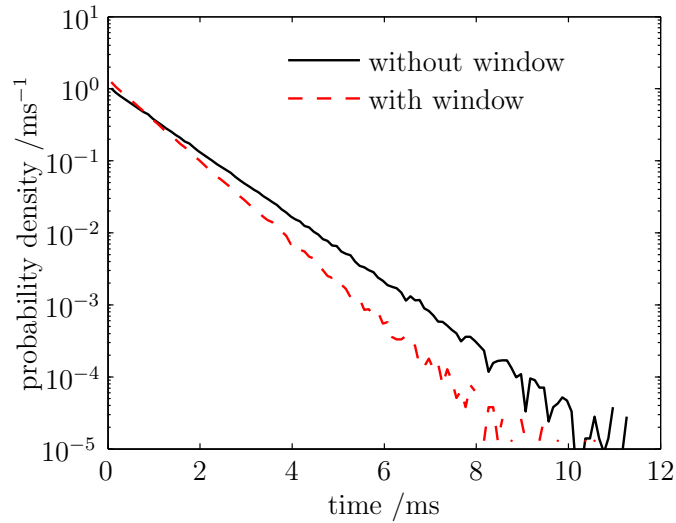


Figure 3.27: Measured pulse interval distributions captured by photodiode sensors with or without window at TRIUMF.

parameters of pulse height spectra in the downstream sensor was lower than the sensor upstream. So the effect of the sensor window was similar to that of the aluminum scatterer, which interacted with neutrons so that second sources were generated and deposited some of their energy in photodiode sensor.

Table 3.19: Measured parameters of pulse height spectra and pulse interval distributions captured by photodiode sensors with or without window at TRIUMF.

sensor type	decay constant /MeV <sup>-1</sup>	pulse rate /s <sup>-1</sup>
delidded photodiode	0.365±0.014	1003.74±1.59
photodiode with window	0.310±0.016	1291.24±2.13

According to the discussion in §3.2, the decay constant of the pulse interval distribution is the interaction rate of event collecting above the threshold energy. The interaction rate of the sensor with window showed an increase of 28.64% more than the other. These results agree with the sensor's response measurements: irradiation with the photodiode sensor with window showed an increase of 28%. The interaction rates depend on three factors: 1) the type of neutron beam irradiated, 2) the neutron flux, and 3) the configuration of the photodiode. Two sensors were irradiated in the same neutron beam; they received similar neutron flux (listed in

table 3.17). The photodiode window interacted with the neutron beam which then led to a higher interaction rate than the other.

The probability of detection for events collecting above 91.35 keV can be determined by the measurements:

$$\begin{aligned}
 P_{pile-up\ window} &= \frac{r}{n} \quad \text{giving} \quad 97.95\% \\
 P_{pile-up\ delidded} &= \frac{r}{n} \quad \text{giving} \quad 97.54\%
 \end{aligned}
 \tag{3.12}$$

where  $P_{pile-up\ window}$  is the probability of detection in the sensor that used photodiode with window, and  $P_{pile-up\ delidded}$  is the other,  $r$  is the detection rate, and  $n$  is the interaction rate, which equals the decay constant of the pulse interval distribution. As discussed in §2.4.1, the probability of detection can also be modified by the rate of detected events and the sensor pulse width:

$$\begin{aligned}
 P_{pile-up\ window} &= 1 - r\tau \quad \text{giving} \quad 98.03\% \\
 P_{pile-up\ delidded} &= 1 - r\tau \quad \text{giving} \quad 97.48\%
 \end{aligned}
 \tag{3.13}$$

where  $\tau$  is the sensor pulse width. So the methods of probability of detection with the effect of the pile-up agree well.

When the sensors were about 0.5 m away from the neutron beam, a number of pulse events were also generated in the photodiode sensors as shown in figure 3.28, which displays the measured pulse height spectra in this condition. These collected events would be due to the beam scattering or the generation of secondary particles by the neutron beam interaction with the facility's equipment. The response of the sensor that used the photodiode with window also showed an increase of 28.27% as listed in table 3.18.

The decay constant of TRIUMF ( $0.365 \pm 0.014$ ) is slightly higher than the LANSCE ( $0.321 \pm 0.015$ ), indicating that the average collected energy from TRIUMF between

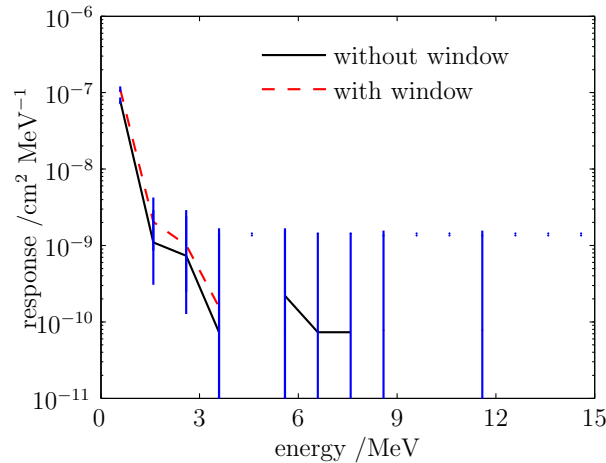


Figure 3.28: Effect of photodiode window on measured pulse height spectra captured about 0.5 m away from beam at TRIUMF, CI=68.27%.

5 MeV and 14 MeV is slightly lower than that from LANSCE. The photodiode response measured at TRIUMF ( $2.41 \times 10^{-4} \text{ cm}^2$  with 91.35 keV minimum collected energy) is much higher at LANSCE ( $4.559 \times 10^{-5} \text{ cm}^2$  with 171.7 keV minimum collected energy). These differences will be discussed in §4.3.

#### 3.4.3 Effect of neutron interactions in the amplifier circuit

To investigate the effect of neutron interactions in the amplifier circuit, sensors 1, 2 and 3 were irradiated at TRIUMF<sup>1</sup>. The pulse shape of these sensors is the same as shown in figure 2.5(a); their amplifier design was not optimised. There were two different circuit configurations: one with the photodiode and preamplifier collocated, and the other with them separated. It was thus possible to irradiate the detector and amplifier separately or together. The measurements of sensors 1, 2 and 3 were made at TRIUMF with the preamplifier immediately adjacent to the photodiode, and therefore with both components in the neutron beam, which showed an increase in the count rate. The experimental results were published in *Transactions on Nuclear Science* [115] ( Appendix F).

<sup>1</sup>These experiments were conducted on behalf of the author by Mr. R. H. Edwards and Mr. C. Allabush of Goodrich Engine Control and Electrical Power Systems, Birmingham.

### 3.4 Experimental results

To further investigate the effect of the amplifier, sensor 8 was irradiated at TRIUMF in 2008. The experiment was first made with the amplifier being tested alone, and then the photodiode was added to the circuit. The experimental conditions and results are summarized in table 3.20.

Table 3.20: Experimental conditions for the photodiode detector and amplifier irradiated separately at TRIUMF.

component exposed	durations /s	neutron fluences, /n.cm <sup>-2</sup>	fluxes /n.cm <sup>2</sup> <sup>-1</sup> s <sup>-1</sup>
amplifier	618	$2.43 \times 10^9$	$3.93 \times 10^6$
photodiode	607	$2.29 \times 10^9$	$3.77 \times 10^6$

The experimental results are summarized in table 3.21 with the pulse events above the collected energy 148.1 keV. The response with the amplifier alone is about 4% with the photodiode alone. These results are also illustrated in figure 3.29, which shows the pulse height spectra.

Table 3.21: Experimental conditions and results for the photodiode detector and amplifier irradiated separately at TRIUMF.

component exposed	pulse of events	pulse rates /s <sup>-1</sup>	max energy /MeV	responses /cm <sup>2</sup>
amplifier	15895	25.72	18.32	$6.55 \times 10^{-6}$
photodiode	395010	650.75	40.35	$1.72 \times 10^{-4}$

#### 3.4.4 Effect of the thermal neutron interaction with sensors

To investigate the effect of the thermal neutron interaction with the photodiode, sensor 1 was irradiated with and without cadmium shielding at TRIUMF in 2007. The measured pulse height spectra and interval distribution without shielding are shown in figures 3.1 and 3.2 respectively. The measured pulse height spectra show a local maximum between 1 MeV and 2 MeV. This peak is attributed to thermal neutron interactions on <sup>10</sup>B present as dopants in the photodiode. Cadmium shielding was found to suppress this peak, albeit not completely as shown in figure 3.30.

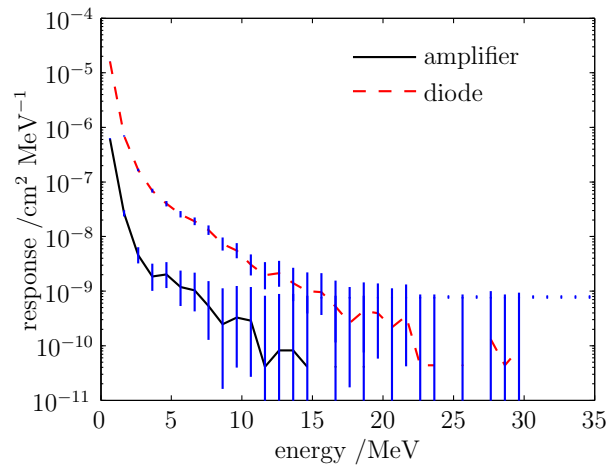


Figure 3.29: The measured pulse height spectra for the photodiode detector and amplifier irradiated separately at TRIUMF, CI=68.27%.

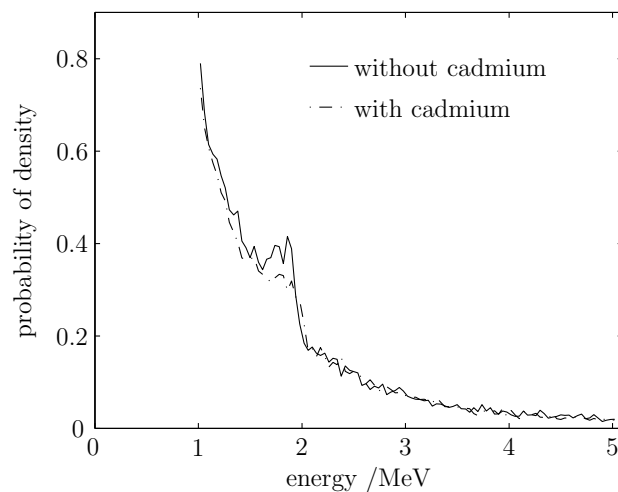


Figure 3.30: Pulse height spectra showing the influence of thermal neutrons at TRIUMF and its reduction by cadmium shielding.

#### 3.4.5 Effect of the photodiode doping profile

Sensors 9 and 10 were irradiated at ASP with 3 MeV and 14 MeV monoenergetic neutron beams in November 2009. Their calculated amplifier gain is  $18.9 \text{ mV} \cdot \text{MeV}^{-1}$ . The 3 MeV neutron beam experimental conditions are summarized in table 3.22. The measured pulse height spectra are shown in figure 3.31. At ASP, the neutron fluence data were directly provided by the neutron facility.

Table 3.22: Experimental conditions at ASP 3 MeV neutron beam.

sensor	duration, /s	fluences, /n.cm <sup>-2</sup>	flux, /n.cm <sup>2-1</sup> s <sup>-1</sup>
9	303	$6.03 \times 10^9$	$1.99 \times 10^7$
10	300	$5.85 \times 10^9$	$1.95 \times 10^5$

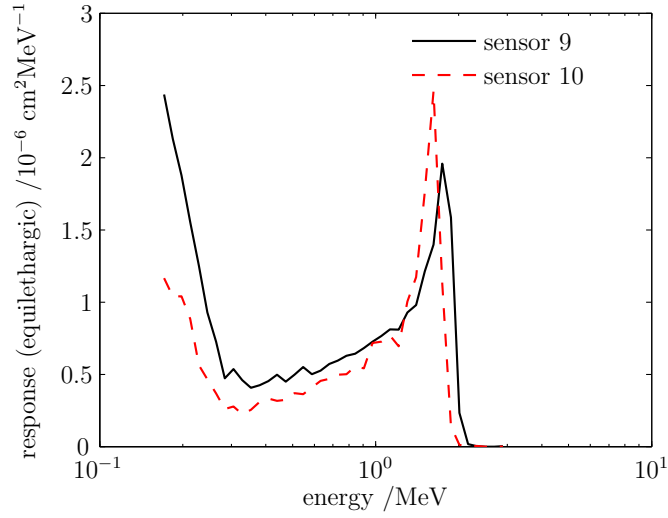


Figure 3.31: Measured pulse height spectra captured at ASP 3 MeV monoenergetic beam.

There are local maxima between 1 MeV and 2 MeV. The peaks in collected energies (1.6 and 1.79 MeV respectively) are not the same. This is because the two sensors' amplifier gains are calculated, while the principal uncertainty of this calculation is in the value of the preamplifier feedback capacitor ( $2.2 \pm 0.25$  pF), and is about 11.4% in the deposited energy.

In order to normalize the pulse height spectra to have the same peak energy, assuming the peak collected voltages in sensor 9 to be  $V_9$ , which was 30.15 mV, and sensor 10 to be  $V_{10}$ , which was 33.9 mV, then the peaks in each run appear at the same energy to be  $E$ , which can be modified by:

$$E = \frac{V_9 + V_{10}}{2A} \quad (3.14)$$

### 3.4 Experimental results

where  $A$  is the calculated amplifier gain in the two sensors. The two sensors should have different gains, assuming sensor 9 to be  $A_9$ , and sensor 10 to be  $A_{10}$ , they are:

$$A_9 = \frac{V_9}{E} \quad (3.15)$$

$$A_{10} = \frac{V_{10}}{E} \quad (3.16)$$

where  $E$  is defined in equation 3.14, so:

$$A_9 = \frac{2V_9}{V_9 + V_{10}}A = 17.79\text{mV} \cdot \text{MeV}^{-1}$$

$$A_{10} = \frac{2V_{10}}{V_9 + V_{10}}A = 20.01\text{mV} \cdot \text{MeV}^{-1}$$

The experimental results by using normalized gain are summarized table 3.23 for events above the collected energy 155.5 keV; the pulse height spectra are shown in figure 3.32, and the pulse interval distribution are shown in figure 3.33.

Table 3.23: Experimental results captured at ASP 3 MeV neutron beam.

sensor	max. energy /MeV	pulse of events	peak energy /MeV	detection rate, /s <sup>-1</sup>	response, /cm <sup>2</sup>
9	2.56	10 515	1.60	37.68	$1.74 \times 10^{-6}$
10	2.78	13 694	1.79	45.65	$2.34 \times 10^{-6}$

The peak of sensor 10 captured is higher than sensor 9, whereas at low collected energies the response in sensor 9 is much higher than sensor 10. According to the Centronic photodiode datasheets [110], the photodiode junction region is produced by either diffusion or ion implantation of boron into selected areas of the surface of a high resistivity n-type silicon wafer. The pulse height spectra suggest that the doping profiles of sensors 9 and 10 may be different<sup>1</sup>.

<sup>1</sup>The photodiode sensors were not controlled for doping profile.

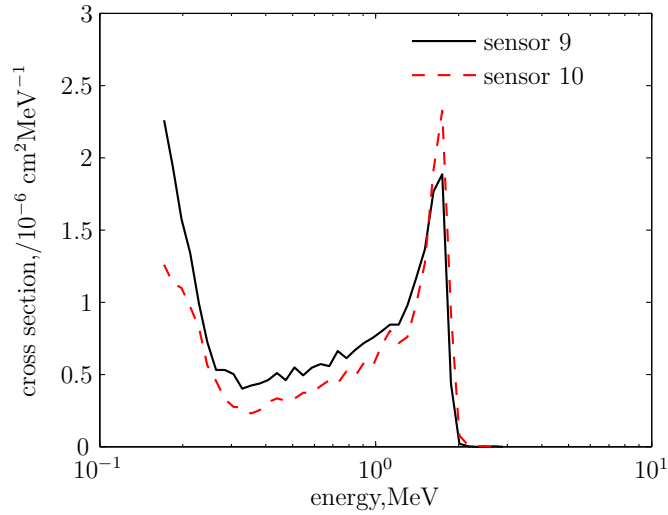


Figure 3.32: Measured pulse height spectra captured at ASP 3 MeV monoenergetic beam with normalized amplifier gains.

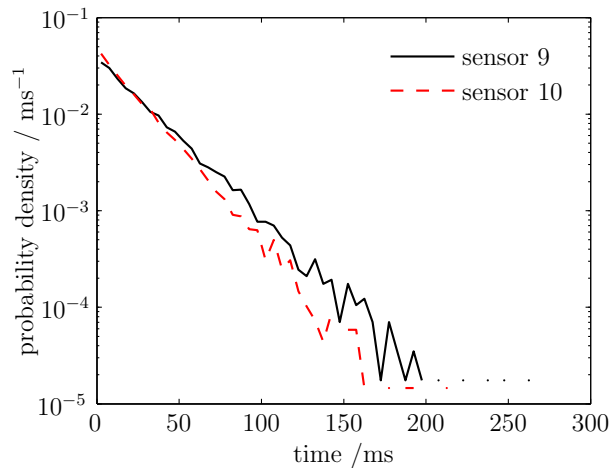


Figure 3.33: Measured pulse interval distributions captured at ASP 3 MeV monoenergetic beam.

The 14 MeV neutron beam experimental conditions are summarized in table 3.24 and results are summarized in table 3.25 for the events above 200 keV collected energy by using the normalized amplifier gain. The measured pulse height spectra are shown in figure 3.34 and interval distribution is shown in figure 3.35, where the pulse interval distribution in sensor 10 is much steeper than the other. This is because sensor 10 received higher neutron flux than sensor 9.

### 3.4 Experimental results

Table 3.24: Experimental conditions and results at ASP 14 MeV neutron beam.

sensor	duration, /s	fluence /n.cm <sup>-2</sup>	flux /n.cm <sup>2-1</sup> s <sup>-1</sup>
9	301	$5.84 \times 10^8$	$1.94 \times 10^6$
10	302	$6.86 \times 10^9$	$2.27 \times 10^7$

Table 3.25: Experimental conditions and results at ASP 14 MeV neutron beam.

sensor	max. energy /MeV	pulse of events	detection rate, /s <sup>-1</sup>	response, /cm <sup>2</sup>
9	9.13	10 509	54.85	$2.82 \times 10^{-5}$
10	11.7	125 763	416.43	$1.83 \times 10^{-5}$

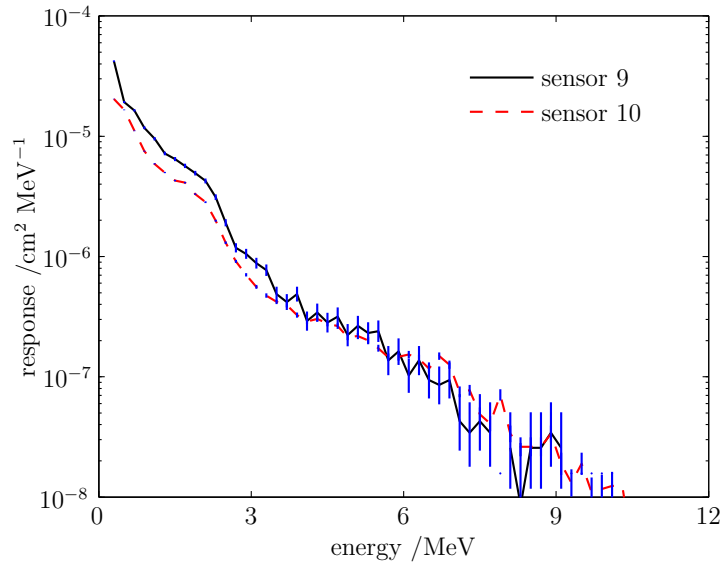


Figure 3.34: Measured pulse height spectra captured at ASP 14 MeV monoenergetic beam, CI=68.27%.

The response in sensor 9 is much higher than sensor 10, especially in low collected energies. Figure 3.36 shows response ratios of sensors 10 and 9 in variation of threshold collected energy. It can be seen that when the collected energy is below about 4 MeV, the response in sensor 9 has more weight than the other. In contrast, the response in sensor 10 is much higher than sensor 9 in high collected energy, because the two sensors have two different doping profiles.

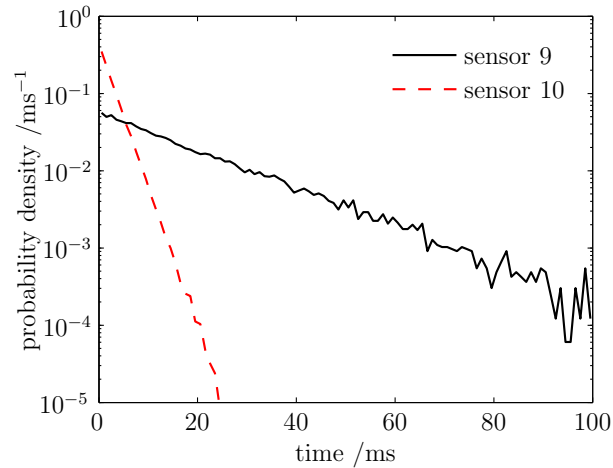


Figure 3.35: Measured pulse interval distribution captured at ASP 14 MeV monoenergetic beam.

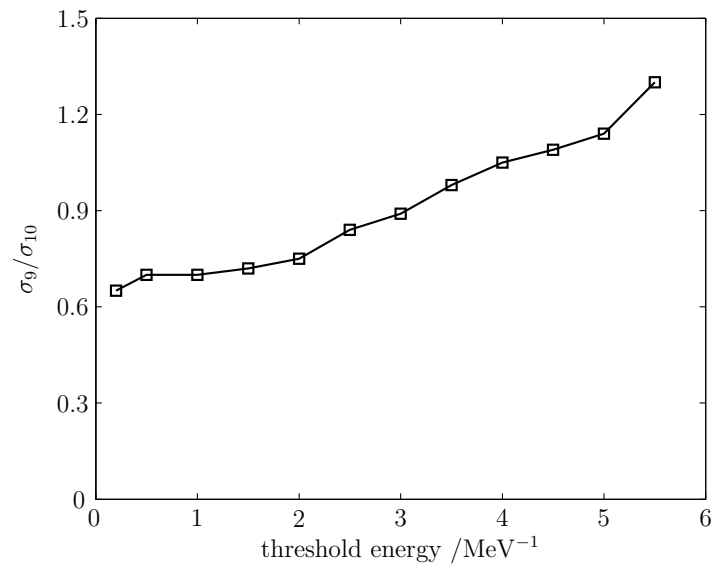


Figure 3.36: Response ratios of sensors 10 and 9 at ASP 14 MeV monoenergetic beam.

Because the interaction of the photodiode sensors with neutrons is a Poisson process, there is always a possibility of pile-up, and the pile-up rate increases with the increase of the interaction rate. However, in the case of the interaction rate is less than  $500 \text{ s}^{-1}$  and the sensor pulse width at  $40 \mu\text{s}$ , the pile-up is not significant (see §4.4.1 for further discussion).

### 3.4.6 Effect of the sensor pulse width

To investigate the probability of detection with different sensor pulse widths, there were two different circuit configurations: sensor 7 with pulse width of  $20\ \mu\text{s}$  and sensor 8 with pulse width of  $40\ \mu\text{s}$ . These two sensors were irradiated at TRIUMF in 2008. The experimental conditions and results are summarized in table 3.26. The measured pulse height spectra are shown in figure 3.27 and the measured pulse interval distributions are shown in figure 3.38 for events collecting above  $148.1\ \text{keV}$ .

Table 3.26: Experimental conditions and results of two sensors in different pulse widths irradiated at TRIUMF.

Sensor width, $\mu\text{s}$	duration /s	fluence $/\text{n.cm}^{-2}$	flux $/\text{n.cm}^{-2}\text{s}^{-1}$	pulse of events	pulse rate $/\text{s}^{-1}$	max energy /MeV	response $/\text{cm}^2$
20	622	$2.54 \times 10^9$	$4.11 \times 10^6$	469 622	755.02	41.47	$1.85 \times 10^{-4}$
40	607	$2.29 \times 10^9$	$3.77 \times 10^6$	395 010	650.75	40.35	$1.72 \times 10^{-4}$

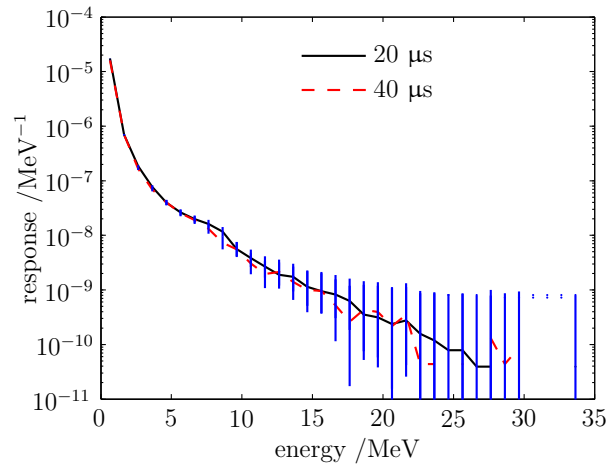


Figure 3.37: Measured pulse height spectra for sensors with different pulse widths irradiated at TRIUMF, CI=68.27%.

The measured parameters of pulse height spectra are similar as listed in table 3.27, where the decay constant of pulse interval distribution in sensor with  $20\ \mu\text{s}$  is higher than the other, this is because the sensor with  $20\ \mu\text{s}$  width received a higher average

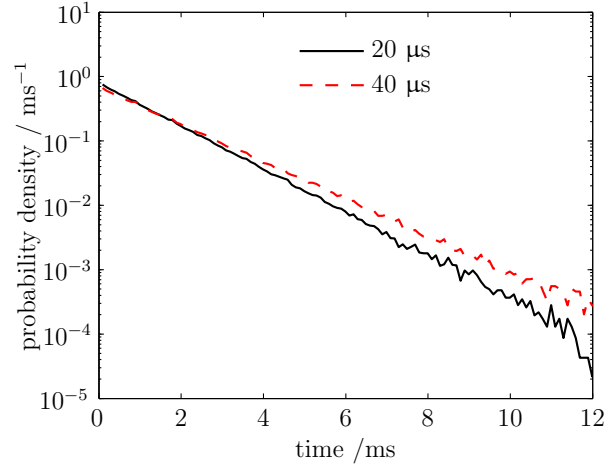


Figure 3.38: Measured pulse interval distributions for sensors with different pulse widths irradiated at TRIUMF.

neutron flux ( $4.11 \times 10^6 \text{cm}^{-2}\text{s}^{-1}$ ) than the other ( $3.71 \times 10^6 \text{cm}^{-2}\text{s}^{-1}$ ). The higher neutron flux led to a higher interaction rate between the sensor and neutrons.

Table 3.27: Measured parameters of pulse height spectra and interval distributions captured by sensors with different pulse widths at TRIUMF.

sensor width	decay constant /MeV <sup>-1</sup>	interaction rate /s <sup>-1</sup>
20 μs	$0.310 \pm 0.032$	$766.37 \pm 2.74$
40 μs	$0.310 \pm 0.016$	$666.21 \pm 3.59$

As discussed in §2.4.1, the probability of detection in two sensors are:

$$P_{20 \mu\text{s}} = \frac{r}{n} \text{ giving } 98.52\%$$

$$P_{40 \mu\text{s}} = \frac{r}{n} \text{ giving } 97.68\%$$

or

$$P_{20 \mu\text{s}} = 1 - r\tau \text{ giving } 98.49\%$$

$$P_{40 \mu\text{s}} = 1 - r\tau \text{ giving } 97.40\%$$

where  $\tau$  is the sensor pulse width,  $n$  is the interaction rate (the decay constant of pulse interval distribution) and  $r$  is the detection rate (pulse event rate). The probability of detection computed using two different equations agree very well. According to the calculation presented in §2.4.6, the probability of detection decreases with the increase of the interaction rate. However the probability of detection at a higher detection rate (in the sensor with 20  $\mu\text{s}$ ) is higher than the other, because these two sensors have different pulse widths. At the similar interaction rate, the probability of detection from the narrower sensor will be higher than the wider sensor.

### 3.4.7 Effect of neutron activation and test results at TSL

Photodiode sensor 1 was tested at TSL as shown in figure 3.39 in April 2007 using several beam configurations: quasi-monoenergetic neutron beams with peak energies near 50 MeV, 110 MeV and 180 MeV, and ANITA. The experiments were made downstream of several other experiments, where the beam was severely degraded. Figure 2.6 shows example 1 s voltage time series captured in each of the neutron beams studied here. These experiments were a preliminary study about this monitor application; these pulse events data included the DC level and 50 Hz external electrostatics<sup>1</sup>. The false alarm pulse rate was unknown.

Figure 3.40 shows the measured pulse height spectra. The weight in low collected energy captured at 50 MeV and 110 MeV neutron beams were more than ANITA. The exponential fits of pulse height distribution above about 5 MeV collected energy are listed in table 3.42. The decay constant captured at 110 MeV neutron beam was higher than ANITA and lower than 50 MeV. It indicates that the number of collected high energy events captured at 110 MeV was greater than 50 MeV and smaller than ANITA.

Immediately after an irradiation at ANITA for about 9 h, the monitor system still

---

<sup>1</sup>DC level and external electrostatics noise are removed by later signal-processing, and the matched filter techniques were not used in these data.

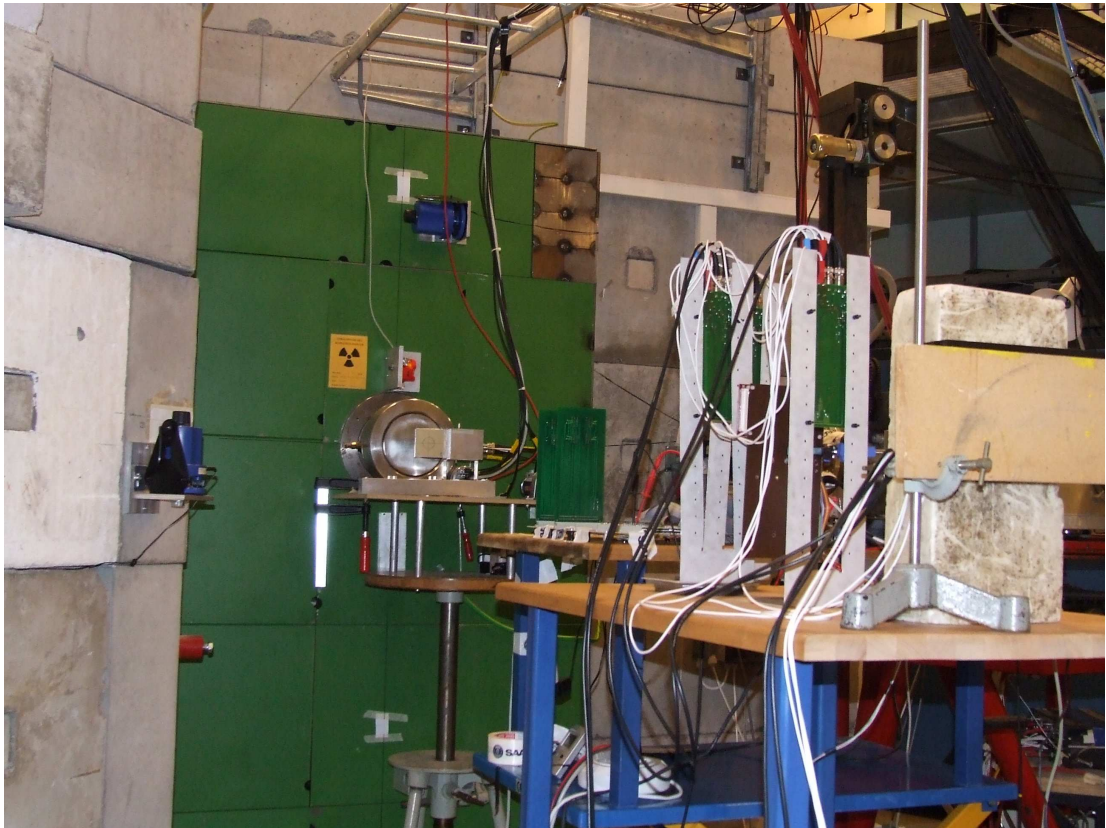


Figure 3.39: Sensors 1, 2 and 3 under test at TSL in 2007.

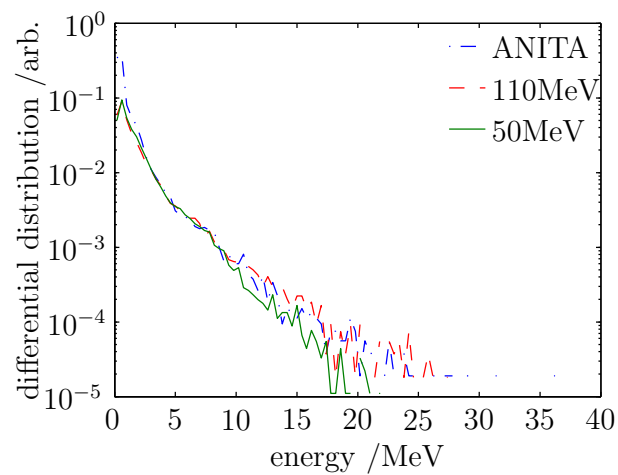


Figure 3.40: Measured pulse height spectra captured at TSL.

captured 34 450<sup>1</sup> pulses over a period of 7 h. 10 pulse events collected energy around

<sup>1</sup>As the pulse events data included the DC level and 50 Hz external electrostatics, some small pulse events may be false

Table 3.28: Measured pulse height spectra parameters at TSL.

neutron	max. energy decay constant	
	MeV	MeV <sup>-1</sup>
TSL2007 ANITA	36.11	0.297±0.015
110 MeV	27.3	0.304±0.013
50 MeV	21.8	0.350±0.014

665.6 keV, one pulse events collected was 1065.72 keV and others collected energy around 400 keV. Figure 3.41 shows the measured pulse height spectrum.

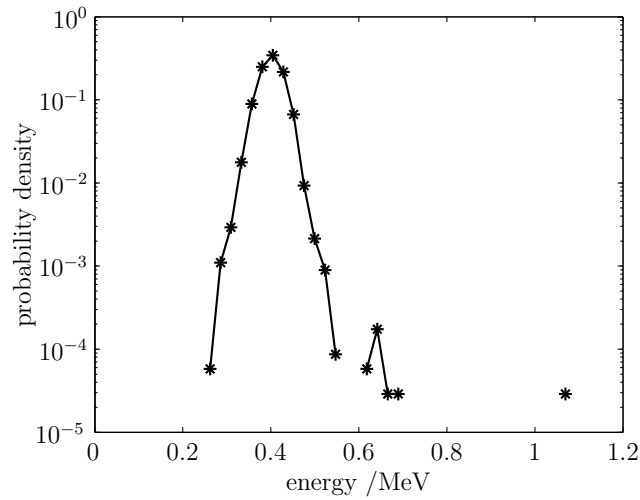


Figure 3.41: Pulse height spectra due to neutron activation of gold in the photodiode.

The pulse height spectrum in figure 3.41 is characteristic of  $\gamma$  radiation generated by the neutron activation of gold. When  $^{197}\text{Au}$  captures a neutron, it forms unstable  $^{198}\text{Au}$ , then:



Gold is present in the device forming the anode and its bond wire and as plating on the interior surfaces and terminal leads of the TO-18 package.  $^{198}\text{Au}$  decays to  $^{198}\text{Hg}$  with the emission of  $\gamma$  rays with energies 411.8 keV (emission probability

### 3.4 Experimental results

---

0.9554), 675.9 keV (emission probability 0.00806) and 1087.7 keV (emission probability 0.00159) [120]. To investigate further the likelihood of this explanation, an estimation of the mass of gold required to achieve the observed rate was undertaken.

The mass of gold can be estimated using neutron activation analysis techniques [121]:

$$m = \frac{N_\gamma \lambda M}{f I_\gamma \epsilon_\gamma N_A (\sigma \phi_{th} + I_{res} \phi_{epi}) B} \quad (3.18)$$

The parameter  $B$  accounts for the characteristic times of the neutron activation measurement:

$$B = (1 - \exp^{-\lambda t_a}) \exp^{-\lambda t_{decay}} (1 - \exp^{-\lambda t_m}) \quad (3.19)$$

where

- $\lambda = \ln 2/T_{\frac{1}{2}}$ , is the decay constant  $2.98 \times 10^{-6}$  /s.
- $t_a$  is the irradiation time, estimated to be 43 200 s.
- $t_0$  is the time between the end of the irradiation and the beginning of the observation (0 s)
- $t_m$  is the measurement duration, 34 200 s.

Giving  $B \approx 0.012$ .

The other parameters are:

- $f$  is the isotopic abundance of the target nuclide,  $^{197}\text{Au}$ , taken to be 100%.
- $I_\gamma$  is the branching ratio of the 411 keV  $\gamma$  ray, taken to be 95.54% [120].
- $M$  is the atomic weight of gold,  $197 \cdot \text{g/mol}$ .
- $N_A$  is Avogadro's number,  $6.022 \times 10^{23}$  /mol

- $\sigma$  is the thermal activation cross-section,  $9.88 \times 10^{-23} \text{ cm}^2$  [122].
- $N_\gamma$  is the number of collected pulse events around 411 keV, which is  $3 \times 10^4$ .
- $\epsilon_\gamma$  is the detection efficiency of the detector, estimated by the depth of the PN photodiode based on the pure silicon in depletion region, which is estimated from photodiode geometry and typical capacitance.
- $\phi_{th}$  is the thermal neutron flux.
- $\phi_{epi}$  is the epithermal neutron flux.
- $I_{res}$  is the neutron resonance integral.

Of these parameters, the detection efficiency, and neutron fluxes are the most uncertain.

Considering thermal neutrons first, Cheminet et al. [123] made measurements of the neutron field at TSL ANITA and determined a thermal flux around 12% of that above 10 MeV. The flux above 10 MeV is typically around  $1 \times 10^6 \text{ cm}^{-2}\text{s}^{-1}$ , leading to an estimated thermal neutron flux of  $1.2 \times 10^5 \text{ cm}^{-2}\text{s}^{-1}$ .

On these assumptions, the mass of gold could be estimated as:

$$m = \frac{N_\gamma \lambda M}{f I_\gamma \epsilon_\gamma N_A (\sigma \phi_{th}) B}$$

giving  $m \approx 23 \text{ mg}$ . This seems to be an implausibly large amount of gold. There are two reasons for this. Firstly, the current gold price is approximately £33/g, which implies a cost of gold plating of £0.75 per device. Secondly, assuming that the thickness of a typical gold plating does not exceed  $3 \mu\text{m}$ , and the density does not go beyond  $19.3 \text{ g/cm}^3$ , a gold-plated surface area of approximately  $4 \text{ cm}^2$  would be expected. The internal surface area of the TO-18 package is about  $0.5 \text{ cm}^2$ . So it seems as though the first estimate of 23 mg is high. However, there are large uncertainties on parameters used to estimate the mass, and these are sufficient not to exclude the possibility of gold activation, for example:

- The detection efficiency of the detector is estimated.
- The thermal neutron flux is estimated on the basis of Cheminet's work in 2011 while the photodiode used in the present work was measured in 2007. Note that before Cheminet's work, the lab was slightly reconfigured.
- The epithermal flux is not considered, which may perhaps have contributed more to activation than the thermal neutron flux.
- Fast neutrons may also have made a contribution.

The spectral and temporal characteristics of the pulses shown in figure 3.41 are consistent with the activation of gold known to be present in the detector assemble, and the uncertainty in system parameters are such that an approximate neutron activation analysis does not exclude this likelihood. Hands et al. [76] reported that low-energy channels in a large PIN diode detector irradiated at TSL ANITA were dominated by gamma events from induced activity in the beam hall and in the detector head itself [124].

In summary, the pulse events shown in figure 3.41 could have been generated by the neutron activation on gold and/or the induced activity from the facility.

### 3.4.8 TSL ANITA testing in 2010

Sensor 9 was irradiated at TSL ANITA in June 2009. The ANITA neutron beam frequency was 160 Hz, and its macropulse length was about 500  $\mu$ s. The sensor was at the standard user position of 2.5 m from the ANITA target. Example time series data are shown in figure. 2.7 on page 40.

The duration of this experiment was 72 s, and the neutron fluence received by sensor 9 was estimated to be  $8.351 \times 10^7$  n.cm<sup>-2</sup>. In that duration, 27 945 pulse events were captured with the events collecting energy above 146.9 keV. Figure 3.42 shows the measured pulse height spectra, where the maximum collected energy is 31.9 MeV

and the decay constant above 5 MeV is  $0.303 \pm 0.017$  (CI=68.27%), agreeing with the experimental decay constant  $0.297 \pm 0.030$  measured in 2007. The response is  $3.34 \times 10^{-4} \text{cm}^2$ .

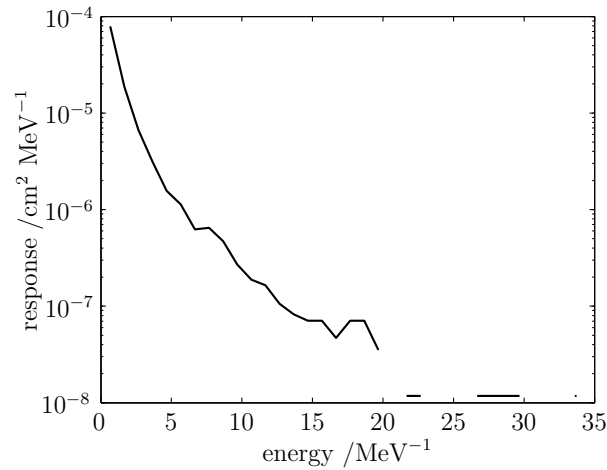


Figure 3.42: Measured pulse height captured at TSL pulsed ANITA.

Figure 3.43 shows the measured pulse interval distributions, which reflect the pulsed beam characteristics. The first peak width is 0.749 ms, and the number of pulse events of this peak is 16 362. This indicates that a large number of pulses above one event generated by the photodiode with the one pulsed neutron beam. The second peak width is 1.648 ms and its peak time is 6.15 ms, which is close to the macropulse neutron beam interval. The number of pulse events in the second peak is 10 800. The third peak width is 1.498 ms, and its peak time is 12.45 ms.

The TSL ANITA beam flux during the experiment was about  $1.16 \times 10^6 \text{cm}^{-2}\text{s}^{-1}$ , which was lower than typical flux ( $4.0 \times 10^6 \text{cm}^{-2}\text{s}^{-1}$ ) at TRIUMF. But the fluence received by the sensor during each neutron pulse was very high, so the pile-up effect was more likely to happen at TSL ANITA than any other neutron facilities currently in use for SEE testing.

As the TSL ANITA is a pulsed neutron beam, the pile-up only occurs in the first peak of the interval distribution as shown in figure 3.43. The number of pulse events in the first peak was 16 362, the detection rate per neutron pulse<sup>1</sup> was about

<sup>1</sup>The method to determine this rate will be presented in §4.4.2.

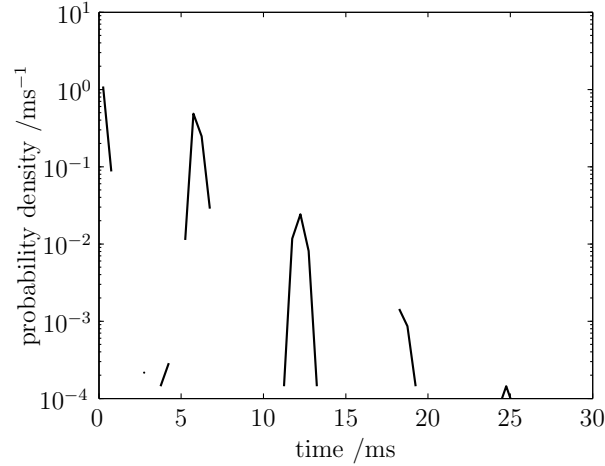


Figure 3.43: Measured pulse interval distributions at TSL pulsed ANITA.

$2841 \text{ s}^{-1}$ . As discussed in §2.4.1 and equation 2.11, the probability of pile-up can be estimated by:

$$P_{pile-up} = r\tau$$

giving 11.36%. The average number of detected pulses per macropulse was about 2.425. Considering the effect of the pile-up, the interaction rate per macropulse was about 2.70. As the interaction between sensors and neutrons is a Poisson process, the possibility of the number of events per macropulse can be determined by using MATLAB function ‘poisscdf’ as summarized in table 3.29.

Table 3.29: Possibilities for various numbers of events per macropulse measured at TSL ANITA.

events number	possibility
0	0.0672
1	0.2052
above 1	0.7276

The total events in this experiment was 27 945, of which the number of events in the first peak was 16 362; the number of events in the second peak was 10 800; and

the number of events in the third and fourth was 783, meaning that there were 783 neutron macropulses in which no pulse events were generated.

The duration of this experiment was 72 s, and the total number of neutron macropulses was 11 520. Based on the possibility for the number of events per macropulse as summarized in table 3.29, there were  $774 \pm 27.82$  (at CI=68.27%) neutron macropulses that had no pulse events generated, and there were  $10\,746 \pm 104$  (at CI=68.27%) neutron macropulses that had pulse events generated. These experimental and analysis results are consistent.

The TSL ANITA beam flux during the experiment was about  $1.16 \times 10^6 \text{ cm}^{-2}\text{s}^{-1}$ , and the pile-up rate was about 11.36%. This pile-up rate must be taken into account in determining the transmission during multiple-experiments at TSL using pulsed neutrons, and these will be discussed in §4.4.1.

## 3.5 Conclusion

This chapter has described the experimental results captured from LANSCE, TRIUMF, ASP and TSL.

The measured pulse interval distributions captured at LANSCE and pulsed TSL ANITA demonstrate that the effect of the neutron beam time structure is clearly visible. The method to determine the neutron beam transmission has been investigated through the experimental results captured at LANSCE. The experimental results from LANSCE have been found to be consistent with measurements and simulations made previously [54]. Photodiode sensors can determine the transmission along the neutron beam during multiple-experiment SEE testing.

The amplifier circuit irradiated with neutron beam alone could increase the rate of detecting pulses by about 4%. The photodiode with window interacting with neutron beam could increase of the interaction rate by about 28%. The narrower sensor pulse width will lead to a higher probability of detection. The experiments with

and without cadmium shielding demonstrated that the sensor is slightly sensitive to thermal neutrons.

The results from ASP irradiation proved that the rate of detecting pulses is different from two kinds of photodiode doping profiles. The experimental results captured from TSL quasi-monoenergetic suggests that the package of the photodiode might contain gold, which could cause the low deposited events on the photodiode sensor. However, the characteristic pulse energy and temporal behavior of these low events ensure that they can be easily identified and excluded.

The measurement experiment made at TSL ANITA shows that the probability of pile-up was about 11.36% when the neutron flux approximated to  $1.1 \times 10^6 \text{cm}^{-2}\text{s}^{-1}$ .

The next chapter will evaluate the beam monitoring system and recommend the testing protocols at each facility.

# Chapter 4

## System evaluation and testing protocols

### 4.1 Introduction

This chapter evaluates the photodiode beam monitor and discusses the testing protocols using various neutron facilities. First, it will discuss the absorbed fraction of the gamma rays interacting with the photodiode sensor. Following from that is a discussion of the experimental results. The potential causes of the pulse height spectra taking more of a power form at deposited energies below about 5 MeV will be analyzed. The uncertainties in these measurements will be discussed, and the response ratios of the LANSCE and TRIUMF measurement results will be evaluated with energies collected at various thresholds.

Next, beam monitoring testing protocols will be investigated. The pile-up of pulse events is a potential source of errors. The relationship between the probability of pile-up and interaction rates will be discussed. Then, based on the experimental results captured from LANSCE and TSL, testing protocols for use at each facility will be recommended. The procedure of using the beam monitoring system at ISIS ChipIr will also be predicted.

Finally, the theoretical and experimental studies of determining pulse height and

counting system will be discussed. The optimum sensor design for a particular test condition will be analyzed. A possible method for determining the sensor's testing life and calibration will be introduced.

## 4.2 The effect of gamma-ray background at neutron facilities

The photodiode's active area is estimated to be  $2.92 \text{ mm}^2$ , and its active (depletion) depth is estimated from geometry and typical capacitance to be about  $43 \mu\text{m}$  (see §2.2).

In passing through a medium, the interaction mechanisms that for a  $\gamma$ -ray to lose energy are: Photoelectric effect, Compton effect and Pair production. Figure 4.1 provides a guide to the relative importance of these three interactions over a wide range of gamma energy  $h\nu$  and atomic number  $Z$  of the attenuating material. The line at the left represents the energy at which Photoelectric absorption and Compton scattering are equally probable as a function of the absorber's atomic number. The line at the right represents the energy at which Compton scattering and Pair production are equally probable [61].

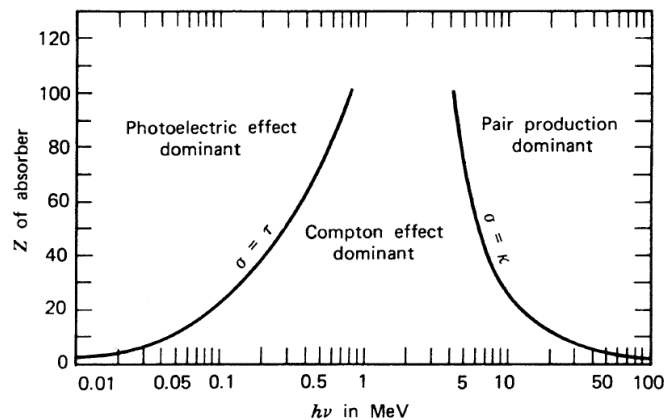


Figure 4.1: Relative importance of the three types of gamma-ray interactions vs. energy and atomic number  $Z$  of the absorber, after Knoll [61].

The atomic number of silicon is 14. When the gamma rays' energy is less than

## 4.2 The effect of gamma-ray background at neutron facilities

---

60 keV, the process by which they interact with the photodiode is dominated by the Photoelectric effect as shown in figure 4.1; and the gamma rays deposit their total energy in a single interaction with an absorber atom. However this deposited energy is too small to be detected by the photodiode sensor. Compton effect is main the absorption mechanism for gamma rays in the energy range 60 keV to 10 MeV. If  $\gamma$ -ray energies exceed 1.02 MeV, it may interact by a process called Pair production, which becomes important as an absorption mechanism at energies over 10 MeV.

The fraction of gamma rays interacting with the medium when traveling a distance  $x$  is [125]:

$$f = 1 - \exp^{-\mu x} \quad (4.1)$$

where  $\mu$  is the linear absorption coefficient, expressed as  $\text{cm}^{-1}$ .  $-\mu/\rho$  ( $\rho$  is the density of the material) is the mass attenuation coefficient, which depends on  $\gamma$ -ray energy and on the material as well as the atomic number ( $Z$ ) and density  $\rho$  of the material. The values of  $-\mu/\rho$  from 1 keV to 20 MeV are available at the web site [126] of the US National Institute of Standards and Technology. Values of the mass attenuation coefficient as a function of photon energy for silicon are shown in figure 4.2.

Based on equation 4.1, and the depth of the photodiode ( $43 \mu\text{m}$ ), the fraction of gamma rays absorbed by the photodiode sensor can be estimated and shown in figure 4.3.

As the attenuation coefficient decreases rapidly with the increase in gamma ray energy as shown in figure 4.2, the fraction of gamma rays absorbed by the photodiode sensor decreases significantly with the increase of gamma energy as shown in figure 4.3. Some example data are given in table 4.1.

High-energy neutron beams such as LANSCE/WNR and TSL ANITA are generated by protons striking a tungsten target. TSL's quasi-monoenergetic neutron beams

## 4.2 The effect of gamma-ray background at neutron facilities

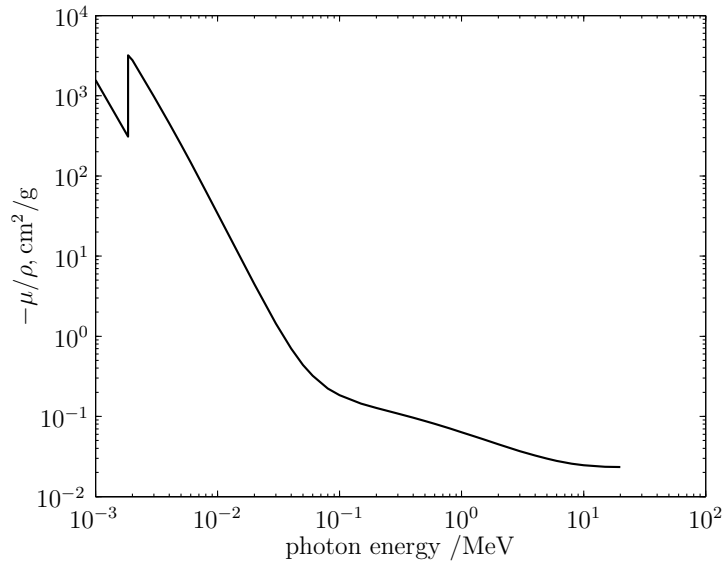


Figure 4.2: Values of the mass attenuation coefficient in silicon as a function of photon energy, after [126].

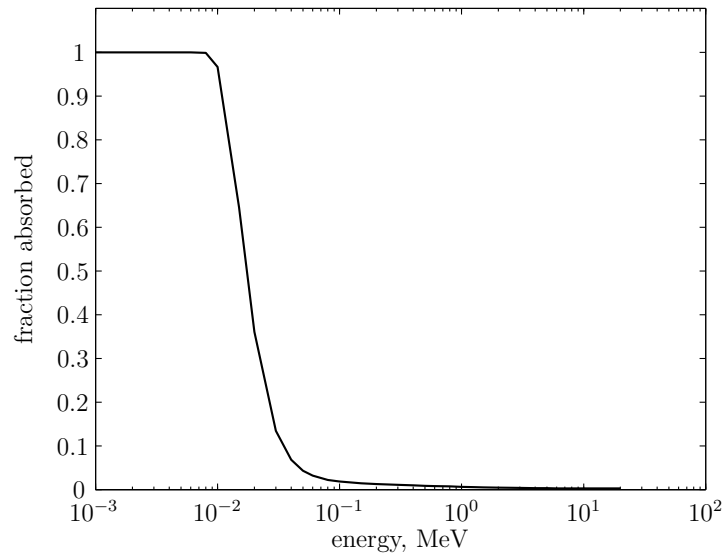


Figure 4.3: The fraction of gamma rays absorbed in interaction with the photodiode sensor with a depth of 43  $\mu\text{m}$ .

are produced by the  ${}^7\text{Li}(p, n){}^7\text{Be}$  reaction. Prompt  $\gamma$  rays (also called  $\gamma$  flash) are generated at the same time. In addition, radioactivity can be induced in the target and surrounding materials, or in samples present in the beam line. Both prompt and induced gamma radiation has the potential for producing spurious responses

## 4.2 The effect of gamma-ray background at neutron facilities

---

Table 4.1: The fraction of gamma rays absorbed by the photodiode as a function of energy.

energy	fraction absorbed, /%
60 keV	$3.2 \times 10^{-2}$
100 keV	$1.8 \times 10^{-2}$
1 MeV	$6.4 \times 10^{-3}$
10 MeV	$2.5 \times 10^{-3}$

in the photodiode detector, and this needs to be taken into consideration.

Few experimental or theoretical investigations have so far been made into the gamma environment in high neutron beams. Consequently, hardly any data can be found on the prompt gamma background at WNR or TSL. Pietropaolo et al. [127] reported some measurements at ISIS VESUVIO, which may be qualitatively similar in some respects to the environment at WNR and TSL. They measured the gamma ray environmental background of pulse height spectra with energy up to 2.5 MeV, which were characterized by a series of peaks superimposed to decreasing Compton continuum. More generally, it is known that prompt gamma radiation arising from interactions of high-energy proton with metal targets is characterized by energies exceeding 5 MeV [128]. It does not seem feasible, therefore, to assess detector susceptibility to the gamma flash by direct measurement using sealed sources, as these are not generally available with photon energies above 3 MeV [61].

However, the temporal characteristics of measured pulse trains provide evidence that the detector is not susceptible to gamma radiation in the beam. As discussed in above, photon energies below approximately 60 keV interact predominately through the photoelectric effect, and those above approximately 60 keV predominately through Compton scattering. Also, the minimum detection threshold used at LANSCE was about 132 keV. In order for the gamma flash to produce a detectable pulse, several interactions must occur effectively at the same time, because it is very unlikely for a single interaction to generate a detectable pulse. The nature of Poisson statistics indicates that if such a set of interactions occur during

## 4.2 The effect of gamma-ray background at neutron facilities

---

any one beam pulse, the probability of any given beam pulse leading to no detected gamma pulse is very low. In practice, most beam pulses did not lead to detector pulses (for example about 17% of beam pulses at LANSCE (see §3.4.1) resulted in detector pulse). It can be safely concluded that the detector sensitivity to prompt gamma radiation in fast neutron beams is not significant.

As regards activation effects, there are several works that have been reported on the evaluation of gamma fields arising from activation in neutron beams; most such works relate to health and safety purposes. For example Yu et al. [129] and Titarenko et al. [130] have conducted simulations and measurements, respectively, of activation of tungsten targets irradiated by GeV protons. In both cases the gamma radiation was mostly below 1 MeV. Prokofiev et al. (2009) is of direct relevance to the current work, which reports that the gamma dose rate in the ANITA beam line is 4 rd/h [50] (At LANSCE, the induced gamma radiation from the target is expected to be negligible because of the range of 20 m from the target to the irradiation position). Induced radioactivity in components in the beam line including the detector itself, however, can be significant. For example, Hands et al. [76] report that low-energy channels in a large PIN diode detector irradiated at TSL ANITA were dominated by gamma events from induced activity in the detector head itself and elsewhere in the beam hall [124]. This was determined by the characteristic build-up and decay of the activity in those channels. Also, as discussed in §3.4.7 of this thesis, the influence of induced radioactivity can be attributed to thermal neutron activation in the photodiode package<sup>1</sup>. However, the characteristic pulse energy and temporal behavior of induced gamma events ensure that they can be easily identified and excluded from analysis if necessary. In this work the low event rate of induced events meant that such exclusion was not necessary.

In conclusion, the influence of gamma radiation (either prompt or induced) can be excluded in this thesis as a significant component of the interactions investigated in the project.

---

<sup>1</sup>This was not observed at LANSCE where the thermal neutron fluence rate is low.

## 4.3 Discussion of the experimental results

The measured results captured at LANSCE, and TRIUMF are shown in figure 4.4 and listed in table 4.2 with the collected energy above 200 keV. The measured response at TRIUMF is much higher than LANSCE in low collected energy, and slightly lower in high collected energy.

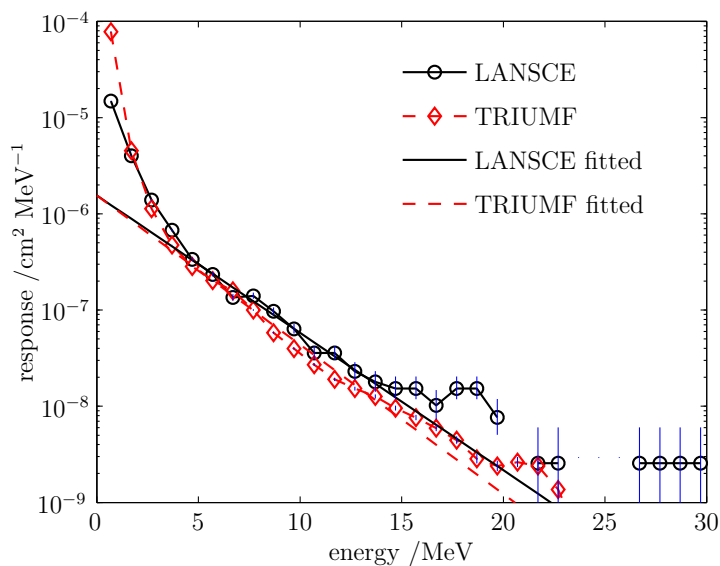


Figure 4.4: Measured responses captured at LANSCE and TRIUMF, CI=68.27%.

Table 4.2: Measured results at LANSCE and TRIUMF for collected energy equal or above 200 keV.

facility	sensor pulse of type	events	max energy /MeV	flux /n.cm <sup>-2</sup> s <sup>-1</sup>	response /cm <sup>2</sup>
TRIUMF	6	749680	43.83	$4.13 \times 10^6$	$8.53 \times 10^{-5}$
LANSCE	11	8694	32.6	$1.82 \times 10^5$	$2.22 \times 10^{-5}$

Figure 4.5 shows the response ratios of LANSCE and TRIUMF as a function of event threshold energy. The bars estimate the standard error in the ratio. This graph suggests that below around 1 MeV, there are more events at TRIUMF than LANSCE. This ratio increases with the increase of the collected threshold energy. Uncertainty increases significantly with the increase of the threshold energy due

### 4.3 Discussion of the experimental results

Table 4.3: Pulse height spectra fitting parameters  $ae^{-bE}$ , CI=68.27%.

	intercept, $a$ /MeV <sup>-1</sup>	decay constant, $b$ /MeV <sup>-1</sup>
TRIUMF	13644±1286	0.365±0.012
LANSCE	608±82	0.309±0.026

to the small number of events collected at high energies. The parameters of pulse height spectra captured at TRIUMF in the energy between 5 MeV and 14 MeV as summarized in table 4.3 are slightly higher than those at LANSCE, because the high pulse events collected at TRIUMF are less probable in the photodiode sensor than at LANSCE. The response ratio is consistent with a study of UCLan's Imaging Single Event Effect Monitor, based on charge-coupled device [97].

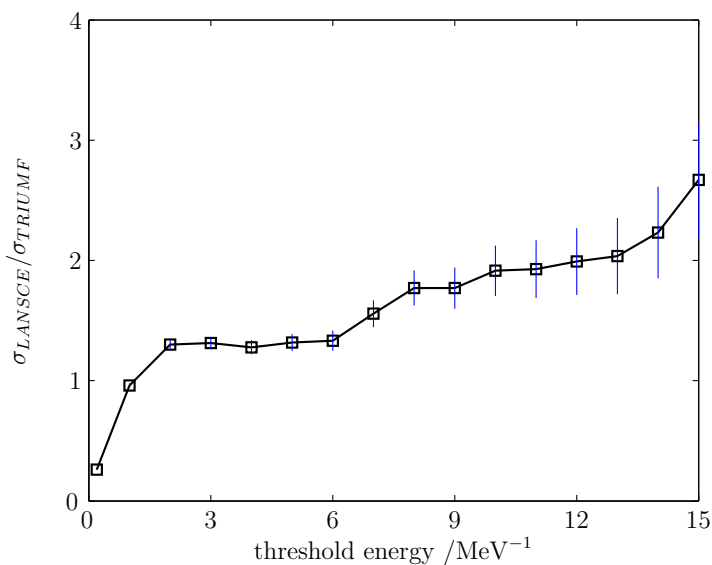


Figure 4.5: LANSCE and TRIUMF response ratio.

There are peaks around 20 MeV collected energy for some pulse height spectra, for example figure 4.4 captured at LANSCE and figure 3.1 captured at TRIUMF (on page 83). And also there were no peaks for some pulse height spectra, for example figure 4.4 captured at TRIUMF and figure 3.8 at LANSCE (on page 93). There is a possibility that these peaks were generated by pile-up, for example by

### 4.3 Discussion of the experimental results

two 10 MeV collected events. But this possibility is very marginal, because the response of 10 MeV collected events captured at LANSCE was  $6.38 \times 10^{-8} \text{cm}^2$ , and at TRIUMF it was  $3.97 \times 10^{-8} \text{cm}^2$ , which were too low. As the calculation results presented in §2.4.6 indicate, if the pulse height spectra follow an exponential curve, the effect of the pile-up will not lead to any peak in pulse height spectra. However, the decay constant of pulse height spectra will decrease with the increase of the pile-up rate. The number of the pulse height spectra around the peak is small as shown in figure 4.6 (CI=68.27% see Appendix E), which is the part of pulse height spectra captured at LANSCE in figure 4.4. These peaks may have been caused by random factors as a result of a small number of pulse events.

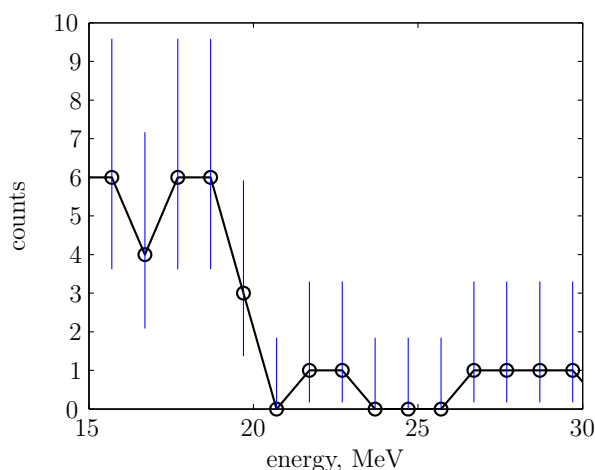


Figure 4.6: Example pulse height spectra at high collected energy captured at LANSCE, CI= 68.27%.

There are several potential sources of errors in these measurements. First, uncertainties in dosimetry are 30% at TRIUMF and 5% at LANSCE. Second, uncertainty from the random error caused by unknown and unpredictable changes in the experiment. For example, the electronic noise in the photodiode is a source of random errors. As calculation results presented in §2.5.3.2 show, when the noise standard deviation was up to  $900 \mu\text{V}^1$ , the uncertainty in energy was about  $\pm 13 \text{keV}$  when sensor pulse width was  $40 \mu\text{s}$  at CI=68.27%, and  $\pm 18 \text{keV}$  when sensor pulse width was  $20 \mu\text{s}$ . A further contribution to the uncertainties is the systematic errors. One source of these is the collected energy displayed in pulse height spectra may

<sup>1</sup>The three times of the photodiode sensor noise is unlikely to exceed this level.

### 4.3 Discussion of the experimental results

---

be slightly different from the true value because the sensor amplifier gains were calculated, and the principal uncertainty of this calculation is in the value of the preamplifier feedback capacitor ( $2.2 \pm 0.25$  pF), about 11%. An source of other reason for systematic uncertainties is that two sensors may have different doping profiles, which a junction produced by diffusion or ion implantation of boron into selected areas of the surface of a high n-type silicon wafer. The experimental results of the photodiode sensors discussed in §3.4.5 suggest that the sensors have different doping profiles, with more events in low collected events by one sensor while, and more high collected events by the other.

The pulse height spectra deviate from exponential at collected energies below about 5 MeV, taking more of a power-law form. This also appears to be consistent with Truscott *et al.* [54] and other work [131], but is more pronounced in photodiode data as the energy threshold is lower (50 keV versus circa 2 MeV). As discussed in §3.4.7, some low energy events were caused by gamma events from induced activity in the beam hall and in the detector head itself. A further contribution to the pulse height spectra, which might be a source of interference in the presence of a significant thermal neutron flux, is the  $^{10}\text{B}(n,\alpha)^7\text{Li}$  reaction. The devices used for these experiments were PN junction photodiodes. Their junction was produced by diffusion or ion implantation of boron into selected areas of the surface of a high n-type silicon wafer, which is believed to be natural boron. Inevitably, this will lead to the presence of  $^{10}\text{B}$  in the active (depletion) region, and it is this that leads to the structure just below 2 MeV in the pulse-height spectrum. The great dependence in low collected energy is mostly the result of high-energy secondary protons passing through the active region, from which only a small fraction of their total energy is collected. A previous study of UCLan's Imaging Single Event Effect Monitor [132], whose detector has a narrower active depth, indicated that protons passing through the active region were likely to dominate the low-energy part of the pulse-height spectra.

The most intense events detected in the monitor system resulted in 43.83 MeV collected in the active region (see table 4.2). The possibility that these events

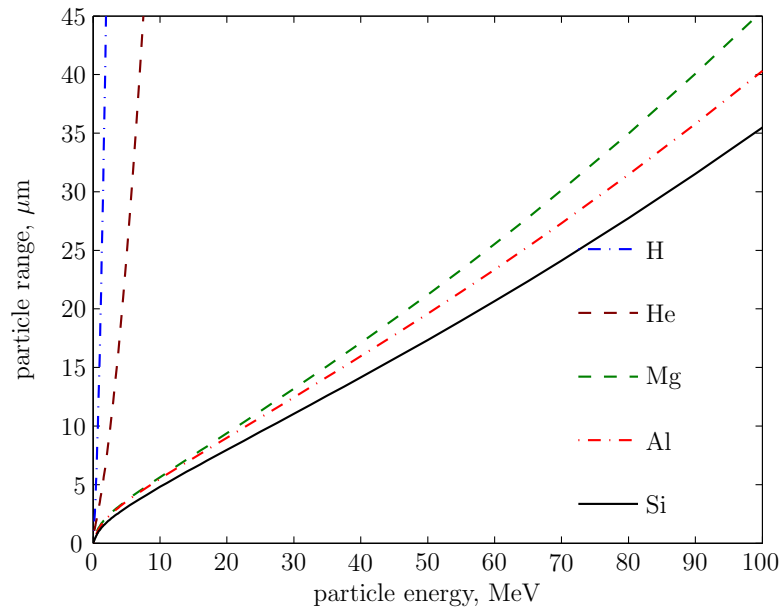


Figure 4.7: Range of selected ions in silicon [134].

were generated by pile-up is very tiny, because the response in the collected energy of 20 MeV was only around  $1 \times 10^{-8} \text{cm}^2$  as shown in figure 4.4. The maximum detectable energy was limited by the relatively shallow depth of the detector used<sup>1</sup>. Main heavy-ion products are expected to be produced (silicon, aluminium and magnesium); the range of 100 MeV ions is around 43  $\mu\text{m}$ , as illustrated by figure 4.7. Early work reported that the detector could not collect all the deposited energy in the active area [133]. So the maximum photodiode detectable energy was much smaller than the range of energy ions produced by heavy-ion products.

## 4.4 Testing protocols at facilities

The purpose of developing photodiode beam monitoring is to determine the transmission along the neutron beam in SEEs testing experiments with multiple devices at facilities such as LANSCE, TSL and ISIS. The method used in this work to determine the transmission is based on the number of pulse events captured from the

<sup>1</sup>Note that the diode was not designed for use as a particle detector.

irradiation and upstream neutron fluence to calculate the downstream fluence. If the probability of pile-up in an upstream device is too high, it will lead to high uncertainty in transmission. So the pile-up rate must be taken into account in testing protocols at neutron beam facilities.

### 4.4.1 Effect of pile-up in testing protocols

The rate of interaction between the photodiode sensor and neutron beam is proportional to the neutron beam flux. However, the beam monitoring system can directly determine the detection rate via the number of pulse events and exposed duration. The relationship of the interaction and the detection rate is discussed in §2.4.1, which can be modeled as:

$$r = \frac{n}{1 + n\tau} \quad (4.2)$$

where  $r$  is the detection rate,  $n$  is the interaction rate and  $\tau$  is the sensor pulse width. As presented in §3.2.1 and §3.4.2, the experimental results of detection and interaction rates agree well with equation 4.2.

The detection rate is positively correlated with the interaction rate, i.e. the former increases with the increase of the latter. The difference between the interaction and detection rates is more significant with the increase of the interaction rate as shown in figure 4.8, because the probability of pile-up increases with the increase of the interaction rate.

Assuming two different neutron fluxes to be  $\phi_1$  and  $\phi_2$ , and their corresponding interaction rates are  $2500 \text{ s}^{-1}$  (high rate) and  $200 \text{ s}^{-1}$  (low rate) respectively, during the multiple-experiments SEEs testing, the neutron flux decreases along the neutron beam line; as a consequence, the interaction rate will decrease along the neutron beam line. Assuming there are two sensors with different pulse widths:  $40 \mu\text{s}$  and

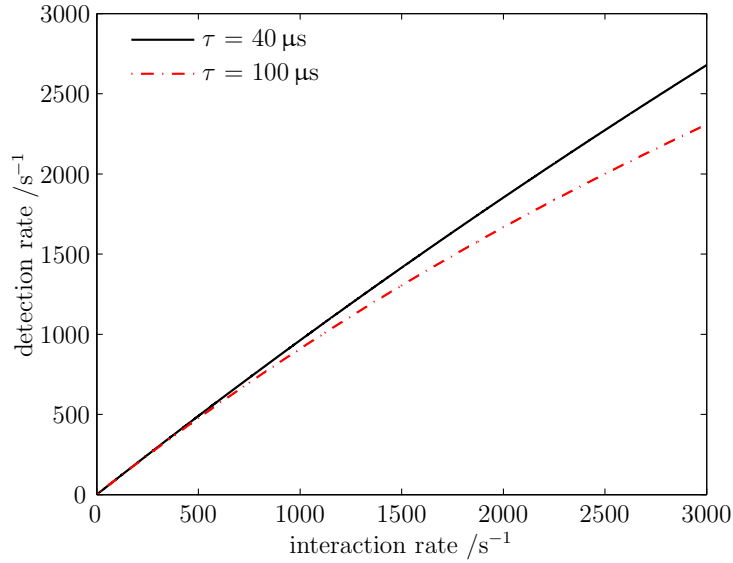


Figure 4.8: Interaction rate and detection rate.

100  $\mu\text{s}$ , according to equation 4.2, when the pulse width is 100  $\mu\text{s}$  and the interaction rate is  $2500\text{ s}^{-1}$ , the detection rate will be  $2000\text{ s}^{-1}$ .

The probability of detection  $P$  is defined as  $r/n$ , giving 80%. When the neutron flux is  $\frac{1}{2}\phi_1$ , the interaction rate will be  $1250\text{ s}^{-1}$ . Based on equation 4.2, the detection rate should be  $1111\text{ s}^{-1}$ , and the probability of detection is 88.89%, which means a significant increase of 11.11% of uncertainty in transmission. Figure 4.9 shows the probability of detection of two different pulse widths with various percentages of the neutron flux. It can be seen that the probability of detection increases with the decrease of the sensor pulse width and the percentage of neutron flux.

At low interaction rates, the probability of detection is insensitive to the neutron flux and the sensor pulse width. In contrast, at high interaction rates, the probability of detection decreases significantly as the percentage of neutron flux and the sensor pulse width both increase. For example, when the pulse width is 100  $\mu\text{s}$  while the neutron flux is  $\phi_1$ , the detection rate is  $2000\text{ s}^{-1}$ ; when the neutron flux is  $\frac{1}{2}\phi_1$ , and the detection rate is  $1111\text{ s}^{-1}$ , the calculated neutron flux will be:

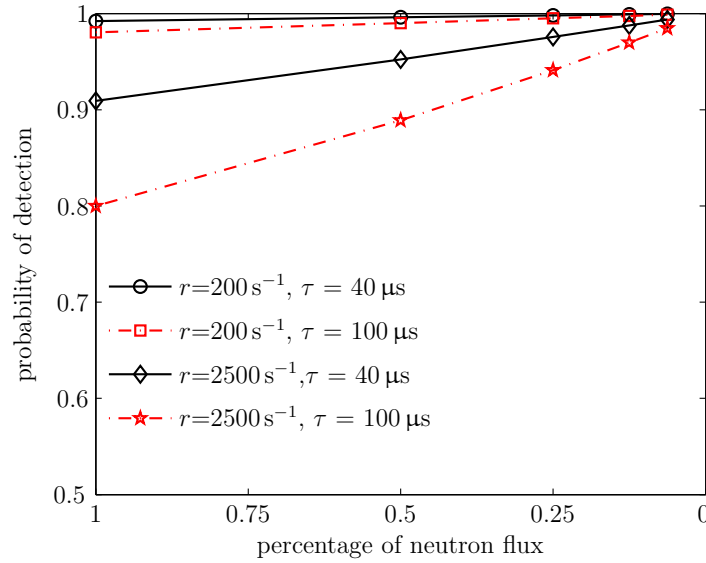


Figure 4.9: Probability of detection of two different pulse widths in various of the neutron flux.

$$\phi_{\frac{1}{2}} = \frac{1111}{2000}\phi_1$$

giving  $\phi_{\frac{1}{2}}$  is  $0.556\phi_1$ . So the calculated neutron flux is much higher than the actual, as a consequence, the transmission should be:

$$\tau(r) = \frac{\phi_{\frac{1}{2}}}{\frac{1}{2}\phi_1}$$

giving  $\tau(r)$  111%, in this case, the calculated transmission (111%) is 11% more than the actual (100%) due to the effect of the pile-up. Figure 4.10 shows the transmission with two different pulse widths and two different neutron fluxes with various percentage of the neutron flux. The worst case is when the interaction rate is  $2500\text{ s}^{-1}$  and the sensor pulse width is  $100\text{ }\mu\text{s}$ , the uncertainty of the transmission can be up to 125%. This uncertainty increases with the increase of the pulse width and interaction rate. To reduce the uncertainty of transmission, the pile-up effect must be accounted for in determining the testing protocols of the photodiode beam monitor.

In the next two subsections, the following parameters are assumed:

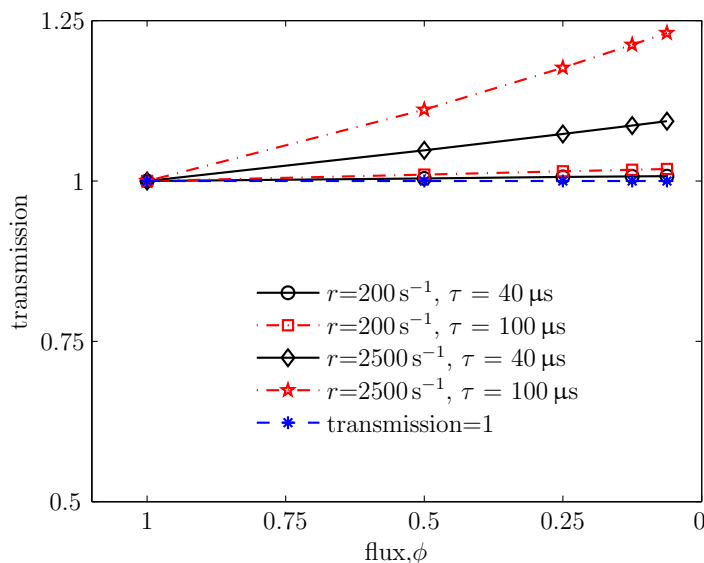


Figure 4.10: Transmission for two different sensor pulse widths and interaction rates with various percentage of the neutron flux.

- $n$  photodiodes are under test and named as  $\psi_1, \psi_2, \dots, \psi_n$ ;
- These sensor pulse widths are  $\tau_1, \tau_2, \dots, \tau_n$  respectively;
- These sensors receive neutron fluence  $\Phi_1, \Phi_2, \dots, \Phi_n$  respectively, where  $\Phi_1$  is known and others are unknown;
- Their responses are  $\sigma_1, \sigma_2, \dots, \sigma_n$  respectively;
- The probability of detection is  $P_1, P_2, \dots, P_n$  respectively.

#### 4.4.2 TSL pulsed neutron beam

In this section, the experimental data captured at TSL ANITA in 2010 are used as the sample to analyze the testing protocols of the pulsed neutron beam at TSL. There were 27 945 pulse events captured during 72s with pulse events collected above 146.9 keV. The notations used in this section are described in table 4.4.

During the multiple experiments, the devices that were positioned further away from the beam source received a reduced neutron flux due to the absorption and scat-

Table 4.4: Symbols used in determining the TSL ANITA testing protocols.

Symbol	describe
$t$	experimental duration
$t_{beamon}$	experimental beam on duration
$\tau_{beam}$	neutron macropulse beam length
$N$	the number of detected pulse events
$N_{1p}$	the number of detected pulse events in the first peak of the pulse interval distribution
$N_{i1}$	the number of interacted pulse events
$r_{1p}$	the detection rate in the first peak of the pulse interval distributions
$P_{1p}$	the probability of detection in the first peak of the pulse interval distribution
$\sigma_{i1}$	the response in the interaction pulse events

tering by upstream experiments. Although a great number of secondary particles were generated through the interaction of the upstream equipments with neutrons, second sources were insignificant by the time the position of downstream device was reached if the downstream device was far away from the upstream. Consequently the pile-up effect was likely to occur in upstream experiments. As shown in the experimental results presented in §3.4.8, the pile-up effect only occurred in the first peak of the pulse interval distribution. There were 16 362 pulse events captured in the first peak at TSL ANITA. The experimental beam on duration  $t_{beamon}$  is:

$$t_{beamon} = f\tau_{beam}t$$

where  $f$  is the neutron beam frequency (160 Hz at TSL ANITA),  $\tau_{beam}$  is the neutron macropulse length (500  $\mu$ s), and  $t$  is the experiment duration (72 s), giving  $t_{beamon}$  5.72 s. The detection rate in the first peak  $r_{1p}$  is:

$$r_{1p} = N_{1p}/t_{beamon} \tag{4.3}$$

where the number of pulse events in first peak  $N_{1p}$  in device  $\phi_1$  is 16 362, giving  $r_{1p}$

2841 s<sup>-1</sup>. As discussed in §2.4.1, the probability of detection upstream in the first peak is:

$$P_{1p} = 1 - r_{1p}\tau_1 \quad (4.4)$$

where the  $\tau_1$  was 40  $\mu$ s, giving  $P_{1p}$  88.64%. The number of pulse events of sensor  $\psi_1$  without pile-up effect  $N_{i1}$  can be estimated by:

$$N_{i1} = \frac{N_{1p}}{P_{1p}} + (N - N_{1p}) \quad (4.5)$$

where  $N$  is the number of collected pulse events of sensor  $\psi_1$ , which was 27 945, giving  $N_{i1}$  30 042. So the sensor  $\psi_1$  response can be determined:

$$\sigma_{i1} = \frac{N_{i1}}{\Phi_1} \quad (4.6)$$

Overall, the steps of determining the downstream device transmission are:

1. Detect the number of pulse events in the first measured pulse interval distributions;
2. Use equations 4.3, 4.4 and 4.5 to determine the number of pulse events without pile-up;
3. Depending on the number of pulse events without the pile-up effect captured by sensor  $\psi_1$  upstream and the neutron fluence  $\Phi_1$ , the response  $\sigma_{i1}$  can be determined.
4. Then the number of pulse events without the pile-up effect captured by other sensor downstream can also be determined. Based on equation 3.10 (see §3.4.1.1), the neutron fluence received by downstream devices can be calculated;

5. So the transmission can be determined by using equation 3.8 (on page 87).

### 4.4.3 LANSCE

At LANSCE, the macropulse frequency delivered to WNR(ICE House) target was 40 Hz, the macropulse length was about 625  $\mu\text{s}$ . Table 4.5 summarized one example result captured in the upstream position. The detected pulse rate was  $6.82\text{ s}^{-1}$  for collected energy above 132 keV, an event probability per macropulse approximately 0.17.

Table 4.5: LANSCE pile-up analysis.

pulse width, / $\mu\text{s}$	duration, /s	pulse of events	detection rate, / $\text{s}^{-1}$	first peak events	first peak rate, / $\text{s}^{-1}$
40	1749	11922	6.82	890	0.51

As discussed in §4.4.1 and illustrated in figure 4.9, when the interaction rate is very low, the downstream fluence can be directly determined by using equation 3.10 (see §3.4.1.1).

### 4.4.4 TSL continuous quasi-monoenergetic neutron beam

These experiments were made at TSL in April 2007 downstream of several other experiments, where the beam was severely degraded. There are no example experimental data measured at upstream available to analyze the testing protocols for continuous quasi-monoenergetic neutron beam. However, as shown in the experimental results presented in §3.4.7, the measured parameters of pulse height spectra above 5 MeV increase with the the decrease of the TSL quasi-monoenergetic neutron beam energy, it indicate that the average energy of pulse events captured at higher neutron beam than lower. The detected rate captured at TSL ANITA was

## 4.5 Predicting the testing protocols using at ISIS ChipIr

---

about  $388\text{ s}^{-1}$  with the neutron flux up to  $1.16 \times 10^6\text{ n.cm}^{-2}\text{ s}^{-1}$ . The typical peak neutron flux at standard point at TSL neutron beam energy [135] was between at  $1 \times 10^4$  and  $5 \times 10^5\text{ n.cm}^{-2}\text{ s}^{-1}$ . So the interaction rate of the photodiode sensor irradiated at TSL continuous beam was unlikely to be exceed than  $200\text{ s}^{-1}$ . In this case, as discussed in the last section, the probability of pile-up was very small.

Moreover, the experimental results captured at TRIUMF (see §3.2.1) indicate the probability of detection was 93.90% when the interaction rate was up to  $1672\text{ s}^{-1}$ . When the interaction rate is below  $200\text{ s}^{-1}$ , the probability of detection will be over 98% if the sensor is under  $100\text{ }\mu\text{s}$ . So the upstream device's response can be directly calculated by the number of events over the neutron fluence, and the neutron fluence received by the downstream device can be determined by the equation 3.10 (see §3.4.1.1).

## 4.5 Predicting the testing protocols using at ISIS ChipIr

ChipIr will be an instrument station for accelerated atmospheric neutron testing for SEEs in semiconductor microelectronic chips planned in the near future. It is designed to provide a pulsed neutron beam with energy up to  $800\text{ MeV}$  [136]. In this section, the notations used are described in table 4.6.

The frequency of ChipIr is planned to be  $10\text{ Hz}$ , the typical flux will be about  $1 \times 10^6\text{ cm}^{-2}\text{ s}^{-1}$ , and the per pulsed beam length is expected to be about  $1.4\text{ }\mu\text{s}$ . If the photodiode sensor is irradiated at ChipIr, it is important to estimate the effect of pile-up. The minimum detected energy should be lower than other facilities due to pile-up, because of the narrow beam length and low frequency.

Given that ChipIr beam spectra are similar to those at LANSCE, the pulse height spectrum captured by the photodiode sensor at ChipIr is also expected to be similar. Hence one example of LANSCE's experimental data is used to predict the

## 4.5 Predicting the testing protocols using at ISIS ChipIr

---

Table 4.6: Symbols used in determining the ChipIr testing protocols.

Symbol	description
$m$	the number of pulse events per pulsed neutron beam
$\mu$	the average of pulse events per pulsed neutron beam
$N$	the number of pulsed neutron beam
$N_i$	the number of interaction pulse events
$N_d$	the number of detected pulse events
$P_m$	the probability of pulse events corresponding to $m$
$n_m$	the number of interaction pulse events corresponding to $m$
$E_{min}$	the minimum of detected energy
$E_m$	the average energy corresponding to $m$
$E_\mu$	the average energy corresponding to $\mu$
$E_{ra}$	the average energy of simulated data
$f$	$E_\mu/E_{ra}$

testing protocols at ChipIr. The number of pulse events is 19 299 above collected energy 132 keV. The pulse height spectra follow the exponential distribution in high collected energy and power law distribution in low deposited energy, which can be expressed:

$$dN = adE^{-b} \tag{4.7}$$

where  $N$  is the number of pulse events, and  $E$  is the deposited energy,  $b$  is called the power law exponent, and  $a$  is the constant, with the value of  $1.25 \pm 0.01$  (MeV <sup>$b$</sup> ) at CI=68.27%. The fitted curve is shown in figure 4.11.

According to equation 4.7, 7515 random numbers are generated with energy between 10 keV<sup>1</sup> and 132 keV. The simulated data (as shown in figure 4.11) include the LANSCE experimental data in combination with the generated data. The mean of the simulated energy is 0.768 MeV.

As discussed in §2.5.1, there is always a minimum detectable energy because of the

---

<sup>1</sup>Below 10 keV is too small to be detected.

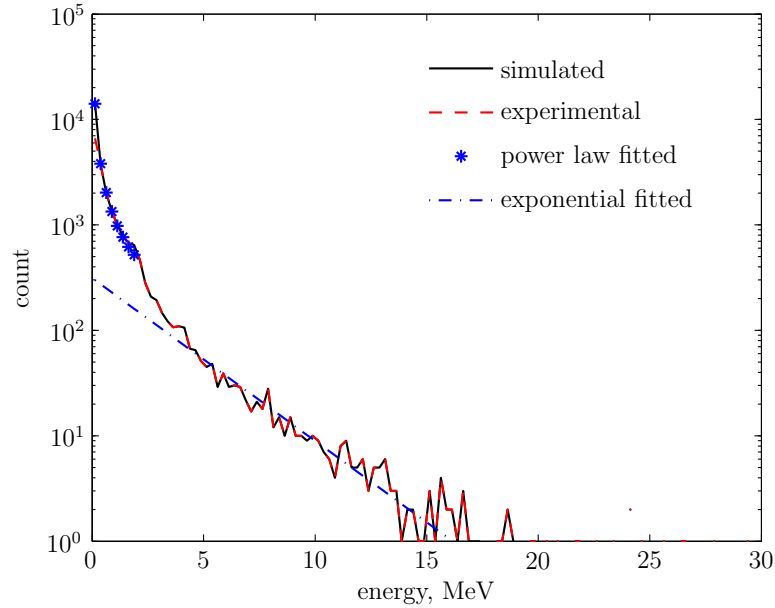


Figure 4.11: simulated and measured pulse height spectra captured at LANSCE.

effect of noise. When pile-up occurs, the minimum detectable energy is the same, but the events which have lower energies than the minimum detected energy can also be detected. To predict the testing protocols at ChipIr, a series of calculations were undertaken first to determine the characteristics of the pulse height spectra when the number of pulse events generated per pulsed neutron beam  $m$  is 2, 3, 5, or 10, and then the average energy  $E_u$  when the average of pulse events per neutron beam  $\mu$  is 2, 3, 5, or 10. The number of calculated pulse is 26 814, the frequency of ChipIr is designed to be 10 Hz, the number of pulsed neutron beams used in these calculation are  $(26814/m)$ . The following parameters are assumed for the calculation:

1. The output of sensor 12 pulse shape is as the input;
2. The pulse height is 1 V
3. The noise level is  $600 \mu\text{V}$ ;
4. The pulse time interval is 1 ms;

## 4.5 Predicting the testing protocols using at ISIS ChipIr

---

5. Simulated data (shown in figure 4.11) as the reference data are selected randomly to meet the characteristics exponential distribution and used to construct the input sequence.

The simulated pulse height spectra with the detected pulse energy above 53.6 keV are shown in figure 4.12. It can be seen that the number of high collected events increases with the increase of  $m$ , which indicates that the average of detected energy increases with the increase of  $m$  as summarized in table 4.7, where the average detected energy is either 91.14 keV (when  $m=1$ ) or approximates to  $m \times 76.8$  keV (when  $m$  is above 1), where 76.8 keV is the average energy of the simulated data as summarized in table 4.7.

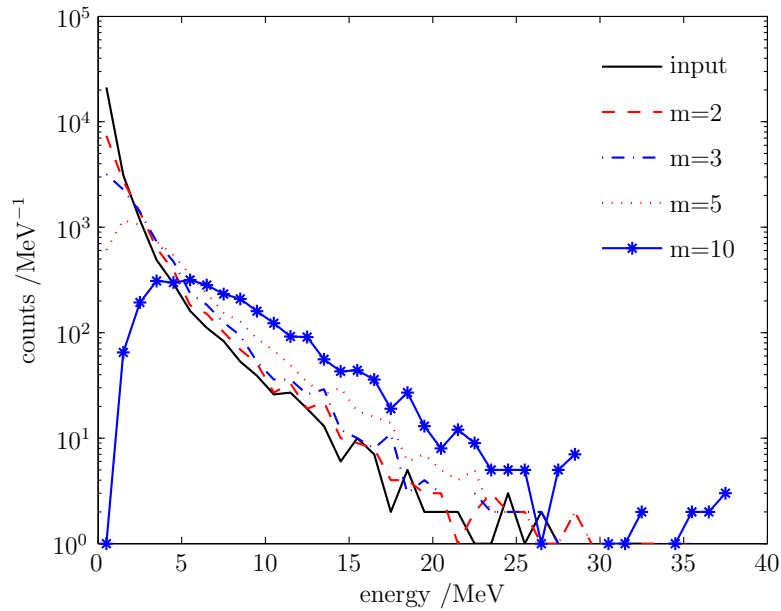


Figure 4.12: Simulated pulse height spectra with various average numbers of pulse events per neutron beam.

In radiation measurements, the interaction between the photodiode sensor and the neutron beam follows the Poisson distribution. No matter how much  $\mu$  is, there is always a possibility of 0, 1, 2, 3... of pulse events generated per pulsed neutron beam. A few examples of the probability with various values of  $\mu$  are listed in table 4.8. For instance, when  $\mu=1$ , 36.79% of the pulsed neutron beam will not

## 4.5 Predicting the testing protocols using at ISIS ChipIr

---

Table 4.7: Simulation summary—the average energy of the number of pulse events per neutron beam.

$m$	detected average energy MeV
1	0.911
2	1.578
3	2.308
5	3.841
10	7.682

generate any pulse events, and 26.42% pulsed neutron beam will generate two or more pulse events, only 36.79% pulsed neutron beam generate one pulse event.

Table 4.8: Probability of pulse events with various the average pulse numbers per neutron beam.

$m$	$\mu = 0.1$ %	$\mu = 1$ %	$\mu = 3$ %	$\mu = 5$ %
0	90.48	36.79	4.98	0.67
1	9.05	36.79	14.93	3.37
2	0.45	18.39	22.40	8.42
3	0.015	6.13	22.40	14.04
4	—	1.53	16.80	17.55
5	—	0.31	10.08	17.55
6	—	0.05	5.04	14.62
7	—	—	2.16	10.44
8	—	—	0.81	6.53
9	—	—	0.27	3.63
10	—	—	0.08	1.81
11	—	—	0.02	0.82
$\vdots$			$\vdots$	$\vdots$

At ChipIr, the number of detected pulse events is expected not to exceed the number of neutron pulses. One reason is that some pulse events are too small to be detected due to the effect of noise. Another possible reason is that the interaction is a Poisson process, meaning that irrespective of  $\mu$  (the average of pulse events per pulsed

## 4.5 Predicting the testing protocols using at ISIS ChipIr

---

neutron beam), there is always a possibility that no pulse events will be generated in some neutron beam. On the other hand, it is also possible that more than one pulse event will be generated in one neutron beam. In the latter, the number of interacted pulse events  $N_i$  is always greater than the number of the detected pulse events  $N_d$ . Assuming the number of neutron beams  $N$  to be 10 000, the number of interacted pulse events  $n_m$  corresponding to  $m$  can be determined by:

$$n_m = P_m N m$$

where  $P_m$  is the probability of pulse events corresponding to  $m$  as listed in table 4.8. Table 4.9 summarizes a few examples of the number of detected and interacted pulse events with varying  $\mu$ . It can be seen that the number of detected pulse events increases with the increase of  $\mu$ , and the number of interacted pulse events is similar to  $\mu N$

Table 4.9: Estimated numbers of detected and interacted pulse events with various the average pulse events generated one neutron beam macropulse at ChipIr.

$m$	$\mu=0.1$		$\mu=1$		$\mu=3$	
	detected number	interacted number	detected number	interacted number	detected number	interacted number
0	0	0	0	0	0	0
1	905	905	3679	3679	1493	1493
2	45	90	1839	3678	2240	4480
3	1	5	613	1839	2240	6720
4	—	—	153	612	1680	6720
5	—	—	31	155	1008	5040
6	—	—	5	30	504	3024
7	—	—	—	—	216	1512
8	—	—	—	—	81	648
9	—	—	—	—	27	243
10	—	—	—	—	8	80
11	—	—	—	—	2	22
total	951	1000	6321	9998	9499	29982

## 4.5 Predicting the testing protocols using at ISIS ChipIr

---

The probability of occurrence per neutron pulse is shown in figure 4.13. It can be seen that the probability increases with the increase of  $\mu$ . When  $\mu$  is equal to or above 5, the probability is around 100%; when  $\mu$  is between 3 and 5, the probability is between 95% and 99%; when  $\mu$  is below 3, the probability increases significantly with the increase of  $\mu$ .

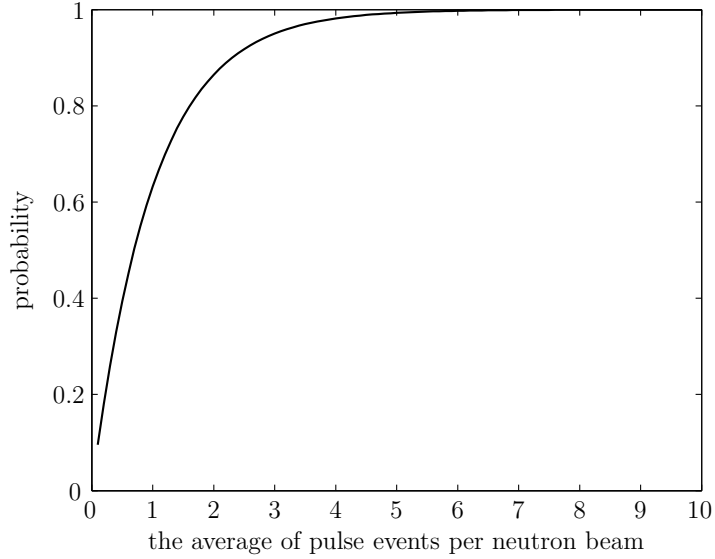


Figure 4.13: The probability of pulse events generated per neutron pulse with various average number of pulse events.

The average energy  $E_\mu$  corresponding to  $\mu$  can be determined:

$$E_\mu = \frac{\sum_{m=1}^N P_m E_m}{\sum_{m=1}^N P_m}$$

where  $P_m$  is the probability of pulse events corresponding to  $m$  summarized in table 4.8, and  $E_m$  is the average energy corresponding to  $m$  given in table 4.7. Figure 4.14 shows  $E_m$  and  $E_\mu$  with various  $m$  or  $\mu$  respectively. The difference between  $E_m$  and  $E_\mu$  increases with the increase of  $m$  or  $\mu$ , this is because the probability of one pulse event generated per neutron decreases with the increase of  $\mu$ ; the average energy is more than  $E_\mu/\mu$  when  $m=1$ . When  $\mu$  is equal to or more than 5, this difference is very tiny.

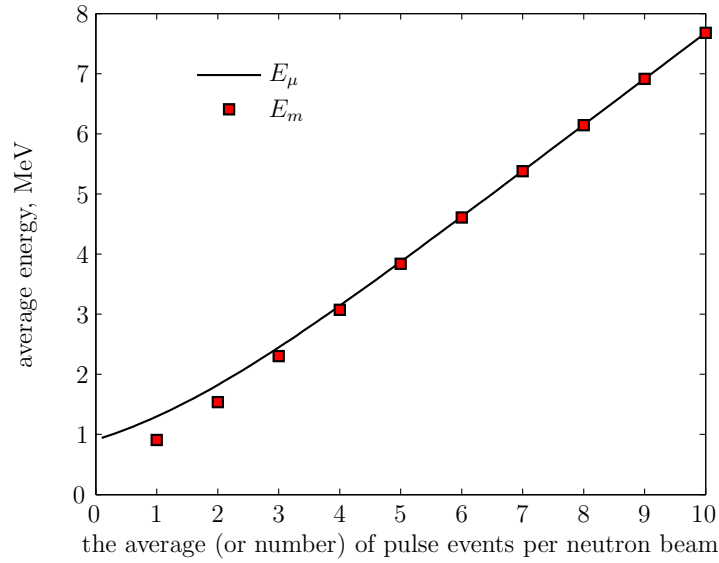


Figure 4.14: Estimated average detected energy with various average (number) of pulse events per neutron pulse.

Table 4.10: The average energy with various mean number of pulse events per neutron macropulse beam.

$m$ or $\mu$	$E_\mu$ /MeV	$E_m$ /MeV
2	1.82	1.56
3	2.44	2.30
4	3.07	3.14
5	3.87	3.84
6	4.61	4.62
7	5.38	5.38
8	6.14	6.15
9	6.01	6.91
10	7.68	7.68

Overall, the transmission along the neutron beam at ChipIr can be predicted as follows:

1. Determine the reference data: the pulse height spectra without significant pile-up should be captured by using photodiode sensor irradiated in low neutron

## 4.5 Predicting the testing protocols using at ISIS ChipIr

---

flux. The minimum detected energy  $E_{min}$  can be determined. Depending on the captured pulse height spectra, the reference pulse height spectra can be simulated (described in the beginning of this section) with a lower minimum detected energy, and its  $E_{ra}$  can be determined.

2. The parameter  $f$  ( $= E_{\mu}/E_{ra}$ ) can be calculated.
3. Based on the captured pulse interval distributions, the probability of the pulse events that occur per neutron beam  $P$  can be determined. As summarized in table 4.8 and illustrated in figure 4.13,  $P$  increases with the increase of  $\mu$ .

(a) If  $P$  is equal to or above 99%, then

$$\mu = f$$

(b) If  $P$  is between 95% and 99%, based on figure 4.13 and table 4.8, the value  $\mu$  should be between 3 and 5. Depending on the average of detected energy  $E_{\mu}$ , table 4.10 and figure 4.14, the value of  $\mu$  can be estimated.

(c) When  $f$  is smaller than 3, the probability of pulse events that occur per neutron beam significantly changes various  $\mu$ , so the value of  $\mu$  can be estimated by the value of  $P$  as displayed in figure 4.8;

The number of interaction pulse events can be determined:

$$N_i = \mu N_d$$

The transmission along the neutron beam can be determined by the number of interaction pulse events for each sensor captured and at the standard point of the neutron fluence. This method is based on the assumption that the spectra of the neutron are constant. However, according Truscott et.al [54] and the results presented in §3.4.1.3, the neutron beam spectra may change for two reasons:

1. Scattering are likely happen to low energy neutrons than high-energy. In this case, there is more dependence in high collected pulse events for the downstream photodiode than upstream.

2. The neutron beam could be enhanced by secondary particles generated by upstream experiments interacting with the neutron beam.

As the experimental results presented in figure 3.22 (see §3.4.1.3) show, the former will not significantly change the transmission along the neutron beam line. The latter is dominant in low collected energy as presented in §3.4.1.2 and §3.4.1.3, so the curve of the captured pulse high spectra by using photodiode sensors in upstream and downstream positions should be different. In summary, it can be seen that the neutron fluence and hardness at multiple locations at ChipIr can be explored by looking at the number of pulse events collected, the mean of detected pulse energy, and the pulse interval distribution together when the beam becomes available.

## 4.6 Discussion

In pulsed neutron beams, such as TSL ANITA, above 10 MeV, the typical flux is  $1 \times 10^6 \text{ n.cm}^{-2}\text{s}^{-1}$ , which is much lower than TRIUMF (typical flux at  $4 \times 10^6 \text{ n.cm}^{-2}\text{s}^{-1}$ ), but the fluence received during each neutron pulse is very high. So the rate of pulses received from the detector becomes a significant fraction of the rate of interacted pulses in the beam. The pulse interval distributions form a comb at multiples of the beam accelerator repetition period modified by the characteristic exponential form resulting from a Poisson process. Therefore pile-up only occurs in the case of more than one pulse event being generated by the neutron beam macropulse. This kind of pile-up rate should be determined in order to get correct transmission along the neutron beam during multiple experiments. According to the theory of the nonparalyzable counting system, the pile-up rate can be calculated on the basis of the sensor pulse width and the rate of detected pulse. However this method will need to be verified by irradiating the beam monitor at facilities in the future.

The prediction of beam monitor testing protocols in using ChipIr has been analyzed. This method should be verified when the beam becomes available with various neutron fluxes. The limitation of this method relates to its assumption that the measured pulse height spectra are constant, but in real multiple-experiments, the measured pulse height spectra might be different in various test positions because the downstream beam is degraded by upstream experiments. In addition, if the distance between other experiments and downstream sensor is near enough, the secondary particles might deposit energy in photodiode sensor as presented in §3.4.1. However, the energy deposited by secondary particles is usually quite low. When ChipIr becomes available, the transmission along the beam line at ChipIr should be explored.

LANSCE is also a pulsed neutron beam. The photodiode received the typical flux under  $2 \times 10^5 \text{ n.cm}^{-2}\text{s}^{-1}$  during the experiments in 2010. The fluence received during each neutron pulse was not very high. So pile-up might have occurred if a large area detector with a high interaction rate were used in this kind of beam, but it is unlikely to be significant from the small  $2.92 \text{ mm}^2$  active area used in this project (see discussions in §4.4.1).

Based on the threshold level of the matched filter, the minimum of detected pulse height of beam monitoring can possibly be as low as the peak of the noise at a low noise level. For instance, the peak of sensor 12's noise amplitude was about 15 mV; based on equation 2.41 (see §2.5.1), the minimum detected pulse height was 15.6 mV when the number of sampling points was 40. However, the minimum of detected pulse height decreases with the increase of the number of sampling points. If the sample rate is 2 MHz, the number of sampling points in sensor 12 pulse will be 80, and the minimum of detected pulse height will be 11 mV, which will be lower than the peak of the noise amplitude.

One noise source generated in the signal is expected to be the photodiode sensor with the preamplifier. This noise passes through multi-order shaping amplifiers, and is amplified by the amplifier gain. Another source is the quantization noise in the DAQ card. In the neutron beam monitoring system, the output of the signal

---

is less than the 1 V. According to DAQ specifications [112], the quantization noise level is less than  $32 \mu\text{V.r m s}$  when the input range is 1 V.

In the project, 12 sensors have been developed, and the measured noise level is between 100 to  $310 \mu\text{V.r m s}$ . So the main noise source in neutron beam monitoring system is generated in the photodiode sensor with preamplifier.

Basically the noise level affects the measurements in two ways. One is the energy resolution, which is poorer with the increase of the noise level. The other is the collected threshold energy, which increases with the increase of the noise level as presented in §2.4.6.

The optimum sensor pulse width by balancing the sensor's random noise and the pile-up effect while also taking into account of the effect of pulse width sampling resolution on diode neutron sensor performance has been analyzed. No attempts have been made to optimise the performance of in experiments reported here. Figure 2.25 shows the optimum pulse width with various interaction rates. In high interaction rates, such as those captured at TSL ANITA, assuming four sensors are under test, the optimum pulse width should be less than  $40 \mu\text{s}$ . However, this optimum pulse width is limited by the sampling resolution of the sensor pulse. As discussed in §2.5.3.2, the sampling of one pulse should not be less than 10. In this case, the pulse width should be balanced by the optimum pulse width as shown in figure 2.25 and the sampling points for each pulse.

The maximum sample rate used to collect the experimental data in this project was 1 MHz. At this sample rate, the minimum collected energy captured by 12 sensors (in four different circuits) were between 50 and 156 keV. If the sample rate was higher, the more sampling points for each pulse would be collected at the same sensor pulse width, and the lower deposited events would be detected; the sensor pulse width would be less at the same sampling points for each sensor, and the pile-up effect would be reduced.

The photodiode monitor system is intended to enable measurements of neutron

fluence (or flux), through measurement of pulse-height (energy deposition) spectra and pulse time interval distributions. It is a simple yet effective neutron detection system. Compared to some neutron monitors, this system has a number of advantages:

1. The photodiode sensor is small, so it can be placed and taken out of the beam without interfering with other devices under test. Other neutron detectors, for example the Proton recoil telescope [137] can measure neutron spectra with better accuracy than the photodiode sensor over a broad energy range, but in general, detectors of such a large size can interfere with other devices during multiple experiments.
2. The beam monitoring system can provide useful information on the fluence and hardness of a neutron field at multiple locations in a high-energy neutron beam. Platt et al. [96] reported that a CCD based neutron imaging monitor (which is much more expensive and intrusive than this photodiode sensor) was used to determine the transmission along the neutron beam at TSL [55]. First the imaging capability is not required to undertake this kind of work; second, the read-out of the CCD sensor is slow; so it is not practical to carry out experiments with several CCD based sensors in cases where several experiments are arranged along a beam line during SEEs testing.

However, there is still further work to be undertaken to improve the system. The photodiode sensor has not been calibrated. The calibration can be conducted by using the peaks of a known source [138], for example, cadmium ( $^{109}\text{Cd}$ ) which emits 88 keV  $\gamma$ -rays, or gold activation with neutron which emits  $\gamma$ -rays with 411 keV energy. When a photon interacts with the detector, it will generate an electrical signal in the photodiode, which is converted into a pulse by the photodiode sensor. The peak of the pulse height spectrum is assumed to be  $V_s$ . In general:

$$E = AV_s + c \tag{4.8}$$

where  $E$  is the  $\gamma$  energy (MeV),  $A$  is the photodiode sensor amplifier gain ( $\text{mV} \cdot \text{MeV}^{-1}$ ), and  $c$  is the intercept (which is usually as close as possible to zero). If only one calibration source is used,  $c$  will be assumed to be zero;  $A$  can be calculated by using equation 4.8. If two or more sources are used, the values of  $A$  and  $c$  can be determined by fitting a linear function to all known source energies and their corresponding deposited pulse heights in the photodiode sensor.

The experimental results were presented in term of the number of pulse events, pulse height spectra, and pulse interval distributions. The pulse height spectra follow the exponential curve as expressed as  $a \exp^{-bE}$  between energy of 5 and 14 MeV, where fit parameter  $a$  is proportional to the number of pulse events, and  $b$  is proportional to the reciprocal of the mean of detected energy. The area under the exponential portion of the pulse height spectra given by the ratio  $a/b$  could provide useful information on the fluence and hardness of the neutron field [139]. But the ratio  $a/b$  has not been exploited yet. As discussed before, the fit parameters were determined between the collected energy between 5 and 14 MeV, and the calculated amplifier gain could cause up to 11% of the deposited energy. This uncertainty could cause significant uncertainties in the ratio  $a/b$ . Moreover, in general, the number of pulse events collected between 5 and 14 MeV is small in short experimental duration, thus leading to high uncertainties in  $a$  and  $b$ .

As the experimental results presented at §3.4.1.3 (see figure 3.22) show, the collected energy in the photodiode sensor generated by secondary particles irradiated at LANSCE was usually below 1 MeV, which was the threshold energy at the lowest of the transmission along the neutron beam line. This is because low-energy neutron spectra are more easily scattered by upstream experiments than high-energy. The information on the neutron fluence and hardness might be explored by using the number of pulse events times the mean detected pulse energy with 1 MeV threshold collected energy.

Silicon neutron detectors suffer from performance degradation (response reduction) due to the neutron damage (see §3.4.1.4, figure 3.23). Kraner et al. [140] suggested that the silicon lifetime can be determined by the following:

$$\frac{1}{t} = \frac{1}{t_0} + \frac{\Phi}{K} \quad (4.9)$$

where  $t_0$  is the initial lifetime,  $\Phi$  is the neutron fluence and  $K$  is the damage coefficient for silicon, which is dependent on the neutron energy and the detector. In this project, the neutron damage in the photodiode sensor is not going to be investigated. But in future work, other kinds of diodes, for example PIN, diamond diode or SiC diodes, which are less likely to suffer from neutron damage, could be used in beam monitoring system instead of photodiode. For example, Seshadri et al [80] reported that neutron detection using SiC diodes was possible without significant degradation in the energy resolution, noise characteristics after exposures to a very high neutron fluence.

## 4.7 Conclusion

This chapter first investigated qualitatively the gamma rays interacting with the neutrons. Following from this is a discussion of the experimental results captured from LANSCE and TRIUMF. And then the beam monitoring system was evaluated and its testing protocols in each testing condition was analyzed.

The mass attenuation coefficient in silicon as a function of gamma rays energy was presented. Based on the mass attenuation shallow depletion depth and the photodiode depletion depth, the fraction of gamma rays absorbed in silicon was analyzed. The effect of  $\gamma$ -ray background at neutron facilities on the photodiode sensor was also investigated. The results show that no significant  $\gamma$  pulse events were generated at LANSCE while some low-energy events were captured at TSL, which could have been produced by gamma events from induced activity in the facility as well as the detector head itself.

Then the potential sources of errors in measurements were discussed. First, uncertainties in dosimetry are between 30% at TRIUMF and 5% at LANSCE. Second,

uncertainties in energy measurements occur because the sensor amplifier gains are calculated. The principal uncertainty indicated by this calculation is in the value of the preamplifier feedback capacitor, which is about 11%; the system noise could cause up to 5% of uncertainty.

Next, the beam monitoring testing protocols using at each facility were analyzed. At low interaction rates, such as LANSCE and TSL continuous beams, the transmission can be directly obtained from the number of pulse events and facility fluence at a standard point. At high interaction rates, such as those captured from TSL ANITA, the pile-up rate must be investigated in order to determine the transmission. The testing protocols at ChipIr were predicted on the basis of the principle of determining the mean of the pulse collected energy and the probability of events generated in one neutron beam as well.

Finally, the advantages of the beam monitor were discussed. For example, the components used are readily available and inexpensive. The system is small, simple, and effective. The methods on how to calibrate photodiode sensors were also recommended. Photodiode sensors suffer from performance degradation (response reduction) due to the neutron damage. In future work, other kinds of diodes for example of PIN, diamond diode or SiC diodes, which are less likely to suffer from neutron damage, can be investigated so that they can be used to replace photodiodes in beam monitoring.

# Chapter 5

## Conclusions

This thesis presents research that has developed a cost-effective and easy to use beam monitoring system. The overall aim and specific objectives put forward in chapter 1 are achieved. In this concluding chapter, a summary of the research undertaken in this project is provided, the major research findings are presented, the contributions and limitations of the present study are discussed, and finally directions for future research are suggested.

### 5.1 A summary of the research in this project

This section provides a brief summary of the research undertaken in the present project.

High-energy particle beams are used widely to enable accelerated testing of electronic devices and systems against neutron-induced SEEs. At some neutron facilities, such as TSL, LANSCE and ISIS, experiments can be carried out with several test sets arranged along a beam line. In such cases, however, the devices that are positioned further away from the beam source receive a degraded beam due to absorption and scattering by upstream experiments. The consequent loss of neutron fluence cannot be accounted for by typical upstream beam monitoring [54, 55]. In

## 5.1 A summary of the research in this project

---

order to make reliable estimates of SEE cross-sections, local neutron beam monitors are required.

As such, the present study has sought to develop a beam monitoring system based on photodiode sensors so that tests can be undertaken on several devices simultaneously at neutron beam facilities such as LANSCE, TSL and ISIS, which demonstrated the utility of correcting for the beam degradation by upstream experiments. In this project, twelve sensors with slightly different circuits and two kinds of pulse widths (20  $\mu\text{s}$  and 40  $\mu\text{s}$ ) have been developed and irradiated at TSL, TRIUMF, ASP and LANSCE. This thesis introduces the system design, signal processing in the system, and the experimental results; the performance of the system is also evaluated and testing protocols recommended.

The beam monitoring system developed in this project is simple, small and inexpensive. In the photodiode sensor, a Centronic OSD1-5T silicon photodiode is used as the detecting element, and TLE207x [111] series of JFET-input operational amplifiers are used in the multi-stage amplifiers. The photodiode detector circuit converts the charge produced by the interaction of a neutron with the photodiode into a pseudo-Gaussian pulse with amplitude which is proportional to the energy collected from a neutron interaction. Time series data are captured by using a PCI-6251 DAQ card that is controlled by a LabVIEW software package. The components and devices used in the system are readily available and inexpensive.

In the beam monitoring signal processing system, the nonparalyzable method is used in a counting system to acquire the arrival times of pulses, which allows the beam monitoring system to determine the interaction rates either based on the sensor pulse width and the detected pulse rate or the decay constant of the pulse interval distributions captured in a continuous neutron beam.

Pulse amplitudes are detected by using matched-filter techniques. The minimum detected pulse height (or detected energy) decreases with the increase of the false alarm rate and sample rate, and increases with the rise of the noise level and the

## 5.1 A summary of the research in this project

---

number of sensors under test. This technique allows the pulse event to be detected effectively at a low false event rate.

The optimum sensor pulse width is examined and selected to achieve the maximum probability of detection by balancing the SNR ratio and the effect of pile-up without degrading energy resolution. At low interaction rates, such as LANSCE and TSL quasi-monoenergetics beams, the optimum pulse width should be quite wide. In contrast, at high interaction rates, such as TSL ANITA, the optimum pulse width should be as narrow as possible. However, this optimum pulse width is limited by the sampling resolution of the sensor pulse; the sampling of one pulse should not be less than 10. In this case, the pulse width should be balanced by the optimum pulse width and the sampling point for each pulse.

A series of calculations has been undertaken to support the correct operation of the detection system and to investigate system performance variations. In each calculation case, the predicted and actually detected probability of detection agreed very well. The pulse height spectra fit parameter (decay constant) decreases with the increase of the pile-up rate.

In order to determine the transmission along the neutron beam, a number of experiments were conducted with two sensors at LANSCE. In the absence of devices the fluence received at a downstream position can be simply determined using upstream beam monitoring and an  $r^{-2}$  law. To determine sensor characteristics and the effect of the pulsed neutron beam, two sensors were irradiated together at the upstream position. The measured pulse interval distribution reflected very clearly the neutron beam time structure, which forms a comb at multiples of the accelerator repetition period (16.7 ms) modified by the characteristic exponential form of a Poisson process. The  $n \times 50$  ms component of the beam (i.e. every third peak) was enhanced by a factor of 2, reflecting the 20 Hz periodicity of the incident neutron beam.

To determine the degrading influence of upstream experiments in the beam line, two sensors were irradiated upstream and downstream with an aluminium scatterer.

## 5.1 A summary of the research in this project

---

The transmission along the beam could be enhanced, because secondary particles knocked out of the aluminium scatterer, but secondary sources were insignificant by the time the position of downstream device was reached if the downstream device was far away from the scatterer.

The photodiode-based beam monitoring system can provide useful information on the fluence and hardness of a neutron field at multiple locations in a beam. Two sensors were also irradiated upstream and downstream with one or three other experiments between them. The trend of the transmissions decrease significantly when the threshold collected energy is below 1 MeV, and slightly increase when the threshold energy is above 1 MeV. These suggest that:

1. Secondary particles can be generated by the upstream experiments interacting with neutrons, and these secondary particles can deposit low energy events in downstream devices.
2. Low-energy neutrons are more likely to suffer scattering than high-energy neutrons.

At 1 MeV threshold energy, the transmission along the beam line was 67% (with one sample between two sensors) and 46% (with three samples), indicating that scattering out of the beam is the dominant mechanism for the decrease in flux.

Determining the transmission along the neutron beam in multi-positions during the SEEs testing is based on the pulse height spectra, pulse interval distribution, and the sensor response. These require that the sensor responses should be similar. A number of experiments were conducted at TRIUMF to investigate the effect of the amplifier, and the influence of the photodiode window on neutrons. The results suggest that the amplifier circuit irradiated with a neutron beam can increase the rate of detection by about 4% over the pulses detected when the photodiode alone is used. In general, the amplifier was outside the nominal beam profile, but downstream sensors are possibly affected by any upstream scatterers and secondary particles. In this case, the false events could be dominated by amplifiers. The

## 5.1 A summary of the research in this project

---

interaction rate of the windowed sensor irradiated in the neutron beam was higher than the sensor with the delidded photodiode, and the results from ASP irradiation showed that pulse detection rates were different with two kinds of photodiode doping profiles, so the responses in these cases were different. In the beam monitoring system, the photodiode sensors should have the same profiles, and all of them should be either delidded or windowed in the beam monitoring system during SEEs testing.

The pulse interval distributions captured at LANSCE suggested that there were no significant interactions between gamma rays and the photodiode sensor. At TSL, induced radioactivity in components in the beam line, including the detector itself, can be significant. However, the characteristic pulse energy and temporal behavior of induced gamma events ensure that they are easily identified and excluded from analysis if necessary. In this work the low event rate of induced events meant that such exclusion was not necessary. Hence, the influence of gamma radiation can be excluded as a significant component of the interactions studied in this thesis.

The pulse height spectra are high at low deposited energy, the potential source are which can be accounted for by the following:

1. There are proton components in the neutron beam [132,141]. Protons passing the active region are likely to dominate the low-energy part of our pulse-height spectrum.
2. The low-energy events in photodiode sensor irradiated at TSL ANITA were dominated by gamma events from induced activity in the detector head itself and the beam hall.
3. Based on the volume of the diode junction region and the boron dopant density in silicon,  $5 \times 10^4$  boron is estimated to be contained in photodiode sensor. The experimental results captured at TRIUMF with or without cadmium shielding, and ASP 3 MeV neutron beam showed that  $^{10}\text{B}(n,\alpha)^7\text{Li}$  reaction. Photodiode sensor contains  $^{10}\text{B}$  in the active (depletion) region which can

## 5.1 A summary of the research in this project

---

interact with thermal neutrons, consistent to the structure just below 2 MeV in the pulse-height spectra.

The potential sources of uncertainties in response measurements include:

1. Dosimetry uncertainty was about 30% at TRIUMF, 5% at LANSCE, and 10% at TSL.
2. In energy measurements, the systematic uncertainty was about 11%. The principal uncertainty of this calculation was in the value of the preamplifier feedback capacitor ( $2.2 \pm 0.25$  pF) while the random uncertainties such as noise were up to 5%, which was decided by the number of sample points in each pulse.
3. The number of pulse events were quoted at upper and lower limits at 68.27% confidence interval(CI) based on standard equations derived from Poisson statistics.

One key parameter to determine the transmission along the beam is the pile-up rate. Different pile-up rates captured at multi-locations during SEEs testing can lead to an significant error in transmission to downstream location. Testing protocols have been investigated on the basis of the pile-up rate as follows:

- LANSCE—The detected rates at LANSCE were quite low, and pile-up was not significant. In such cases, the transmission can simply be calculated on the basis of the number of pulse events in the sensor and the neutron fluence at the facility standard point.
- TSL pulsed neutron beam — The average of pulse events per macropulse was 2.45 at TSL ANITA when the neutron flux was up to  $1.1 \times 10^6$  cm<sup>-2</sup>s<sup>-1</sup>. The pile-up rate should be significant. In high flux pulse neutron beams, the pile-up rate should be determined since it can be calculated on the basis of

the pulse detection rate and the sensor pulse width using the nonparalyzable counting system. Then the transmission can be calculated based on the pile-up rate, the number of pulse events and the neutron fluence at the facility standard point.

- TSL continuous neutron beam—The transmission can simply be determined on the basis of the number of pulse events in the sensor and the neutron fluence at the facility standard point.
- Predicted testing protocols at ChipIr — A reference measurement of pulse height spectrum should be acquired when there is no significant pile-up rate. The transmission can be determined by examining the ratio of the mean of the detected energy, the mean of the reference pulse height spectrum and the pulse interval distribution.

## 5.2 Major research findings

This section presents the major research findings through an evaluation of the performance of the beam monitoring system developed in the research project.

In the beam monitoring system, the technique of matched-filter are used in signal processing to strengthen the pulses height at a low false alarm. The minimum detected pulse height increases with the decrease of the sample rate (sample of the pulse), the increase of the noise level and the number of photodiode sensors under test.

The calculation results (see §2.4.6) show that the interaction rate in the photodiode sensor can be determined by investigating the exponential fit of the pulse interval distribution for irradiation in a continuous neutron beam. In pulsed neutron beams, the pulse interval distributions are a combination of the Poisson distribution and pulsed neutron beam interval distribution. The experimental results and the theory

of this counting system agree very well in determining the pile-up rate (see §3.4.2). This pile-up rate can be used to determine the beam monitoring testing protocols at each beam facility. The beam monitoring testing protocols for testing at LANSCE and TSL were developed on the basis of pulse pile-up rates. The testing protocols for testing at ChipIr was predicted on the basis of the pulse height spectra captured at LANSCE.

Analysis of the pulse height spectra and pulse interval distribution captured from the neutron facilities shows that the beam monitor can measure the transmission of the neutron beam by measuring the neutron fluence simultaneously at key locations along the the beam in cases where several experiments are arranged along a beam line during SEEs testing.

### 5.3 Contributions and limitations

This project has demonstrated minimally-intrusive measurements in an accelerated testing campaign. The photodiode-based beam monitoring system have been developed in the project so that tests can be undertaken on several devices simultaneously in neutron beams such as LANSCE and TSL. The system has also demonstrated the utility of local beam monitoring to correct for beam degradation by upstream experiments.

Overall, the photodiode based beam monitoring system is simple yet effective in detecting neutrons, which can provide useful information on the fluence and hardness of a neutron field at multiple locations in a high-energy neutron beam. The components used are readily available and inexpensive. The system is small in size and simple to use, and can be easily incorporated into test sets or otherwise used to instrument SEE experiments.

With that said, the beam monitoring system has a limitation associated with the

diode used in the system. As the experiment results in §3.4.5 show, photodiode has two doping profiles. One can result in a higher interaction rate than the other; and also the measurements of the pulse height spectra in the diodes with the two profiles are slightly different [142]. If the beam monitoring system is irradiated with several photodiode sensors simultaneously, in order to reduce uncertainty and get the accurate transmission, these photodiode sensors should have the same doping profile.

In addition, there is further work to be undertaken to improve the system. For example, the system does not attempt to optimise sensor amplifier gains, and the circuit for data collection in the present version also needs calibration. A Geant4 model of the detector can also be implemented in order to better understand the detailed physics of its operation (see §5.4).

## 5.4 Suggestions for future research

As noted earlier, several areas have been identified in writing up this thesis where future work is required:

First, simulations can improve the understanding of the underlying phenomena of the interaction of the particle radiation with the photodiode sensor. They can thus play a major role in understanding beam monitoring performance. In future, nuclear physics code, eg. Geant4 [58], MCNPX [59] and Fluka [60] techniques can be used to model pulse height spectra so as to enable direct comparisons of theoretical simulations and empirical experiment data. Simulations can also help to investigate the use of other types of diode, such as PIN, SiC, and diamond diode which are less likely to suffer neutron damage as detect elements in beam monitoring.

Secondly, as discussed in §4.3, the sensor amplifier gains were calculated in this project. This led to a systematic uncertainty in determining the transmission. In future work, the sensor should be calibrated, for example, by using a cadmium

## 5.4 Suggestions for future research

---

source, or applying gold to the sensor during the high-energy neutron beam SEEs testing.

Thirdly, the experimental results from LANSCE showed that the beam monitoring system can provide useful information about the fluence and hardness of a neutron field at multiple locations in a beam. In future the predicted SEEs rate from photodiode monitoring should be compared with the SEEs testing results of other experiments.

Finally, the protocols of beam monitoring system used in determining the transmission along the neutron beam at LANSCE, TSL and ISIS were developed in this project. In future, experiments should be designed to verify the correct measurement of the neutron fluence at several locations at ISIS ChipIr or TSL ANITA.

# Appendix A

## Photodiode sensor circuit

Figures A.1 and A.2 show example schematics of the photodiode sensor circuit, which was designed by Dr. Platt. The first stage of amplification consists of a charge-amplifier with a feedback capacitor. Second stages provide a multi-order shaping filter following the design of Ohkawa et al. [143], providing a pseudo-gaussian pulse.

In figure A.2, ‘CAN1’ and ‘CAN2’ were designed to shield the sensor from external static noise. The sensor can be tested by sending a square signal at ‘Test in’, which will then the preamplifier pulse at ‘UNCOMP’ point output and deliver the shaping pulse at ‘PULSEOUT’ point.

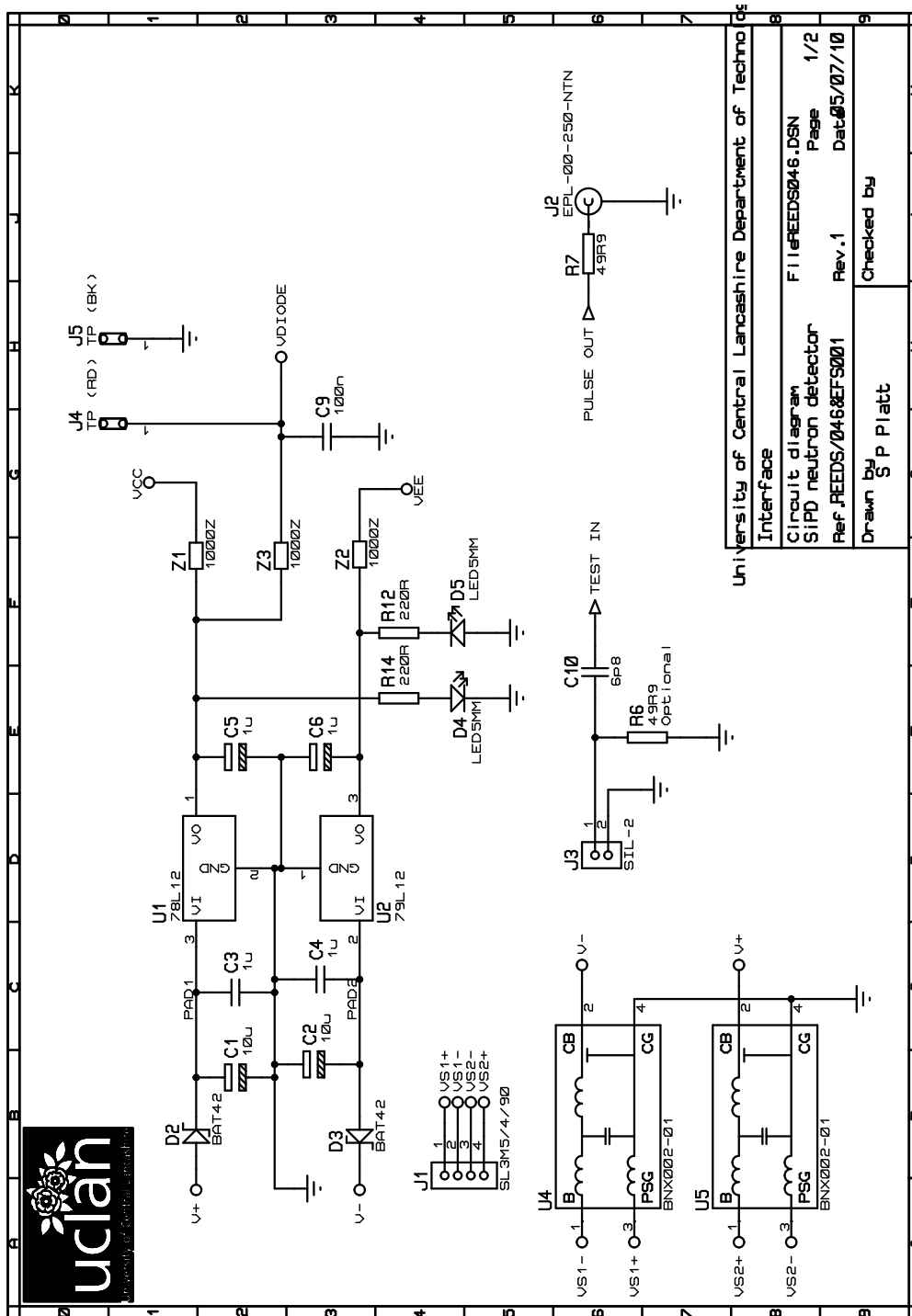


Figure A.1: Schematics of photodiode sensor power circuit

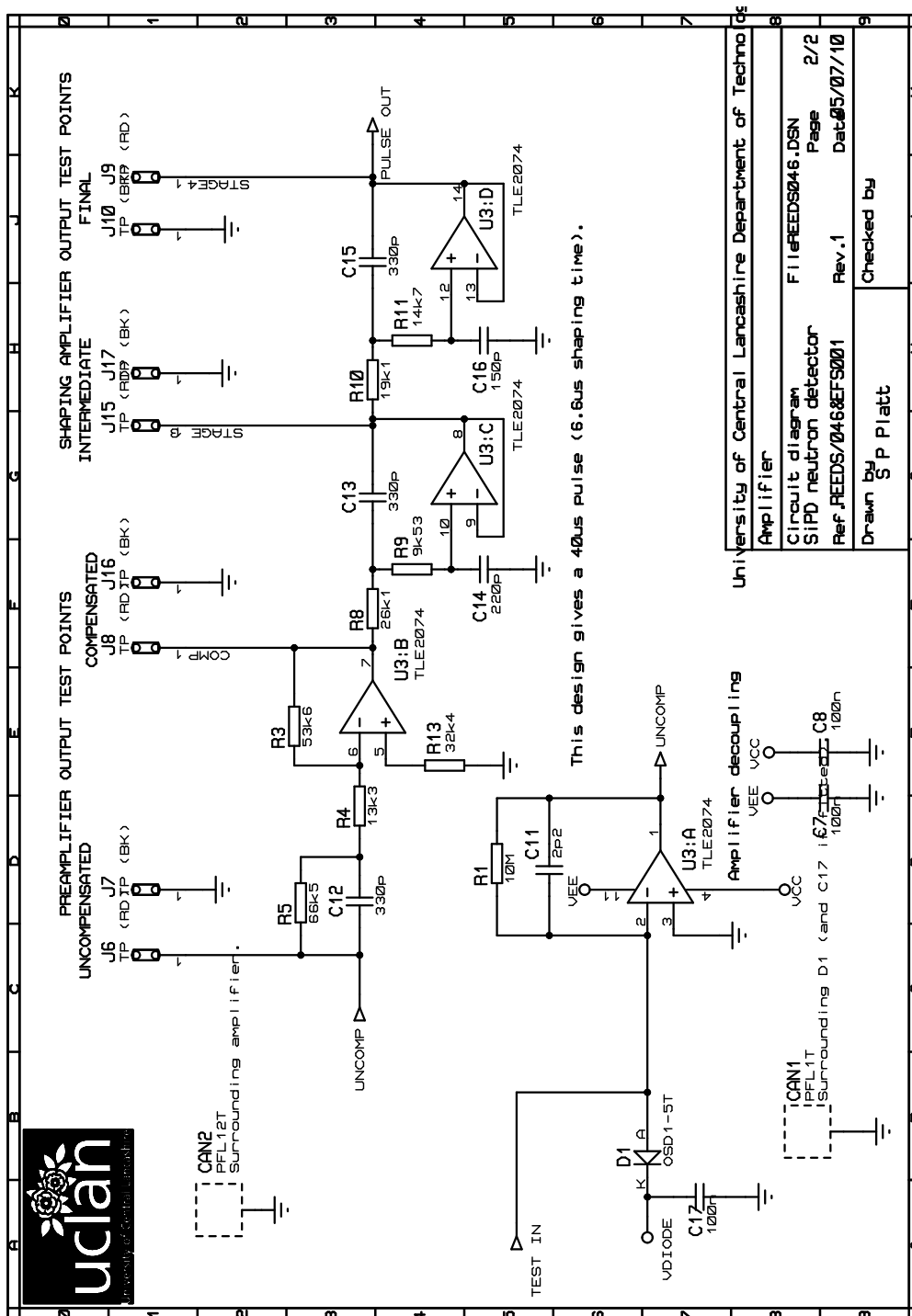


Figure A.2: Schematics of photodiode sensor amplifier circuit

# Appendix B

## Matched filter threshold level determination

This appendix is a description of the determination of the matched filter technique based on Kay [114].

### B.1 Fundamental probability density function

The Gaussian white noise (GWN) Probability density function (PDF) (also referred to as normal PDF) for a scalar random  $x$  is defined as:

$$p(x) = \frac{1}{\sqrt{2\pi\delta^2}} \exp\left[-\frac{1}{2\delta^2}(x - \mu)^2\right] \quad -\infty < x < \infty \quad (\text{B.1})$$

where  $\mu$  is the mean and  $\delta^2$  is the variance of  $x$ . It is denoted by  $N(\mu, \delta^2)$ , which is the normal distribution with the mean  $\mu$  and variance  $\delta^2$ .

The Cumulative distribution function (CDF) for  $\mu = 0$  and  $\delta^2 = 1$ , for which the PDF is termed a standard normal PDF, is defined as

$$\Phi(x) = \int_{-\infty}^x \frac{1}{\sqrt{2\pi}} \exp\left(-\frac{1}{2}t^2\right) dt \quad (\text{B.2})$$

A more convenient description, which is termed the right-tail probability and is the probability of exceeding a given value, is defined as  $Q(x) = 1 - \Phi(x)$ , where

$$Q(x) = \int_x^{\infty} \frac{1}{\sqrt{2\pi}} \exp\left(-\frac{1}{2}t^2\right) dt \quad (\text{B.3})$$

The function  $Q(x)$  is also referred to as the *complementary cumulative distribution function*, which is the probability that a  $N(0, 1)$  random variable exceeds  $x$ . An approximation is

$$Q(x) \approx \frac{1}{\sqrt{2\pi}x} \exp\left(-\frac{1}{2}x^2\right) \quad (\text{B.4})$$

## B.2 Threshold level

Consider the detection problem

$$\begin{aligned} H_0 : x[n] &= \omega[n] & n=0,1,\dots,N-1 \\ H_1 : x[n] &= s[n] + \omega[n] & n=0,1,\dots,N-1 \end{aligned}$$

where  $H_0$  is the hypotheses with noise only, and  $H_1$  is the hypothesis with both signal and noise.  $P(H_1; H_0)$  is referred to as the probability of false alarm  $P_{FA}$  while  $P(H_1; H_1)$  is the probability of detection, which is expressed as  $P_D$ .

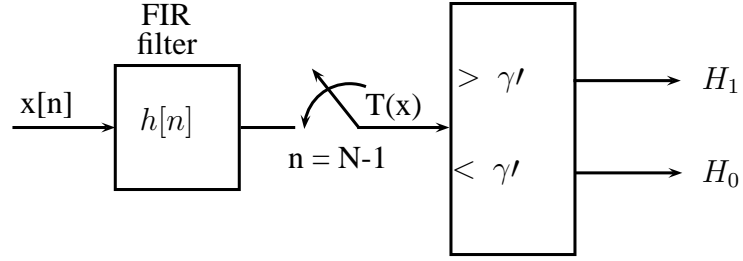


Figure B.1: Detecting signal in Matched filter

The output of the matched filter is:

$$T(x) = \sum_{n=0}^{N-1} x[n]s[n] > \gamma' \quad (\text{B.5})$$

where  $x[n]$  is the input signal, and  $s[n]$  is the reference signal. The detector of the matched filter is shown in figure B.1.

Let  $E(T; H_i)^1$  and  $var(T; H_i)^2$  denote the expected value and variance  $T(x)$  under  $H_i$ , then

$$E(T; H_0) = E\left(\sum_{n=0}^{N-1} \omega[n]s[n]\right) = 0$$

$$E(T; H_1) = E\left(\sum_{n=0}^{N-1} (s[n] + \omega[n])s[n]\right) = \varepsilon$$

where  $\varepsilon$  is the energy.

<sup>1</sup> $E(x; H_i)$ : expected value of  $x$  assuming  $H_i$  true.

<sup>2</sup> $var(x; H_i)$ : variance of  $x$  assuming  $H_i$  true.

$$\begin{aligned}
 \text{var}(T; H_0) &= \text{var}\left(\sum_{n=0}^{N-1} \omega[n]s[n]\right) \\
 &= \sum_{n=0}^{N-1} \text{var}(\omega[n])s^2[n] \\
 &= \delta^2 \sum_{n=0}^{N-1} s^2[n] = \delta^2 \varepsilon
 \end{aligned}$$

Similarly,  $\text{var}(T; H_1) = \delta^2 \varepsilon$ . Thus, the test statistic  $T$  is

$$T \sim \begin{cases} N(0, \delta^2 \varepsilon) & \text{under } H_0 \\ N(\varepsilon, \delta^2 \varepsilon) & \text{under } H_1 \end{cases} \quad (\text{B.6})$$

Note that the scaled test  $T' = \frac{T}{\sqrt{\delta^2 \varepsilon}}$ , which is:

$$T \sim \begin{cases} N(0, \delta^2 \varepsilon) & \text{under } H_0 \\ N(\varepsilon, \delta^2 \varepsilon) & \text{under } H_1 \end{cases} \quad (\text{B.7})$$

The PDF of matched filter test statistic is shown in figure B.2.

The probability of false alarm  $P_{FA}$  is:

$$\begin{aligned}
 P_{FA} &= \text{Pr}(T > \gamma'; H_0) \\
 &= Q\left(\frac{\gamma'}{\sqrt{\delta^2 \varepsilon}}\right)
 \end{aligned} \quad (\text{B.8})$$

where (see last section)

$$\begin{aligned}
 Q(x) &= \int_x^\infty \frac{1}{\sqrt{2\pi}} \exp\left(-\frac{1}{2}t^2\right) dt \\
 &= 1 - \phi(x)
 \end{aligned}$$

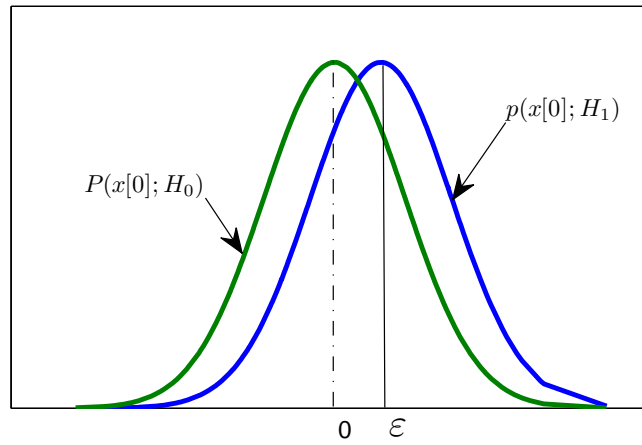


Figure B.2: PDFs for a hypothetical testing problem

Based on equation B.8, the threshold level  $\gamma'$  of the output of the matched filter is:

$$\gamma' = \sqrt{\delta^2 \epsilon} Q^{-1}(P_{FA}) \quad (\text{B.9})$$

# Appendix C

## Additional information of experimental results captured at LANSCE

This appendix contains additional experimental results captured at LANSCE.

The experimental data in runs LAN01 to LAN05 were collected for each sensor at the 0.5 MHz sample rate. At this sample rate, the minimum detected energy from sensor 11 was 132 keV and sensor 12 was 112 keV, the numbers of events are summarized in table C.1.

The transmission (see §3.4.1.2) of the two sensors with or without a scatterer with various threshold energy level for collecting events above 171.7 keV captured at LANSCE are summarized in table C.2, which also gives the numbers of pulse events in sensor 11 and 12 in runs LAN06, LAN07 and LAN08.

The photodiode monitor system was irradiated over four days during the experiments, including 18 runs (see §3.4.1.4). In all runs, sensor 11 was tested in the

---

Table C.1: Experimental results of two sensors irradiated in the upstream position at LANSCE

FacilitySignal		Pulse number	
Run	Processing	sensor 11	sensor 12
LAN01	post-processing	5760	6162
LAN02	real-time	11 922	13 091
LAN03	real-time	8335	8933
LAN04	real-time	5090	5466
LAN05	real-time	19 299	21 149

upstream position without other any experiments in front of it. Table C.3 summarizes the numbers of pulse events and the responses with the collected energy above 171.7 keV.

Table C.2: The transmission of two sensors irradiated at LANSCE with or without a scatterer with various collected threshold energy

Deposited energy Threshold, MeV	Facility Run	sensor 11 pulse number	sensor 12 pulse number	transmission $\tau(r)$ , %
0.1717	LAN06	4806	4377	102.73
	LAN07	4352	4830	101.77
	Lan08	4710	6707	160.58
0.5	LAN06	2783	2526	102.36
	LAN07	3026	2706	100.84
	LAN08	2644	3078	131.28
1	LAN06	1726	1570	102.58
	LAN07	1875	1674	100.68
	LAN08	1687	1706	114.04
1.5	LAN06	1194	1082	102.19
	LAN07	1285	1142	100.22
	LAN08	1169	1106	106.69
2	LAN06	748	656	98.90
	LAN07	806	733	102.56
	LAN08	740	662	100.88
2.5	LAN06	531	477	101.3
	LAN07	586	525	101.03
	LAN08	540	441	92.91
3	LAN06	396	362	104.19
	LAN07	462	404	98.61
	LAN08	429	334	87.80

Table C.3: The numbers of pulse events and responses in sensor 11 captured at LANSCE

Day	Run	Pulse of events	response,cm <sup>2</sup>	
			above1.5 MeV	above10 MeV
1	LAN01	4609	$2.424 \times 10^{-5}$	$4.495 \times 10^{-5}$
	LAN02	9635	$2.459 \times 10^{-5}$	$4.559 \times 10^{-5}$
	LAN03	6775	$2.418 \times 10^{-5}$	$4.483 \times 10^{-5}$
	LAN04	4181	$2.332 \times 10^{-5}$	$4.322 \times 10^{-5}$
	LAN05	16106	$2.309 \times 10^{-5}$	$4.281 \times 10^{-5}$
	LAN09	11188	$2.244 \times 10^{-5}$	$4.160 \times 10^{-5}$
2	LAN12	7833	$2.115 \times 10^{-5}$	$3.943 \times 10^{-5}$
	LAN13	6731	$2.084 \times 10^{-5}$	$3.887 \times 10^{-5}$
	LAN14	32057	$2.093 \times 10^{-5}$	$3.902 \times 10^{-5}$
3	LAN10	3639	$2.069 \times 10^{-5}$	$3.868 \times 10^{-5}$
	LAN15	5341	$1.985 \times 10^{-5}$	$3.711 \times 10^{-5}$
	LAN06	4806	$1.966 \times 10^{-5}$	$3.677 \times 10^{-5}$
	LAN07	5352	$1.913 \times 10^{-5}$	$3.566 \times 10^{-5}$
	LAN08	4710	$1.950 \times 10^{-5}$	$3.646 \times 10^{-5}$
	LAN16	9811	$1.903 \times 10^{-5}$	$3.558 \times 10^{-5}$
4	LAN17	2277	$1.926 \times 10^{-5}$	$3.516 \times 10^{-5}$
	LAN18	5598	$1.925 \times 10^{-5}$	$3.513 \times 10^{-5}$
	LAN11	12250	$1.967 \times 10^{-5}$	$3.589 \times 10^{-5}$

## Appendix D

### Neutron penetrating the aluminum scatterer

The aluminum scatterer (see §3.4.1.2) is about 4 mm thick, The percentage of neutron fluence that could penetrate the scatterer can be determined by:

$$P_{fluence} = e^{-\mu_1 x} \quad (D.1)$$

where  $x$  is the thickness of the aluminum scatterer and  $\mu_1$  is the linear attenuation coefficient for neutron calculated by:

$$\mu_1 = \sigma_T N_A \rho / A \quad (D.2)$$

where  $N_A$  is the Avogadro's number,  $\rho$  is the density of aluminum,  $A$  is the aluminum atomic mass and  $\sigma_T$  is the total cross section of neutron interaction with aluminum.

When neutron energy is about 1 MeV,  $\sigma_T$  is about 2b [144], which is  $2 \times 10^{-24} \text{cm}^2$ ,  $\mu_1$  will be  $-0.12 / \text{cm}$ . According to equation D.1, the percentage of neutron penetrating the aluminum is about 95.31%

# Appendix E

## Confidence limits for the number of pulse events in beam monitoring system

The number of pulse events is typically quoted as the upper limit at a specified confidence level or as a measured value with error bars containing a specified confidence interval. Conventionally, error bars plotted in the measured pulse height spectra in this thesis are 84.13% confidence upper and lower limits containing a 68.27% confidence interval(CI). The calculation of limits for the number of pulse events is based on standard equations derived from Poisson statistics [118].

The standard deviation of  $N$  events is  $\sqrt{N}$  (assuming to be  $\sigma$ ). The fraction of standard deviation is  $\sqrt{N}/N$ . A large number of pulse events approach a Gaussian distribution [119], The probability that the true value of the measured pulse events within the CI  $(N - \sqrt{N}, N + \sqrt{N})$  is 68.27%, and CI  $(N - 2\sqrt{N}, N + 2\sqrt{N})$  is 95%.

When  $N$  is small, the distribution is Poisson rather than Gaussian. The upper limit  $\lambda_u$  and lower limit  $\lambda_l$  are defined by [118]:

$$\sum_{x=0}^N \frac{\lambda_u^x e^{-\lambda_u}}{x!} = 1 - CL \quad (\text{E.1})$$

---


$$\sum_{x=0}^N \frac{\lambda_l^x e^{-\lambda_l}}{x!} = CL \quad (\text{E.2})$$

where CL is the confidence level. Double-side CL of CI can be obtained by [118]:

$$CL = (1 + CI)/2 \quad (\text{E.3})$$

$\lambda_u$  and  $\lambda_l$  can be determined by Matlab function `chi2inv(P, V)`:

$$\lambda_u = 0.5 * (\text{chi2inv}(CI, 2 * (N + 1))) \quad (\text{E.4})$$

$$\lambda_l = 0.5 * (\text{chi2inv}((1 - CI), 2 * N)) \quad (\text{E.5})$$

Table E.1 lists one standard deviation, and the confidence levels for some numbers of events described by the Poisson distribution and their standard deviation.

Table E.1: Limits of confidence interval of Poisson distribution for CI of 68.27% and 95%, and to one of standard deviation

Events	Standard deviation		CI=68.27%		CI=95%	
	$N + \sqrt{N}$	$N - \sqrt{N}$	upper	lower	upper	lower
0	0.0	0.0	1.84	0.0	3.69	0.0
1	2.0	0.0	3.30	0.17	5.57	0.03
2	3.41	0.56	4.64	0.71	7.22	0.24
3	4.73	1.27	5.92	1.37	8.77	0.62
4	6.0	2.0	7.16	2.09	10.24	1.09
5	7.24	2.76	8.38	2.84	11.67	1.62
6	8.45	3.55	9.58	3.62	13.06	2.20
7	9.65	4.35	10.77	4.42	14.42	2.81
8	10.83	5.17	11.94	5.23	15.76	3.45
9	12.0	6.0	13.11	6.06	17.08	4.12
10	13.16	6.83	14.26	6.89	18.39	4.80
11	14.32	7.68	15.42	7.73	19.68	5.49
12	15.46	8.54	16.56	8.58	20.96	6.20
13	16.61	9.39	17.70	9.44	22.23	6.92
14	17.74	10.26	18.83	10.30	23.49	7.65
15	18.87	11.13	19.96	11.17	24.74	8.40
16	20.0	12.0	21.08	12.04	25.98	9.15
17	21.12	12.88	22.20	12.92	27.22	9.90
18	22.24	13.76	23.32	13.80	28.45	10.67
19	23.36	14.64	24.44	14.68	29.67	11.44
20	24.47	15.53	25.55	15.57	30.89	12.22
100	110.	90.0	111.03	90.02	121.63	81.36
200	214.14	185.86	215.17	185.87	229.72	173.24
300	317.32	282.68	318.34	282.69	335.94	267.01
400	420.0	380.0	421.02	380.01	441.19	361.76
500	522.36	477.64	523.38	477.65	545.81	457.13
600	624.49	575.51	625.51	575.51	649.99	552.94
700	726.46	673.54	727.47	673.55	753.83	649.10
800	828.28	771.72	829.30	771.72	857.41	745.52
900	930.0	870.0	931.01	870.0	960.77	842.15
1000	1031.62	968.38	1032.60	968.38	1064.0	938.97

# Appendix F

## Publications

1. L. Zhang, S. Platt, R. Edwards, and C. Allabush, “In-situ neutron dosimetry for single-event effect accelerated testing,” *IEEE Transactions on Nuclear Science*, vol. 56, no. 4, pp. 2070-2076, Aug. 2009.
2. Lyn. H. Zhang, S. P. Platt, “Minimally invasive neutron beam monitoring for single-event effects accelerated testing” in *Proc. European Conf. Rad. Effects. Compon. Syst. (RADECS 2011)*, Sep. 2011

# In-situ neutron dosimetry for single-event effect accelerated testing

Lyn H. Zhang\*, S. P. Platt\*, R. H. Edwards† and C. Allabush‡

**Abstract**—We describe an in-situ fast neutron dosimetry system using silicon photodiodes, and discuss its application to accelerated testing for single-event effects (SEEs). Experimental data and theoretical analyses are presented and concept feasibility demonstrated.

## I. INTRODUCTION

High-energy particle beams are widely used to enable accelerated testing of electronic devices and systems against neutron-induced single-event effects (SEEs) [1]–[5]. Intense beams of high-energy neutrons or proxy protons can be used to simulate effects due to cosmogenic neutrons, generating events with rates several orders of magnitude greater than those experienced in typical terrestrial or avionic applications. The penetrating power of neutrons permits testing to be carried out in cases where several experiments are arranged along a beam line. In such cases, however, the devices that are positioned further away from the beam source receive a reduced neutron flux due to absorption and scattering by upstream experiments [6], [7]. The consequent loss of neutron flux cannot be accounted for by facility dosimetry. In order to make reliable estimates of SEE cross-sections in such cases, in-situ dosimetry is required; this may also provide additional benefits, for example in benchmarking between beams. We are developing a system to provide this capability, and have undertaken preliminary tests at the Theodor Svedberg Laboratory (TSL [8], [9]) and the Tri-University Meson Facility (TRIUMF [10]) accelerators. In this paper, we will introduce the system design, discuss signal processing in the system, and present our initial results from the experiments.

## II. METHOD

### A. Photodiode neutron detector

Our detector system uses a Centronic OSD1-5T silicon PN photodiode [11] as the detecting element. This device has an active area of  $1\text{ mm}^2$  and its active (depletion) depth is estimated from its geometry and typical capacitance to be about  $15\text{ }\mu\text{m}$ . The TO-18 diode packages were delidded to remove the optical window and covered with aluminium foil to exclude ambient light. The diodes were operated with  $12\text{ V}$  reverse bias and d.c. coupled to a two-stage amplifier comprising a charge-sensitive preamplifier followed by a pulse shaper. An example

\*School of Computing, Engineering and Physical Sciences, University of Central Lancashire, Preston, Lancs. PR1 2HE, England, Tel: +44 (0)1772 895167 Fax: +44 (0)1772 892915 Email: hzhang@uclan.ac.uk

†Goodrich Engine Control and Electrical Power Systems, York Road, Hall Green, Birmingham, B28 8LN, England.

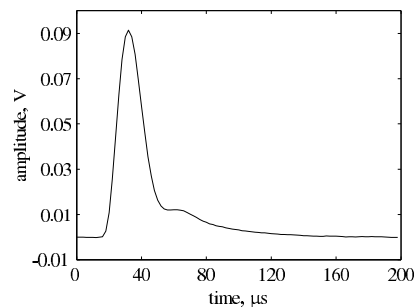


Fig. 1: Example detector pulse from a 23 MeV interaction

output pulse is shown in Fig. 1. The amplifier design is not yet optimised and the circuits used to gather the experimental data presented here were not calibrated; however, based on the nominal value of amplifier parameters and assuming an ionization energy of  $3.6\text{ eV}$  [12], the nominal sensitivity of the amplifier (expressed simply as pulse peak voltage  $\div$  collected energy) is  $4\text{ mV}\cdot\text{MeV}^{-1}$ . This value is assumed in the results presented in §IV below. The pulse shown in Fig. 1, an example from an exposure at TRIUMF, corresponds to a collected energy of 23 MeV.

To investigate the effect of neutron interaction in the amplifier circuit, we have two different circuit configurations: with the diode and preamplifier collocated and with them separated. In this way were able to irradiate the detector and amplifier separately or together.

### B. Experimental conditions

Exposures were made at TRIUMF, an atmospheric-like neutron source with maximum energy around  $400\text{ MeV}$  [10], and at TSL using several beam configurations: quasi-monoenergetic neutron beams with peak energies near  $25\text{ MeV}$ ,  $50\text{ MeV}$  and  $110\text{ MeV}$  [8], and the new atmospheric-like neutron source, ANITA, with energies up to about  $180\text{ MeV}$  [9]. Pulse data were captured using a standard data acquisition system at sample rates up to  $1\text{ MHz}$ . Fig. 2 shows example  $1\text{ s}$  voltage time series captured in each of the neutron beams studied here. The greater pulse rate at TRIUMF reflects both the greater neutron flux at that facility and also the effect of upstream experiments at TSL, which degrade the neutron beam further down the beam line. Our experiments at TSL were made downstream of several other experiments, where

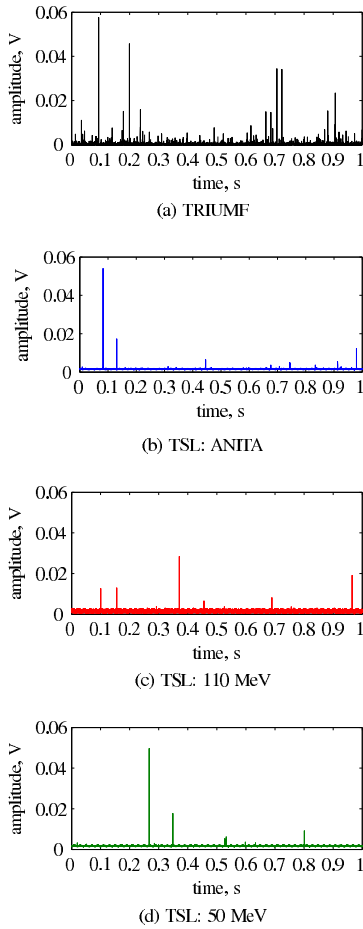


Fig. 2: Example voltage time series

the beam was severely degraded. In addition, the TSL cyclotron is operated in pulsed mode when at the higher energies, so that interactions are possible only at discrete times. The implications of pulsed beams are discussed in §V, below. In each pulsed field discussed here (ANITA and 110MeV, our detected interaction rate was significantly less than the beam repetition rate. Observed interaction rates ranged from about  $1 \text{ s}^{-1}$  to over  $1600 \text{ s}^{-1}$  at TRIUMF.

We investigated the influence of thermal neutrons by making irradiations with and without cadmium shielding at TRIUMF, where the low-energy neutron flux is a little under a third of that above 10MeV.

### C. Signal processing

Pulses were extracted from the time series data gathered from the preamplifier output using a matched filter technique [13], [14]. A block diagram of the pulse detection and estimation system is shown in Fig. 3.

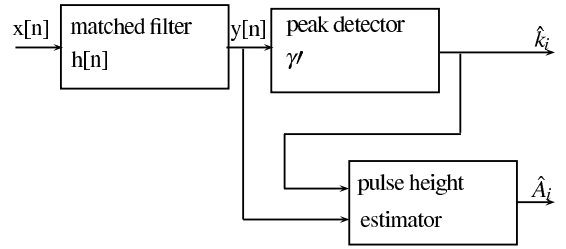


Fig. 3: Pulse detection and estimation system

The input  $x$  at sample  $n$  can be expressed as

$$x[n] = \sum_i A_i s[n - k_i] + \omega[n]$$

where  $A_i$  is the height and  $k_i$  the location in time of pulse  $i$ ,  $s$  is the pulse shape, and  $\omega$  is noise. The matched filter impulse response is

$$h[n] = s[M - 1 - n]$$

where  $M$  is the length of the reference signal  $s$ .

Pulses are detected if the matched filter output exceeds a threshold level  $\gamma$ . Matched filter detection is optimum in additive white gaussian noise, which is a close approximation to the statistics of most intrinsic noise processes. In that case the threshold can be chosen to control the probability of false alarm,  $P_{FA}$  using the (standard) inverse  $Q$  function [14]:

$$\gamma = \sigma Q^{-1}(P_{FA}) \sqrt{\sum_{n=0}^{M-1} s^2[n]}$$

where  $\sigma$  is the r.m.s. value of the noise signal  $\omega[n]$ . Peak detection determines the estimated locations  $\hat{k}_i$  of pulses where  $y[n]$  exceeds  $\gamma$ ; pulse heights are estimated as

$$\hat{A}_i = \frac{y[\hat{k}_i]}{\sum_{n=0}^{M-1} s^2[n]}$$

Statistics of pulse heights  $\hat{A}_i$  and intervals  $\hat{k}_i - \hat{k}_{i-1}$  are straightforward to generate from simulated or real sample sequences.

External noise sources may be more significant than intrinsic noise. Accelerator facilities are often electrically noisy environments, and our measurements at TRIUMF were subject to intermittent interference. We are redesigning our circuit to mitigate external noise. But in the present study we used Rao test detection [14], an enhanced matched filtering technique which is suitable for pulse detection in more demanding noise environments at the cost of greater computational complexity.

### III. SIMULATION

We undertook a series of simulations in order to verify the correct operation of the detection software and to investigate system performance variations, as illustrated by Fig. 4. For the simulations we assumed a Gaussian pulse with width (to 0.2% points)  $40 \mu\text{s}$ . We postulated a true pulse height distribution based on the exponential characteristic reported by Truscott et al. [6], that is with a decay constant  $0.15 \text{ MeV}^{-1}$ . Simulated

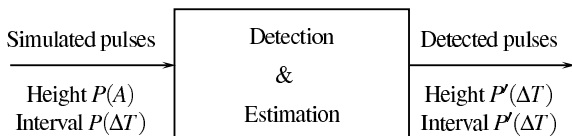


Fig. 4: Pulse simulation system

TABLE I: Simulation summary results – probability of detection

	threshold energy, keV	
	0	112
$r = 0\text{s}^{-1}$	1.000	0.984
$r = 200\text{s}^{-1}$	0.992	0.976
$r = 2000\text{s}^{-1}$	0.927	0.910

TABLE II: Simulation summary results – estimated rate,  $\text{s}^{-1}$

	threshold energy, keV	
	0	112
$r = 200\text{s}^{-1}$	$200 \pm 1$	$197.8 \pm 0.8$
$r = 2000\text{s}^{-1}$	$2003 \pm 9.9$	$1965 \pm 6.9$

pulse heights were selected randomly to meet this distribution and used to construct the input sequence  $x[n]$ .

We considered first the effect of thresholds  $\gamma$  corresponding to minimum detectable pulse energies 0 keV and 112 keV. The latter case corresponds to a false alarm probability of  $1 \times 10^{-9}$  at noise level  $110 \mu\text{V}_{\text{rms}}$  and sensitivity  $1.88 \text{ mV} \cdot \text{MeV}^{-1}$ . These conditions are somewhat worse than those experienced in practice in our detector. The expected proportion of simulated input pulses exceeding 112 keV is 98.3%.

We considered secondly the effect of pulse coincidences, or “pile-up”. We investigated the effect of mean interaction pulse rates,  $r$ , of  $2000\text{s}^{-1}$  and  $200\text{s}^{-1}$ . The former value is somewhat greater than the pulse rates detected at TRIUMF (§IV). We believe it is unlikely to be exceeded in practice in a system with a detector similar to ours.

Pulse intervals were selected randomly according to the exponential distribution characteristic of Poisson processes with the mean interval  $r^{-1}$ . Simple analysis assuming a non-paralysable detection process [12] predicts that at these rates pile-up should cause simulated detection probabilities to reduce to 92.3% and 99.2%, respectively.

Table I shows the probability of detection in our simulations. The probability of detection is as expected; in particular, the influence of noise and of pile-up combine as expected for independent variables ( $P_{\gamma,r} = P_{0,r}P_{\gamma,0}$ , where  $P_{\gamma,r}$  is the probability of detection given threshold  $\gamma$  and rate  $r$ ).

In each case exponential fits to the detected pulse height spectra agree with the input decay constant ( $0.15 \text{ MeV}^{-1}$ ) to within 1%. Fig. 5 illustrates the pulse-height spectra for the worst case studied, at  $2000\text{s}^{-1}$  and 112 keV threshold, and Fig. 6 shows the worst-case distribution of detected pulse intervals, which exhibits the exponential form characteristic of Poisson processes. The effect of pile-up is visible. The decay constants of exponential fits to distributions such as those in

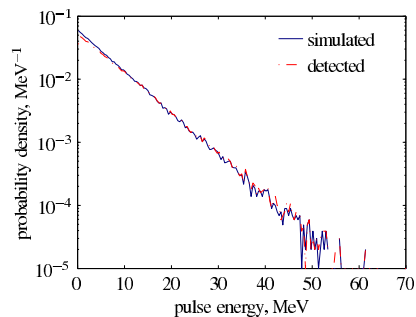


Fig. 5: Example simulated pulse-height spectra

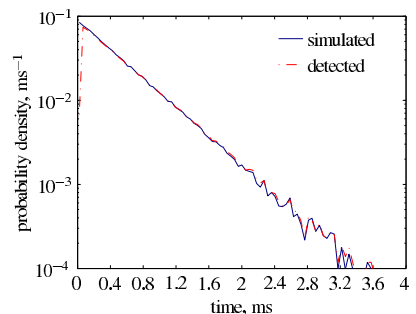


Fig. 6: Example simulated pulse interval distributions

TABLE III: Pulse height spectra parameters

	max. energy MeV	decay constant $\text{MeV}^{-1}$
ANITA	36.1	$0.297 \pm 0.031$
110 MeV	27.3	$0.304 \pm 0.025$
50 MeV	21.8	$0.350 \pm 0.028$
TRIUMF	33.9	$0.286 \pm 0.020$

Fig. 6 are listed in Table II. These values represent the mean rates of events with energy above the given thresholds. The system correctly determines these rates, which for the 112 keV threshold are 98.3% of those for the 0 keV threshold.

#### IV. EXPERIMENTAL RESULTS

In this section we present experimental results from irradiations at TRIUMF and TSL.

Fig. 7 shows measured pulse height spectra captured in the TSL ANITA, 110 MeV, and 50 MeV beams. Fig. 8 compares measured pulse height spectra at TRIUMF and ANITA. The distributions are approximately exponential above about 5 MeV collected energy, with decay constants as listed in Table III. The spectrum obtained in the 50 MeV quasi-monoenergetic beam is significantly steeper than those seen in the other fields studied here.

The pulse height spectrum measured at TRIUMF shows a local maximum between 1 MeV and 2 MeV. This peak is attributed to thermal neutron interactions on  $^{10}\text{B}$  present as

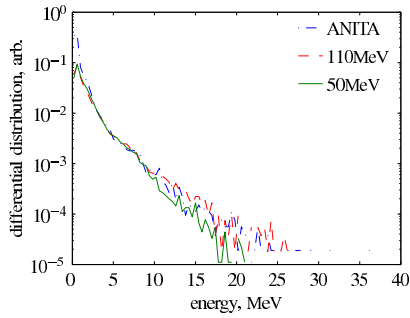


Fig. 7: Measured pulse height spectra at TSL

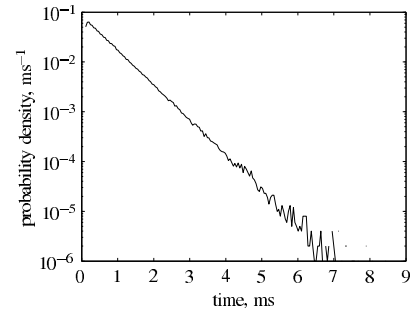


Fig. 10: Measured pulse interval distribution at TRIUMF

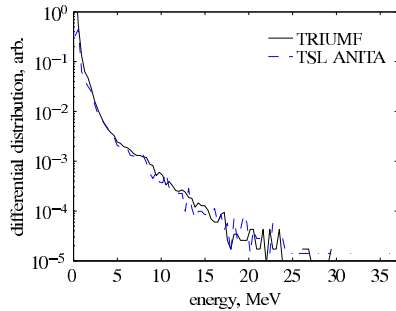


Fig. 8: Measured pulse-height spectra at TRIUMF and ANITA

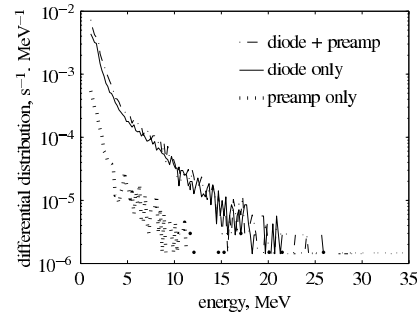


Fig. 11: Measured pulse rate distributions at TRIUMF for the photodetector and preamplifier irradiated separately and together

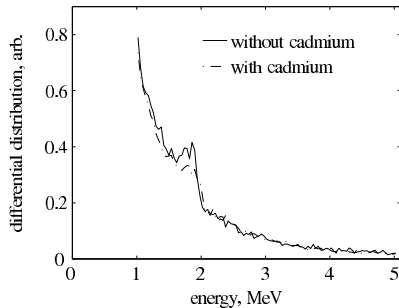


Fig. 9: Pulse height spectra showing the influence of thermal neutrons at TRIUMF and its reduction by cadmium shielding

dopants in the photodiode. Measurements were also made with cadmium shielding, which was found to suppress this peak, although not completely as shown by Fig. 9.

Fig. 10 shows the distribution of time intervals between events depositing above 50 keV at TRIUMF. From this we are able to estimate that the rate of interactions was  $1672 \pm 9.6 \text{ s}^{-1}$ . This is 6% greater than the rate estimated roughly from the number of detected events and run duration ( $1570 \text{ s}^{-1}$ ).

Irradiations at TRIUMF with the preamplifier immediately adjacent to the photodiode, and therefore with both components in the neutron beam, showed an increase of about 10%

in the count rate as illustrated by Fig. 11 which shows the distribution of events when the photodiode alone, amplifier alone, and photodiode and amplifier together were irradiated, in each case without cadmium shielding.

## V. DISCUSSION

Our system is intended to enable in-situ relative measurements of neutron fluence (or flux), through measurement of pulse-height (energy deposition) spectra and pulse time interval distributions. We are interested in potential sources of error in these measurements, of which there are several.

Counting statistics lead to an irreducible uncertainty in fluence measurements. However, even from the small ( $1 \text{ mm}^2$ ) detector used here, we observe typical pulse rates greatly in excess of SEE rates typically observed during accelerated testing. It is unlikely that uncertainty in fluence estimates determined with a system like ours would be a significant contributor to the uncertainty in measured SEE cross-sections. If necessary, similar devices with larger active volumes could be used; these are readily available (e.g. [11]).

Intrinsic noise processes lead to an energy threshold below which pulses cannot be detected, and limit pulse-height spectrum energy resolution. No attempt has been made to optimise the noise performance of the circuit used in the experiments reported here; nonetheless it has been possible to detect pulses

exceeding an energy threshold of 50 keV with a negligible intrinsic false alarm rate. We expect that circuit optimization could increase the dynamic range of approximately 30 dB observed in the TRIUMF data set presented here.

Pile-up is a potential source of error in both counting rate and pulse-height spectrum measurements. However, our results give us confidence that this is unlikely to be significant in practice. The system can correctly determine pulse-height spectra and counting rates even in what are likely to be extreme cases. The true rate of events can be inferred from the characteristic exponential distribution of event intervals. This approach is likely to be effective so long as the beam flux is sensibly constant over the period required to generate a pulse interval distribution. When pile-up is significant this interval is likely to be short and it is likely that the requirement for a constant flux will be met.

In addition, pile-up mostly affects less energetic events, as these are more common. Bearing in mind that what is required in practice is to detect a sufficiently large number of events that relative flux measurements can be made with acceptable counting uncertainties, the effect of pile up can be mitigated by selecting the detection threshold to achieve a desirable range of counting rates.

System optimization for performance in the presence of pile up involves a number of design trade-offs. The promising performance of our initial design in the challenging pile-up environment at TRIUMF leads us to expect that our system could be optimised by increasing pulse widths, permitting a reduction in sampling rate or, alternatively, the ability to operate several detector channels simultaneously from the same data acquisition system. This would be a valuable feature in several practical applications.

In pulsed neutron beams it may happen that the rate of pulses received from the detector becomes a significant fraction of the rate of pulses in the beam, or even that a pulse is detected for each neutron pulse (assuming that the detector pulse is wider than the neutron pulse). This could be considered as an extreme case of pile-up, where the fluence received during each neutron pulse is very high even though the average flux might be quite low. This might occur if a large area detector were used in an intense beam with a low repetition rate. We did not experience such conditions in the pulsed beams investigated here, although we think it is possible that it could happen in principle. In such cases we would expect the pulse-height spectrum to have a composite form, with a quasi-gaussian main peak encoding the average number of interactions per neutron pulse, and an exponential upper tail corresponding to the characteristic form of the pulse-height spectra shown here. We think that either the position of the peak or the rate of events in the upper tail would provide useful measures of the beam intensity. Simulation studies would be useful to confirm this.

Our pulse-height spectra agree qualitatively with that reported by Truscott *et al.* [6] at TRIUMF and TSL. We think that the discrepancy in exponential decay constants (e.g.  $0.29 \text{ MeV}^{-1}$  versus  $0.15 \text{ MeV}^{-1}$  for TRIUMF data) is consistent with the difference in detector active depths (circa  $15 \mu\text{m}$  depletion depth versus  $300 \mu\text{m}$ ). The most intense

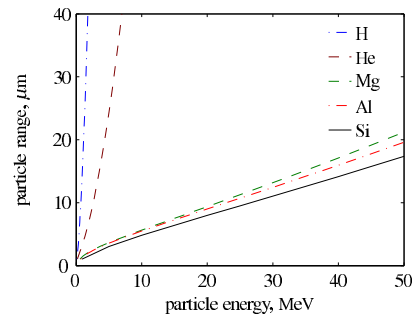


Fig. 12: Range of selected ions in silicon [15]

events detected in our system deposited 36 MeV in the active region (Table III). We expect that the maximum detectable energy is limited by the relatively shallow depth of the detector we used<sup>1</sup>. We observe that for the main heavy-ion products we expect to be produced (silicon, aluminium and magnesium) the range of 36 MeV ions is around  $15 \mu\text{m}$ , as illustrated by Fig. 12. We think it likely that highly energetic ions of such types will be produced predominantly in the forward direction, limiting the detectable energy range to around that seen here – at least where the neutrons are normally incident, as in all the experiments we have made to date. The pulse height spectra at TRIUMF and the higher energies at TSL (ANITA and 110 MeV) are very similar in form and appear to be limited by the geometry of the device. At the lower neutron energy at TSL (50 MeV), the higher decay constant arises as the neutron energy is insufficient to generate ionizing particles with the limiting energy.

Our pulse height spectra deviate from exponential at deposited energies below about 5 MeV, taking more of a power-law form. This also appears to be consistent with Truscott *et al.* [6] and other work [16], but is more pronounced in our data as our energy threshold is lower (50 keV versus circa 2 MeV). We think it is mostly the result of high-energy secondary protons passing through the active region and from which only a small fraction of their ionizing energy is collected. In fact, the high event rate observed in our detector at TRIUMF indicates very strongly that interactions outside the nominal active volume are significant. Although we have yet to perform simulations of the irradiations described in this work, such a study of UCLan’s Imaging Single Event Effect Monitor, whose detector has a similar active depth, indicate that protons passing through the active region are likely to dominate the low-energy part of our pulse-height spectrum [17].

Nonetheless, other sources of radiation can make a contribution, particularly  $\gamma$  photons arising from induced radioactivity in the detector or its immediate surroundings. For example, the package of the photodiode which we used contains gold, which can be activated in neutron beams leading to the emission of  $\gamma$  radiation predominantly at 0.4 MeV [18]. This contributes to the pulse-height spectrum at the lowest energies, and is visible for example in Fig. 7. To illustrate further, Fig. 13

<sup>1</sup>Note that the diode was not designed for use as a particle detector.

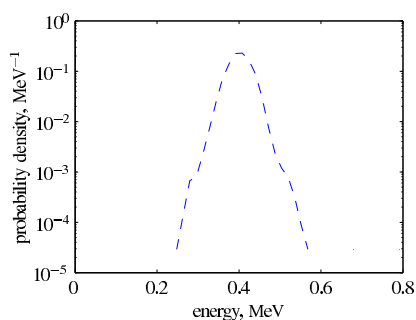


Fig. 13: Pulse height spectrum due to neutron activation of gold in the photodiode package (note energy scale)

shows the pulse height spectrum of 34450 pulses captured over a period of 7 h immediately after an irradiation of about 9 h in the ANITA beam at TSL. The effect of gold activation is clear.

Although we have not fully characterised the  $\gamma$  response of the detectors we used, we think it is unlikely to be significant in our application as we expect  $\gamma$  interactions to be inefficient at the energies of interest.

A further contribution to our pulse height spectrum, and which might be a source of interference in the presence of a significant thermal neutron flux, is that due to the  $^{10}\text{B}(n,\alpha)^7\text{Li}$  reaction whose effect is visible in Fig. 9. The device we used for these experiments was a PN junction diode with the p-type region formed by a diffusion of boron, believed to be natural boron (i.e. approximately 20%  $^{10}\text{B}$ ). Inevitably, this will lead to the presence of  $^{10}\text{B}$  in the active (depletion) region, and it is this which leads to the structure just below 2MeV in the pulse-height spectrum.

It is a simple matter to discriminate against interference sources such as  $\gamma$  radiation and  $^{10}\text{B}(n,\alpha)^7\text{Li}$  reactions by selection of a suitable energy threshold. As we have been able to generate useful pulse rates above a threshold of a few MeV collected, we think that a suitable device of this type could be selected or a design optimised to meet requirements for in-situ dosimetry during accelerated testing for neutron SEE.

It would be advantageous to have available a range of detectors from which to select the optimum for a particular test condition. Preliminary considerations for detector optimisation might include the following points, although theoretical and experimental studies will be necessary to determine optimal designs. Where beam flux is significantly lower than that observed at the TRIUMF NIF, for example in flood-room applications for testing larger systems, it may be advantageous to increase the interaction volume and hence count rate. This might be achieved either by producing a device designed to operate with a deeper depletion region, perhaps with a PIN structure, or else one having a larger active area. A combination of a larger active area within the same die dimensions, and a greater depletion depth, might be advantageous. Designs which maximised detection of light particles generated from neutron interactions in material surrounding the depletion

region, for example exploiting thick  $p^+$  and  $n^+$  regions, might be particularly suitable in our application despite making poor photodiodes. The use of isotopically enriched boron dopants, either deliberately to exclude or else to include  $^{10}\text{B}$  interactions, would be valuable. In some practical cases it would be advantageous to operate a detector at 5 V or lower bias voltages, which might require an alternative design. Finally, detector dies should be repackaged both for convenience of mounting onto test sets and also to exclude optical interference as well as induced  $\gamma$  radiation from package materials such as gold. Aluminium contacts may be better.

## VI. CONCLUSION

We have presented a preliminary study of a simple but effective neutron detection system with application to in-situ dosimetry during SEE testing. The components used are readily available and inexpensive. Our system is small and simple and can be easily incorporated into test sets or otherwise used to instrument SEE experiments. With that said, there is still further work to be undertaken to improve the system. For example, the amplifier design is not yet optimised, and the circuit for data collection in the present version needs calibration. These are all on our agenda, along with the implementation of a Geant4 model of the detector, the better to understand the detailed physics of its operation. In conclusion, we can confidently say that our system is a promising candidate for adoption in future SEE testing protocols.

## ACKNOWLEDGMENTS

The authors would like to thank staff at TRIUMF and TSL for their support during the experiments described here, particularly Ewart Blackmore, Alexander Prokofiev, Carl-Johan Friden and Gunilla Rosquist.

Simon Platt would also like to thank the University of Central Lancashire for a period of sabbatical leave without which this work could not have been undertaken.

## REFERENCES

- [1] *Measurement and Reporting of Alpha Particle and Terrestrial Cosmic Ray-Induced Soft Errors in Semiconductor Devices*, Std. JESD89A, Oct. 2006. [Online]. Available: <http://www.jedec.org/download/search/jesd89a.pdf>
- [2] *Test Method for Beam Accelerated Soft Error Rate*, Std. JESD89-3A, Nov. 2007. [Online]. Available: <http://www.jedec.org/download/search/jesd89-3a.pdf>
- [3] *JEITA SER Testing Guideline*, Std. EDR-4705, Jun. 2005. [Online]. Available: <http://tsc.jeita.or.jp/tsc/standard/pdf/EDR-4705.pdf>
- [4] *Semiconductor devices – Mechanical and climatic test methods – Part 38: Soft error test method for semiconductor devices with memory*, Std. IEC 60749-38:2008, May 2008.
- [5] *Process management for avionics – Atmospheric radiation effects – Part 2: Guidelines for single event effects testing for avionics systems*, Std. IEC/TS 62396-2:2008, Aug. 2008.
- [6] P. Truscott, C. Dyer, A. Frydland, A. Hands, S. Clucas, and K. Hunter, "Neutron energy-deposition spectra measurements, and comparisons with Geant4 predictions," *IEEE Transactions on Nuclear Science*, vol. 53, no. 4, pp. 1883–1889, Aug. 2006.
- [7] S. Platt and Z. Török, "Analysis of SEE-inducing charge generation in the neutron beam at The Svedberg Laboratory," *IEEE Transactions on Nuclear Science*, vol. 54, no. 4, pp. 1163–1169, Aug. 2007.

# Minimally invasive neutron beam monitoring for single-event effects accelerated testing

Lyn H. Zhang and S. P. Platt, *Member, IEEE*

**Abstract**—The use of silicon photodiodes for local beam monitoring during neutron SEE tests is demonstrated. Results from irradiations at the LANSCE ICE House are presented and analyzed. Local fluence measurements can be made without significant pile-up, even in pulsed beams. Beam degradation by scatterers such as upstream experiments can be quantified.

**Index Terms**—Neutron radiation effects, Particle beam measurements, Semiconductor device testing, Silicon radiation detectors

## I. INTRODUCTION

High-energy particle beams are widely used to enable accelerated testing of electronic devices and systems against neutron-induced single-event effects (SEEs) [1]. At some neutron facilities, such as the Theodor Svedberg Laboratory (TSL [2], [3]), Los Alamos Neutron Science Center (LANSCE) ICE House [4], and ISIS [5], [6], experiments can be carried out with several test sets arranged along a beam line. In such cases, however, the devices that are positioned further away from the beam source receive a degraded beam due to absorption and scattering by upstream experiments. The consequent loss of neutron fluence cannot be accounted for by typical upstream beam monitoring [7], [8]. In order to make reliable estimates of SEE cross-sections, local neutron beam monitors are required. We are developing a system to provide this capability [9], and as part of this work we have recently undertaken tests at the Los Alamos Neutron Science Center (LANSCE). In this paper, we present and evaluate results from these tests.

## II. METHOD

Our neutron sensor is a minimally invasive circuit exploiting a commercially-available Centronic OSD1-5T PN photodiode as the sensing element. The TO-18 diode packages were de-lidded and mounted directly onto a standard printed circuit board. Pulses from the board were collected by a multi-stage amplifier based on a Texas Instruments TL074 quad operational amplifier located approximately 100mm from the detector and outside the nominal footprint of the neutron beam. The first stage of amplification consisted of a charge-amplifier with feedback capacitance  $2.20 \pm 0.25$  pF. Subsequent stages provide a fifth-order shaping filter following the design of

Manuscript submitted on September 18, 2011. Beam time for this project was provided by the SEEDER project ([www.seeder.org.uk](http://www.seeder.org.uk)), supported by the United Kingdom Technology Strategy Board

School of Computing, Engineering and Physical Sciences, University of Central Lancashire, Preston, Lancs. PR1 2HE, England, Tel: +44 1772 895167 Fax: +44 1772 892915 Email: [splatt@uclan.ac.uk](mailto:splatt@uclan.ac.uk)

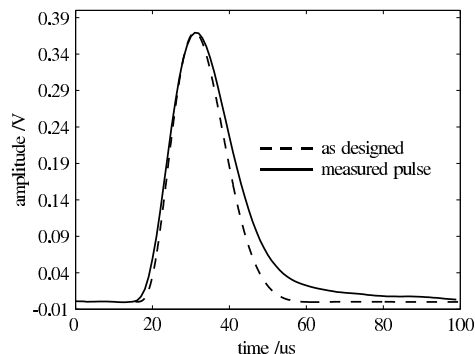


Fig. 1. Example pulse from a 20MeV interaction compared with the nominal pulse shape (6.6 $\mu$ s pseudo-gaussian)

Ohkawa et al. [10], providing pseudo-gaussian pulses with the form shown in Fig. 1. The pulses have a nominal shaping time of 6.6 $\mu$ s, chosen to provide a pulse width to 1% points approximately 40 $\mu$ s. In practice the pulses are slightly broadened, largely due to imperfect pole-zero cancellation in the coupling between the preamplifier and shaping amplifier. Fig. 1 compares the nominal pseudo-gaussian pulse shape (i.e. as designed) with a pulse resulting from a neutron interaction from which approximately 20MeV was collected.

Exposures were made at the LANSCE ICE house, which provides a pulsed neutron beam with an atmospheric-like spectrum up to almost 800MeV [4]. The beam is generated from a 60Hz linac beam which is shared between the WNR facility (of which the ICE House is part) and the Lujan Neutron Scattering Center. Two out of every three pulses are delivered to the WNR, leading to the temporal structure illustrated in Fig. 2. Macropulse length is about 625 $\mu$ s leading to a duty cycle about 1/40. Fluence rates during our experiments were typically  $1.3 \times 10^5$  ncm $^{-2}$ s $^{-1}$ .

The arrangement of detectors in the beam line is illustrated in Fig. 3. Primary fluence measurement was provided by the facility beam monitor, using an ionization chamber [11] in the upstream position. Correction for the effects of beam divergence at detector positions was made assuming an  $R^{-2}$  law. Detector positions were measured from a convenient datum position approximately 7cm downstream of the ionization chamber centre line. To determine sensor characteristics and the effect of the pulsed neutron beam, two nominally identical sensors ('A' and 'B') were irradiated together at the upstream

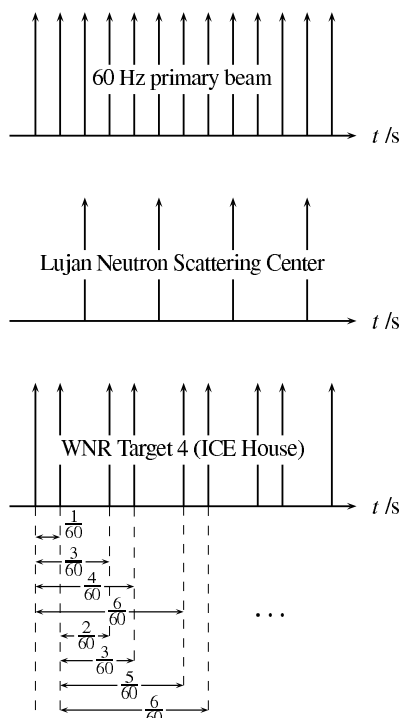


Fig. 2. LANSCE neutron beam macropulse timing. The primary particle beam at 60Hz is shared between the Lujan Neutron Scattering Center and the WNR facility (which included the ICE House). The beam delivered to the ICE house has a 40Hz average pulse rate with a strong fundamental frequency at 20Hz. The intervals between any two macropulses are  $(3n-2)/60$  s and  $(3n-1)/60$  s each with probability  $P$ , and  $n/20$  s with probability  $2P$ , for  $n = 1, 2, \dots$ .

position (78cm). To investigate the influence of degrading experiments in the beam line the sensors were also irradiated upstream and downstream of an aluminum scatterer placed in one of the two positions shown in the figure.

### III. EXPERIMENTAL RESULTS

#### A. Measurements at upstream position

Sensors A and B were irradiated together at the upstream position, 78cm below the datum point. The numbers of detected events from which at least 132.2keV was collected are given in Table I. Corresponding cross-sections are listed in Table II. Reproducibility between runs and across sensors is discussed later in this section.

*Pulse height spectra:* Pulse height spectra are shown in Fig. 4 and show very close agreement between the two detectors. The distributions are approximately exponential above 5MeV collected energy, with parameters (at 68% confidence interval, CI) as listed in Table III. The largest detected events in this run were 32.69MeV (sensor A) and 32.48MeV (sensor B).

*Pulse intervals:* Fig. 5 shows the measured pulse interval distribution. The effect of the neutron beam time structure is

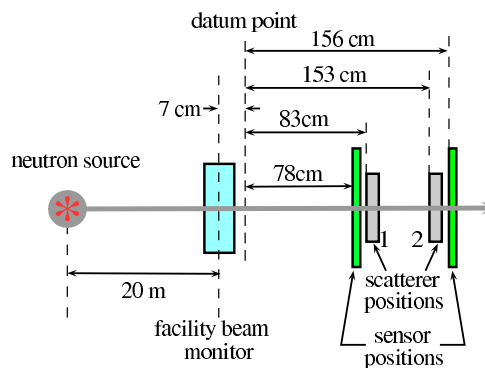


Fig. 3. Schematic diagram showing the experimental geometry (not to scale). Each measurement run included exposure of at least one detector at the upstream position. In some runs detectors were irradiated at the two, separate, positions shown, with and without a scatterer (Al plate) at one or other of the positions shown.

TABLE I  
SUMMARY RESULTS FROM UPSTREAM EXPERIMENTS

run	fluence <sup>a</sup> /n/cm <sup>2</sup>	Number of events <sup>b</sup>	
		sensor A	sensor B
1	$2.11 \times 10^8$	11922	11499
2	$1.51 \times 10^8$	8335	7864
3	$9.67 \times 10^7$	5090	4802
4	$3.76 \times 10^8$	19299	18656

a Integral fluence above 10MeV.  
b Events above 132.2keV.

TABLE II  
CROSS SECTION FOR EVENTS FROM WHICH AT LEAST 132.2keV WAS COLLECTED

run	cross section /cm <sup>2</sup>	
	sensor A	sensor B
1	$5.64 \times 10^{-5}$	$5.67 \times 10^{-5}$
2	$5.52 \times 10^{-5}$	$5.43 \times 10^{-5}$
3	$5.26 \times 10^{-5}$	$5.18 \times 10^{-5}$
4	$5.13 \times 10^{-5}$	$5.17 \times 10^{-5}$

clearly visible, the distribution forming a comb at multiples of the accelerator repetition period (16.7ms) modified by the characteristic exponential form resulting from a Poisson process. The  $n \times 50$ ms component of the beam (i.e. every third peak) is enhanced by a factor of 2, reflecting the 20Hz periodicity of the incident neutron beam illustrated in Fig. 2.

*Reproducibility:* We determined the sensitivity of our sensors ( $VMeV^{-1}$ ) by calculation. The principal uncertainty of this calculation is in the value of the preamplifier feedback capacitor, and is about 11%. The effect of this variability is visible in the data in Table I and Table II. Fig. 6 shows a proportional fit between the counts observed in the two sensors. The constant of proportionality is  $0.959 \pm 0.019$  (95% CI). The number of events in sensor A is predicted well by dividing the number of events in sensor B by this constant.

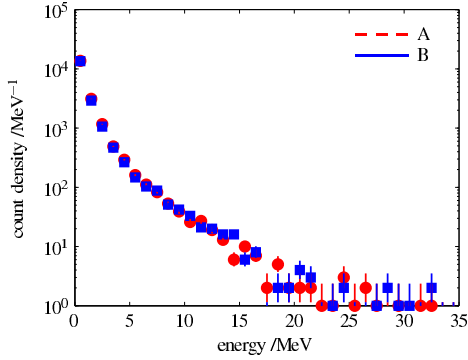


Fig. 4. Measured pulse height spectra, run 4 (68% confidence intervals shown)

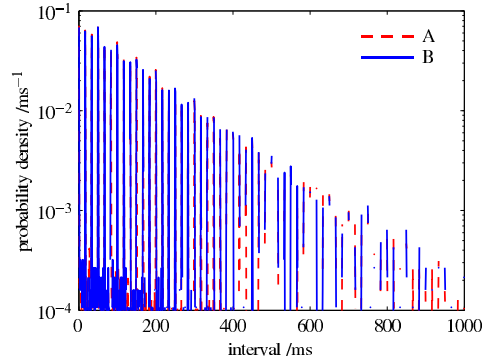


Fig. 5. Measured pulse interval distributions, run 4

TABLE III  
RUN 4 PULSE HEIGHT SPECTRA FITTING PARAMETERS  $ae^{-bE}$

sensor	intercept, $a$ /MeV <sup>-1</sup>	decay constant, $b$ /MeV <sup>-1</sup>
A	1166 ± 116	0.321 ± 0.030
B	1019 ± 159	0.301 ± 0.046

*Effect of radiation damage:* Fig. 7 shows how the cross-section for sensor A and the adjusted cross-section for sensor B vary with received fluence. The best estimate, assuming cross-section not to vary, is also shown. This value is  $(5.34 \pm 0.03) \times 10^{-5} \text{cm}^2$  (68% CI), and does not model the observed trend well (confidence intervals on the individual measurements are also plotted in Fig. 7, but are scarcely visible behind the symbols). In fact, the reduced  $\chi^2$  values for the data in Fig. 7 greatly exceed 1 (13.8 for sensor A, 12.5 for sensor B), indicating that the trend of reducing cross-section with received fluence is real, and attributable to radiation damage.

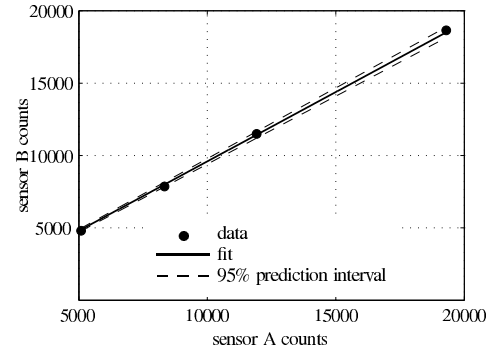


Fig. 6. Proportional fit between counts in sensor A and those in sensor B, also showing 95% prediction interval (PI)

*B. Measurements with and without an aluminum scatterer*

Irradiations were made with sensor A in the upstream position and sensor B in a downstream position, with and without an aluminium scatterer intervening. The scatterer, an aluminium plate with thickness approximately 4mm, was placed either in position 1 or position 2 as illustrated in Fig. 3, and simulates the presence of additional SEE experiments in the neutron beam. The experimental conditions are summarized in Table IV.

In the absence of a scatterer the fluence received at a downstream position can be simply determined using upstream beam monitoring and an  $R^{-2}$  law. In our geometry, the  $R^{-2}$  factor is 0.92. In the presence of intervening materials (for example, upstream experiments) the beam at downstream locations is degraded by interactions upstream. Neutrons can scatter elastically or inelastically out of their original direction, leading to a more rapid (than  $R^{-2}$ ) reduction in fluence and a hardening of the neutron field. Neutrons can be absorbed by non-elastic and spallation reactions in the material, leading

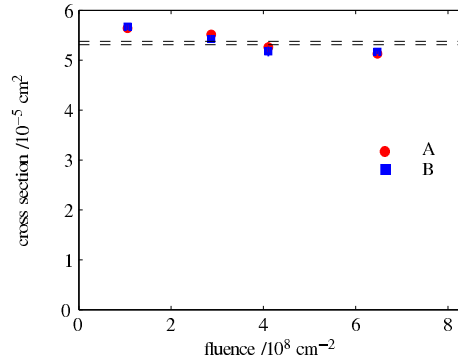


Fig. 7. Cross sections for sensor A and sensor B (adjusted), illustrating the degree of reproducibility and the deleterious effect of received fluence. The 68% confidence interval on the best estimate for cross-section, assuming constant cross-section, is also shown.

TABLE IV  
SUMMARY CONDITIONS FOR EXPERIMENTS WITH A SCATTERER

run	upstream fluence <sup>a</sup> / $\text{ncm}^{-2}$	scatterer position /cm
5	$2.44 \times 10^8$	
6	$2.80 \times 10^8$	83
7	$2.42 \times 10^8$	151

a Integral fluence above 10MeV.

TABLE V  
SUMMARY RESULTS OF EXPERIMENTS WITH A SCATTERER

run	sensor A	sensor B pulses <sup>a</sup>		transmission /%
	pulses <sup>a</sup>	raw	adjusted	
5	4806	4377	4587	102.7
6	5352	4830	5061	101.8
7	4710	6707	7028	160.6

a Events above 171.7keV.

to a reduction in the primary fluence. Neutron multiplication can occur, leading to an increase but softening of the neutron fluence. Finally, charged particles can be emitted into the beam line – affecting both detectors and also devices of interest under test for single-event effects.

Table V records the observed number of events from which the collected energy was at least 171.7keV, and also presents an effective transmission of fluence from the upstream to the downstream position. A transmission less than 100% implies that the beam has decayed more rapidly than  $R^{-2}$ , a transmission greater than 100% indicates an enhancement of the beam, or a decay less rapid than  $R^{-2}$ . In the case with no scatterer (run 5), the measured transmission is within counting uncertainties of 100%. The small decrease in transmission in run 6 (with a scatterer in position 1), indicates that there is only a small effect in degrading the beam. However, in run 7 there is an apparent large enhancement of the beam, probably due to particles knocked out of the aluminium scatterer. The same phenomenon must occur in run 6, but in that case the highly divergent secondary source (the scatterer) has become insignificant by the time the position of sensor B is reached.

If only larger events are considered, the transmissions of run 5 and run 6 are still similar and there is not a significant variation with threshold collected energy, as shown in Fig. 8. In contrast, the transmission in run 7 decreases rapidly with the increase of the threshold for collected energy.

Fig. 9 shows the corresponding pulse height spectra for these runs, and Table VI lists estimated parameters for exponential fits above 5MeV in each case. (Note that the scale parameter,  $a$ , increases with received fluence and therefore varies with run length; approximately the same fluence is received by each sensor in each run, but fluence varies somewhat from run to run.) The pairs of pulse height spectra in run 5 and run 6, as shown in Fig. 9(a) and Fig. 9(b), are similar. In contrast, in run 7 (Fig. 9(c)) the number of pulse events in sensor A (upstream of the scatterer) is significantly lower than in sensor B (downstream of the scatterer) at lower collected

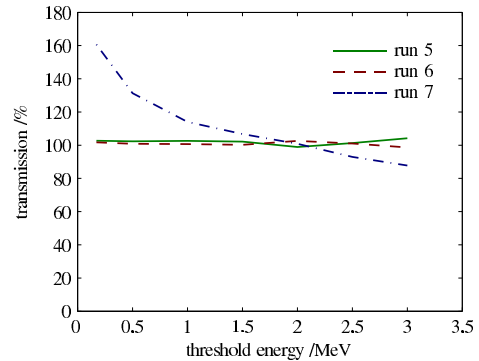


Fig. 8. Measured transmission with and without an intervening scatterer – variation with threshold collected energy (68% CI shown)

TABLE VI  
PULSE HEIGHT SPECTRA FITTING PARAMETERS  $ae^{-bE}$ .

		A	B
		run 5	$a$ / $\text{MeV}^{-1}$
	$b$ / $\text{MeV}^{-1}$	$0.321 \pm 0.037$	$0.349 \pm 0.042$
run 6	$a$ / $\text{MeV}^{-1}$	$442 \pm 29$	$341 \pm 61$
	$b$ / $\text{MeV}^{-1}$	$0.360 \pm 0.011$	$0.334 \pm 0.030$
run 7	$a$ / $\text{MeV}^{-1}$	$352 \pm 31$	$197 \pm 45$
	$b$ / $\text{MeV}^{-1}$	$0.336 \pm 0.015$	$0.286 \pm 0.037$

energies (below about 2MeV), whereas at higher collected energies the number of events in sensor B is reduced compared to that in sensor A. The fit parameters shown in Table VI indicate that the beam at the position of sensor B has been significantly degraded by the presence of the scatterer just upstream.

#### IV. DISCUSSION

A neutron detector based on a simple silicon diode can operate in typical pulsed neutron beams without significant pile-up. Typical detected pulse rates at the LANSCE ICE House (40Hz average macropulse frequency;  $1.3 \times 10^5 \text{ncm}^{-2}\text{s}^{-1}$  fluence rate; 1/40 duty cycle) were approximately  $7\text{s}^{-1}$ , an event probability per macropulse of approximately 0.18.

Silicon neutron detectors suffer from performance degradation (cross-section reduction) due to neutron damage (cf. Fig. 7). However, Fig. 7 also provides evidence that this damage is repeatable from device to device, enabling the desired relative fluence measurement (i.e. between two or more locations in a beam line) to be made, enabling transmission to be determined and absolute fluence to be derived by reference to facility beam monitors.

Detectors of our type can provide useful information on the fluence and hardness of a neutron field at multiple locations in a beam. Our results (cf. Fig. 9) are consistent with measurements and simulations made previously [7].

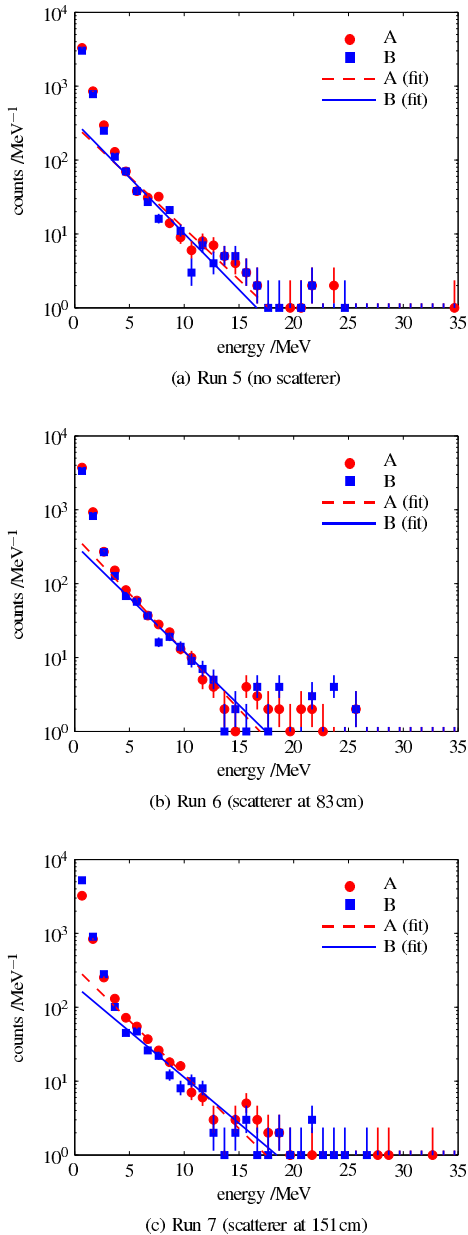


Fig. 9. Measured pulse height spectra with and without an intervening scatterer

We are considering how best to exploit these results. For example, the area under the exponential portion of the pulse-height spectra (cf. Fig. 9) is given by the ratio  $a/b$  (Table VI), and represents the number of events detected in this region.

Values of this ratio are listed in Table VII. We are exploring the usefulness of this parameter as a measure of local beam fluence in cases where the beam is degraded by upstream experiments. For example, according to this approach the effective transmission from sensor A to sensor B in run 7 is estimated to be  $0.657 \pm 0.185$ . Additional analysis of experimental data are required to confirm whether this is a useful measure.

TABLE VII  
VALUES OF THE CANDIDATE BEAM FLUENCE MEASURE,  $a/b$

	A	B
no scatterer	$922 \pm 231$	$951 \pm 258$
case I	$1228 \pm 90$	$1021 \pm 204$
case II	$1048 \pm 104$	$689 \pm 181$

#### ACKNOWLEDGMENT

We gratefully acknowledge the support of our collaborators on the SEEDER project, and also Steve Wender and co-workers at LANSCE for their support to the irradiations.

#### REFERENCES

- [1] *Measurement and Reporting of Alpha Particle and Terrestrial Cosmic Ray-Induced Soft Errors in Semiconductor Devices*, JEDEC Solid State Technology Association Std. JESD89A, Oct. 2006.
- [2] A. V. Prokofiev, O. Byström, C. Ekström, V. Ziemann, J. Blomgren, S. Pomp, M. Osterlund, and U. Tippawan, "A new neutron beam facility at TSL," in *Proc. International Workshop on Fast Neutron Detectors and Applications (FNDA2006)*, Apr. 2006, poS(FNDA2006)016. [Online]. Available: [http://pos.sissa.it/archive/conferences/025/016/FNDA2006\\_016.pdf](http://pos.sissa.it/archive/conferences/025/016/FNDA2006_016.pdf)
- [3] A. V. Prokofiev, J. Blomgren, M. Majerle, R. Nolte, S. Röttger, S. P. Platt, X. X. Cai, and A. N. Smimov, "Characterization of the ANITA neutron source for accelerated SEE testing at The Svedberg Laboratory," in *2009 IEEE Radiation Effects Data Workshop Record*, 2009, pp. 166–173.
- [4] About WNR beam. [Online]. Available: <http://wnr.lanl.gov/newwnr/About/Beam.shtml>
- [5] C. Andreani, A. Pietropaolo, A. Salsano, G. Gorini, M. Tardocchi, A. Paccagnella, S. Gerardin, C. D. Frost, S. Ansell, and S. P. Platt, "Facility for fast neutron irradiation tests of electronics at the ISIS spallation neutron source," *App. Phys. Lett.*, vol. 92, no. 11, pp. 114 101–114 101–3, 2008.
- [6] C. D. Frost, S. Ansell, and G. Gorini, "A new dedicated neutron facility for accelerated SEE testing at the ISIS facility," in *Proc. Int. Rel. Phys. Symp.*, 2009, pp. 952–955.
- [7] P. Truscott, C. Dyer, A. Frydland, A. Hands, S. Clucas, and K. Hunter, "Neutron energy-deposition spectra measurements, and comparisons with Geant4 predictions," *IEEE Trans. Nucl. Sci.*, vol. 53, no. 4, pp. 1883–1889, Aug. 2006.
- [8] S. P. Platt and Z. Török, "Analysis of SEE-inducing charge generation in the neutron beam at The Svedberg Laboratory," *IEEE Trans. Nucl. Sci.*, vol. 54, no. 4, pp. 1163–1169, Aug. 2007.
- [9] L. H. Zhang, S. P. Platt, R. H. Edwards, and C. Allabush, "In-situ neutron dosimetry for single-event effect accelerated testing," *IEEE Trans. Nucl. Sci.*, vol. 56, no. 4, pp. 2070–2076, Aug. 2009.
- [10] S. Ohkawa, M. Yoshizawa, and K. Husimi, "Direct synthesis of the gaussian filter for nuclear pulse amplifiers," *Nucl. Inst. Meth.*, vol. 138, no. 1, pp. 85–92, 1976.
- [11] S. A. Wender, S. Balestrini, A. Brown, R. C. Haight, C. M. Laymon, T. M. Lee, P. W. Lisowski, W. McCorkle, R. O. Nelson, W. Parker, and N. W. Hill, "A fission ionization detector for neutron flux measurements at a spallation source," *Nucl. Inst. Meth. Phys. Res., A*, vol. 336, no. 1–2, pp. 226–231, Nov. 1993.

# Bibliography

- [1] J. F. Ziegler, H. W. Curtis, H. P. Muhlfeld, C. J. Montrose, B. Chin, M. Nicewicz, C. A. Russell, W. Wang, L. Freeman, P. Hosier, L. E. LaFave, J. L. Walsh, J. M. Orro, G. J. Unger, J. M. Ross, T. J. O’Gorman, B. Messina, T. D. Sullivan, A. J. Sykes, H. Yourke, T. A. Enger, V. Tolat, T. Scott, A. H. Taber, K. W. A. Sussman, R.J., and C. Wahaus, “IBM experiments in soft fails in computer electronics (1978–1994),” *IBM J. Res. Dev.*, vol. 40, no. 1, pp. 3–18, 1996. 1, 2, 21
- [2] J. F. Ziegler, “Terrestrial cosmic rays,” *IBM J. Res. Dev.*, vol. 40, no. 1, pp. 19–39, 1996. 1, 3, 5
- [3] C. A. Gossett, B. W. Hughlock, M. Katozi, G. S. LaRue, and S. A. Wender, “Single event phenomena in atmospheric neutron environments,” *Nuclear Science, IEEE Transactions on*, vol. 40, no. 6, pp. 1845 –1852, Dec. 1993. 1
- [4] E. Normand, “Single-event effects in avionics,” *Nuclear Science, IEEE Transactions on*, vol. 43, no. 2, pp. 461 –474, Apr. 1996. 1, 3
- [5] ———, “Single event upset at ground level,” *Nuclear Science, IEEE Transactions on*, vol. 43, no. 6, pp. 2742 –2750, Dec. 1996. 1
- [6] J. L. Barth, C. S. Dyer, and E. G. Stassinopoulos, “Space, atmospheric, and terrestrial radiation environments,” *Nuclear Science, IEEE Transactions on*, vol. 50, no. 3, pp. 466 – 482, Jun. 2003. 1
- [7] C. S. Dyer and P. R. Truscott, “Cosmic Radiation Effects on Avionics,” *Radiation Protection Dosimetry*, vol. 86, no. 4, pp. 337–342, 1999. 1, 3

- [8] *Process management for avionics – Atmospheric radiation effects – Part 2: Guidelines for single event effects testing for avionics systems*, IEC Std. IEC/TS 62 396-2:2008, Aug 2008. 1, 4, 6, 7, 8, 9
- [9] T. Nakamura, M. Baba, E. Ibe, E. Yahagi, and H. Kameyama, *Terrestrial Neutron-Induced Soft Errors in Advanced Memory Devices*. River Edge, NJ, USA: World Scientific Publishing Co. Inc., 2008. 3, 4, 11, 16
- [10] J. T. Wallmark and S. M. Marcus, “Minimum size and maximum packing density of nonredundant semiconductor devices,” *Proceedings of the IRE*, vol. 50, no. 3, pp. 286 –298, Mar. 1962. 2
- [11] D. Binder, E. C. Smith, and A. B. Holman, “Satellite Anomalies from Galactic Cosmic Rays,” *Nuclear Science, IEEE Transactions on*, vol. 22, no. 6, pp. 2675 –2680, Dec. 1975. 2
- [12] T. C. May and M. H. Woods, “Alpha-particle-induced soft errors in dynamic memories,” *Electron Devices, IEEE Transactions on*, vol. 26, no. 1, pp. 2 – 9, Jan. 1979. 3
- [13] C. S. Guenzer, E. A. Wolicki, and R. G. Allas, “Single Event Upset of Dynamic Rams by Neutrons and Protons,” *Nuclear Science, IEEE Transactions on*, vol. 26, no. 6, pp. 5048 –5052, Dec. 1979. 3
- [14] J. F. Ziegler and W. A. Lanford, “Effect of Cosmic Rays on Computer Memories,” *Science*, vol. 206, no. 4420, pp. 776–788, 1979. 3
- [15] P. E. Dodd and L. W. Massengill, “Basic mechanisms and modeling of single-event upset in digital microelectronics,” *Nuclear Science, IEEE Transactions on*, vol. 50, no. 3, pp. 583 – 602, Jun. 2003. 3
- [16] *Measurement and Reporting of Alpha Particle and Terrestrial Cosmic Ray-Induced Soft Errors in Semiconductor Devices*, JEDEC Std. JESD89A, Oct. 2006. [Online]. Available: <http://www.jedec.org/download/search/jesd89a.pdf> 3, 5, 7, 8, 9, 15, 20

- [17] D. Lambert, J. Baggio, V. Ferlet-Cavrois, O. Flament, F. Saigne, B. Sagnes, N. Buard, and T. Carriere, “Neutron-induced SEU in bulk SRAMs in terrestrial environment: Simulations and experiments,” *Nuclear Science, IEEE Transactions on*, vol. 51, no. 6, pp. 3435 – 3441, Dec. 2004. 3
- [18] E. Ibe, H. Kameyama, Y. Yahagi, and H. Yamaguchi, “Single event effects as a reliability issue of IT infrastructure,” vol. 1. Information Technology and Applications, 2005. ICITA 2005. Third International Conference on, Jul. 2005, pp. 555 – 560 vol.1. 3
- [19] P. Peronnard, R. Velazco, and G. Hubert, “Real-life SEU experiments on 90 nm SRAMs in atmospheric environment: Measures versus predictions done by means of MUSCA SEP3 platform,” *Nuclear Science, IEEE Transactions on*, vol. 56, no. 6, pp. 3450–3455, Dec 2009. 3
- [20] E. Normand and L. Dominik, “Cross comparison guide for results of neutron SEE testing of microelectronics applicable to avionics,” in *Radiation Effects Data Workshop (REDW), 2010 IEEE*, July 2010, p. 8. 3
- [21] E. Ibe, H. Taniguchi, Y. Yahagi, K.-I. Shimbo, and T. Toba, “Impact of scaling on neutron-induced soft error in SRAMs from a 250 nm to a 22 nm design rule,” *Electron Devices, IEEE Transactions on*, vol. 57, no. 7, pp. 1527 –1538, July 2010. 3
- [22] T. Loveless, S. Jagannathan, T. Reece, J. Chetia, B. Bhuvu, M. McCurdy, L. Massengill, S.-J. Wen, R. Wong, and D. Rennie, “Neutron- and proton-induced single event upsets for D- and DICE-Flip/Flop designs at a 40 nm technology node,” *Nuclear Science, IEEE Transactions on*, vol. 58, no. 3, pp. 1008 –1014, June 2011. 3
- [23] M. Gordon, P. Goldhagen, K. Rodbell, T. Zabel, H. Tang, J. Clem, P. Bailey, and T. J. Watson, “Measurement of the flux and energy spectrum of cosmic-ray induced neutrons on the ground,” *Nuclear Science, IEEE Transactions on*, vol. 51, no. 6, pp. 3427 – 3434, Dec 2004. 4, 5, 16

- [24] H. Goldhagen, “Cosmic-ray neutrons on the ground and in the atmosphere,” *MRS bulletin*, vol. 28, pp. 131–135, 2003. 5
- [25] M. Kowatari, K. Nagaoka, S. Satoh, Y. Ohta, J. Abukawa, S. Tachimori, and T. Nakamura, “Evaluation of the altitude variation of the cosmic-ray induced environmental neutrons in the Mt. Fuji area,” *J Nucl Sci Technol*, vol. 42, no. 6, pp. 495–502, 2005. 5
- [26] E. Normand and T. J. Baker, “Altitude and latitude variations in avionics SEU and atmospheric neutron flux,” *Nuclear Science, IEEE Transactions on*, vol. 40, no. 6, pp. 1484–1490, Dec. 1993. 5, 6
- [27] P. Goldhagen, M. Reginatto, T. Kniss, J. W. Wilson, R. C. Singleterry, I. W. Jones, and W. V. Steveninck, “Measurement of the energy spectrum of cosmic-ray induced neutrons aboard an ER-2 high-altitude airplane,” *Nuclear Instruments and Methods in Physics Research Section A: Accelerators, Spectrometers, Detectors and Associated Equipment*, vol. 476, no. 1-2, pp. 42–51, 2002. 5, 16, 17
- [28] P. Goldhagen, J. M. Clem, and J. W. Wilson, “Recent results from measurements of the energy spectrum of cosmic-ray induced neutrons aboard an ER-2 airplane and on the ground,” *Advances in Space Research*, vol. 32, no. 1, pp. 35–40, 2003, space Life Sciences: Structure and Dynamics of the Global Space Radiation Field at Aircraft Altitudes. 5, 16
- [29] ———, “The energy spectrum of cosmic-ray induced neutrons measured on an airplane over a wide range of altitude and latitude,” *Radiation Protection Dosimetry*, vol. 110, no. 1-4, pp. 387–392, 2004. 5
- [30] H. Koshiishi, H. Matsumoto, A. Chishiki, T. Goka, and T. Omodaka, “Evaluation of the neutron radiation environment inside the international space station based on the Bonner ball neutron detector experiment,” *Radiation Measurements*, vol. 42, no. 9, pp. 1510–1520, 2007. 5

- [31] C. Dyer, F. Lei, A. Hands, and P. Truscott, "Solar Particle Events in the QinetiQ Atmospheric Radiation Model," *Nuclear Science, IEEE Transactions on*, vol. 54, no. 4, pp. 1071–1075, Aug. 2007. 6
- [32] *Process management for avionics – Atmospheric radiation effects – Part 2: Guidelines for assessing thermal neutron fluxes and effects in avionics systems*, Std. IEC/TS 62 396-5:2008, Oct. 2008. 6
- [33] *JEITA SER Testing Guideline*, JEITA Std. EDR-4705, Jun 2005. [Online]. Available: <http://tsc.jeita.or.jp/tsc/standard/pdf/EDR-4705.pdf> 7, 8, 9
- [34] C. Dyer, S. Clucas, C. Sanderson, A. Frydland, and R. Green, "An experimental study of single-event effects induced in commercial SRAMs by neutrons and protons from thermal energies to 500 MeV," *Nuclear Science, IEEE Transactions on*, vol. 51, no. 5, pp. 2817–2824, 2004. 7
- [35] A. Hands, P. Morris, K. Ryden, C. Dyer, P. Truscott, A. Chugg, and S. Parker, "Single event effects in power MOSFETs due to atmospheric and thermal neutrons," *Nuclear Science, IEEE Transactions on*, vol. 58, no. 6, pp. 2687–2694, Dec. 2011. 7
- [36] *Test Method for Beam Accelerated Soft Error Rate*, JEDEC Std. JESD89-3A, Nov. 2007. [Online]. Available: <http://www.jedec.org/download/search/jesd89-3a.pdf> 7, 9
- [37] *Semiconductor devices – Mechanical and climatic test methods – Part 38: Soft error test method for semiconductor devices with memory*, IEC Std. IEC 60 749-38:2008, May. 2008. 7, 9
- [38] C. Slayman, "Theoretical correlation of broad spectrum neutron sources for accelerated soft error testing," *Nuclear Science, IEEE Transactions on*, vol. 57, no. 6, pp. 3163–3168, Dec. 2010. 8
- [39] K. Roed, V. Boccone, M. Brugger, A. Ferrari, D. Kramer, E. Lebbos, R. Losito, A. Mereghetti, G. Spiezia, and R. Versaci, "FLUKA Simulations for SEE Studies of Critical LHC Underground Areas," *Nuclear Science, IEEE Transactions on*, vol. 58, no. 3, pp. 932–938, June 2011. 8

- [40] S. Serre, S. Semikh, S. Uznanski, J. Autran, D. Munteanu, G. Gasiot, and P. Roche, “GEANT4 analysis of n-Si nuclear reactions from different sources of neutrons and its implication on soft-error rate,” pp. 11–14, Sept. 2011. 8
- [41] J.-L. Autran, P. Roche, J. Borel, C. Sudre, K. Castellani-Coulie, D. Munteanu, T. Parrassin, G. Gasiot, and J.-P. Schoellkopf, “Altitude SEE Test European Platform ASTEP and first results in CMOS 130 nm SRAM,” *Nuclear Science, IEEE Transactions on*, vol. 54, no. 4, pp. 1002–1009, Aug. 2007. 8
- [42] J. Autran, D. Munteanu, P. Roche, G. Gasiot, S. Martinie, S. Uznanski, S. Sauze, S. Semikh, E. Yakushev, S. Rozov, P. Loaiza, G. Warot, and M. Zampalo, “Soft-errors induced by terrestrial neutrons and natural alpha-particle emitters in advanced memory circuits at ground level,” *Microelectronics Reliability*, vol. 50, no. 9-11, pp. 1822–1831, 2010. 8
- [43] E. Blackmore, P. Dodd, and M. Shaneyfelt, “Improved capabilities for proton and neutron irradiations at TRIUMF,” in *IEEE Radiation Effects Data Workshop*, 2003, pp. 149–155. 9, 16
- [44] E. Blackmore, “Development of a large area neutron beam for system testing at TRIUMF,” *Radiation Effects Data Workshop, 2009 IEEE*, pp. 157–160, Jul. 2009. 9, 16
- [45] ICE House. [Online]. Available: <http://lansce.lanl.gov/NS/instruments/ICEhouse/index.html> 9
- [46] H. Sakai, H. Okamura, H. Otsu, T. Wakasa, S. Ishida, N. Sakamoto, T. Uesaka, Y. Satou, S. Fujita, and K. Hatanaka, “Facility for the (p, n) polarization transfer measurement,” *Nuclear Instruments and Methods in Physics Research Section A: Accelerators, Spectrometers, Detectors and Associated Equipment*, vol. 369, no. 1, pp. 120–134, 1996. 9
- [47] ISIS pulsed neutron and muon source,. [Online]. Available: <http://www.isis.stfc.ac.uk> 9

- [48] M. Violante, L. Sterpone, A. Manuzzato, S. Gerardin, P. Rech, M. Bagatin, A. Paccagnella, C. Andreani, G. Gorini, A. Pietropaolo, G. Cardarilli, S. Pontarelli, and C. Frost, “A new hardware/software platform and a new 1/e neutron source for soft error studies: Testing FPGAs at the ISIS facility,” *Nuclear Science, IEEE Transactions on*, vol. 54, no. 4, pp. 1184–1189, 2007. 9, 20
- [49] ISIS - Target station 2. [Online]. Available: <http://www.isis.stfc.ac.uk/about-isis/target-station-2/> 10, 17
- [50] A. V. Prokofiev, J. Blomgren, M. Majerle, R. Nolte, S. Rottger, S. Platt, X. X. Cai, and A. Smirnov, “Characterization of the ANITA Neutron Source for Accelerated SEE Testing at The Svedberg Laboratory,” *Radiation Effects Data Workshop, 2009 IEEE*, pp. 166–173, Jul. 2009. 10, 15, 16, 146
- [51] A. V. Prokofiev, O. Byström, C. Ekström, V. Ziemann, J. Blomgren, S. Pomp, M. Osterlund, and U. Tippawan, “A new neutron beam facility at TSL,” in *Proc. International Workshop on Fast Neutron Detectors and Applications (FNDA2006)*, Apr. 2006, poS(FNDA2006)016. [Online]. Available: [http://pos.sissa.it/archive/conferences/025/016/FNDA2006\\_016.pdf](http://pos.sissa.it/archive/conferences/025/016/FNDA2006_016.pdf) 10
- [52] A. V. Prokofiev, J. Blomgren, R. Nolte, S. P. Platt, S. Röttger, and A. N. Smirnov, “Characterization of the ANITA neutron source for accelerated SEE testing at The Svedberg Laboratory,” in *Proceedings of the 8th European Workshop on Radiation Effects on Components and Systems*, 2008, pp. 260–267. 10
- [53] Boeing Radiation Effects Laboratory. [Online]. Available: <http://www.boeing.com/brt/brel/neutron.html> 11
- [54] P. Truscott, C. Dyer, A. Frydland, A. Hands, S. Clucas, and K. Hunter, “Neutron energy-deposition spectra measurements, and comparisons with Geant4 predictions,” *IEEE Transactions on Nuclear Science*, vol. 53, no. 4, pp. 1883–1889, Aug. 2006. 12, 13, 71, 104, 105, 114, 139, 150, 167, 175

- [55] S. Platt and Z. Török, “Analysis of SEE-inducing charge generation in the neutron beam at The Svedberg Laboratory,” *IEEE Transactions on Nuclear Science*, vol. 54, no. 4, pp. 1163–1169, Aug. 2007. 12, 20, 171, 175
- [56] F. Lei, R. Truscott, C. Dyer, B. Quaghebeur, D. Heynderickx, R. Nieminen, H. Evans, and E. Daly, “MULASSIS: a Geant4-based multilayered shielding simulation tool,” *Nuclear Science, IEEE Transactions on*, vol. 49, no. 6, pp. 2788 – 2793, Dec. 2002. 12
- [57] P. Truscott, F. Lei, C. Dyer, B. Quaghebeur, D. Heyndericks, P. Nieminen, H. Evans, E. Daly, A. Mohammadzadeh, and G. Hopkinson, “MULASSIS - Monte Carlo Radiation Shielding Simulation Tool for Space Applications Made Easy,” in *Radiation and its Effects on Components and Systems, RADECS 2003, Proceedings of the 7th European Conference*, Noordwijk, The Netherlands, Sept. 2004, pp. 191–196. 12
- [58] Geant 4. [Online]. Available: <http://geant4.cern.ch/> 13, 183
- [59] MCNP. Los Alamos National Laboratory. [Online]. Available: <https://laws.lanl.gov/vhosts/mcnp.lanl.gov/> 13, 183
- [60] FLUKA. [Online]. Available: <http://www.fluka.org/fluka.php> 13, 183
- [61] G. F. Knoll, *Radiation Detection and Measurements*. John Wiley & Sons, 2000. 15, 16, 17, 21, 22, 23, 34, 37, 42, 54, 66, 82, 84, 142, 145
- [62] R. C. Haight, S. Noda, R. O. Nelson, J. M. O’Donnell, M. Devlin, A. Chatillon, T. Granier, J. Taieb, B. Laurent, G. Belier, J. A. Becker, and C.-Y. Wu, “Fission neutron spectra measurements at LANSCE—status and plans,” *AIP Conference Proceedings*, vol. 1175, no. 1, pp. 241–248, 2009. 15
- [63] S. Wender, S. Balestrini, A. Brown, R. Haight, C. Laymon, T. Lee, P. Lisowski, W. McCorkle, R. Nelson, W. Parker, and N. Hill, “A fission ionization detector for neutron flux measurements at a spallation source,” *Nuclear Instruments and Methods in Physics Research Section A: Accelerators, Spectrometers, Detectors and Associated Equipment*, vol. 36, no. 1-2, pp. 226–231, 1993. 15

- [64] L. Tommasino, N. Klein, and P. Solomon, “Thin-film breakdown counter of fission fragments,” *Journal of Applied Physics*, vol. 46, no. 4, pp. 1484–1488, Apr. 1975. 15
- [65] V. Eismont, A. Prokofyev, and A. Smirnov, “Thin-film breakdown counters and their applications (review),” *Radiation Measurements*, vol. 25, no. 1-4, pp. 151–156, 1995. 15
- [66] A. Prokofyev, A. Smirnov, and P.-U. Renberg, “A monitor of intermediate-energy neutrons based on Thin Film Breakdown Counters,” TSL, Tech. Rep. 0284-2769, Jan. 1999. [Online]. Available: [http://www4.tsl.uu.se/rapporter/tsl\\_lisv/1999/tslisv990203.pdf](http://www4.tsl.uu.se/rapporter/tsl_lisv/1999/tslisv990203.pdf) 15
- [67] A. Smirnov, A. V. Prokofyev, E. E. Rodionova, C. D. Frost, S. Ansell, E. Schooneveld, G. Gorini, and A. Pietropaolo, “Characterisation of the high-energy neutron field at the ISIS-VESUVIO facility by means of thin-film breakdown counters,” Science & Technology Facilities Council, Tech. Rep. RAL-TR-2010-024, Jul. 2010. [Online]. Available: <http://epubs.cclrc.ac.uk/epub/bitstream/5379/RALTR-2010-024.pdf> 15
- [68] A. V. Prokofyev, J. Blomgren, O. Byström, C. Ekström, S. Pomp, U. Tip-pawan, V. Ziemann, and M. Österlund, “The TSL neutron beam facility,” *Radiation Protection Dosimetry*, vol. 126, no. 1-4, pp. 18–22, 2007. 16
- [69] V. Auzelyte, F. Andersson, M. Elfman, P. Kristiansson, J. Pallon, M. Wegdd, M. Nilsson, and N. Arteaga Marrero, “On-line measurement of proton beam current in pA range,” *Nuclear Instruments and Methods in Physics Research Section B: Beam Interactions with Materials and Atoms*, vol. 249, no. 1-2, pp. 760 – 763, 2006. 16
- [70] NIF Beam Specifications. [Online]. Available: <http://www.triumf.ca/pif-nif/nif-beam-specifications-0> 16
- [71] R. Bramblett, R. I. Ewing, and T. Bonner, “A new type of neutron spectrometer,” *Nuclear Instruments and Methods*, vol. 9, no. 1, pp. 1 – 12, 1960. 16

- [72] M. Takada, T. Nunomiya, T. Ishikura, T. Nakamura, B. J. Lewis, L. G. I. Bennett, I. L. Getley, and B. H. Bennett, “Measuring cosmic-ray exposure in aircraft using real-time personal dosimeters,” *Radiation Protection Dosimetry*, 2011. [Online]. Available: <http://rpd.oxfordjournals.org/content/early/2011/05/31/rpd.ncr221.abstract> 16
- [73] P. Danyluk, “Measurement of neutron spectra in the AWE workplace using a Bonner sphere spectrometer,” *Journal of Radiological Protection*, vol. 30, pp. 699 – 715, Dec. 2010. 16
- [74] C. Piocha, V. Maresa, W. Ruhma, H. Iwaseb, T. Satoc, M. Hagiwarb, Y. Satohc, D. Nakanec, H. Nakashimc, Y. Sakamotoc, H. Yashimad, T. Matsumotoe, A. Masudae, J. Nishiyamae, T. Itogaf, C. Theisg, E. Feldbaumerg, L. Jagerhoferg, A. Tamiih, K. Hatanakah, and T. Nakamurai, “Calibration of a Bonner sphere spectrometer in quasi-monoenergetic neutron fields of 244 and 387 MeV,” *Journal of Instrumentation*, vol. 6, 2011. 17
- [75] R. Schütz, G. Fehrenbacher, J. P. Biersack, M. Wielunski, and W. Wahl, “Energy deposition distributions caused by fast neutrons in converter type silicon detectors,” *Radiation Effects and Defects in Solids*, vol. 157, no. 4, p. 427, 2002. 17, 18
- [76] A. Hands and C. Dyer, “A Technique for Measuring Dose Equivalent and Neutron Fluxes in Radiation Environments Using Silicon Diodes,” *Nuclear Science, IEEE Transactions on*, vol. 56, no. 6, pp. 3442 –3449, Dec. 2009. 17, 19, 136, 146
- [77] D. Prokopovich, M. Reinhard, I. Cornelius, and A. Rosenfeld, “Response of a PIN Diode and SOI Microdosimeter to the TSL Quasi-Monoenergetic Neutron Field,” *Nuclear Science, IEEE Transactions on*, vol. 58, no. 6, pp. 3321 –3327, Dec. 2011. 17
- [78] M. Angelone, G. Aielli, S. Almaviva, R. Cardarelli, D. Lattanzi, M. Marinelli, E. Milani, G. Prestopino, M. Pillon, R. Santonico, A. Tucciarone, C. Verona,

- and G. Verona-Rinati, "Neutron Detectors Based Upon Artificial Single Crystal Diamond," *Nuclear Science, IEEE Transactions on*, vol. 56, no. 4, pp. 2275–2279, Aug. 2009. 17, 19
- [79] M. Angelone, M. Pillon, M. Marinelli, E. Milani, A. Paoletti, A. Tucciarone, G. Pucella, and G. Verona-Rinati, "Development and application of CVD diamond detectors to 14 MeV neutron flux monitoring," *Radiation Protection Dosimetry*, vol. 110, no. 1-4, pp. 233–236, 2004. 17, 19
- [80] S. Seshadri, A. Dulloo, F. Ruddy, J. Seidel, and L. Rowland, "Demonstration of an SiC neutron detector for high-radiation environments," *Electron Devices, IEEE Transactions on*, vol. 46, no. 3, pp. 567–571, Mar. 1999. 17, 173
- [81] H. Asai, K. Sugimoto, I. Nashiyama, Y. Iide, K. Shiba, M. Matsuda, and Y. Miyazaki, "Terrestrial neutron-induced single-event burnout in SiC power diodes," pp. 238–243, Sept. 2011. 17
- [82] A. Mainwood, "CVD diamond particle detectors," *Diamond and Related Materials*, vol. 7, no. 2-5, pp. 504–509, 1998. 18
- [83] S. Agosteo, G. D'Angelo, A. Fazzi, A. F. Para, A. Pola, L. Ventura, and P. Zotto, "Performance of a neutron spectrometer based on a PIN diode," *Radiat Protection Dosimetry*, vol. 116, no. 1-4, pp. 180–184, 2005. 18
- [84] R. Schütz, M. Wielunski, G. Fehrrnbacher, J. Biersack, and W. Wahl, "Calculation of pulse height distributions for neutron irradiated  ${}^6\text{LiF}$  converter silicon detectors," *Radiation Protection Dosimetry*, vol. 84, pp. 393–397, 1999. 18
- [85] R. Schütz, G. Fehrenbacher, M. Wielunski, and W. Wahl, "A three Si detector system for personal neutron dosimetry developed by means of Monte Carlo simulation calculations," *Radiation Protection Dosimetry*, vol. 104, no. 1, pp. 17–26, 2003. 18
- [86] C. Dyer, P. Truscott, C. Sanderson, C. Watson, C. Peerless, P. Knight, R. Mugford, T. Cousins, and R. Noulty, "Radiation environment measurements from CREAM and CREDO during the approach to solar maximum,"

- Nuclear Science, IEEE Transactions on*, vol. 47, no. 6, pp. 2208 –2217, Dec. 2000. 19
- [87] C. Dyer, F. Lei, A. Hands, S. Clucas, and B. Jones, “Measurements of the atmospheric radiation environment from CREAM and comparisons with models for quiet time and solar particle events,” *Nuclear Science, IEEE Transactions on*, vol. 52, no. 6, pp. 2326 – 2331, 2005. 19
- [88] C. Dyer, A. Sims, P. Truscott, C. Peerless, C. Watson, and C. Underwood, “Measurement of the radiation environment from LEO to GTO using the CREAM and CREDO experiments,” *Nuclear Science, IEEE Transactions on*, vol. 42, no. 6, pp. 1975 –1982, Dec. 1995. 19
- [89] C. Dyer, P. Truscott, C. Peerless, C. Watson, H. Evans, P. Knight, M. Cosby, C. Underwood, T. Cousins, and R. Noulty, “Updated measurements from CREAM and CREDO and implications for environment and shielding models,” *Nuclear Science, IEEE Transactions on*, vol. 45, no. 3, pp. 1584 –1589, Jun. 1998. 19
- [90] C. S. Dyer, P. R. Truscott, C. L. Peerless, C. J. Watson, H. E. Evans, P. Knight, M. Cosby, C. Underwood, T. Cousins, R. Noulty, and C. Maag, “Implications for space radiation environment models from CREAM & CREDO measurements over half a solar cycle,” *Radiation Measurements*, vol. 30, no. 5, pp. 569 – 578, 1999. 19
- [91] M. Pillon, M. Angelone, P. Batistoni, R. Villari, S. Almaviva, M. Marinelli, E. Milani, G. Prestopino, C. Verona, and G. Rinati, “Development of on-line tritium monitor based upon artificial diamond for fusion applications,” *Advancements in Nuclear Instrumentation Measurement Methods and their Applications (ANIMMA), 2009 First International Conference on*, pp. 1 –4, Jun. 2009. 19
- [92] R. Bailey, C. Damerell, R. English, A. Gillman, A. Lintern, S. Watts, and F. Wickens, “First measurement of efficiency and precision of CCD detectors for high energy physics,” *Nuclear Instruments and Methods in Physics Research*, vol. 213, pp. 201–215, 1983. 20

- [93] Z. Török, “Development of image processing system for cosmic ray effect analysis,” Ph.D. dissertation, University of Central Lancashire, 2007. 20
- [94] A. Chugg, R. Jones, P. Jones, P. Nieminen, A. Mohammadzadeh, M. Robbins, and K. Lovell, “A CCD miniature radiation monitor,” *Nuclear Science, IEEE Transactions on*, vol. 49, no. 3, pp. 1327 – 1332, Jun. 2002. 20
- [95] A. M. Chugg, M. J. Moutrie, A. J. Burnell, and R. Jones, “A statistical technique to measure the proportion of MBU’s in SEE testing,” *Nuclear Science, IEEE Transactions on*, vol. 53, no. 6, pp. 3139 –3144, 2006. 20
- [96] S. Platt, B. Cassels, and Z. Török, “Development and application of a neutron sensor for single-event effects analysis,” *Journal of Physics:Conference Series* 15, pp. 172–176, 2005. 20, 171
- [97] Z. Török and S. Platt, “Application of imaging systems to characterization of single-event effects in high-energy neutron environments,” *IEEE Transactions on Nuclear Science*, vol. 53, no. 6, pp. 3718–3725, Dec. 2006. 20, 148
- [98] S. Platt, Z. Török, C. Frost, and S. Ansell, “Charge-collection and single-event upset measurements at the ISIS neutron source,” *IEEE Transactions on Nuclear Science*, vol. 55, no. 4, pp. 2126–2132, Aug. 2008. 20
- [99] S. Platt, A. Prokofiev, and X. Cai, “Fidelity of energy spectra at neutron facilities for single-event effects testing.” Reliability Physics Symposium (IRPS), 2010 IEEE International, May 2010, pp. 411 –416. 20
- [100] J. F. Ziegler, H. P. Muhlfeld, C. J. Montrose, H. W. Curtis, T. J. O’Gorman, and J. M. Ross, “Accelerated testing for cosmic soft-error rate,” *IBM J. Res. Dev.*, vol. 40, no. 1, pp. 51–72, 1996. 20
- [101] R. Harboe-Sorensen, F.-X. Guerre, and A. Roseng, “Design, Testing and Calibration of a ”Reference SEU Monitor” System,” *Radiation and Its Effects on Components and Systems, 2005. RADECS 2005. 8th European Conference on*, pp. B3–1 –B3–7, Sept. 2005. 21

- [102] R. Harboe-Sorensen, C. Poivey, F.-X. Guerre, A. Roseng, F. Lochon, G. Berger, W. Hajdas, A. Virtanen, H. Kettunen, and S. Duzellier, “From the Reference SEU Monitor to the Technology Demonstration Module On-Board PROBA-II,” *Nuclear Science, IEEE Transactions on*, vol. 55, no. 6, pp. 3082–3087, Dec. 2008. 21
- [103] H. Spieler, *Semiconductor Detector Systems*. Oxford University Press, 2005. 21, 22, 23, 75
- [104] CR-200 Gaussian shaping amplifier: application guide. [Online]. Available: <http://www.fastcomtec.com/fwww/datashee/amp/cr-200.pdf> 21
- [105] F. S. Goulding and D. A. Landis, “Signal processing for semiconductor detectors,” *Nuclear Science, IEEE Transactions on*, vol. 29, no. 3, pp. 1125–1141, 1982. 21
- [106] Y. Hosono, Sjafruddin, T. Iguchi, and M. Nakazawa, “Fast neutron detector using PIN-type silicon photodiode,” *Nuclear Instruments and Methods in Physics Research Section A: Accelerators, Spectrometers, Detectors and Associated Equipment*, vol. 361, no. 3, pp. 554–557, 1995. 23
- [107] S. Rocheman, F. Wrobel, J.-R. Vaille, F. Saigne, C. Weulersse, N. Buard, and T. Carriere, “Neutron induced energy deposition in a silicon diode,” *IEEE Transactions on Nuclear Science*, vol. 55, no. 6, pp. 3146–3150, Dec. 2008. 23
- [108] I. Peric, L. Blanguart, G. Comes, P. Denes, K. Einsweiler, P. Fischer, E. Mandelli, and G. Meddeler, “The FEI3 readout chip for the ATLAS pixel detector,” *Nuclear Instruments and Methods in Physics Research Section A: Accelerators, Spectrometers, Detectors and Associated Equipment*, vol. 565, no. 1, pp. 178–187, 2006. 23
- [109] S. M. Kay, *Fundamentals of Statistical Signal Processing, Estimation Theory*. Prentice-Hall PTR, 1993, vol. 1. 30, 42
- [110] Silicon photodetector series 5T. Centronic. [Online]. Available: <http://www.captron.com.au/Photodetectors/Centronicdf> 30, 31, 32, 125

- [111] TLE2072 datasheet. Texas Instruments. [Online]. Available: <http://www.datasheetcatalog.org/datasheet/texasinstruments/tle2072.pdf> 31, 176
- [112] NI PCI 6251 datasheet. National Instruments. [Online]. Available: <http://www.ni.com/pdf/products/us/044063301101dlr.pdf> 31, 170
- [113] NI BNC-2120. National Instruments. [Online]. Available: <http://sine.ni.com/nips/cds/view/p/lang/en/nid/10712> 31
- [114] S. M. Kay, *Fundamentals of Statistical Signal Processing, Detection Theory*. Prentice-Hall PTR, 1998, vol. 2. 42, 45, 47, 48, 50, 69, 188
- [115] L. Zhang, S. Platt, R. Edwards, and C. Allabush, “In-situ neutron dosimetry for single-event effect accelerated testing,” *IEEE Transactions on Nuclear Science*, vol. 56, no. 4, pp. 2070–2076, Aug. 2009. 42, 54, 71, 121
- [116] Inverse error function. [Online]. Available: <http://www.mathworks.com/help/techdoc/ref/erfinv.html> 66
- [117] S. Winitzki. (2008, February) A handy approximation for the error function and its inverse. [Online]. Available: <http://homepages.physik.uni-muenchen.de/~Winitzki/erf-approx.pdf> 66
- [118] N. Gehrels, “Confidence limits for small numbers of events in astrophysical data,” *The Astrophysical Journal*, vol. 303, pp. 336–346, 1986. 82, 198, 199
- [119] E. Petersen, “Single-event data analysis,” *Nuclear Science, IEEE Transactions on*, vol. 55, no. 6, pp. 2819–2841, Dec. 2008. 85, 198
- [120] *Update of X ray and gamma ray decay data standards for detector calibration and other applications Volume 1: Recommended decay data, high energy gamma ray standards and angular correlation coefficients*, International Atomic Energy Agency Std. Tech. Rep. STI/PUB/1287, November 2007. [Online]. Available: [http://www-nds.iaea.org/reports-new/tecdocs/sti-pub-1287\\_Vol1.pdf](http://www-nds.iaea.org/reports-new/tecdocs/sti-pub-1287_Vol1.pdf) 134

- [121] N. Kerness, T. Hossain, and S. McGuire, “Impurity study of alumina and aluminum nitride ceramics: Microelectronics packaging applications,” *Applied Radiation and Isotopes*, vol. 48, no. 1, pp. 5 – 9, 1997. 134
- [122] PENDL: Plotter for Evaluated Nuclear Data Libraries. Japan Charged-Particle Nuclear Reaction Data Group (JCPRG). [Online]. Available: <http://www.jcprg.org/endl/work/pendl-276.html> 135
- [123] A. Cheminet, V. Lacoste, V. Gressier, M. A. Hubert, G, and M. Pepino. Characterization of the IRSN neutron multisphere spectrometer (HERMEIS) at European standard calibration fields. 2nd International workshop on fast neutron neutron detectors and applications, November 6-11 2011. [Online]. Available: [http://iopscience.iop.org/1748-0221/7/04/C04007/pdf/1748-0221.7\\_04\\_C04007.pdf](http://iopscience.iop.org/1748-0221/7/04/C04007/pdf/1748-0221.7_04_C04007.pdf) 135
- [124] A. Hands. Personal communication. 136, 146
- [125] H. Spieler. Introduction to radiation detectors and electronics. UC-Berkeley course notes. [Online]. Available: [http://www-physics.lbl.gov/~spieler/physics\\_198\\_notes\\_1999/](http://www-physics.lbl.gov/~spieler/physics_198_notes_1999/) 143
- [126] X-ray mass attenuation coefficients. [Online]. Available: <http://physics.nist.gov/PhysRefData/XrayMassCoef/tab3.html> 143, 144
- [127] M. Pietropaolo, M. Tardocchi, E. Schooneveld, and R. Senesi, “Characterization of the  $\gamma$ -rays background in epithermal neutron scattering measurements at pulsed neutron sources,” *Nuclear Instruments and Methods in Physics Research Section A: Accelerators, Spectrometers, Detectors and Associated Equipment*, vol. 568, no. 2, pp. 826 – 838, 2006. 145
- [128] J. Brückner, R. Reedy, P. Englert, and D. Drake, “Experimental simulations of planetary gamma-ray spectroscopy using thick targets irradiated by protons,” *Nuclear Instruments and Methods in Physics Research Section B: Beam Interactions with Materials and Atoms*, vol. 269, no. 22, pp. 2630 – 2640, 2011. 145

- [129] Q. Z. Yu, T. J. Liang, and W. Yin, “Activity and radiation protection studies for the W-Ta target of CSNS,” *Radiat Protection Dosimetry*, vol. 136, no. 3, pp. 216–221, 2009. 146
- [130] Y. E. Titarenko, V. F. Batyaev, A. Y. Titarenko, M. A. Butko, K. V. Pavlov, S. N. Florya, R. S. Tikhonov, V. M. Zhivun, A. V. Ignatyuk, S. G. Mashnik, S. Leray, A. Boudard, J. Cugnon, D. Mancusi, Y. Yariv, K. Nishihara, N. Matsuda, H. Kumawat, G. Mank, and W. Gudowski, “Measurement and simulation of the cross sections for nuclide production in  $^{nat}\text{W}$  and  $^{181}\text{Ta}$  targets irradiated with 0.04- to 2.6-GeV protons,” *PHYSICS OF ATOMIC NUCLEI*, vol. 74, no. 4, pp. 551–572, Apr. 2011. 146
- [131] E. Normand, D. Oberg, J. Wert, J. Ness, P. Majewski, S. Wender, and A. Gavron, “Single event upset and charge collection measurements using high energy protons and neutrons,” *IEEE Transactions on Nuclear Science*, vol. 41, no. 6, pp. 2203–2209, Dec 1994. 150
- [132] X. X. Cai, S. Platt, and W. Chen, “Modelling neutron interactions in the imaging SEE monitor,” *Nuclear Science, IEEE Transactions on*, vol. 56, no. 4, pp. 2035–2041, Aug. 2009. 150, 179
- [133] X. X. Cai and S. Platt, “Modeling neutron interactions and charge collection in the imaging single-event effects monitor,” *Nuclear Science, IEEE Transactions on*, vol. 58, no. 3, pp. 910–915, June 2011. 151
- [134] J. Ziegler. SRIM & TRIM. [Online]. Available: <http://www.srim.org> 151
- [135] TSL testing service. [Online]. Available: [http://www.tsl.uu.se/radiation\\_testing/tsl\\_beam\\_data\\_qmn.html](http://www.tsl.uu.se/radiation_testing/tsl_beam_data_qmn.html) 159
- [136] ISIS Second Target Station Project. [Online]. Available: <http://www.isis.stfc.ac.uk/instruments/chipir/publications> 159
- [137] A. Donzella, M. Barbui, F. Bocci, G. Bonomi, M. Cinausero, D. Fabris, A. Fontana, E. Giroletti, M. Lunardon, S. Moretto, G. Nebbia, M. Nocchi, S. Pesente, G. Prete, V. Rizzi, G. Viesti, and A. Zenoni, “A proton

- recoil telescope for neutron spectroscopy,” *Nuclear Instruments and Methods in Physics Research Section A: Accelerators, Spectrometers, Detectors and Associated Equipment*, vol. 613, no. 1, pp. 58 – 64, 2010. 171
- [138] G. Hopkinson, T. Goodman, and S. Prince, *A guide to the use and Calibration of Detector Array Equipment*. SPIE— The International Society for Optical Engineering, 2004. 171
- [139] L. Zhang and S. Platt, “Minimally invasive neutron beam monitoring for single-event effects accelerated testing,” in *Radiation Effects On Components System*, 2011. 172
- [140] H. Kraner, Z. Li, and K. Posnecker, “Fast neutron damage in silicon detectors,” *Nuclear Instruments and Methods in Physics Research Section A: Accelerators, Spectrometers, Detectors and Associated Equipment*, vol. 279, no. 1-2, pp. 266 – 271, 1989. 172
- [141] A. Prokofiev, J. Blomgren, S. Platt, R. Nolte, S. Rottger, and A. Smirnov, “ANITA — a new neutron facility for accelerated SEE testing at the svedberg laboratory,” *Reliability Physics Symposium, 2009 IEEE International*, pp. 929 –935, Apr. 2009. 179
- [142] Personal communication from D. Boe to S.P.Platt. 183
- [143] S. Ohkawa, M. Yoshizawa, and K. Husimi, “Direct synthesis of the Gaussian filter for nuclear pulse amplifiers,” *Nuclear Instruments and Methods*, vol. 138, no. 1, pp. 85 – 92, 1976. 185
- [144] ENDF/B-VII Incident Neutron Data. [Online]. Available: <http://t2.lanl.gov/data/neutron7.html> 197